Studies on Solid State Hydrogen Storage Materials

By

PRIYANKA RUZ
Enrolment No. CHEM01201104020

BHABHA ATOMIC RESEARCH CENTRE

A thesis submitted to the
Board of Studies in Chemical Sciences

In partial fulfillment of requirements
for the Degree of
DOCTOR OF PHILOSOPHY
of
HOMI BHABHA NATIONAL INSTITUTE

August, 2017

Homi Bhabha National Institute

Recommendations of the Viva Voce Committee

As members of the Viva Voce Committee, we certify that we have read the dissertation prepared by **Mrs. Priyanka Ruz** entitled "**Studies on Solid State Hydrogen Storage Materials**" and recommend that it may be accepted as fulfilling the thesis requirement for the award of Degree of Doctor of Philosophy.

Chairman - Dr. D. Das D. Das. **Date:** 12-07-2018

Guide / Convener - Dr. V. Sudarsan Sudarsan.V **Date:** 12/7/2018.

Co-guide - Dr. C. Majumder **Date:** 12/7/18

Examiner – Prof. P. Muthukumar 12/7/18 **Date:** 12/7/18

Member 1- Dr. A.K. Tripathi Tripathi **Date:** 12.07.2018

Member 2- Dr. S.C. Parida **Date:** 12/07/2018

Member 3- Dr. K.R.S. Chandrakumar **Date:** 12/07/2018

Final approval and acceptance of this thesis is contingent upon the candidate's submission of the final copies of the thesis to HBNI.

I/We hereby certify that I/we have read this thesis prepared under my/our direction and recommend that it may be accepted as fulfilling the thesis requirement.

Date: 12/7/2018

Place: Anushaktinagar

Sudarsan V
Dr. V. Sudarsan

12/7/18
Dr. C. Majumder

STATEMENT BY AUTHOR

This dissertation has been submitted in partial fulfillment of requirements for an advanced degree at Homi Bhabha National Institute (HBNI) and is deposited in the Library to be made available to borrowers under rules of the HBNI.

Brief quotations from this dissertation are allowable without special permission, provided that accurate acknowledgement of source is made. Requests for permission for extended quotation from or reproduction of this manuscript in whole or in part may be granted by the Competent Authority of HBNI when in his or her judgment the proposed use of the material is in the interests of scholarship. In all other instances, however, permission must be obtained from the author.

Priyanka Ruz

DECLARATION

I, hereby declare that the investigation presented in the thesis has been carried out by me. The work is original and has not been submitted earlier as a whole or in part for a degree / diploma at this or any other Institution / University.

Priyanka Ruz

List of Publications arising from the thesis

Journal

1. "Hydrogen absorption characteristics and Mössbauer spectroscopic study of $Ti_{0.67}Nb_{0.33-x}Fe_x$ (x = 0.00, 0.13, 0.20) alloys", **Priyanka Ruz**, Asheesh Kumar, Seemita Banerjee, S.S. Meena, C.G.S. Pillai, *J Alloys Comp*, **2014**, *585*, 120-128.
2. "Comparative evaluation of hydrogen storage behavior of Pd doped carbon nanotubes prepared by wet impregnation and polyol methods" Seemita Banerjee, Kinshuk Dasgupta, Asheesh Kumar, **Priyanka Ruz**, B. Vishwanadh, J. B. Joshi, V. Sudarsan, *Int J Hydrogen Energy*, **2015**, 40, 3268-3276.
3. "An investigation of hydriding performance of $Zr_{2-x}Ti_xNi$ (x = 0.0, 0.3, 0.7, 1.0) alloys", **Priyanka Ruz**, V. Sudarsan, *J Alloys Comp*, **2015**, 627, 123-131.
4. "Structural Evolution of Turbostratic Carbon: Implications in H_2 storage", **Priyanka Ruz**, Seemita Banerjee, M. Pandey, V. Sudarsan, P. U. Sastry, R. J. Kshirsagar, *Solid State Sci*, **2016**, 62, 105-111.
5. "Influence of Laves phase on microstructure and hydrogen storage properties of Ti-Cr-V based alloy", Seemita Banerjee, Asheesh Kumar, **P. Ruz**, P. Sengupta, *Int J Hydrogen Energy*, **2016**, 41, 18130-18140.
6. "Thermodynamic, Kinetic and microstructural evolution of $Ti_{0.43}Zr_{0.07}Cr_{0.25}V_{0.25}$ alloy upon hydrogenation", **Priyanka Ruz**, Seemita Banerjee, Rumu Halder, Asheesh Kumar, V. Sudarsan, *Int J Hydrogen Energy*, **2017**, 42, 11482-11492.

Chapters in books and lectures notes

1. "Application of Metal Hydride Systems for Hydrogen Storage", Seemita Banerjee, **Priyanka Ruz**, Asheesh Kumar, V. Sudarsan, SMC Bulletin, Volume 5, No. 2, August 2014.

Conferences

1. Hydrogen absorption characteristics of Ti-Nb alloys: Effect of Fe substitution, **Priyanka Das**, Asheesh Kumar, Seemita Banerjee, C.G.S. Pillai, ICAER, 9-11 December, 2011, IIT Mumbai.
2. Effect of Ti Substitution for Hydrogen Absorption properties of Zr_2Ni Alloy, **Priyanka Das**, Asheesh Kumar, Seemita Banerjee, C.G.S. Pillai, ISMC, 11-15 December, 2012, BARC, Mumbai.
3. Hydrogen Absorption Kinetics Study of $Ti_2Nb_{1-x}Fe_x$ (x = 0, 0.4, 0.6) alloys, **Priyanka Das**, Asheesh Kumar, Seemita Banerjee, C.G.S. Pillai, ISMC, 11-15 December, 2012, BARC, Mumbai.
4. Effect of carbonization temperature on the structure of zeolite templated carbon, **Priyanka Ruz**, V. Sudarsan, THERMANS, 19-21 December, 2013, BARC, Mumbai.
5. Structural and Mössbauer Spectroscopic Study of Cubic Phase Hydrogen Storage Alloys $Ti_2Nb_{1-x}Fe_x$, S. S. Meena, **Priyanka Das**, A. Kumar, S. Banerjee, C. G. S. Pillai, S. M. Yusuf, AIP Conf. Proc. 1512 (2013) 1096-1097.
6. Hydrogen Storage Properties of Zeolite Templated Porous Carbon, **Priyanka Ruz,** Seemita Banerjee, V. Sudarsan, ISMC, 9-13 December, 2014, BARC, Mumbai.
7. Hydrogen Storage Studies of Zr Substituted Ti_2CrV Alloy, **Priyanka Ruz**, Seemita Banerjee, V. Sudarsan, ISMC, 9-13 December, 2014, BARC, Mumbai.
8. Comparative Evaluation of Hydrogen Storage Behavior of Pd Doped Carbon Nanotubes Prepared by Wet Impregnation and Polyol Methods, S. Banerjee, K. Dasgupta, A. Kumar, **P. Ruz**, J. B. Joshi, V. Sudarsan, ISMC, 9-13 December, 2014, BARC, Mumbai.

9. Synthesis, characterization and hydrogen storage studies on porous carbon, **Priyanka Ruz,** Seemita Banerjee, M. Pandey, V. Sudarsan, AIP Conference proceedings, 1665, (2015) 140047(1)-140047(3).
10. Turbostartic carbon: A potential candidate for hydrogen adsorption, **Priyanka Ruz**, Seemita Banerjee, V. Sudarsan, ISMC, 6-10 December, 2016, BARC, Mumbai.

Priyanka Ruz

Dedicated

To my Parents

ACKNOWLEDGEMENTS

It would not have been possible to write this thesis without the help and support of the nice people around me. I take this opportunity to express my gratitude to all of them. Please forgive me whom I forget to mention.

First and foremost, I would like to convey my sincere thanks and appreciation to my guide **Dr. V. Sudarsan** for his sincere guidance, care, patience and continuous support during my Ph.D work. I have been fortunate to have such a supervisor who gave me the freedom to explore on my own, and at the same time the guidance to recover when my steps faltered. It has been really a privilege being his student. I am equally grateful to **Dr. C. G. S. Pillai**, who guided me at the initial stages of my Ph.D work. My special thanks goes to my co-guide **Dr. C. Majumder** for his insightful comments, constructive criticism and generous advice throughout the Ph.D work.

I must thank to all the past and present members of my doctoral committee members: **Dr. D. Das, Dr. S. R. Bharadwaj, Dr. A. K. Tripathi, Dr. S. C. Parida, Dr. K. R. S. Chandrakumar** for their encouragement, timely cooperation, critical evaluation and valuable suggestions during the course of my Ph.D work.

I would take this opportunity to express my deep gratitude to **Dr. P. D. Naik,** Associate Director, Chemistry Group and **Dr. (Mrs.) K. I. Priyadarsini**, Head, Chemistry Division of BARC for providing me financial, academic and technical support in BARC to carry out my Ph.D work.

I would like to express my sincere gratitude to **Asheesh Bhaiya** and **Seemita Di** who have introduced me to this field. Their innumerable support in crucial experiments has helped me a lot to bring out the proper shape of this Ph.D work. Heartiest thanks to my other lab mates **Tapas Das** and **Dr. Pradip Kumar** for their continuous help and encouragement. I am indebted to all the Chemistry Division colleagues and staffs for their help and support from time to time.

My sincere thanks to all my fellow lab mates: **Dr. Atindra Mohan Banerjee, Dr. (Mrs.) Mrinal Pai, Dr. Rajini P Antony, Dr. Deepak Tyagi, Mr. Ashish Nadar, Ms. Sushma Rawool, Mr. Rajendra Singh, Mr. Nilesh Kumar** for their direct or indirect support which made my daily work enjoyable and fun.

I am very grateful to have some excellent **teachers** throughout my academic career. Their influence and support helped me a lot to pursue this career.

How can I forget to thank my friends **Aparajita** and **Debashree** for being with me whenever and for whatever I needed? Special thanks to my University friends: **Amrita, Aattreyidi, Somdutta** and **Abhishake**.

Finally, I thank my **parents**, **parents-in-law, brother** for their unconditional love and immense support without which I may not arrive at this point of my life. No words of acknowledgment will be sufficient for them. **Soumen** (my husband) – simply thanking you will be less for what you mean to me. You always encouraged me up at every step of life. I would like to express thanks to my little son **Spandan** who in his own way geared me up to reach the goal.

Priyanka Ruz

CONTENTS

CHAPTER 2: Synthesis Methods and Experimental Techniques 40

CHAPTER 5: Hydrogen Storage Properties of Ti-V Based Alloys 128

Synopsis

Today hydrogen is considered as one of the most promising fuels of future because of its large abundance, light weight, high gravimetric energy density, non-polluting and renewable nature [1]. To make hydrogen fuelled automobiles a reality in near future, it is necessary to develop suitable hydrogen storage medium that is safe, cost-effective, possesses high storage capacity with fast charge-discharge properties and favorable thermodynamics [2]. Hydrogen can be stored in any of the three states namely gaseous, liquid or solid. However, storage as compressed gas and cryogenic liquid is not suitable for on-board vehicular application due to safety issues and large amount of energy consumption. On the other hand, solid state hydrogen storage technology has received tremendous attention in recent years mainly due to its inherent safety over conventional storage methods [3]. Hydrogen can interact with solid materials either by means of physisorption or chemisorption. Most of the physisorbed systems show good reversibility, rapid kinetics but suffer from poor gravimetric storage capacity at ambient conditions. On the other hand, chemisorbed systems such as alloys/intermetallic compounds can absorb hydrogen at room temperature. However, they release hydrogen at relatively higher temperature and need rigorous activation prior to hydrogen absorption. Thus both physisorbed and chemisorbed systems are having their own advantages and disadvantages. A detailed understanding of the fundamental aspects of hydrogen storage characteristics of both physisorbed and chemisorbed systems will be beneficial for the future development of suitable solid state hydrogen storage materials with improved performance characteristics. With this view, basic studies on hydrogen storage properties of representative systems, namely carbon based materials and transition metal (Ti, Zr) based alloys/intermetallic compounds, which absorb hydrogen through physisorption and chemisorption processes respectively, have been undertaken. Results of hydrogen storage

studies carried out on carbon based materials have been presented initially in the thesis and this is followed by the results of alloys/intermetallic compounds. Present thesis consists of seven chapters, with the work carried out described in four chapters (chapters 3, 4, 5 and 6). The first chapter gives an introduction regarding different hydrogen storage materials and motivation for carrying out the present study. The second chapter deals with the basic principle of techniques used for the present investigations. The last chapter is on summary of the present work and its future scope. A brief description of all the seven chapters is given below.

Chapter 1: Introduction

This chapter describes why hydrogen energy should be considered as a viable alternative to the conventionally used fossil fuels. The relevance of hydrogen storage for the development of hydrogen fuel based technologies is described in detail. The revised 2020 targets set by Department of Energy, USA (DOE) for onboard hydrogen storage systems are mentioned in this chapter as it acts as guide lines for the development of new hydrogen storage materials. Three different types of hydrogen storage methods namely compressed hydrogen gas, cryogenic liquid hydrogen and solid state hydrogen have been discussed while emphasis has been given to third method. The solid state hydrogen storage materials have been divided into two main categories depending on the nature of interaction of hydrogen with the solids, namely physisorption and chemisorption. This chapter describes the basic principles of physical adsorption as well as chemisorption. The thermodynamics of both the sorption processes are explained which is necessary to get an idea about the interaction energy associated with hydrogen sorption. Along with thermodynamics, kinetic aspects of interstitial hydride formation are also described in this chapter. Some examples of widely studied solid state hydrogen storage materials belonging to both the categories are discussed briefly. Finally, the chapter ends with the objective and motivation of the present study.

Chapter 2: Experimental

This chapter deals with different experimental methods used during PhD work. Two different methods, namely wet impregnation and polyol, employed for doping Pd nanoparticle in carbon nanotubes are discussed briefly in this chapter. After this, the arc melting method used for preparation of alloys and intermetallic compounds is described in detail. Carbon based materials, alloys and intermetallic compounds were characterized by using a variety of characterization techniques which include X-Ray Diffraction (XRD), Scanning Electron Microscopy (SEM), Energy Dispersive X-ray (EDX) analysis, Transmission Electron Microscopy (TEM), Electron Probe Micro-analysis (EPMA), Small Angle X-ray Scattering (SAXS), Thermogravimetric analysis (TGA), Differential Scanning Calorimetry (DSC), Temperature Programmed Desorption (TPD) and Particle Size Distribution. Some of the spectroscopic techniques like Nuclear Magnetic Resonance (NMR), Mössbauer, Fourier Transform Infrared (FTIR) and Raman spectroscopy were also used for characterization. A brief description of each of these techniques is given in this chapter. For the evaluation of hydrogen storage properties, the synthesized materials were subjected to interact with hydrogen gas in a fully automated Sievert's type of volumetric set up. The experimental data are cross-checked in an indigenously developed Sievert's type set up, whenever required.

Chapter 3: Hydrogen storage properties of carbon based materials

As far as hydrogen storage is concerned, carbon based materials have attracted significant attention of material scientists due to prospect for numerous structural modifications, availability of several inexpensive synthesis methods from a wide range of low-cost precursors, low density, chemical stability and biocompatibility [4]. Carbon nanotubes (CNT) are well known carbonaceous materials for gas adsorption as they possess high surface area [5]. CNT like all other carbon based materials interacts with hydrogen gas through weak van der Waals forces which results in poor hydrogen storage capacity at ambient condition. To increase the interaction energy with hydrogen bare CNTs should be modified either by doping with metal or non-metal elements or by introducing defects. This chapter focuses on the hydrogen storage characteristics of Pd doped CNTs. Pd doped CNTs have been synthesized through two different routes, namely, wet impregnation and polyol methods. The Pd doped CNTs are characterized using XRD, EDX, TEM and FTIR techniques. Room temperature hydrogen uptake of bare CNTs is only 0.056 wt% under 50 bar of pressure and this is due to weak interaction of hydrogen with the carbon support. From hydrogen adsorption studies it is confirmed that Pd doped CNTs can store more hydrogen compared to pristine CNTs. Moreover, Pd doped CNTs prepared by polyol method have higher hydrogen storage capacity than samples prepared by conventional wet impregnation method. Hydrogen storage capacities of these two samples are found to be 0.29 wt% and 0.05 wt%, respectively at 333K. Observed hydrogen adsorption properties have been explained in terms of spill over mechanism. The extent of spillover can be correlated with the extent of dispersion of Pd nanoparticles on CNT surfaces. TEM images show that polyol route gives much better dispersion of smaller Pd nanoparticles on CNTs. In wet impregnation route, the Pd nanoparticles are agglomerated whereas in polyol method, ethylene glycol acts as both reducing and capping agent thereby preventing agglomeration of Pd nanoparticles. Thus it has been established from the study that just by changing preparation method, the same element (Pd) can behave in a different way on the CNT surface and can effectively improve hydrogen storage properties.

This chapter also focuses on the hydrogen storage properties of turbostratic carbon which is having structural ordering in between that of amorphous carbon and crystalline graphite phases. The synthesis of turbostratic carbon samples from sucrose, a commonly available carbon precursor, has been described in this chapter. As-prepared samples have been annealed at three different temperatures and their structural evolution has been studied using SAXS, solid state NMR and Raman spectroscopic techniques. Results of XRD and thermo-gravimetric analysis show that the interlayer distance decreases and ordering of carbon network increases with increase in annealing temperatures. This chapter also presents hydrogen adsorption isotherms of the samples over a range of temperatures. A maximum hydrogen storage capacity of 1.25 wt% was found for the turbostratic carbon sample annealed at 900°C. The isosteric heat of adsorption (Q_{st}) was evaluated from the experimental isotherms. We have also shown the variation of Q_{st} values with extent of hydrogen uptake to get an idea about the interaction energy between turbostratic carbon and hydrogen.

Chapter 4: Hydrogen storage properties of Ti-Nb based alloys

This chapter presents hydrogen storage properties of Ti-Nb based BCC alloys. Ti based body centered cubic (BCC) alloys are attractive candidates for hydrogen storage because it can accommodate a large number of hydrogen in its open structure [6]. It is reported that Group V elements of periodic table (like Nb, V) act as stabilizer for BCC form of titanium metal (β phase). This motivated us to study the hydrogen storage properties of Nb and V stabilized BCC Ti alloys. The results of Ti-Nb based alloys have been described in this chapter whereas chapter 5 deals with hydrogen storage properties of Ti-V based alloys. Ti-Nb based alloys suffer from activation problem due to oxide layer formation on the surface. Fe incorporation in Ti-Nb alloys is known to improve their oxidation resistance [7]. Hence, hydrogen storage properties of Fe substituted Ti-Nb alloys have been investigated and the results are presented in this chapter. Three alloys with compositions $Ti_{0.67}Nb_{0.33-x}Fe_x$ (x = 0.00, 0.13, 0.20) were prepared by arc melting method and hydrogenated in a Sievert's type of set up. The alloys exist in BCC phase and get converted to FCC phase upon hydrogenation. This study shows that the alloy with higher Fe substitution (composition $Ti_{0.67}Nb_{0.13}Fe_{0.20}$) has maximum room temperature hydrogen storage capacity (2.62 wt%) with fastest kinetics.

The hydrogenation kinetics of $Ti_{0.67}Nb_{0.13}Fe_{0.20}$ alloy has been studied in detail over the temperature range from 298K to 473K. Two different types of rate equations are required to fit the kinetics data, indicating two different rate limiting steps during the progress of hydrogen absorption reaction. Activation energies for the two rate limiting steps have been calculated using the experimental kinetics data at different temperatures. In addition to that, structural studies have also been carried out using ^{57}Fe Mössbauer spectroscopic technique to see the effect Fe substitution and hydrogenation on structure of the alloys.

Chapter 5: Hydrogen storage properties of Ti-V based alloys

This chapter deals with two different approaches for improving the hydrogen storage behaviour of Ti-V based alloys. Our group has earlier developed different types of Ti-V based BCC phase alloys and some of them, like Ti_2CrV, exhibit hydrogen storage capacities as high as 4.37 wt% [8]. However, the alloy suffers from significant disadvantage of relatively higher desorption temperature. The two approaches used for solving this practical problem are elemental substitution and composite formation. The central idea of both the approaches is to use the catalytic effect of Zr based Laves phase on hydrogen absorption-desorption processes [9]. In the first approach Ti is partially substituted with Zr to form Laves phase related BCC alloy [10] whereas in the second approach we have focused on composite formation between Ti_2CrV BCC alloy and Zr based Laves phase compounds such as $ZrFe_2$.

For the Zr substituted alloy, pressure-composition absorption isotherms have been recorded at three different temperatures and the enthalpy of hydride formation (ΔH) has been evaluated. The Zr substituted alloy has lower value of ΔH (-56.33 kJ/mol H_2) compared to the unsubstituted one (-64.4 kJ/mol H_2). In this context, we have also compared the desorption temperatures of both substituted and unsubstituted alloys. The desorption temperature of the hydride of Zr substituted alloy is found to be significantly lower (by ~50K) compared to that of Ti_2CrV hydride. This indicates lower thermal stability of the hydride of

Zr substituted alloy compared to its unsubstituted analogue. In addition to this, cyclic stability of Zr substituted alloy is found to be better over the unsubstituted one. However, hydrogen storage capacity of Zr substituted alloy (3.19 wt% at room temperature) is slightly lower than that of parent alloy. This work also offers mechanistic insight into hydrogen absorption reaction of Zr substituted alloy by analyzing experimental kinetics data with standard kinetic models available in literature. The rate-limiting steps of hydriding reaction have been identified as random nucleation and growth of hydride followed by one and three dimensional diffusion of hydrogen atoms through hydride layer.

Like Zr substituted alloy, pressure composition absorption isotherms of the composite materials have also been studied over a range of temperatures which reveals that with increase in concentration of Zr based secondary phase, hydrogen storage capacity decreases. However, the plateau pressure increases indicating lesser stability of the corresponding hydrides. This is further confirmed from in situ desorption study of composite materials which shows that desorption temperature decreases as percentage of $ZrFe_2$ based Laves phase compound increases. Like Zr substituted alloy, all the composite materials exhibit satisfactory hydrogenation kinetics. From both the approaches it has been inferred that in presence of Zr rich secondary Laves phase, hydrogen uptake of the parent Ti_2CrV alloy decreases slightly whereas desorption temperature reduces remarkably.

Chapter 6: Hydrogen storage properties of Zr-Ti-Ni based compounds

In chapter 5, it is inferred that presence of Zr based Laves phase is effective in improving the hydrogen storage properties of Ti based BCC alloys. Hence, it will be interesting to know hydryding performance of similar Zr based Laves phases formed with elements like Fe, Co, Mn, Cr, Ni etc. It is known that both Fe and Ni are poor hydrogen absorbing elements with low enthalpy of hydride formation. In the previous chapter, the effect of Fe containing Laves phase compounds on hydrogen storage properties has been discussed. Present chapter, deals with hydrogen storage studies on Zr-Ti-Ni based ternary Laves phase compounds. Four compounds with compositions ZrTiNi, $Zr_{1.3}Ti_{0.7}Ni$, $Zr_{1.7}Ti_{0.3}Ni$ and Zr_2Ni were prepared by arc melting method and characterized using XRD. The intermetallic compound with ZrTiNi composition exists as pure C14 Laves phase [11]. On increasing Zr concentration, the fraction of C14 phase decreases and that of C16 phase increases. Crystal structures of the hydrides mimic those of their parent alloys with a change in lattice parameters. Hydrogen absorption studies show that hydrogen uptake increases with increase in Zr concentration, however the plateau pressure decreases. Present studies have revealed that hydrogen uptake values of these compounds are strongly influenced by the relative concentration of the two phases (C14 and C16 phases). Further, to get an idea about the rate limiting step, kinetics data have been analyzed using well established Kolmogorov–Johnson–Mehl–Avrami (KJMA) model [12]. The rate constants and activation energies of hydriding reaction of all the four alloys have been calculated using both classical and modified KJMA models. Our study shows the importance of modified KJMA model over the classical one in explaining the hydriding kinetics of the studied compounds.

Chapter 7: Conclusion and future scope

In this chapter major findings and highlights of the present study have been discussed. Knowledge gathered by studying basic aspects of hydrogen storage properties of both physisorbed and chemisorbed systems has been used to give future direction to the present work. This chapter proposes the synthesis of alloy-carbon composite systems to utilize the synergistic effect of physisorption and chemisorption. It is thought that alloy-carbon composite of suitable compostion and surface caharcteristics may lead to development of better hydrogen storage materials by overcoming the limitations of both physisorptive and chemisorptive processes.

References:

1. Schlapbach L, Zuttel A. Hydrogen-storage materials for mobile applications. Nature 2001;414:353-8.
2. Eberle U, Felderhoff M, Schüth F. Chemical and physical solutions for hydrogen storage. Angew Chem Int Ed 2009;48:6608-30.
3. Sakintuna B, Lamari-Darkrim F, Hirscher M. Metal hydride materials for solid hydrogen storage: A review. Int J Hydrogen Energy 2007;32:1121-40.
4. Xu WC, Takahashi K, Matsuo Y, Hattori Y, Kumagai M, Ishiyama S, et al. Investigation of hydrogen storage capacity of various carbon materials. Int J Hydrogen Energy 2007;32:2504-12.
5. Dillon AC, Jones KM, Bekkedahi TA, Kiang CH, Bethune DS, Heben MJ. Storage of hydrogen in single-walled carbon nanotubes. Nature 1997;386:377-9.
6. Maeland AJ, Libowitz GG, Lynch JF. Hydride formation rates of titanium-based b.c.c. solid solution alloys. J Less Common Met 1984;104:361-4.
7. Nedyakha IM, Chernyi VG. Increasing the oxidation resistance of niobium at elevated temperatures. Soviet Mater Sci 1968;2:457-8.
8. Kumar A, Shashikala K, Banerjee S, Nuwad J, Das P, Pillai CGS. Effect of cycling on hydrogen storage properties of Ti_2CrV alloy. Int J Hydrogen Energy 2012;37:3677-82.
9. Guéguen A, Joubert JM, Latroche M. Influence of the C14 $Ti_{35.4}V_{32.3}Fe_{32.3}$ Laves phase on the hydrogenation properties of the body-centered cubic compound $Ti_{24.5}V_{59.3}Fe_{16.2}$. J Alloys Compd 2011;509:3013-8.
10. Young K, Ouchi T, Nei J, Meng T. Effects of Cr, Zr, V, Mn, Fe, and Co to the hydride properties of Laves phase-related body-centered-cubic solid solution alloys. J Power Sources 2015;281:164-72.

11. Bououdina M, Lambert-Andron B, Ouladdiaf B, Pairis S, Fruchart D. Structural investigations by neutron diffraction of equi-atomic Zr-Ti(V)-Ni(Co) compounds and their related hydrides. J Alloys Compd 2003;356: 54-8.
12. Khawam A, Flanagan DR. Solid-state kinetic models: basics and mathematical fundamental. J Phys Chem B 2006;110:17315-28.

List of Figures

List of Tables

Chapter 1

Introduction

Energy plays a major role for the economic development and growth of any country. In the twentieth century, the main source of energy was fossil fuel based resources. Unfortunately, due to tremendous consumption of fossil fuel in industries and transport sector the limited resources will be totally depleted after some time. In addition, their consumption produces green house gases leading to environmental pollution, ozone layer depletion and global warming [1, 2]. Keeping all these challenges in mind, there is an urgent need for next-generation energy sources that are renewable, sustainable, environment-friendly and abundant. Hydrogen economy is considered as one of the most promising solution to address these problems because of its high gravimetric energy density; about three times higher than that of current fossil fuels (see Fig. 1.1). Moreover, hydrogen is light weight [3, 4] and abundant in the sense that it can be produced from a large variety of sources such as water, organic materials and biomass [1, 5]. It is relevant to mention here that hydrogen is not an energy source rather it is an energy carrier because it does not occur naturally in its elemental form. It has to be produced from some primary energy sources. Unlike fossil fuels, hydrogen is regarded as a clean energy carrier because its by-product is only pure water. Nowadays hydrogen gas is produced mostly from natural gas or higher hydrocarbon by steam reforming method which releases green house gases in atmosphere [6]. However, in ultimate “hydrogen economy” the production of hydrogen should be from electrolysis of water in a renewable way. This means the required electricity should be generated from some renewable sources such as solar, wind, hydro-power etc. [7]. But the main concern in realizing ‘‘hydrogen economy’’ is exceptionally low volume density of gaseous hydrogen, namely 0.09 kg/m^3 of

H_2 gas under ambient condition [8]. As a result unusual large space is required to store hydrogen gas. The size of the hydrogen storage tank will be unrealistic for practical vehicular application and thus “hydrogen storage” appears to be the major bottleneck in the way towards future hydrogen economy.

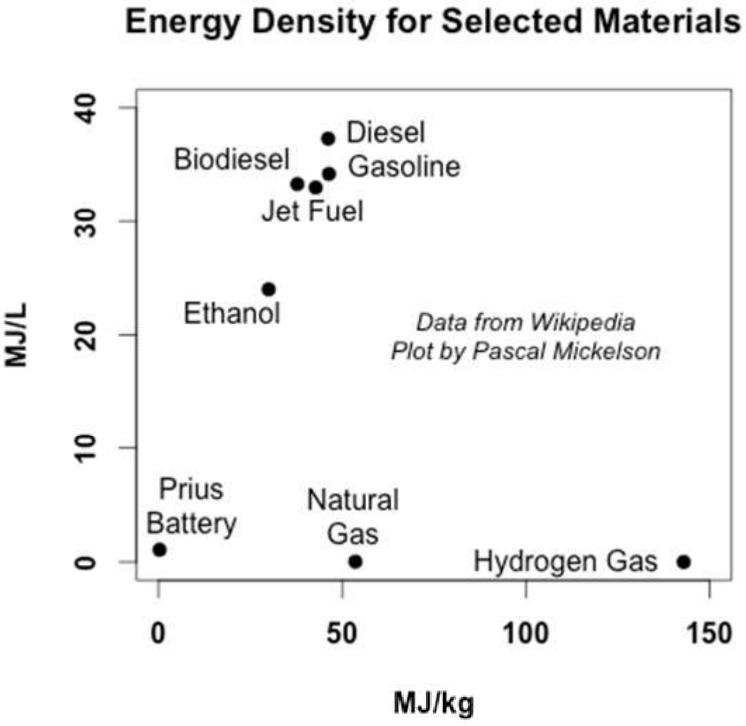

Fig. 1.1 *Gravimetric (horizontal axis) and volumetric (vertical axis) energy densities for selected materials. A hypothetical ideal energy storage system should appear in the uppermost right-hand corner of the plot. (Source: Pascal Mickelson)*

1.1 Hydrogen storage

In hydrogen economy, energy conversion of hydrogen fuel either in fuel cell (FC) or in internal combustion engine (ICE) requires convenient means of on board hydrogen storage. To be successor of conventional fossil fuels, the hydrogen storage material should have high enough storage capacity so that it can drive at least 300 miles on a single charge [9]. Besides storage capacity, an ideal hydrogen storage material should fulfill the criteria of safety, efficiency, cost etc. For the sake of focused research in the field of hydrogen storage, the US Department of Energy (DOE) has set some targets for practical light duty vehicular application.

Table 1.1 *System targets for onboard hydrogen storage system for Light-Duty Fuel Cell vehicles [10].*

Storage parameters	Unit	2020 target
System gravimetric capacity	kWh/kg (wt.%)	1.8 (5.5)
System volumetric capacity	kWh/L (kg H_2/L system)	1.3 (0.04)
Fuel cost	\$ / kg H_2	333
Min/Max delivery temperature	˚C	-40/85
Cycle life (1/4th tank to full)	Cycles	1500
Delivery pressure of storage system	bar	5-12
System fill time for 5 kg fill	Min	3.3
Toxicity	Meet or exceed applicable standards	
Safety		

Moreover, a practical hydrogen storage system should store hydrogen reversibly. At present investigated techniques for storing hydrogen include conventional hydrogen compression (applying high pressure) and hydrogen liquefaction as well as latest approaches like chemical storage in solids and adsorption on high surface area materials. These methods are briefly discussed in the following paragraphs. The chemistry of hydrogen being very diverse, there can be a wide range of compounds with high potential for hydrogen storage application. Hydrogen shows ambivalent behavior and can exist either as cation (H^+) or anion (H^-) in ionic compounds. It can also form covalent bond with some elements such as carbon, oxygen, nitrogen etc. It can even behave like a metal when interacts with alloys or intermetallic compounds. Fig. 1.2 shows different types of systems investigated in this research area and their efficiencies in comparison to 2020 targets of DOE and its ultimate targets. Unfortunately none of the studied systems meets all the goals of DOE at a time for successful use in vehicular application.

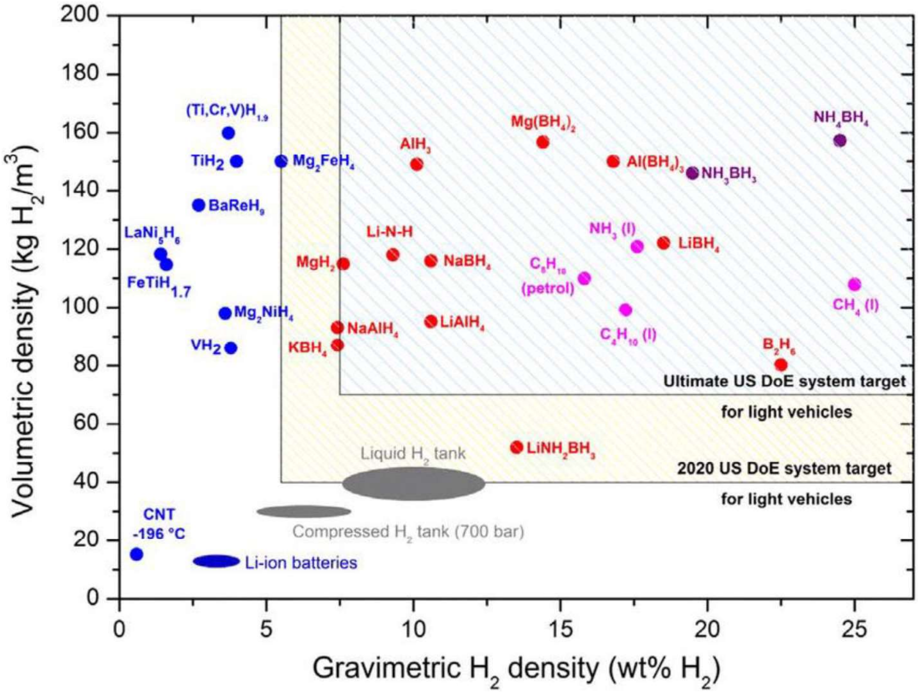

Fig. 1.2 *Volumetric and gravimetric hydrogen density of selected materials [11].*

1.1.1 Compressed hydrogen gas

Hydrogen can be stored as compressed gas in specially designed storage tanks by applying very high pressure. The critical temperature of hydrogen is very low (33 K) and due to this special property hydrogen remains as gas whatever be the applied pressure down to 33 K.The most common storage tanks are of cylindrical shape to take care of stability aspect. The high pressure gas cylinder should be made of a material which has high tensile strength, low density, is immune to hydrogen. Furthermore, hydrogen should not diffuse through the cylinder wall. Most of the pressure cylinders to date are made of stainless steel. But heavy weight of steel cylinder leads to poor gravimetric hydrogen density of the overall storage system containing the compressed gas. Lightweight cylinders have been designed from composite materials (composite of aluminium and carbon fibre) that are much lighter than steel cylinders and thus provide better gravimetric storage capacity. These high performance light-weight cylinders can withstand pressure upto 800 bar such that its volumetric storage capacity reaches 36 kg/m^3. Even though “compressed H_2 gas” is a mature technology it is not so promising because of the drawbacks listed below:

1. There is always possibility of leakage from high pressure hydrogen gas cylinders
2. Compression of gas at very high pressure is an energy demanding process (theoretical energy of isothermal compression of H_2 gas from 1 bar to 800 bar is 2.21 kWh/kg of H_2)
3. Cylinders are not compact, hence not practical for modern age light weight vehicles.

1.1.2 Cryogenic liquid hydrogen

Liquid hydrogen is another way of storing hydrogen where super-insulated tanks are used to keep liquefied hydrogen at 20.3 K and ambient pressure. To minimize heat transfer, these tanks are wrapped with multilayer super insulating material [12]. The heat of vaporization for liquid hydrogen is very low and there is always some loss of hydrogen through evaporation (the phenomenon is called “boil-off”), no matter whatever the level of isolation. The degree of boil-off depends also on the size of the tank. Larger the size of the tank lesser is the extent of boil-off loss. As a result, use of liquid hydrogen as fuel for automotive application does not seem to be practical whereas it is extensively used as fuel for space shuttles. Again, the energy required for liquefaction of hydrogen is very high, almost 30% of energy of hydrogen combustion [13]. Moreover proper refrigeration is required to maintain liquid H_2 temperature which again adds up to its cost.

Liquid hydrogen has higher energy density compared to compressed hydrogen gas and store hydrogen at comparatively lower pressure. But the above mentioned drawbacks like energy requirements for liquefaction, boil-off losses, cost of maintaining cryogenic temperature and super-insulating tank fabrication still hinder its practical application in transport sector.

1.1.3 Solid state hydrogen

Besides these two storage methods, hydrogen can also be stored in suitable solid state materials and a thorough literature survey on different types of hydrogen storage materials ascertain that "solid state hydrogen storage" is the most promising and diverse way of storing hydrogen. There are two different ways by which hydrogen can interact with solids viz., chemisorption and physisorption. In case of chemisorption, hydrogen atoms interact with the host material through strong chemical bonding. On the other hand, during physisorption hydrogen remains in the molecular form and interacts with the material through weak van der Waals interaction. Some external energy is required to release stored hydrogen in both the cases and these accounts for the safety assured by solid state hydrogen storage materials. However, both the strategies have their own advantages and disadvantages. Chemically absorbed hydrogen can not be desorbed at ambient conditions and reversibility of absorption-desorption process is often questionable. The advantage of physisorption process is fast adsorption-desorption of hydrogen and the process is found almost reversible irrespective of the adsorbent material. However, it is impossible to store reasonable amount of hydrogen at ambient condition through physical adsorption and trapped hydrogen can retain only at lower temperatures.

To overcome this problem several approaches have been tried such as spillover by metal nanoparticle [14], use of σ-π H_2 complexes (the Kubas interaction) [15]. Different adsorbents have been explored for hydrogen storage studies such as porous carbon [16], metal organic frameworks (MOFs) [17], zeolites [18], covalent organic frameworks (COFs) [19], porous polymers [20] etc. Hydrogen adsorption by such type of porous materials is mainly governed by specific surface area and pore characteristics of the materials.

There is large number of candidates in the category of chemisorption materials and some of the prominent candidates are metal hydrides [21], hydrides of alloys and intermetallic compounds [2], complex hydrides [22], ammonia borane (chemical hydride) [23] etc. In the following paragraphs the hydrides of metals, alloys and intermetallic compounds are categorized as interstitial hydrides. The volumetric energy density found for interstitial hydrides are remarkably higher compared to compressed hydrogen gas or cryogenic liquid hydrogen and pictorially depicted in Fig. 1.3.

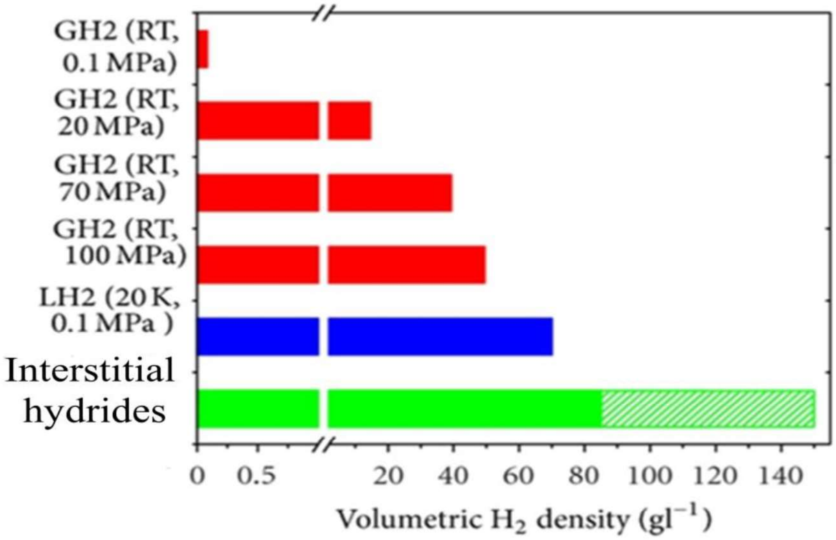

Fig. 1.3 *Comparison of volumetric densities of different hydrogen storage technologies: compressed hydrogen (GH2); liquid hydrogen (LH2); and interstitial hydrides [24].*

Group I and II salts (lithium, sodium, beryllium, magnesium) of $[AlH_4]^-$, $[BH_4]^-$ and $[NH_2]^-$(alanates, borohydrides and amides) are usually referred as complex hydrides and show high gravimetric density for hydrogen. All the complex hydrides are light weight and in this class of hydrides hydrogen is covalently attached to the central atoms of complex anions. Among them, Li based complex hydride, $LiBH_4$ can store upto 18 wt.% of H_2 at room temperature. It is difficult to safely handle complex hydrides and in some cases they decompose to highly stable elements. Thus, use of complex hydrides for vehicular application seems to be challenging due to their irreversible nature and kinetic limitation is also an unavoidable obstacle. Like complex hydrides ammonia borane is also light weight hydrogen storage material and has potential to store large amount of hydrogen (19.6 wt.%). But efficient recycling of ammonia borane is the major hindrance to its practical use for onboard hydrogen storage application.

Interstitial hydrides are formed from the reversible reaction of hydrogen gas with metals, alloys or intermetallic compounds. Unlike complex and chemical hydrides, interstitial hydrides offer several advantages such as inherent safety, ability to work at comparatively lower temperature and pressure suitable for light duty fuel cell vehicles. Release of hydrogen from interstitial hydrides occurs through endothermic reaction which accounts for the associated safety with these systems. The volumetric hydrogen storage densities of interstitial hydrides are comparable to those of complex and chemical hydrides as obvious from Fig. 1.2 whereas they suffer from poor gravimetric storage capacities. In the following sections of this chapter hydrogen storage by physisorption and chemisorption processes have been discussed briefly.

1.1.3.1 Hydrogen storage by physisorption

Physisorption of hydrogen is a surface phenomenon where hydrogen molecules adhere to the surface of host materials by some physical forces (interplay of attractive and repulsive forces). The interatomic potential resulting from these forces can be described by Lennard-Jones potential which is represented as:

$$\phi(r) = 4\varepsilon\left[\left(\frac{\sigma}{r}\right)^{12} - \left(\frac{\sigma}{r}\right)^{6}\right] \tag{1.1}$$

It can also be expressed as:

$$\phi(r) = \frac{A}{r^{12}} - \frac{B}{r^{6}} \tag{1.2}$$

where, $A = 4\varepsilon\sigma^{12}$ and $B = 4\varepsilon\sigma^{6}$. ε signifies the depth of the potential and σ is the interparticle distance where the potential is zero. The variation of potential energy (ϕ) with interparticle distance (r) is shown in Fig. 1.4. The deeper the potential well (larger value of ε), the stronger is the interaction between two gas molecules.

To apply Lennard-Jones potential for adsorption of gas molecules on the surface of solid, the adsorbent surface is assumed as individual atoms and the adsorbate gas as isolated gas molecules. Now, the potential energy can be represented as:

$$\phi_m(r) = \sum_n \phi_{mn}(r_{mn}) \tag{1.3}$$

Here, r_{mn} is the distance between the molecule "m" of adsorbate and atom "n" of the adsorbent. The potential energy, $\phi_m(r)$ of the adsorbate gas molecule is expressed as a function of distance. While approaching the adsorbate surface, a balance between attractive and repulsive forces is established at a distance $r = r_{min}$ where the potential energy becomes minimum and physisorption occurs.

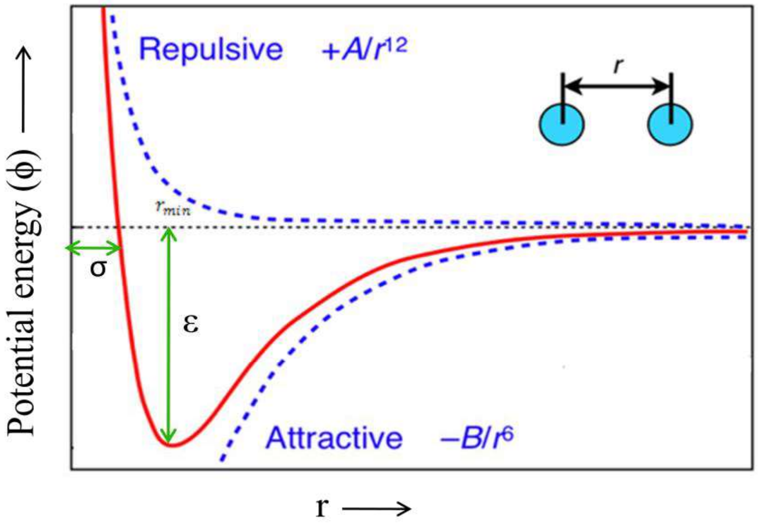

Fig. 1.4 *Lennard-Jones potential as a function of interparticle distance [25].*

1.1.3.1.1 Adsorption isotherms

The gas uptake by a solid adsorbent depends on temperature (T), pressure (p) of the adsorbed gas, and the characteristics of the solid and gas. If "n" is the quantity of gas adsorbed, then for a particular solid-gas combination:

$$n = f(T, p) \qquad (1.4)$$

For a given temperature the equation becomes,

$$n = f(p)_T \qquad (1.5)$$

The characteristic adsorption isotherm of an adsorbate-adsorbent system is obtained by plotting the amount of gas adsorbed on a solid absorbent as a function of pressure. According to IUPAC there are six different types of adsorption isotherms which are illustrated in Fig. 1.5.

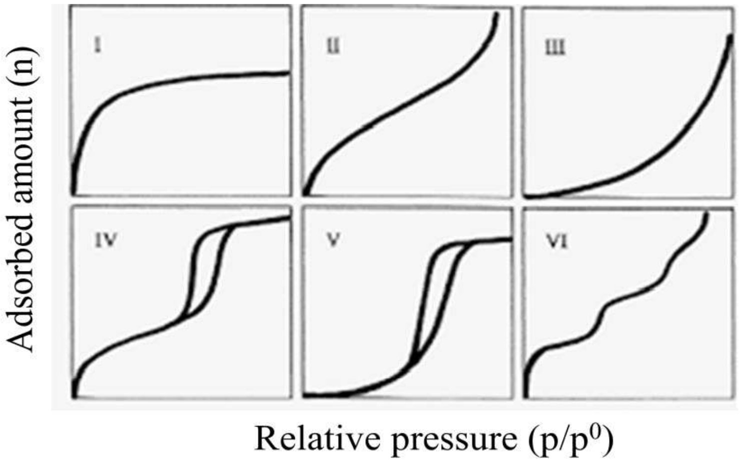

Fig. 1.5 *IUPAC classification of adsorption isotherms [25].*

Type I isotherms occurs from adsorption of gases on 'microporous' adsorbents, whilst type II isotherms are characteristic of adsorption of gases on 'non-porous' adsorbents. The plot of either type III or type V isotherm is convex to relative pressure axis and characteristic of weak adsorbate-adsorbent interactions. Type III isotherms are generally found for non-porous adsorbents whereas mesoporous adsorbents having weak interaction with adsorbates show type V isotherm. Type IV isotherms are typical for mesoporous adsorbents. Hysteresis loop is associated with both types IV and V isotherms and arises due to capillary condensation. Type VI isotherms are obtained from layer-by-layer adsorption of gases on extremely well-defined, homogeneous surfaces where the monolayer capacity corresponds to the step height.

There are different models to interpret the experimental adsorption isotherms such as Langmuir, Freundlich, Sips (Langmuir-Freundlich), Tóth, Dubinin-Radushkevich etc. among which only the first two models are described here.

1.1.3.1.2 Langmuir and Freundlich models

Langmuir isotherm is based on the following assumptions

1. All the adsorbent sites are equivalent i.e. the surface is homogeneous.
2. Monolayer adsorption occurs at the surface i.e. the adsorption involves attachment of only one layer of gaseous molecules to the surface of adsorbent.
3. Fixed number of adsorption sites is available on the surface of adsorbent.
4. Dynamic equilibrium exists between adsorbed gaseous molecules and the free gaseous molecules.
5. There is no interaction between adjacent adsorbate molecules and the energy of adsorption is independent of site occupancy

Langmuir adsorption isotherm is generally expressed as

$$\theta = \frac{k_{ads}P}{1 + k_{ads}P} \qquad (1.6)$$

where, "θ" is the number of adsorbent sites occupied by gas molecules; "k_{ads}" is the equilibrium constant and "P" represents pressure of adsorbate gas. Fig. 1.6 shows a general representation of Langmuir isotherm where the surface coverage "θ" is varied with pressure. Unfortunately, no real adsorbate-adsorbent system has been found which can be characterized by single Langmuir adsorption isotherm throughout the whole pressure range, rather it is valid only at low pressure region. Where there are different types of adsorption sites (with different adsorption energies), equation 1.6 would not give a good fit of the adsorption data; rather multiple Langmuir isotherms in the following form will be much more applicable

$$\theta = \sum_i \alpha_i \frac{(k_{ads})_i P}{1 + (k_{ads})_i P} \qquad (1.7)$$

$$\sum_i \alpha_i = 1$$

where, α_i is fraction of adsorption sites with energy of adsorption E_i.

In the low pressure region Langmuir isotherm resembles Henry's law which states that the amount of adsorbed gas is directly proportional to the equilibrium pressure:

$$\theta = \lim_{p \to 0} \frac{k_{ads} P}{1 + k_{ads} P} = k_{ads} P \qquad (1.8)$$

At high pressure region $\theta = \frac{k_{ads} P}{k_{ads} P} = 1$ and θ becomes independent of pressure. Hence, adsorption is zero order at high pressure region.

$$\theta \propto \mathrm{P}^1, \text{at low presure}$$

$$\propto \mathrm{P}^0, \text{at high pressure}$$

At an intermediate pressure, surface coverage "θ" is directly proportional to the pressure raised to the power "$1/n$".i.e. $\theta \propto P^{1/n}$ (1.9)

$$\text{or, } \theta = kP^{1/n} \qquad (1.10)$$

$$\text{or, } \frac{x}{m} = kP^{\frac{1}{n}} \qquad (1.11)$$

where, "k" and "n" are constants for a particular adsorbate-adsorbent system at a particular temperature. "x" is the amount of gas adsorbed by "m" amount of adsorbent. "$1/n$" indicates the strength of adsorption; higher the value of "$1/n$", more favourable is the adsorption. Equation 1.11 is known as Freundlich equation or Freundlich isotherm. Linear form of the Freundlich equation is given below:

$$log\left(\frac{x}{m}\right) = log(k) + \frac{1}{n} log(P) \qquad (1.12)$$

Basically the isotherm represents variation of quantity of gas adsorbed by unit mass of adsorbent with pressure and graphically shown in Fig. 1.7.

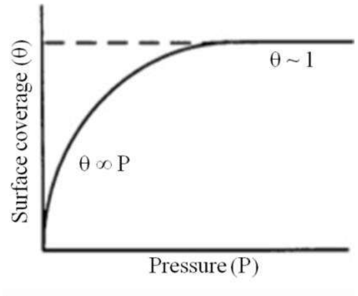

Fig. 1.6 *Graphical representation of Langmuir isotherm.*

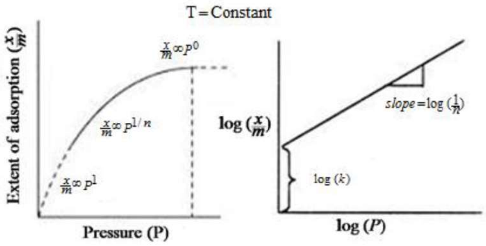

Fig. 1.7 *Graphical representation of Freundlich isotherm.*

The valid pressure range for Freundlich isotherm varies from one adsorbate-adsorbent system to another. However, the isotherm shows poor agreement at high pressures and low temperatures and it does not reduce to Henry's law in the low pressure region [26]. This type of isotherm has been extensively used for the interpretation of a wide range of heterogeneous surfaces such as activated carbon, silica, polymers etc. [27-31].

1.1.3.1.3 Thermodynamics of adsorption

Adsorption is a spontaneous process; hence the total free energy of the adsorbate-adsorbent system must decrease on adsorption and consequently it is characterized as an exothermic process with positive value of entropy change. The isosteric enthalpy of adsorption (enthalpy of adsorption at constant gas uptake) is the key thermodynamic parameter to reveal information regarding adsorbate-adsorbent interaction. It is usually derived from the condition of phase equilibrium between the free gas phase and adsorbed phase. Phase equilibrium is reached when the chemical potential of the two phases become equal. Q_{st} can be calculated from the adsorption isotherms at different temperatures using the Clausius-Clapeyron equation [32, 33],

$$Q_{st=} - R\left[\frac{dlnP}{d\left(1/_{T}\right)}\right]_n \qquad (1.13)$$

During calculation of isosteric enthalpy of adsorption only the adsorbate-adsorbent interactions should be considered. This does not take care of the adsorbate-adsorbate interactions that would occur at increased surface coverage. Hence, the isosteric heat of adsorption is obtained from the low pressure regime of the adsorption isotherm i.e. the Henry's law region is of prime importance to characterise an adsorbate-adsorbent system. The value of isosteric enthalpy of adsorption should be ~ 15 kJ mol^{-1} of H_2 for significant hydrogen adsorption at room temperature under moderate pressure [34].

1.1.3.1.4 Different physisorbed systems

Physisorption of hydrogen is largely correlated with surface area of the adsorbents and hence high surface area materials are expected to be good for hydrogen storage applications [35-37] as already mentioned in section 1.1.3. In the last two decades, a large number of theoretical as well as experimental research works have been done on different types of adsorbents to show their potential as hydrogen storage material and some of them are listed below.

1.1.3.1.4.1 Carbon nanotubes

Carbon nanotubes were discovered by Iijima during synthesis of fullerene by arc discharge method [38]. Three types of carbon nanotubes are available namely single-(SWNT), double-(DWNT) and multi-walled (MWNT). SWNTs can be described as rolled up graphene sheets in the form of cylindrical tubes as illustrated in Fig. 1.8. On the other hand there are two and more than two concentric cylindrical walls in DWNTs and MWNTs, respectively and the separation between adjacent walls is around 0.3 nm [39, 40]. The SWCNTs with inner diameters of 0.6-0.7 nm are found to be thermodynamically favourable for physisorption of molecular hydrogen [41]. For DWNTs and MWNTs both diameter and inter-wall spacing have to be optimized for getting maximum hydrogen adsorption [42].

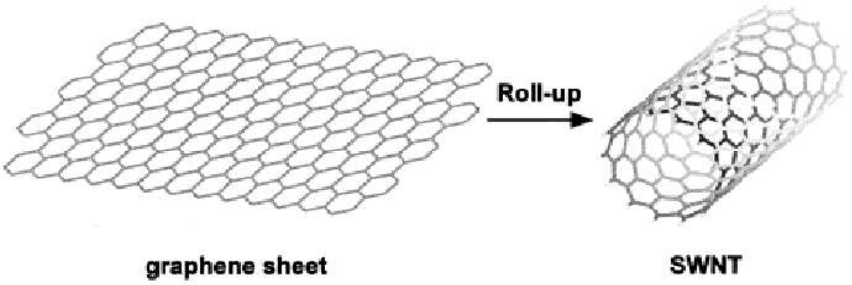

Fig. 1.8 *Representation of single walled CNT as a rolled up graphene sheet [44].*

Dillon et al. [44] reported the first experimental hydrogen uptake by CNTs and suggested that CNTs could store around 10 wt.% of hydrogen at room temperature. Soon after this work, a large number of reports published showing high hydrogen storage capacities of CNTs [45-47]. A few years later, reports showing very low hydrogen storage capacities of CNTs began to emerge questioning the reproducibility of the previously reported values. It is now scientifically justified that the ambiguity is mainly due to water impurities, metal impurities or erroneous instrumentation [48-51]. Despite the ambiguity, significant extent of works is going on regarding the hydrogen storage properties of CNTs or CNT-like materials/functionalized CNTs [52-56].

1.1.3.1.4.2 Activated carbon

Activated carbons are known as good adsorbents since long back and they have a wide range of applications such as removal of impurities from gases and water, metal extraction and many others. They do have porous structures with large surface areas, relatively low cost and well established methods for large scale production. As a result, they are commercialized for so many applications. They can be produced from a variety of organic feedstocks including wood, coconut shells and fibres, nut shells, rice husk, corncob, sugarcane bagasse etc. [57-59]. It is worth mentioning here that the carbon filament used in high resistance incandescent lamp by Thomas Edison was also made from biomass [60]. Synthesis of activated carbon involves two steps namely carbonization and activation [61]. Carbonization is done by heating the organic precursor at high temperature (usually in the range of 600 to 800 °C) and the carbon-rich product thus obtained is subjected to activation. The activation can be carried out in two ways: (i) physical activation with suitable oxidizing gases such as CO_2, steam or their mixture and (ii) chemical activation via chemical reaction between carbon rich product and KOH/ NaOH/ H_3PO_4/ $ZnCl_2$ [62]. Among different chemical reagents, KOH is mostly used because KOH activation leads to formation of micropores (pore size as small as 0.3 nm) with very high surface area (> 3000 m^2 g^{-1}) and high pore volume (> 1 cm^3 g^{-1}) [63-67]. The mechanism of KOH activation is shown below:

$$2\ KOH \rightarrow K_2O + H_2O \quad \text{..}(1.14)$$

$$C + H_2O\ (steam) \rightarrow H_2 + CO \quad \text{..................................}(1.15)$$

$$CO + H_2O \rightarrow H_2 + CO_2 \quad \text{..}(1.16)$$

$$K_2O + CO_2 \rightarrow K_2CO_3 \quad \text{..}\ (1.17)$$

$$K_2O + H_2 \rightarrow 2\ K + H_2O \quad \text{..}(1.18)$$

$$K_2O + C \rightarrow 2\ K + CO \quad \text{...}(1.19)$$

$$K_2CO_3 + 2\ C \rightarrow 2\ K + 3\ CO \quad \text{.................................}\ (1.20)$$

Chemical activation is advantageous over the physical activation method because it (i) requires lower pyrolysis temperature (ii) gives higher carbon yield with high surface area and tailored porosity [62]. Xiao et al. [68] have prepared a series of activated carbons from biomass resources, melaleucas bark and activated by KOH treatment. The maximum hydrogen storage capacity is found to be 4.08 wt.% at 77 K and 10 bar pressure for the KOH activated sample with BET surface area > 3000 m^2 g^{-1} and total pore volume > 1.5 cm^3 g^{-1}. Nijkamp et al. [69] reported hydrogen uptake as high as 2.14 wt.% at 77 K under 1 bar of pressure for activated carbon having surface area ~ 2000 m^2 g^{-1}. Wang et al. [70] have investigated hydrogen storage properties of KOH activated fungi-based porous carbons which have surface areas in the range of 1600-2500 m^2 g^{-1} and pore volumes varying from 0.8 to 1.56 cm^3 g^{-1}. The saturated hydrogen storage density reached 4.2-4.7 wt.% at 77 K for these fungi-based activated porous carbons under 35 bar of hydrogen pressure. Wang et al. [71] applied a combination of physical and chemical activation method and one of the activated carbon products exhibited surface area over 3100 m^2 g^{-1}. The activated carbon material can store hydrogen upto 7.08 wt.% at 77 K and 20 bar which is one of the highest value of gravimetric hydrogen storage capacities reported for porous carbons. The activated carbons have disordered structure as shown in Fig. 1.9. The degree of disorder depends on the carbon precursor and also on heat treatment.

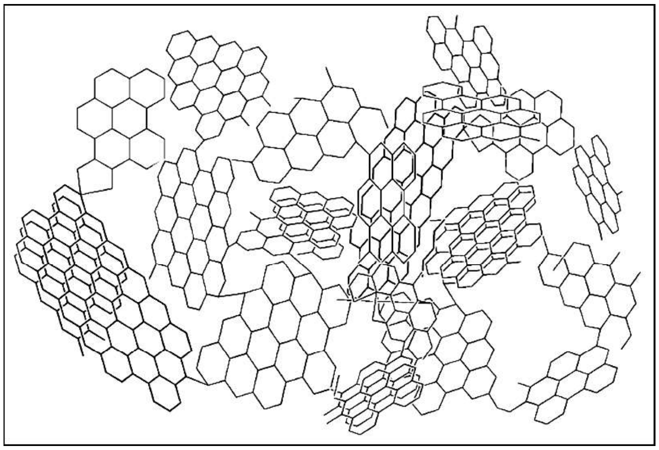

Fig. 1.9 *Schematic representation of activated carbon* [72]

1.1.3.1.4.3 Templated carbon

Unlike the disordered structure of activated carbons, porous carbon with regular array of pores can be produced using hard templating route. The highly ordered structure of templated carbon is a replica of the long range order existing in inorganic templates. A wide variety of inorganic frameworks including zeolites, clays, some silica sources etc. can be used as templates. The synthesis of templated carbon involves following steps [73, 74]:

(i) Incorporation of organic precursor into the pores/channels of the inorganic template either by impregnation or chemical vapour deposition.

(ii) Carbonization of the organic precursor.

(iii) Removal of the inorganic template.

The template carbonization route is attractive because it can control the structure of final carbon products in terms of pore structure as well as microscopic morphology which play important role in hydrogen adsorption.

Han et al. [75] obtained mesoporous carbon with surface area of 850 m^2 g^{-1} and a pore volume of 1.5 cm^3 g^{-1} by using sodium silicate as hard template and sucrose as organic precursor. Stadie et al. [76] successfully synthesized zeolite templated carbons (ZTC) with surface area upto 3600 m^2 g^{-1} starting from furfuryl alcohol and investigated their hydrogen storage properties. The resultant ZTCs are mainly microporous and exhibited maximum hydrogen storage capacity of 5.5 wt.% at 77 K and 24 bar. In addition, post synthesis treatment can be carried out to introduce higher degree of graphitization in the template carbon framework and sometimes to further enhance the surface area which will be beneficial for adsorptive hydrogen storage [77].

1.1.3.1.4.4 Zeolite

Zeolites are crystalline aluminosilicate structures having lots of open micropores with high internal surface area. Zeolites are represented by the general formula: $M_{x/n}[(AlO_2)_x(SiO_2)_y].mH_2O$, where M, an exchangeable cation with valence “n”, neutralize the negative charge of zeolite framework. Zeolites consist of tetrahedral building blocks and depending on their assembly different types of zeolite frameworks are possible. A, X, Y, beta, mordentite, ZSM-5 are some of the commercially available zeolites. Mainly two types of open cages, β (sodalite cage) and α (supercage), are present in zeolite structure as shown in Fig. 1.10.

For zeolites X, Y and A, β cages are too small [78] compared to the kinetic diameter of hydrogen molecule making them inaccessible for hydrogen physisorption. Therefore, only α cages take part in adsorption of hydrogen molecules for zeolites X, Y and A. Langmi et. al. [79] measured hydrogen adsorption of different types of zeolites and found a maximum hydrogen storage capacity of 2.19 wt.% at 77 K and 15 bar of hydrogen pressure for calcium exchanged zeolite sample with surface area 669 m^2 g^{-1}. A theoretical study on storage of hydrogen in zeolite framework suggests that the maximum hydrogen storage density of zeolite is intrinsically limited to 2.86 wt.% which is much below the targets set by DOE for vehicular application [80].

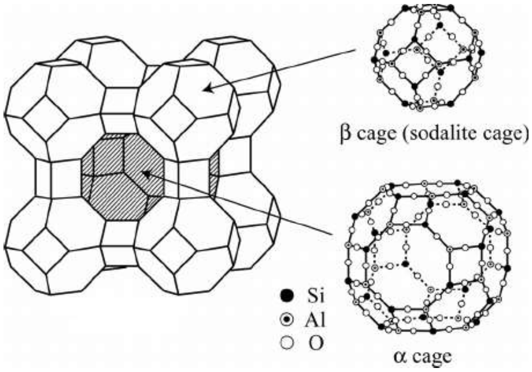

Fig. 1.10 *Schematic representation of zeolite framework showing β and α cages [78].*

1.1.3.1.4.5 Metal organic frameworks

Metal organic frameworks (MOFs) represent a new class of synthetic porous material with extended framework structure of metal-oxide corner groups assembled together by aromatic ligands. As an example, the single crystal structure of MOF-5 is represented in Fig. 1.11 which shows extended 3D cubic frameworks formed by joining Zn_4O tetrahedra through benzene carboxylate linkage [81]. Compared to conventional zeolites, MOFs offer flexibility during designing just by changing the ligand linkages. They are characterized by exceptionally high internal surface area and large pore volume. This makes MOFs attractive for gas storage applications and in the last decades numerous studies have been performed to evaluate their hydrogen storage properties. The successful practice of “reticular chemistry” enables researchers to tune the structure of MOFs as per requirement [82, 83]. Rosi et al. [84] investigated the hydrogen storage properties of MOF material for the first time and reported a maximum hydrogen uptake of 4.5 wt.% by MOF-5 at 78 K under 20 bar hydrogen pressure. Subsequently, many researchers performed hydrogen storage studies on MOF-5 which revealed that hydrogen storage capacities of MOF-5s significantly differ depending on their preparation method and handling [81, 85]. Moreover, these materials are susceptible to decompose whilst exposed to air or water. Hence, to use high surface area MOF material for vehicular application, its stability in general working condition has to be improved [86]. Recent studies show that zeolitic imidazolate frameworks (ZIFs) have better chemical and thermal stabilities compared to MOFs with metal carboxylate linkages. ZIF-8 is reported to exhibit a maximum hydrogen uptake of 3.3 wt.% at 77 K and 30 bar [87]. To be a potential hydrogen storage material there should be cost effective synthesis methods for highly stable MOFs in bulk scale and they should be highly porous with very large surface area.

1.1.3.1.4.6 Porous organic polymer

Unlike MOFs porous organic polymers are chemically and thermally stable. Besides, they offer attractive features such as low intrinsic density (consists of light atoms like C, H, N and O), production reproducibility and chemical homogeneity [88, 89]. Polymers of intrinsic microporosity (PIM) based on triptycene subunits are reported to store hydrogen upto 2.7 wt.% at 77 K and 10 bar [90]. Among different types of porous organic polymers, PIMs show pore size distributions typically in the micropore region (< 2 nm). The intrinsic porosity is due to continuous network of interconnected intermolecular voids as shown in Fig. 1.12. Like other porous materials (activated carbons, MOFs), the hydrogen uptake by PIMs vary almost linearly with BET surface area and their hydrogen storage capacities are also comparable. The highest hydrogen uptake of 3.94 wt.% was found for OFP-3 (surface area 1159 $m^2 g^{-1}$), a class of PIM material under 10 bar of hydrogen pressure at 77 K [91].Research related to porous organic polymers are rapidly growing (most of the research related to adsorptive hydrogen storage on porous polymer were performed at temperatures as low as 77K), however a drastic improvement is required for its practical application as hydrogen storage material under ambient conditions.

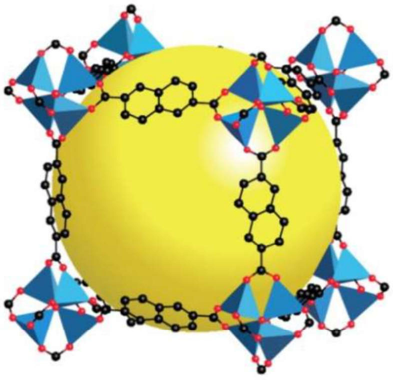

Fig. 1.11 *Structure of MOF-5.*

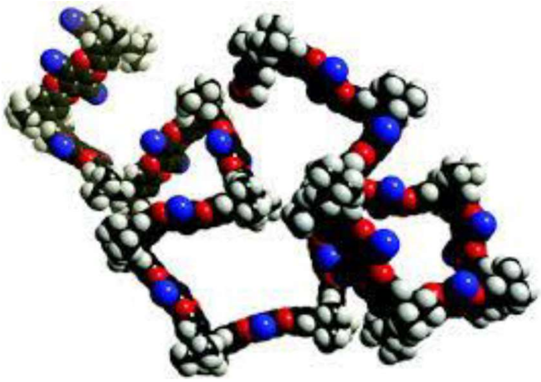

Fig. 1.12 *Molecular model of PIM [92].*

1.1.3.2 Hydrogen storage by chemisorption

Among different types of chemical storage systems, interstitial hydrides are well known for providing safest approach to store hydrogen. The advantages of conventional interstitial hydrides over other chemisorbed systems are already discussed in section 1.1.3. This section deals with the basics of metal hydrogen interaction which occurs during chemical storage of hydrogen. The overall process of interstitial hydride formation is schematically represented in Fig. 1.13.

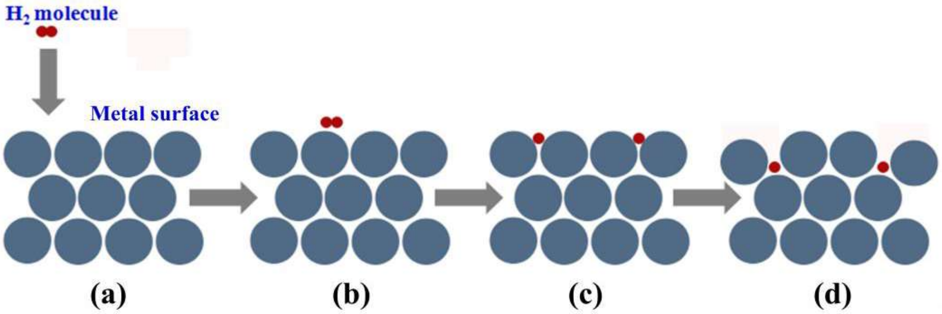

Fig. 1.13 *Different steps involved in the formation of interstitial hydride.*

At first the hydrogen molecules approach the metal (alloy/intermetallic compound) surface and get adsorbed through weak van der Waals interaction as depicted in Fig 1.13 (a) and (b). The physisorbed hydrogen molecules dissociate into individual hydrogen atoms and get chemically absorbed at the surface (Fig 1.13 (c)) and this step is named as dissociative chemisorption. In the next step, the hydrogen atoms diffuse into the bulk and go to the interstitial positions of the metal to form interstitial solid solution (Fig 1.13 (d)). This solid solution is called α phase and the lattice parameter of α phase is larger compared to that of parent metal. Hydrogen atoms in the interstitial position may form hydride phase by trapping more and more hydrogen atoms and crystal structure of the metal may change due to hydride formation. The hydride thus formed is called β phase.

During dehydrogenation the reverse process is followed i.e. the β phase hydride releases hydrogen atoms which diffuse from bulk to surface. At the surface the hydrogen atoms recombine to form hydrogen molecule and desorbs as hydrogen gas.

1.1.3.2.1 Pressure composition isotherm (PCI)

The process of interstitial hydride formation could be best explained by pressure composition isotherm (PCI) which is characteristic of a metal (alloy/intermetallic compound) hydride system. A typical PCI diagram is shown in Fig 1.14 (a). The PCI diagram is obtained by plotting hydrogen pressure against H/M at a fixed temperature, where H/M stands for hydrogen to metal ratio. When hydrogen goes into interstices of metal/alloy/intermetallic compound forming α phase solid solution the hydrogen pressure increases sharply with H/M as indicated by initial steep region of the plot. With further increase in hydrogen pressure the solubility of hydrogen in α phase would reach the maximum limit and hydride phase (β phase) formation starts. During hydride phase formation the pressure remains constant as indicated by the plateau region of the plot. The plateau region continues as long as both α and β phases coexist. After the complete formation of β phase hydride, the hydrogen pressure increases sharply with further absorption of hydrogen. The last steep portion of the plot corresponds to interstitial solid solution of hydrogen in the β phase hydride. The width of the plateau implies the amount of hydrogen that could be stored reversibly by a metal/alloy/intermetallic compound. Like plateau width, position of the plateau (i.e. plateau pressure) also bears valuable information regarding stability of the metal hydride. Greater the stability of the hydride higher is the temperature requirement to reach a certain plateau pressure.

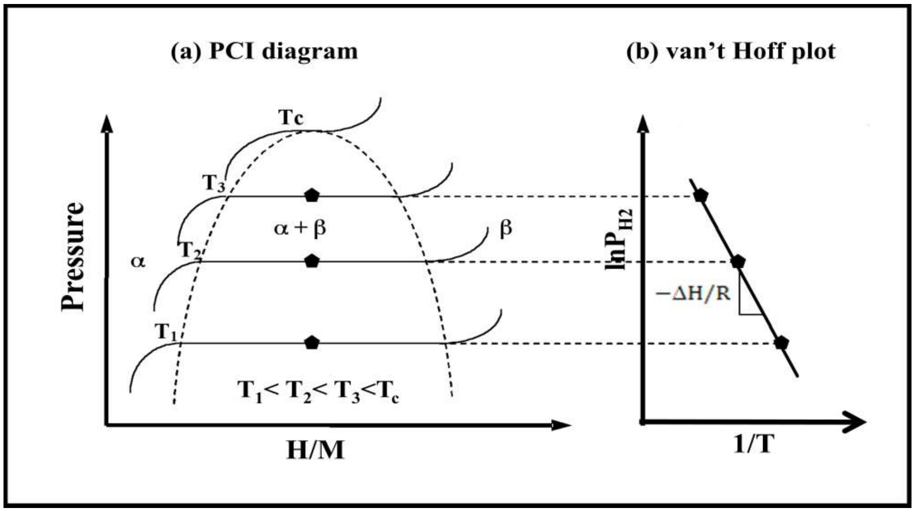

Fig. 1.14 (a) *Pressure composition isotherms at different temperatures and* **(b)** *van't Hoff plot.*

In many metal-hydrogen systems desorption does not follow the same path as absorption and the equilibrium plateau pressure of desorption is usually lower than that of absorption. The difference between absorption and desorption curves is known as hysteresis which arises mainly due to irreversible plastic deformation caused by hydride formation.

1.1.3.2.2 Thermodynamics of interstitial hydride formation

The reaction between a metal (alloy/intermetallic compound) and hydrogen gas can be represented by the following equation:

$$M + \frac{x}{2}H_2 = MH_x \qquad (1.21)$$

where, M stands for metal (alloy/intermetallic compound) and x indicates the molar ratio of hydrogen to metal.

For the above reaction, the change in standard Gibbs free energy at equilibrium condition is represented by,

$$\Delta G = -RTlnK \qquad (1.22)$$

K is the equilibrium constant and given by, $K = P_{H_2}^{-1}$ where P_{H_2} denotes equilibrium plateau pressure. Now, equation 1.22 can be written as,

$$\Delta G = RT ln P_{H_2} \qquad (1.23)$$

We know from the definition of standard Gibbs free energy change that,

$$\Delta G = \Delta H - T\Delta S \qquad (1.24)$$

Hence, equation 1.24 can be rearranged as,

$$ln P_{H_2} = \frac{\Delta H}{RT} - \frac{\Delta S}{R} \qquad (1.25)$$

where, ΔH and ΔS are the change in enthalpy and entropy, respectively during hydrogenation of metal. Equation 1.25 is known as van't Hoff relation. Applying van't Hoff relation, the two most important thermodynamic parameters ΔH and ΔS can be determined from the measurements of equilibrium plateau pressures at different temperatures. The effect of temperature on plateau pressure is demonstrated in Fig. 1.14 (a). Generally, with increase in temperature miscibility gap reduces resulting in smaller plateau width, however the plateau pressure increases. At some critical temperature (T_c) plateau region totally disappears and α phase continuously converts into β phase as evident from Fig. 1.14 (a). Fig. 1.14 (b) shows the van't Hoff plot which is obtained by plotting logarithm of pressure ($\ln P_{H_2}$) versus reciprocal temperature ($^1/_T$). From the slope and intercept of the plot ΔH and ΔS can be calculated. ΔH varies widely for different metal-hydrogen systems whereas the entropy change of almost all the systems is ~ 130 J K^{-1} mol^{-1} H_2 which corresponds to loss of translational degree of freedom upon hydrogen dissolution in solid matrix [2]. For practical use, enthalpy of hydride formation should be as negative as ~ -39 kJ mol^{-1} H_2.

1.1.3.2.3 Kinetics of interstitial hydride formation

Considering the hydride formation mechanism as described in section 1.1.3.2 the rate of hydrogenation is governed by the following factors:

(i) The rate of physisorption of hydrogen molecule at metal surface.

(ii) The rate of H_2 dissociation and chemisorption at the surface.

(iii) The rate at which hydrogen atoms diffuse through the bulk.

(iv) The rate of nucleation and growth of β-phase hydride.

As the hydride formation reaction is controlled by a number of steps, it is really difficult to numerically find out the rate constants following the conventional method. Moreover, it is difficult to get enough information of each reaction step. Hence, there is a practice of using mathematical models for identification of the rate limiting step and thereby determining the rate constants. This is also true for dehydrogenation kinetics.

A kinetic model is actually mathematical description of experimental phenomena. When a set of experimental kinetics data (applicable for both hydrogenation and dehydrogenation) is fitted with a model (rate equation), it is assumed that the hydrogenation/dehydrogenation follows the mechanism based on which the model was derived. There are several kinetic models (g (ξ)) and some of them are listed in Table 1.2.

This section briefly describes the general procedure for finding rate constants and activation energies using kinetic models.

The rate of a solid-gas reaction is generally expressed by,

$$\frac{d\xi}{dt} = k.f(\xi) \qquad (1.26)$$

where ξ is the reacted fraction at time t, k is rate constant, f (ξ) is a function determining the mechanism of reaction and g (ξ) is the integral form of f (ξ).

$$g(\xi) = \int \frac{d\xi}{dt} = kt \qquad (1.27)$$

For a volumetric measurement, ξ is given by

$$\xi = \frac{P(0) - P(t)}{P(0) - P(\infty)}$$

where, P(0) is the initial hydrogen pressure; P(t) and P(∞) are the hydrogen pressures at time 't' and after reaching the final equilibrium, respectively.

The kinetic model (equation) with largest co-relation coefficient (R^2) is considered as the best fitting model to describe the kinetics of hydrogen absorption/desorption. Using the best fitting model, the rate constants "k" are determined at different temperatures and the activation energy of hydrogen absorption/desorption is calculated using the Arrhenius equation:

$$lnk = lnA - \frac{E_a}{RT} \qquad (1.28)$$

where, k is the rate constant, A is the pre-exponential factor, E_a in the activation energy, T is the temperature and R is the universal gas constant.

Table 1.2 *List of some of the kinetic models from literature.*

Model		Kinetic Equation	Reference
Zero order chemical reaction		$\xi = \mathrm{k}t$	[93]
1st order chemical reaction		$-\ln(1-\xi) = \mathrm{k}t$	[93]
2nd order chemical reaction		$[1/(1-\xi)] - 1 = \mathrm{k}t$	[93]
One-dimensional diffusion		$\xi^2 = \mathrm{k}t$	[94, 95]
2-D diffusion		$(1-\xi)\ln(1-\xi) + \xi = \mathrm{k}t$	[94, 95]
3-D diffusion	Ginsling-Braunshteinn model	$1 - {}^2/_3\,\xi - (1-\xi)^{2/3} = \mathrm{k}t$	[94, 96]
	Jander diffusion model	$[1-(1-\xi)^{1/3}]^2 = \mathrm{k}t$	[95, 97]
Kolmogorov-Johnson-Mehl-Avrami		$\ln(-\ln(1-\xi)) = \mathrm{nlnk} + \mathrm{nln}t$	[96, 98]
2-D contracting area		$1-(1-\xi)^{1/2} = \mathrm{k}t$	[93]
3-D contracting volume		$1-(1-\xi)^{1/3} = \mathrm{k}t$	[93]

In order to be used as a practical hydrogen storage material, the hydrogenation-dehydrogenation kinetics should be fast enough. Apart from enthalpy and kinetic criteria some other requirements should be fulfilled by the interstitial hydride to meet DOE goals as claimed by Ivey and Northwood [99]:

- high hydrogen storage density
- good cyclic stability
- low hysteresis
- resistance to surface poisoning by gaseous impurities
- safety
- low cost

Several types of alloys and intermetallic compounds have been investigated with the purpose to improve their hydrogen storage properties, but none of them can satisfy all the criteria. From literature survey it has been found that in most of the cases they contain at least one stable hydride forming element and one non hydride forming element. Some of the major interstitial hydride systems are discussed in the next section.

1.1.3.2.4 Interstitial hydride systems

Light weight Mg based hydrides

Magnesium is considered as one of the most promising hydrogen storage materials due to its high hydrogen storage density (7.6 wt.%), high abundance and low cost. However, there are some barriers which limit its practical use for vehicular application. The large negative value of enthalpy of MgH_2 formation ($-75\ kJ\ mol^{-1}\ H_2$) results in a desorption temperature ~300°C at 1 bar of hydrogen pressure. Besides, the kinetics is inherently sluggish because of slow dissociative chemisorption at the metallic Mg surface [100] and the diffusion of hydrogen atoms through the growing MgH_2 layer is also slow [101].

To reduce the desorption temperature, Mg is usually alloyed with non hydride forming elements viz. Fe, Co, Ni, Zn, Ag, Cd, In [102-107] etc. Alloying may also improve hydrogenation-dehydrogenation kinetics. Addition of catalysts like Pd, Ni is known to promote the hydrogenation-dehydrogenation kinetics either by decreasing the dissociation barrier for molecular hydrogen or by reducing the activation energy for hydrogen desorption [108-110]. Apart from metallic element, addition of some metal oxides (especially Nb_2O_5), carbides, halides etc. are also known to accelerate the hydrogen absorption desorption kinetics considerably [111].

Another approach to improve hydrogenation-dehydrogenation kinetics is through ball milling which produces nanostructered magnesium with increased surface area and large extent of defects [112-115]. By ball milling the grain size decreases and diffusion length for hydrogen reduces which boost both hydrogen absorption and desorption kinetics. It is worth mentioning that nanoconfinement of MgH_2 within the mesoporous materials improves desorption kinetics [116]. Bulk MgH_2 ball milled with various types of carbon species [117-120] is reported to show improved kinetics and better cyclic stability. This is due to the conversion of carbon materials into graphene layers which encapsulate the MgH_2 nanoparticles in successive hydrogen absorption desorption cycles and prevent grain growth. This also provides a hydrogen transferring interface at the phase boundaries of carbon and MgH_2 making hydrogen diffusion easier and kinetics faster [121]. Plenty of research works have been carried out but no reversible Mg-based hydride with suitable thermodynamics and high hydrogen storage capacity has been found.

Classical intermetallic compounds

Over the years it is known that intermetallic compounds can be used for hydrogen storage purposes. Among different types of intermetallic compounds, $LaNi_5$ based systems are well studied and are also employed for practical applications. Except the limitation of lower gravimetric catapacity (only 1.5 wt.%), it shows quite good other hydrogen storage properties such as easy activation, fast hydrogen absorption desorption kinetics, low hysteresis, tolerance towards gas impurities [122] etc. The advantage of these systems is that the absorption desorption thermodynamics can be tuned simply by varying the composition or by partial substitution with other elements like Ce (in La site), Al, Fe, Co, Mn etc. (in Ni site) [122, 123]. Due to poor storage capacity they are not directly suited for vehicular application but utilized as stationary energy storage systems.

FeTi is another well known hydrogen storage material which is the cheapest among all reported intermetallic compounds. Unlike $LaNi_5$, rigorous activation is required for FeTi based systems prior to hydrogenation and they are highly sensitive to gas impurities [124]. The hydrogen storage capacity of FeTi is little higher (1.9 wt.%) compared to $LaNi_5$ but it suffers from intense hysteresis. Several approaches have been tried to improve hydrogen absorption desorption performances of FeTi compound such as partial elemental substitution of Fe or Ti, surface modification, mechanical alloying etc. Among all these approaches, addition of Pd has been found to be most effective [125].

Intermetallic compounds with laves phase structure have also received considerable interest in hydrogen storage research because of faster kinetics and better hydrogen storage density (~ 2 wt.%) compared to $LaNi_5$ based systems. They are represented by the general formula AB_2 where A = Ti or Zr and B = V, Cr, Mn, Fe, Co. Proper elemental substitution has been proven to improve the thermodynamic and kinetic properties of different hydrogen storage materials in Laves phase group [126, 127].

Body centered cubic (BCC) phase alloys

Unlike the conventional intermetallic compounds described above the Ti-V based BCC alloys have advantages of higher hydrogen storage capacities. It is reported that the maximum gravimetric hydrogen storage density can reach ~ 4 wt.% at room temperature for

Ti-V based alloys with BCC structure [128, 129] as can be seen from Fig. 1.15. Vanadium being an expensive element adds cost penalty to these Ti-V based alloys which is one of the major limitations for their practical automobile application. Substitution of V with much cheaper Fe appears to be a fruitful remedy and a lot of research has been carried out with Ti-V-Fe ternary alloys [130, 131]. Ti-V based alloys are difficult to activate. Fe substitution reduces the cost of the alloy, makes the activation easier and reduces hysteresis. All Ti-V based BCC alloys such as Ti-V-Cr, Ti-V-Fe, Ti-V-Mn show fast hydrogenation kinetics at ambient conditions [132].

Fig. 1.15 clearly shows that the hydrogen storage capacities of Ti-V based BCC alloys are higher compared to other intermetallic compounds but they are far from the DOE 2020 targets for light duty vehicular application.

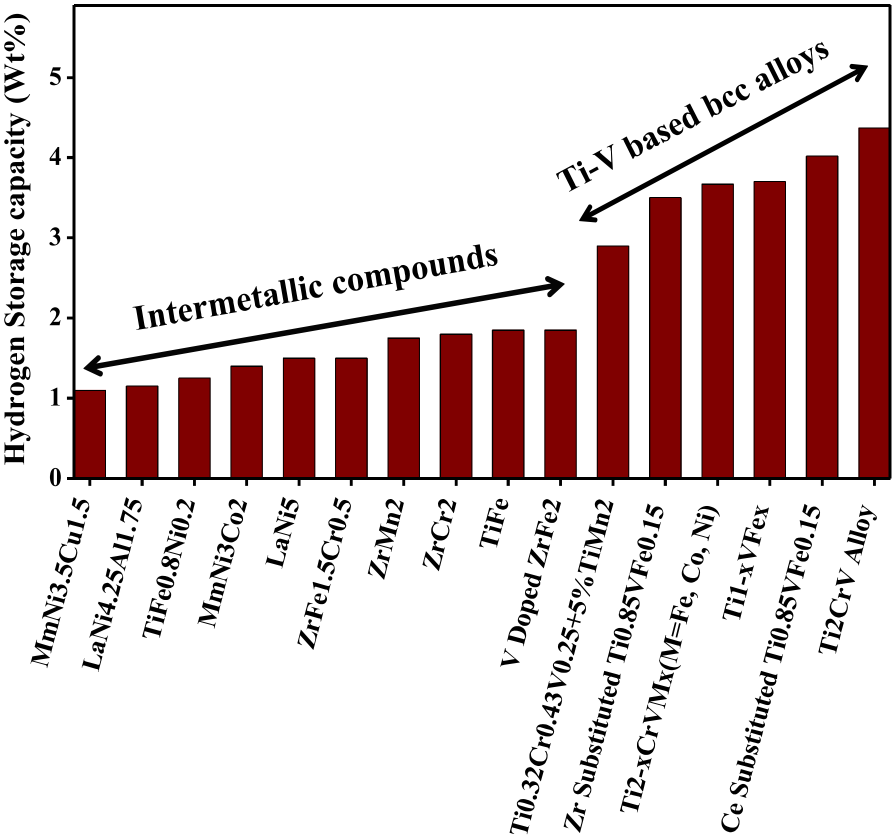

Fig. 1.15 *Hydrogen storage capacities of different alloys and intermetallic compounds.*

1.2 State of art

Absorption-desorption studies

Hydrogen absorption desorption properties of different physisorbed systems have been discussed in section 1.1.3.1.4. Hydrogen storage properties of chemisorbed systems such as light weight Mg based hydrides, classical intermetallic compounds, body centered cubic (BCC) phase alloys have been mentioned in section 1.1.3.2.4 under the heading "interstitial hydride systems". In the following paragraph hydrogen storage properties of some of the complex hydrides with very high hydrogen storage capacities have been discussed.

Sodium alanates

Sodium alanates are considered as potential solid state hydrogen storage material since 1997. Bogdanovic and Schwickardi demonstrated that $NaAlH_4$ can reversibly desorb hydrogen with fast enough kinetics under moderate conditions by Ti doping [133]. Upon heating, $NaAlH_4$ releases hydrogen in three steps as shown below [134]:

$$NaAlH_4 \leftrightarrow 1/3\ Na_3AlH_6 + 2/3\ Al + H_2 \quad (3.7\ wt.\%)$$

$$Na_3AlH_6 \leftrightarrow 3\ NaH + Al + 3/2\ H_2 \quad (1.9\ wt.\%)$$

$$3\ NaH \leftrightarrow 3\ Na + 3/2\ H_2 \quad (1.8\ wt.\%)$$

The first decomposition step occurs in the temperature range from 185 and 230ºC, and the decomposition temperature for second step is 260ºC. Finally, the complete decomposition of NaH occurs above 400ºC. However the last decomposition step is not considered for practical application. Moreover, regeneration of $NaAlH_4$ from the end products adds further hurdles towards the practical application of sodium alanate. Recent researches on $NaAlH_4$ show that nano-confinement is effective in destabilizing the material [135]. $NaAlH_4$ loaded in MOF started hydrogen release at 70ºC and 80% of the theoretical hydrogen was released at relatively lower temperature (155ºC) [136]. $NaAlH_4$ loaded into ordered mesoporous silica was also found to desorb at lower temperature with faster kinetics compared to pristine $NaAlH_4$ [137].

Lithium boro-hydrides

Lithium boro-hydride ($LiBH_4$) has received significant attention as potential solid state hydrogen storage material due to its high gravimetric hydrogen density (18.5 wt.%). Despite its high storage density, it faces some serious challenges such as air sensitivity, high decomposition temperature (> 400ºC), lack of reversibility at ambient condition [138, 139]. Enormous efforts such as addition of different types of catalysts, nanoscaling, destabilization were attempted to reduce their high thermal stability, enhance the reaction kinetics and resolve the poor reversibility [140-143]. Like sodium alanate, lithium borohydride releases hydrogen in different steps under different temperature regimes. Intially slight hydrogen release (0.3 wt.%) occurs in between 100 to 200ºC. The first and second significant hydrogen desorption occur at ~ 320ºC and 400ºC, respectively. The overall decomposition of $LiBH_4$ can be expressed by the following equation:

$$LiBH_4 \leftrightarrow LiH + B + 3/2\ H_2$$

Around 13.8 wt.% hydrogen is released when it is heated upto 900ºC. The decomposition product LiH contains rest 4.4 wt.% of hydrogen.

Amide-imide system

Since the discovery of reversible hydrogen storage in lithium nitride (Li_3N) by Chen et al. [144] in 2002, lithium based amide-imide systems have attracted considerable attraction. The chemical processes that occur during the hydrogenation and dehydrogenation of Li_3N are represented by the following equation

$$Li_3N+2H_2 \leftrightarrow Li_2NH+LiH+H_2 \leftrightarrow LiNH_2+2LiH$$

The above chemical processes offer very high value of hydrogen storage capacity (11.5 wt.%), theoretically. However, it suffers from various drawbacks such as high operational temperature (especially in terms of desorption), sluggish kinetics, and poor reversibility (only the amide-imide inter-conversion is reversible at practical operating temperatures). Studies revealed that addition of catalysts and reduction of particle size are effective in improving the kinetics [145, 146]. Luo et al. have found that Li-Mg-N-Hsystem exhibits absorption and desorption at much lower temperatures compared to Li-N-H system [147].

Kinetics of hydrogen absorption and desorption

Number of reports are available on hydrogen absorption desorption kinetics of different chemisorbed systems including metal hydride, alanates, amino borane etc. A detailed literature survey on the hydriding dehydriding kinetics of these systems is reported in the following paragraphs.

Goodell et al. [148] studied hydrogen absorption desorption kinetics of $LaNi_5$ based systems and concluded that the rate of hydriding reaction is controlled by surface process and bulk process (similar to diffusion) whereas the dehydriding reaction is only surface process limited. Recently Briki et al [149] have investigated the effect of different experimental conditions on the hydriding kinetics of $LaNi_5$ alloy and found a strong dependence of reaction rate on pressure and temperature. Lee et al. [150] experimentally studied the hydriding kinetics of $LaNi_5$ in the temperature range 293-333 K and obtained the activation energy of 20 kJ/mol of H_2. They reported the dissociative chemisorption of hydrogen molecules on the surface of $LaNi_5$ as the rate limiting step. Han et al [151] have investigated hydrogen absorption and desorption kinetics of MgH_2 systems and found that the hydriding dehydriding kinetics of MgH_2 is remarkably enhanced in presence of MoS_2 and MoO_2 catalysts. Zou et al. [152] studied hydrogen storage properties of Mg and showed that hydriding kinetics of Mg powder can be significantly improved by addition of small amount of rare earth materials such as Nd, Gd, Er to Mg. Li et al. have prepared nanocrystalline Ni@C and shown the synergetic effect of Ni nanoparticle and carbon to enhance absorption/desorption kinetics of MgH_2 by providing more H diffusion channels and active catalytic sites. As already mentioned, with nanoconfinement of complex hydrides in porous scaffolds, dehydrogenation-rehydrogenation has been achieved with faster kinetics at comparatively milder conditions [153]. Metal based oxides, hydrides, chloride and fluoride are the mostly used dopants for catalyzing de-/rehydrogenationof complex hydrides.

Cycle life

For practical applications it is crucial that the sorption characteristics such as storage capacity, kinetics, reversibility, equilibrium plateau pressure etc. of the hydrogen storage system remain almost constant during the whole life of the hydrogen storage device. Different applications need different number of cycles but for most of the applications, the number of cycles usually ranges from few hundreds to many thousands. Cycling life of a hydrogen storage material depends on many factors [154, 155]. An important factor is disproportionation of the alloy or intermetallic compound on repeated hydrogenation dehydrogenation cycles [156]. Kim et al. [157] have suggested that the dislocations formed during hydrogen cycling are responsible for the degradation of hydrogen storage capacity in V based BCC alloys. Another reason for the reduction in cycle life is poisoning by impurities in the hydrogen gas [158, 159]. A special way to improve cycling stability of alloy or intermetallic compound is by elemental substitution. Lim et al. [160] have reported that the partial substitution of La and Ni by Ce and Al, respectively is effective in improving the cycle life of La-Mg-Ni based hydrogen storage alloy.

Thermo-physical properties

Any metal hydride formation reaction is associated with a certain amount of heat release. The heat of reaction should be removed properly for providing optimal energy efficiency and fast kinetics for hydrogen absorption/desorption process. For example, the enthalpy of hydride formation is ~75 kJ mol^{-1} H_2 for the formation of MgH_2 from metallic

Mg. Without proper heat removal, this heat will raise the temperature and as a consequence the hydriding reaction will stop. However, common strategy for improving heat removal from metal hydride (MH) bed is to increase the effective thermal conductivity. Good thermal conductivity is also required for dehydrogenation process to promote the fast and uniform heating of metal hydride fuel tank. The thermal conductivity can be improved by using conductive matrices such as foams, fins or meshes of high conductivity materials such as Cu, Al, Fe and Ni [161-163]. Suda et al. [164] have reported that the impregnation of porous aluminium foam to the metal hydride bed is effective in increasing the thermal conductivity by 9-10 times compared to that of unmodified hydride bed. Thermal conductivity can also be increased by compacting metal hydride with graphite (e.g. graphite has a thermal conductivity of 1390 $Wm^{-1}K^{-1}$ at 400 K). However, these additives increase the system weight and thereby decrease the storage capacity. Therefore, accurate measurement of thermal conductivity is required to optimize the amount of the additives. Moreover, pressed metal hydrides are better compared to powder form due to their higher thermal conductivity.

In addition to thermal conductivity, specific heat capacity of metal hydride is another important parameter for thermal management of the MH bed. It describes the ability of a material to store thermal energy, and indicates the amount of thermal energy required to heat the material to a specified temperature. The specific heat capacity of $NaAlH_4$ is 86.24 J $mol^{-1}K^{-1}$ [165] whereas that of MgH_2 is only 24.9 J $mol^{-1}K^{-1}$. Hence $NaAlH_4$ decomposes at a relatively lower temperature compared to MgH_2.

Design and testing of lab scale and large scale hydrogen storage systems

Several theoretical and experimental studies have been carried out to optimize the design parameters of metal hydride based hydrogen storage devices (MHHSD). It is important to have a profound knowledge of heat and mass transfer of the metal hydride bed for fabricating such MHHSD. Several investigations were performed to develop models for predicting heat and mass transfer characteristics of lab scale hydrogen storage systems. Mayer et al [166] have evaluated heat and mass transfer behaviours of $LaNi_5$ based systems and suggested that factors like improved heat and mass transfer inside the metal hydride bed, higher value of external heat transfer coefficient and better thermal contact between metal hydride bed and the reactor wall increased the effective reaction rate. Numerical investigations on $MmNi_{4.6}Al_{0.4}$ based MHHSD by Muthukumar's research group have shown that 13.1 g hydrogen can be stored per kg of the alloy at 298 K under hydrogen pressure of 30 bar.

Muthukumar et al [167] have developed models for evaluating hydriding kinetics of industrial scale metal hydride based hydrogen storage reactor with 48 embedded cooling tubes and capacity of 120-150 kg of alloy (mainly $MmNi_{4.6}Al_{0.4}$ based) and shown that the hydriding kinetics becomes faster compared to the reactor without cooling tubes. In order to optimize heat and mass transfer properties of $LaNi_5$ based MHHSD equipped with finned spiral tube heat exchanger, Mellouli et al. [168] have developed a mathematical model and studied the effect of pitch, length, thickness and arrangement of fins on the hydriding performance of MHHSD. They have proposed that use of circular fins is effective to enhance the heat transfer and to improve the reaction kinetics.

Reports are also available on the complex hydride based hydrogen storage tanks [169, 170]. Employing sodium alanate, Johnson et al. [171] developed and tested a vehicle-scale hydrogen storage reactor. They have shown that the distribution of fluid flow plays a vital role during the design of hydrogen storage reactor.

Literature Summary

Literature survey has been summarised in the following section

- Both physisorbed and chemisorbed systems have their own advantages and disadvantages with respect to hydrogen storage applications. The problem associated with physisorbed system is its extremely low hydrogen binding energy. In contrast, most of the chemisorbed systems suffer from high value of M-H bond strength. They have the disadvantage of relatively higher desorption temperature and suffers from rigorous activation prior to hydrogenation. The complex hydrides show high hydrogen storage capacities but suffer from poor reversibility, which means that they cannot be used for long term hydrogen absorption-desorption cycles. The physisorbed systems show good reversibility, rapid kinetics but suffer from poor gravimetric storage capacity under ambient conditions. Unlike intermetallic compounds/alloys, physisorbed systems do not require high energy for releasing the adsorbed hydrogen gas. Further, recent advancement in the synthesis of high surface area materials has made physisorptive hydrogen storage an attractive option.

- Among various types of physisorbed systems, carbon based materials seems to be prospective because of their high surface area, wide variety of possible structural modifications, availability of many inexpensive synthesis methods, low density, chemical stability and biocompatibility.
- Different types of carbon based systems such as carbon nanotubes, activated carbons, templated carbons etc. have been explored for hydrogen storage studies. Though some of the previous works on carbon based physisorbed systems claim very high hydrogen storage capacities, those are mainly due to methodological error during measurement.
- Reported works on carbon based systems revealed that combination of proper instrumentation and careful measurement (including volume correction for sample) is essential for generating accurate hydrogen uptake data of carbonaceous materials. This is one of the major gap areas which have been addressed in the present study.

- Hydrogen storage studies on carbon based systems is currently focused on improvement of hydrogen uptake by surface functionalization, modification of pore texture and improving surface area.
- Hydrogen absorption desorption studies of different chemisorbed systems, such as, MgH_2, $LaNi_5$, Ti/Zr based alloys have been widely reported. These previous reports enlighten Ti based BCC alloys as very promising candidates for hydrogen storage applications, because such alloys exhibit reasonable hydrogen uptake at ambient conditions, fast hydrogen charging discharging and are easy to handle.
- Earlier studies on hydrogen absorption desorption properties of Ti based BCC alloys show that the desorption temperatures of these systems are relatively higher. Worldwide research effort is going on to optimise the desorption temperature of such alloys without significant reduction in storage capacity. This is another important aspect which has been addressed in the present study.
- Mechanistic aspects of hydriding reaction gives in-depth information regarding hydrogen metal interaction and this aspect is very important to optimize the hydrogen storage properties of Ti based BCC alloy systems. In the present thesis detailed mechanistic studies were carried out on such alloys.

Based on the above literature summary, objectives of the present thesis are mentioned below.

- Careful evaluation of the hydrogen storage properties of carbon based physisorbed systems in a sophisticated and fully automated Sieverts' type of set up (HTP1, HidenIsochema, UK) which takes care of the sample volume.
- To understand the effect of functionalization on the hydrogen storage properties of carbon nanotubes.

- Explore the effect of pore structure and surface area on hydrogen storage performance of turbostratic carbon prepared from sucrose, a readily available and cost effective carbon precursor.
- To develop Ti based BCC alloys with improved desorption behaviour (lowering the desorption temperature below 100 ºC) for integrated hydrogen production and storage test facility.
- To investigate hydrogenation kinetics of Ti based alloy systems for predicting their absorption mechanism.

Chapter 2

Synthesis Methods and Experimental Techniques

This chapter gives an overview of different synthesis methods used for preparing various types of carbon based materials and alloys/intermetallic compounds. Different techniques were employed for characterization of synthesized materials such as X-Ray diffraction (XRD), Scanning electron microscopy (SEM), Energy dispersive X-ray spectroscopy (EDS), Electron probe micro-analysis (EPMA), Transmission electron microscopy (TEM), Small angle X-ray scattering (SAXS), Thermogravimetric analysis (TGA), Differential scanning calorimetry (DSC) and Temperature programmed desorption (TPD). Some of the spectroscopic techniques like Solid state nuclear magnetic resonance (NMR), Mössbauer, Fourier transform infrared (FTIR) and Raman spectroscopy were also used for characterization. The instrumental and experimental details of all these techniques are provided in this chapter. This chapter also describes the methods for evaluating hydrogen storage properties of these materials using Sievert's type set up.

2.1 Material preparation

2.1.1 Synthesis of carbon based materials

This section gives a brief account of different methods used to prepare various types of carbonaceous materials. Two types of carbon based materials namely carbon nanotubes (CNTs) and turbostratic carbons were explored in the present study for investigating their hydrogen storage properties. CNTs were provided by the Rare Earth Development Section

(REDS) of Bhabha Atomic Research Centre, Mumbai. The samples were synthesized by chemical vapour deposition of acetylene diluted with nitrogen in a fixed bed reactor at 700ºC. Cobalt Formate dispersed over magnesia was used as catalyst [172]. This section presents the general principles of two different techniques, namely wet impregnation and polyol methods, through which Pd doping was achieved on CNTs. However, detailed description of these techniques is presented in Chapter 3.

2.1.1.1 Wet Impregnation method

Wet impregnation is a well-known method for doping metal nanoparticles on CNTs. In this method, impregnating metal precursor solution is added to the support (here CNT) and thoroughly mixed. The metal precursor migrates progressively from solution into the pores of support through diffusion process and the support becomes saturated. The driving force is the concentration gradient between the bulk solution and the solution within the pores of the wetted support. Finally, the metal precursor is reduced and the volatile component of the solution is removed by drying.

2.1.1.2 Polyol method

Polyol method is a simple route to disperse fine metal nanoparticles on CNTs by reduction of inorganic metal precursor in polyol (ethylene glycol, glycerol etc.). In this method, the metal precursor is thoroughly mixed with polyol and the mixture is heated to reflux upto the boiling point of the polyol. With increase in temperature, the reduction potential of the polyol increases leading to nucleation of metal nanoparticles. The advantages of polyol methods are:

i. Availability of large number of polyols with different boiling points and molecular weights which offers flexibility and adaptability to the polyol process

ii. The same polyol acts as solvent, reducing agent, capping agent thus implementing possibility of continuous flow synthesis

iii. Polyols are water equivalent solvents thus allowing low-cost metal salts (e.g., halides, nitrates, sulfates) to be used as precursor of metal nanoparticles

iv. The same polyol acts as reducing agent beneficial for direct preparation of elemental metals from metal precursor

v. Due to chelating property, polyols can also act as capping agent and thus effective for controlling particle nucleation and growth by preventing agglomeration of nanoparticles.

Synthesis of turbostratic carbon samples is described in detail in the second part of Chapter 3.

2.1.2 Synthesis of alloys/intermetallic compounds

Arc melting was performed to prepare alloys/intermetallic compounds. High purity constituent elements were weighed in the proper stoichiometric ratio and melted together in a DC arc melting furnace in a water cooled copper hearth under Ar atmosphere. The ingots were remelted 4-5 times to ensure alloy homogeneity. The detail of arc melting is presented herein.

Arc melting setup

The basic principle of an electric arc melting furnace is transfer of electrical energy to thermal energy in the form of an electric arc, generated in between the electrodes. In case of direct current (DC) electric arc furnace, the current flows from non-consumable electrode, which acts as cathode, to an anode embedded in the bottom of the furnace and act as a metallic bath. The DC arc melting set up used in the present work is shown in Fig. 2.1.

In this setup, few grams of samples can be melted and the ingot is obtained in "button" form. The non-consumable cathode is made up of tungsten, a refractory electrically conducting material. Before each arc melting the residual oxygen concentration in the arc chamber is reduced by melting a Zr getter. The zone volume of generated arc depends on several factors. The zone volume can be increased either by decreasing Ar pressure or increasing the current. The nature of inert gas also affects the arc zone volume. The arc zone volume increases when inert gas of higher ionization potential is used. After melting, the sample is cooled under Ar flow to room temperature before taking it out.

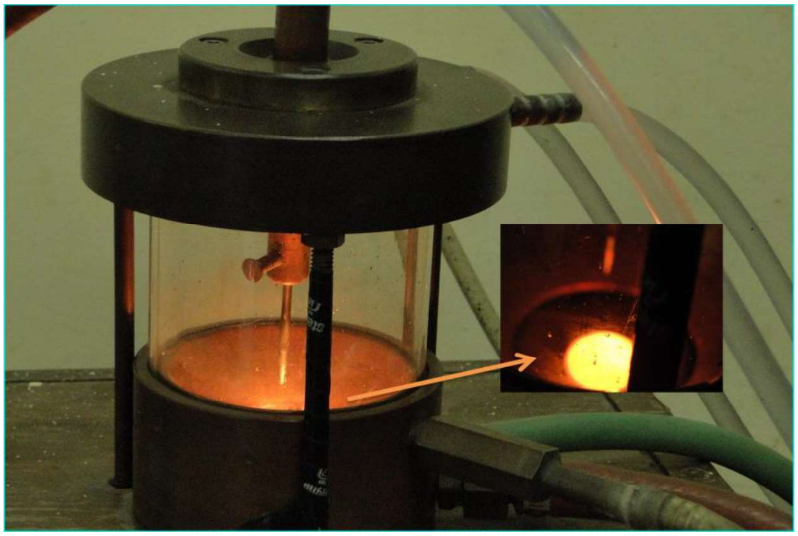

Fig. 2.1 *The arc melting furnace used during present study; inset shows melted alloy in the Cu hearth of the furnace.*

2.2 Characterization techniques

2.2.1 X-Ray diffraction

X-ray diffraction (XRD) is the most popular characterization technique used for the determination of crystal structures. In our present study, we used this technique to identify the phase of alloys/intermetallic compounds and their corresponding hydrides. Palladium doped carbon nanotubes and turbostratic carbon samples were also characterized using this diffraction technique. The wavelength of X-rays (range from approximately 0.04 Å to 1000 Å) being comparable to the size of atoms, it’s a good choice to use X-ray for probing the structural arrangement of atoms and molecules for a wide range of materials.

The principle of X-ray diffraction is based on scattering of X-rays by a crystal consisting of parallel arrays of atoms (equivalent to parallel lines of diffraction grating). When the X-rays are incident on a crystalline material, they are coherently/in-coherently scattered or absorbed. The coherent scattering of X-rays can interfere with each other giving bright (constructive interference) and dark (destructive interference) fringes. From the separation of bright fringes, the inter-planar spacing of a crystalline material can be determined. The bright fringes are obtained while the scattered rays interfere constructively at a particular angle so that path difference between the two rays differs by an integral number of wavelength. The classical Bragg condition for occurrence of such constructive diffraction is given by the following equation:

$$n\lambda = 2d \, \text{Sin}\theta \qquad (2.1)$$

where λ is wavelength of X-rays, θ is glancing angle (called as Bragg's angle), d is inter-planar separations, and n is the order of diffraction. Each plane is characterized by miller indices given by (hkl). A schematic representation of the X-ray diffraction from lattice planes is given in Fig. 2.2.

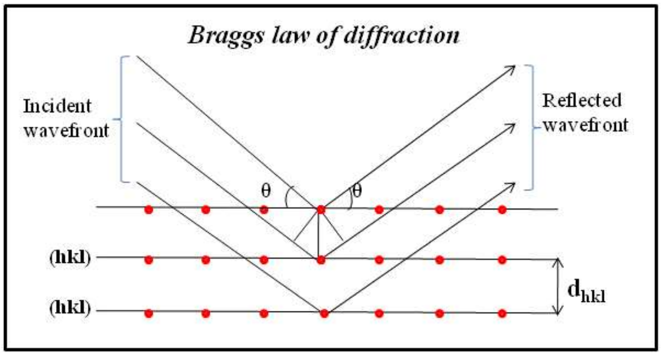

Fig. 2.2 *Schematic diagram of X-ray diffraction.*

X-rays being electromagnetic radiations interact with electrons of the atom, which oscillate with the same frequency as that of X-rays. These oscillating electrons act as source and re-emit radiation of the same frequency. Thus, incident radiation appears to be scattered by the atoms. Intensity of radiation of this coherently scattered X-rays is given by classical Thomson equation and called scattering power of an electron. Atom consists of many electrons and thus the overall scattering factor of an atom is given by,

$$f = f_0 e^{\frac{-B\sin^2 \vartheta}{\lambda^2}} \tag{2.2}$$

where f_0 is the scattering factor of an atom when it is at rest and at 0 K, λ is the wavelength of X-ray, θ is diffraction angle, B is a constant (usually called isotropic temperature factor, which is related to the amplitude of atom vibration and is given by $B = 8\pi^2 u^2$, where u^2 is mean square displacement of the atom from the mean position). The exponential term is called Debye-Waller factor. A crystal lattice consists of 3D atomic planes, which are made of numerous electrons. The scattering power of a particular plane in the crystal lattice is called structure factor of that plane. The structure factor of a plane is represented by the equation

$$F_{hkl} = \sum_{j\to 1}^{j\to N} f_j e^{2\pi i(hx_j + ky_j + lz_j)} \tag{2.3}$$

where F_{hkl} is amplitude of scattered radiation from (hkl) plane, f_j is the scattering factor of j^{th} atom at a diffraction angle θ, (x,y,z) are the position coordinates of j^{th} atom, N is the number of atoms in the unit cell of crystal lattice. The total exponential factor is denoted as phase of the wave. This structure factor is related to distribution of electron density in the unit cell, which in turn represents atomic distribution in the crystal.

A typical powder X-ray diffractometer consists of X-ray source, sample holder and a detector to pick up diffracted X-rays. A block sketch of typical powder diffractometer is shown in Fig. 2.3. X-rays are generally produced by bombarding high-speed electrons on a metal target in a sealed X-ray tube. During this process, a fraction of total electron energy is used for generation of X-ray beam whereas the rest is lost by heating the target. Hence, the target metal requires a continuous cooling. X-rays are produced in all directions and it is allowed to escape from a particular direction through a beryllium (Be) window in a diffractometer. Also the background and β radiation are filtered using β filters, which should essentially have low absorption for the characteristic X-ray radiation. Hence, if Z is the atomic number of the target metal then generally the filter is made of an element with atomic number (Z-1). The details of X-ray generation and typical X-ray spectra are explained in several monographs [173, 174].

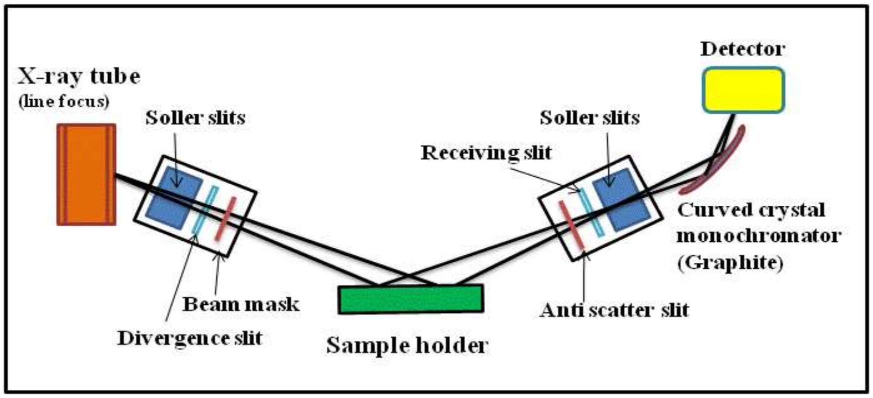

Fig. 2.3 *Ray diagram of a typical reflection mode diffractometer.*

As seen from Fig. 2.3, X-ray beam passes through the soller and divergence slits and then fall on the sample, which is spread uniformly over a glass slide. For better adhesion of sample to the slide, certain binders such as collodion, grease or wax are used. X-rays scattered (diffracted) from the sample pass though the receiving slits and soller slits and then fall on a monochromator before detection. The monochromator separates out stray wavelength radiation as well as any fluorescent radiation emitted by the sample. For detection of X-rays, scintillation counters or gas filled tube are commonly used. The gas filled tubes can either be a proportional counter or Geiger-Muller counter. Diffracted X-rays are scanned by sweeping the detector from one angle to another. A sharp rise in intensity (peak) is obtained when the detector angle is such that the Bragg's law is satisfied. Thus the output is obtained as plot of intensity of diffracted X-rays versus angle (2θ). This plot is generally termed as XRD pattern of the sample.

A powder X-ray diffractometer is usually based on Bragg-Brentano geometry as shown in Fig. 2.4. The X-ray source, specimen sample and detector are located on the focusing circle making an angle θ. During measurements, the detector moves by angle 2θ with respect to the sample, which is at the center of the measuring circle.

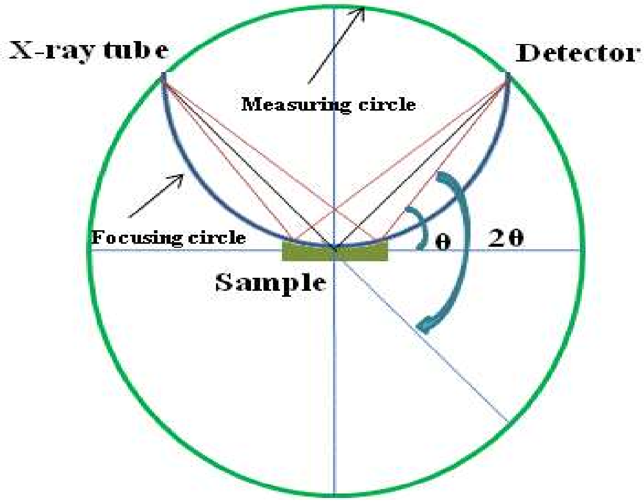

Fig. 2.4 *Bragg-Brentano geometry.*

The peaks (also called as reflections) in the XRD pattern correspond to a set of parallel planes with inter-planar spacing d_{hkl}. The position of the peaks is used to calculate d values. A particular sample gives a characteristic set of d-values. Thus, these values generally act as fingerprint for crystalline materials and they can be used for identification of the material. The intensity distribution of reflections is governed by the nature and kind of distribution of atoms in the unit cell. Absolute intensities of reflections depend on several factors like the intensity of source, counting time, nature and kind of distribution of atoms in the unit cell.

In the present work, most of the X-ray diffraction experiments were carried out using Ni filtered Cu K_α radiation on a computer controlled Philips PW1710 X-ray diffractometer, with X-ray generator operated at 30 kV and 20 mA and a proportional counter (Argon filled) as X-ray detector. The diffracted beam is monochromatized with a curved graphite single crystal. Philips PW1710 diffractometer is based on the Bragg-Brentano reflection geometry.

The data collection procedure often depends on specific requirements. In general, a short time scan over the 2θ range of 10 to 80° is sufficient for identification of a well crystalline inorganic material. However, low symmetry samples and samples with poor X-ray scattering power may need a slow scan. The scan time can be optimized for getting good intensity peaks. Prior to data collection, goniometer needs to be properly aligned for correct zero position. After proper alignment, instrument needs to be calibrated with standard known material like silicon, for determining the accurate peak position. In the present study, observed diffraction patterns were compared with JCPDS (Joint Committee on Powder Diffraction Standards, 1974) files available for reported crystalline samples. Unit cell parameters were calculated by least square method using the computer software "Powderx" [175].

Average crystallite size has been estimated from broadening of XRD peak by the Scherrer formula (equation 2.4):

$$\beta = \frac{0.9\lambda}{B cos\theta} \qquad (2.4)$$

where β is the average crystallite size (in angstroms), λ is the X-ray wavelength measured in angstrom, θ is the Bragg angle (in radians) and B is the corrected line width of the XRD peak.

The corrected line width B is measured from the full width at half maxima (FWHM) of the peak and is obtained from the Warren formula:

$$B^2 = B_M^2 - B_S^2 \qquad (2.5)$$

where B_M is the measured peak width (in radians) at half peak height and B_S is the measured peak width of a peak of a standard material, mixed in the sample, having a diffraction peak near to the relevant peak of the sample. There can be other factors like microstrain etc. which also contributes to the peak broadening but these factors are not considered here.

2.2.2 Scanning electron microscopy (SEM) and energy dispersive X-ray spectroscopy (EDS)

Electron microscopy technique is widely used to determine morphology, crystallographic defects, composition of phases and estimation of particle size etc. The technique is based on interaction of a focused electron beam with matter. Several phenomena occur when a focused beam of electrons interact with matter (specimen). They include processes like (i) emission of secondary electrons (SE) (ii) back-scattering of electrons (BSE) and (iii) transmission of electrons etc. Emissions of characteristic X-rays and absorption of electrons also occur during the interaction of primary electrons with matter. All these phenomena are illustrated in Fig 2.5.

In the present study, Scanning Electron Microscopy (SEM) has been used to study particle size and surface morphology of the hydrides of alloy samples using the instrument SEM SERON INC, South Korea made, Model number ATS 2100.

In a typical scanning electron microscope, a well-focused electron beam is incident and scanned over the sample surface by electro-magnetic deflection coils. Usually secondary electrons (SE) and/or backscattered electrons (BSE) are collected by a detector and the resulting signal is amplified and displayed on a cathode ray tube (CRT) screen [176]. Thus, the specimen image on CRT screen gives a map of surface topography of the sample. The CRT raster width divided by electron probe scanning width determines image magnification. It can be used in wide range of magnifications. The best reported resolution is around 2 nm. The main components of a typical SEM are (i) electron optical system, (ii) specimen stage, (iii) display and recording system, and (iv) vacuum system.

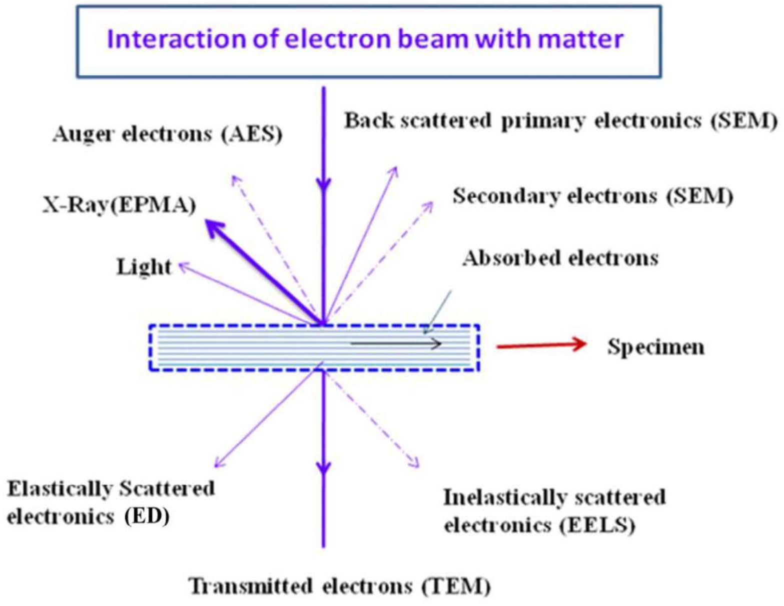

Fig. 2.5 *Depiction of different phenomena occurring as a result of interaction of electron beam with specimen.*

For SEM measurements sample should be vacuum compatible. Since electrons are charged particles they require vacuum environment for traversing without change in their number and density. Further, the sample should also be electrically conducting; otherwise there is a charge buildup due to accumulation of impinging electrons. This gives rise to jumping of beam leading to its instability. The surfaces of non-conductive materials are made conductive by coating with a thin film of gold, platinum or graphite.

The secondary electrons have low energies (typically below 50 eV), so only those originating from the surface can be detected. During SEM measurements, elements present in the sample also emit characteristic X-rays by excitation of inner shell electrons. These X-rays can be separately detected using a silicon-lithium detector. The signal from the detector is collected, amplified and corrected for absorption and other effects, for both qualitative and quantitative analysis of the elements present in the sample. This technique is known as energy dispersive X-ray spectroscopy (EDS). In the present study, compositions of the samples have been evaluated by EDS using the EDS instrument, made by Oxford

Instrumentation, UK, Model Number INCAE350, attached to the SEM instrument mentioned above.

2.2.3 Electron probe micro analyzer (EPMA)

The principle of EPMA is almost similar to SEM. Like SEM, EPMA also include an electron optical column to produce a well-focused electron beam, a scanning system, one or more electron detectors and a CRT display system. Differences arise from the fact that in EPMA emphasis is given on micro chemical analysis while SEM is mainly used for microscopic imaging [177]. In EPMA, micro chemical analysis is carried out with the aid of Moseley's law, which relates wavelength of each observed spectral line to a specific element through the relationship

$$1/\lambda = k(Z - \sigma)^{1/2} \qquad (2.6)$$

Where, λ is the wavelength, k is a constant for each spectral line series, Z is the atomic number of the element from which X-ray originates and σ is a constant associated with atomic screening effects. Both qualitative and quantitative analyses are possible by EPMA and involves normalizing the measured X-ray line intensities with pure elemental standard intensities and correcting for atomic number (Z), absorption coefficient (A) and fluorescence (F). The basic operating principles of EPMA instrument are depicted in Fig.2.6.

An electron beam is incident on the sample with sufficient energy to exceed the excitation potential, leading to ejection of core electron from the atom. The process leaves a vacancy, which is then filled by electron from higher energy state by electronic relaxation. This is accompanied by simultaneous release of characteristic X-ray (energy corresponding to difference between the orbital energy levels). .These X-rays are detected and characterized either by means of an energy-dispersive spectrometer (EDS) or a wavelength-dispersive spectrometer (WDS). In WDS, wave length distribution of emitted X-ray is measured by means of one or more crystal diffraction spectrometers. The basic principle of EDS is explained in section 2.2.2.

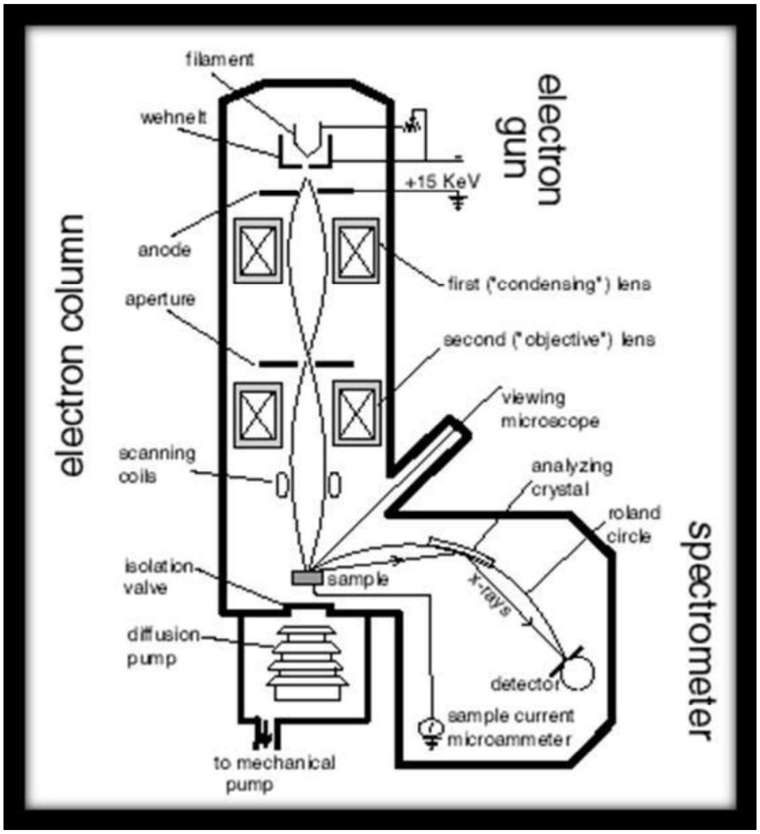

Fig. 2.6 *Schematic diagram of EPMA.*

In the present study EPMA analyses of alloy samples have been carried out using the CAMECA SX 100 electron probe micro-analyzer. In this instrument thoriated tungsten filament is used as a source of electron beam. A potential difference of 20 keV is applied between the filament (which acts as a cathode) and the anode, which is grounded.

Characterization of alloy samples by EPMA requires proper dressing of samples. The intensity of spectral lines can be influenced by absorption of primary beam and also absorption and enhancement of fluorescent radiation. This is mainly caused by surface roughness of alloy sample. Hence the alloy surfaces are required to be polished upto 0.1 – 1 micron level. The sample preparation is mainly divided into three parts namely (a) mounting, (b) grinding/fine polishing, and (c) coating.

2.2.4 Transmission electron microscopy (TEM)

Transmission Electron Microscopic (TEM) technique is used for determining morphology of particles upto 1nm or even lower in case of High Resolution TEM. In TEM, a beam of highly focused electrons is directed towards an ultra-thin sample specimen. Information is obtained from both transmitted and diffracted electrons. The first type of electrons gives image whereas the second type of electrons is responsible for diffraction mode in TEM. The image mode provides information regarding micro-structural features whereas the diffraction mode is used for obtaining crystallographic information.

A pin-shaped cathode is heated by passing current to produce ray of electrons which travels through ultra-high vacuum towards anode under an applied high voltage. The accelerated electron beam passes through a drill-hole in the anode. Condenser lenses focus the ray of electrons and allow it to pass through object. The object consists of a thin (< 200 nm), electron transparent, evaporated carbon film containing sample. After passing through the object, transmitted electrons are focused by an objective lens and subsequently lead to the formation of an image. The image is enlarged by a projector lens system and is visualized on a fluorescent screen placed at the bottom of the microscope. The image can be observed directly by an operator or can be captured by an image recording system.

In the present study, TEM measurements have been used to get the morphology and diameter of Pd nanoparticles, bare CNTs and Pd doped CNTs. The TEM studies were carried out using Jeol 2000 FX instrument operating at 120 kV. The samples were prepared by ultrasonication of finely ground samples in ethanol and then dispersing on a carbon film supported on a Cu grid.

2.2.5 Small angle X-ray scattering (SAXS)

Small Angle X-ray scattering (SAXS) is a powerful technique to probe inhomogeneities or density fluctuations in a sample matrix, on a length scale ranging from one nanometer upto one micron. The lower limit of length scale resolved by SAXS, overlaps with the length scale of interest in crystallography while the upper limit coincides with the length scale accessed by conventional microscope. The inhomogeneities are second phases in an otherwise structure-less sample matrix. These may be precipitates in an otherwise homogeneous material, pores in porous material, macromolecules in solvent etc. It involves measurement of elastically scattered X-rays (wavelength 0.1nm to 0.2 nm) at very small angles (typically 0.1-10°) [178, 179]. The technique is nondestructive and provides information about size or size distribution, shape, dimensionality, inter-particle spatial correlation etc. The technique also allows large specimen to be analyzed without any special sample preparation. It can be used in almost all domains of science and technology including metals, colloids, oil, polymers, cement, plastics, proteins, foods and pharmaceuticals for fundamental research as well as for quality control. SAXS experiment can be performed using a laboratory X-ray source or synchrotron light source (higher X-ray flux).

When a collimated beam of monochromatic X-rays is incident on an object, part of it undergoes elastic scattering. The scattering intensity (or amplitude) is a function of scattering angle (2θ) or scattering vector $\vec{q}$. The scattering vector is defined as difference between the incident and scattered wave vector $\overrightarrow{K_i}$ and $\overrightarrow{K_s}$. As the wave vectors $\overrightarrow{K_i}$ and $\overrightarrow{K_s}$ are proportional to the linear momentum of the incident and scattered photon respectively (p = hK where "h" denotes the Plank constant), the scattering vector $\vec{q} = \overrightarrow{K_s} - \overrightarrow{K_i}$ denotes the momentum transfer vector. For elastic scattering, $|\overrightarrow{K_i}| = |\overrightarrow{K_s}|$ and the scattering vector can be described as

$$\vec{q} = |\vec{q}| = |\overrightarrow{K_s} - \overrightarrow{K_i}| = 4\pi \sin(\theta)/\lambda \qquad (2.7)$$

where 2θ is the scattering angle and λ is the wavelength of incident X-ray. The strength of scattering interaction is dependent on "scattering length" which is proportional to atomic number of an element. Hence heavier the element the more it scatters. In addition, X-ray scattering length is always positive and for small angle scattering region it is almost independent of θ.

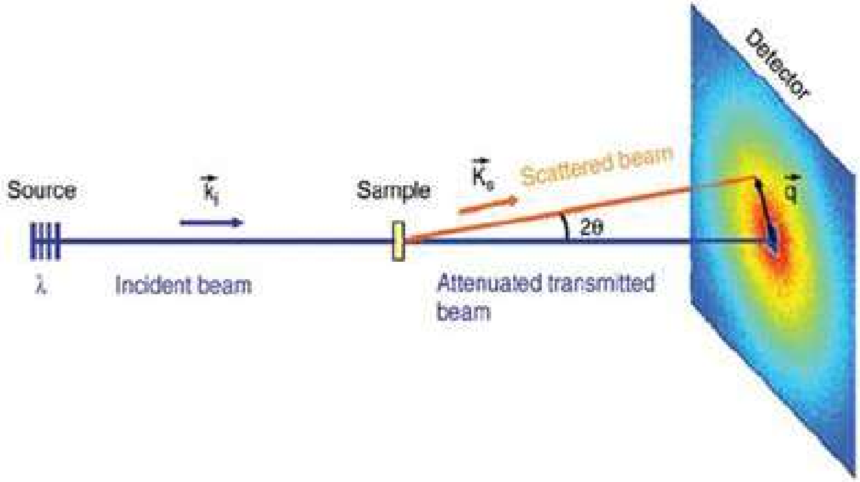

Fig. 2.7 *Schematic representation of SAXS experimental set up.*

Fig. 2.7 gives a schematic representation of an experimental set up for SAXS. A typical laboratory based SAXS experimental setup consists of X-ray source, monochromator, collimator, and detector. As 2θ is small in SAXS, a longer sample to detector distance is maintained to improve angular resolution. During SAXS experiment, the non-scattered beam that travels through the sample must be blocked without blocking the closely adjacent scattered radiation. Most of the available X-ray sources produce divergent beams and this enhances the above mentioned problem. In principle, this can be overcome by making beam parallel by a multilayer parabolic mirror (Gobble mirror) in conjunction with slit collimation.

In the present study, SAXS was used for investigating morphology, pore size and surface area of carbon based materials. It gave an idea about the heterogeneity existing on the surfaces of carbon based materials studied. SAXS measurements were carried out using a small angle goniometer mounted on the 12 kW Rigaku rotating anode X-ray generator. Scattered X-ray intensity was measured by transmission method using a scintillation counter with pulse height analyzer. Nickel filtered CuK_α radiation was used as the incident radiation.

2.2.6 Thermal analysis

Thermal analysis techniques evaluate heat and compositional changes associated with chemical and physical processes. In the context of hydrogen storage studies, thermal analysis is required mainly to get an idea about the desorption behavior of the hydrides and also to determine the stability of carbon samples.

2.2.6.1 Thermo gravimetric analysis (TGA)

In TGA, sample is heated at a controlled uniform heating rate and the sample mass is monitored as function of temperature/time [180]. In this technique, heating can be carried out under nitrogen/argon (inert) or air (oxidative) atmosphere. Thermogravimetric data can be presented either by plotting mass against temperature/time (TG curve) or by plotting rate of change in mass with respect to temperature/time (DTG curve). In the present study, TGA has been performed for carbon samples under air to know their oxidation temperatures using a thermogravimetric analyzer (Setaram, France). Oxidation of carbon to CO_2 appears as mass loss in TG curve whereas in DTG curve it appears as a peak.

TGA instrument essentially consists of a micro-balance and during measurements change in sample mass affects the equilibrium of the balance. This imbalance is fed back to a force coil, which generates an additional electromagnetic force to regain equilibrium. The additional electromagnetic force is proportional to change in mass. During heating process, temperature of furnace inside the instrument may go as high as 1500 °C depending upon its configuration.

2.2.6.2 Differential scanning calorimeter (DSC)

Any transition occurring in the sample, which is associated with either absorption or evolution of heat can be monitored by Differential scanning calorimetric technique. During DSC experiment, the sample is placed in one pan, and a standard sample (like Al_2O_3) in the other pan as shown in Fig. 2.8. During measurement, the sample and reference material are simultaneously heated or cooled at a constant controlled heating rate inside a furnace [181]. In case of any exothermic/endothermic transition, the amount of heat flow from system to sample and reference material varies in order to keep them at same temperature. In DSC technique this difference in heat flow is recorded against temperature and time. This technique is extensively used in the field of polymer science for determining thermal transitions of polymer such as melting point and glass transition temperatures. Desorption of hydrogen from hydride occurs by absorbing heat, hence it can be detected as an endothermic peak during DSC scan.

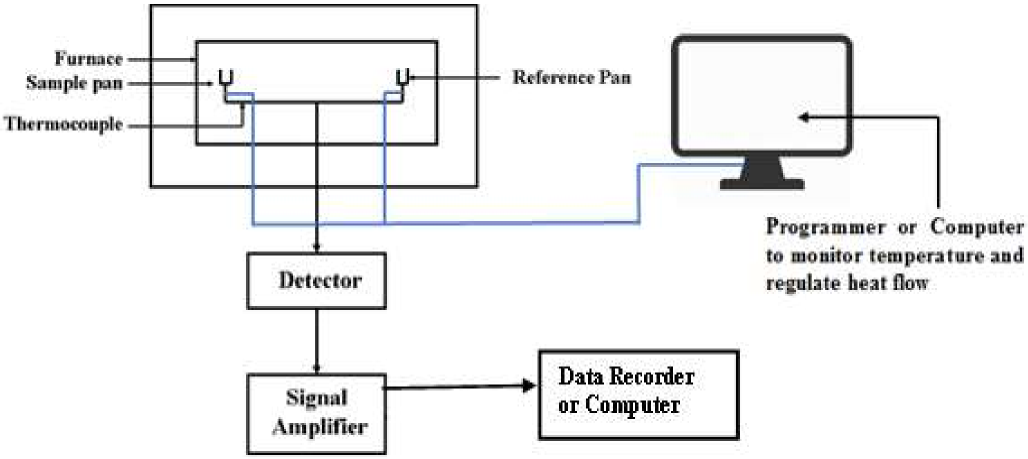

Fig. 2.8 *Schematic diagram of DSC.*

2.2.6.3 Temperature programmed desorption (TPD)

Temperature programmed desorption (TPD) is an important technique for studying the desorption behavior of hydrides by means of programmed heating. With help of this technique number of different hydrogen absorption sites and their relative stability can be determined in a hydride sample [182]. In the present study, in situ TPD experiments of alloy hydrides have been carried out in a fully automated Sievert's type of set up (described in section 2.3).

During TPD experiment a small amount of sample is placed in a sample holder that can be heated by a furnace. An inert carrier gas (helium) is allowed to flow continuously over the hydride sample. The desorption profile is recorded by heating the hydride sample at a fixed heating rate under the controlled flow of helium. A mass flow controller (MFC) is used to monitor change in hydrogen concentration with time. Initially, as temperature is low (desorption can hardly occur) a steady baseline is obtained. With increase in temperature, desorption process starts and the hydrogen concentration in effluent stream increases and this is recorded by MFC. As the hydride is heated to higher temperature, desorption rate increases and so does the signal intensity. The desorption rate goes through a maximum with increase in temperature and then drops back to baseline when hydride desorption is complete from a particular site. The sample is cooled after completion of the analysis. If desorption involves different hydrogen binding sites in the hydride specimen, the TPD profile may contain more than one peak.

2.2.7 Spectroscopic techniques

2.2.7.1 Vibrational spectroscopy

Vibrational spectroscopy is the most widely used spectroscopic technique for structural characterization and in particular for identification of different linkages present in a material. It is mainly based on interaction of electromagnetic radiation with different vibrational energy levels in a molecule. The interaction can result in transition between various quantized energy states. Depending on the absorption region of electromagnetic radiation and energy state transition, different sorts of structural information can be obtained from such vibrational spectroscopy. Two types of vibrational techniques, namely IR and Raman spectroscopy have been used in the present study and their principles are briefly described below.

IR spectroscopy

The infrared region of the electromagnetic spectrum encompasses radiation with wavelengths ranging from 1 to 1000 microns. This range is divided into three regions; Near IR (12500 – 4000 cm^{-1}), Mid IR (4000 – 200 cm^{-1}) and Far IR (200 – 10 cm^{-1}). Most of the analytical applications are limited to a portion of the middle range extending from 4000 to 400 cm^{-1} or 2.5 to 25 μm. When infrared (IR) radiation interacts with a molecule, transition between vibrational (along with rotational) levels of the bond occurs by absorption of equivalent energies. These absorptions appear as bands in IR spectra. Wave number corresponding to absorption can be calculated by the harmonic oscillator model given below:

$$\overline{\upsilon} = 1/2\pi c\sqrt{\mathrm{k}/\mu} \qquad (2.8)$$

where, k is the force constant and μ is the reduced mass defined by

$$\mu = \frac{m_A m_B}{m_A + m_B} \qquad (2.9)$$

Therefore, wavenumber corresponding to absorption is related to force constant and reduced mass. Since the force constant is directly related to chemical bond strength, the groups with stronger chemical bond and smaller reduced mass show absorption band at higher wavenumbers. Assuming molecule as a harmonic oscillator, energy of vibrational levels can be expressed as:

$$E_\upsilon = \left(V + \frac{1}{2}\right)h\omega \qquad (2.10)$$

The primary requirement for observing vibrational spectra from molecules is that there should be change in electric dipole moment with absorption of radiation. The allowed transitions in between vibrational levels are guided by selection rule $\Delta\upsilon = \pm 1$.

Modern IR instruments are based on Fourier transformation (FT) method to improve the signal to noise ratio. Unlike conventional IR instrument, in FTIR instrument, all the frequencies are used simultaneously to excite all the vibrational modes of different types of bonds/linkages present in the sample. This reduces experimental time and improves the signal to noise ratio considerably.

In the present study, all infrared data were recorded using a Bomem MB102 FTIR machine having a range of 200-4000 cm^{-1}, with a resolution of 2 cm^{-1}. IR radiation was generated from globar source (silicon carbide rod). The instrument used CsI single crystal, as the beam splitter and deuterated triglycine sulphate (DTGS) as a detector. Prior to IR measurements, the samples were ground thoroughly by mixing with dry KBr powder, pressed to form a thin pellet and introduced into the sample chamber of the instrument.

Raman spectroscopy

Raman spectroscopy is based on interaction of monochromatic light with electron cloud and bonds present in a molecule. Usually, the source of light is a laser in the visible, near infrared, or near ultraviolet region. During interaction with light, a part of the incident photon energy is absorbed by the molecule and this leads to excitation of molecule to a virtual energy state. As the molecule cannot remain within this virtual state, it relaxes to ground state by emission of a photon whose energy is same as that of the exciting radiation, and the phenomenon is known as Rayleigh scattering and is schematically shown in Fig. 2.9. There is no frequency change in the emitted photon for Rayleigh scattering with respect to the incident light. However, if molecule’s excitation or relaxation involves different energy levels then the frequency of scattered light is different from that of incident light (inelastic scattering). This process is called Raman scattering. If the frequency of scattered light is higher than that of incident light, anti Stoke lines (peaks) are observed. Scattered light with lower frequency than that of incident light leads to appearance of Stokes lines. Primary requirement for observing Raman spectra is that there should be change in polarizability of the molecules/bonds upon interaction with an incident radiation [183, 184].

According to group theory, if a molecule has a center of symmetry, vibrations that are Raman active will be IR inactive and vice versa. Since there are fewer molecules in upper vibrational state than in the lower one, intensity of anti-Stokes line is much less than that of Stokes line. Both Stokes and anti Stokes lines are extremely weak compared to intensity of the Rayleigh scattered light and is 10^{-7} times less than that of the intensity of incident light [185].

Raman spectroscopy is widely used to investigate vibrational, rotational, and other low-frequency modes in different compounds. In the present study, the technique was used for studying the structure of carbon based materials. Home-made Raman spectrometer was used for these studies. A diode pumped solid state laser with an output wavelength of 532nm was used for excitation of the carbon samples. Rayleigh scattered light from the samples is removed by placing a holographic edge or notch filter. Raman spectra are recorded using liquid nitrogen cooled CCD detector with atypical spectral resolution of 4 cm^{-1}.

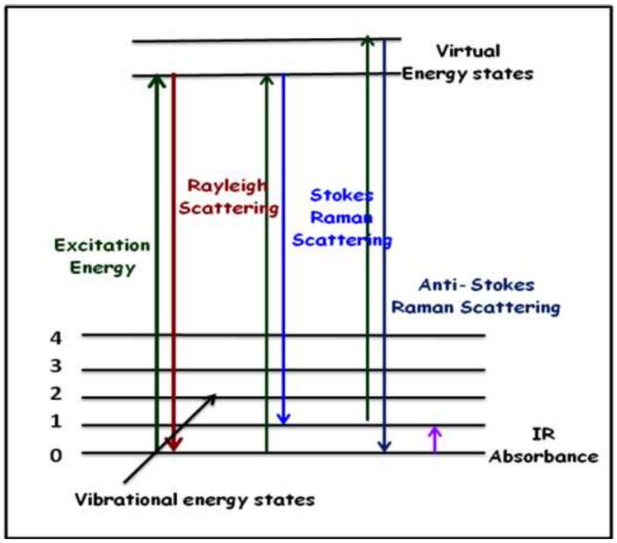

Fig. 2.9 *Schematic representation of Raman scattering.*

2.2.7.2 Nuclear magnetic resonance (NMR) spectroscopy

NMR is a spectroscopic technique that is used for structure elucidation in Chemistry, Biology, Material Science etc. The technique is non-destructive and does not require elaborate sample preparation. In NMR, nuclear magnetic properties of atomic nuclei are exploited to get valuable information about the structure, dynamics and chemical environment around a particular nucleus in a molecule/lattice.

Chemical shift (δ)

The chemical shift of any nucleus is defined as the difference between its resonance frequency and the resonance frequency of the same nuclei in a reference sample. It is given by:

$$\delta = \frac{\omega - \omega_0}{\omega_0} * 10^6 \qquad (2.11)$$

where ω and ω_0 represent resonance frequencies of nuclei in a sample and in the reference, respectively. The δ values are independent of applied magnetic field and can be used to monitor the structural changes taking place around a particular nucleus.

Chemical shielding

This quantity is directly related to Chemical shift. In NMR chemical shielding arises because of the polarization effect of electron cloud around the nuclei. Hence, the effective magnetic field felt by nucleius is different from the applied magnetic field. Chemical shift in NMR is an anisotropic parameter i.e. it has a directional dependence. In terms of Hamiltonian chemical shift can be written as [147]:

$$H_{cs} = \gamma I_z \sigma B_0 \qquad (2.12)$$

where σ is a second rank tensor and known as the chemical shielding tensor. This tensor can be diagonalised for a specific principal axis system and σ_{11}, σ_{22} and σ_{33} are the corresponding diagonal components. The isotropic component of chemical shift tensor can be expressed as:

$$\sigma_{iso} = \frac{1}{3}\left(\sigma_{11} + \sigma_{22} + \sigma_{33}\right) \qquad (2.13)$$

The symmetry parameter is defined as: $\eta = \dfrac{\sigma_{22} - \sigma_{11}}{\sigma_{33} - \sigma_{iso}}$ (2.14)

Due to the presence of chemical shielding anisotropy, the nuclear precession frequency depends on the orientation of principal axis system with respect to the external applied magnetic field and can be expressed by the relation [186]:

$$\omega_p\left(\theta,\phi\right) = \gamma B_0 \left\{\left(1-\sigma_{11}\right)^2 cos^2\phi \sin^2\theta + \left(1-\sigma_{22}\right)^2 \sin^2\phi \sin^2\theta + \left(1-\sigma_{33}\right)^2 \cos^2\theta\right\}^{1/2} \qquad (2.15)$$

where, θ and Φ represent the orientation of principal axis system with applied magnetic field direction. For axial symmetry η = 0 and the precession frequency can be expressed by the relation:

$$\omega_p\left(\theta\right) = \gamma B_0 \left[1 - \sigma_{iso} - \Delta\sigma.\left(3\cos^2\theta - 1\right)/3\right] \qquad (2.16)$$

For θ = 54.7° the term ($3\cos^2\theta$-1) becomes zero and the dependence of chemical shielding anisotropy term on Larmor frequency gets averaged out to a very small value.

In solution NMR spectroscopy, dipolar interactions and anisotropic effects are averaged out by the molecular motion, but this does not happen in case of solid state NMR spectroscopy. NMR spectra of solids tend to be broadened because of

a. magnetic interactions of nuclei with the surrounding electron cloud (chemical shielding interaction)
b. magnetic dipole-dipole interactions among nuclei
c. interactions between electric quadrupole moment of nuclei and surrounding electric field gradient.

Hence it is too difficult to get any meaningful information from such NMR patterns. However, the interactions can be averaged out by using suitable experimental strategies. One such technique used to get high resolution solid state NMR pattern in solids is the magic angle spinning nuclear magnetic resonance (MAS NMR) technique which is briefly described below.

Magic angle spinning nuclear magnetic resonance (MAS NMR)

MAS NMR technique involves rotating powder samples at high speeds, about an axis oriented at 54.74° (magic angle) with respect to the applied magnetic field direction. When θ=54.7°, the term ($3\cos^2\theta$-1) becomes unity as already mentioned and anisotropic interactions get averaged out in time during fast spinning. This is schematically shown in Fig. 2.10.

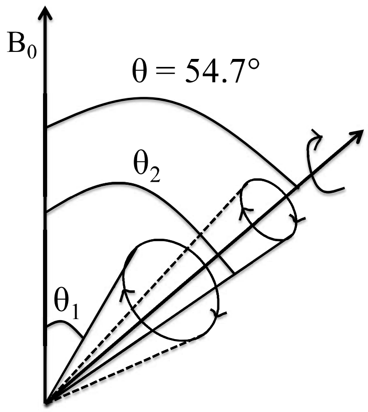

Fig. 2.10 *Principle of MAS NMR experiment.*

Thus, MAS NMR technique simplifies solid state NMR patterns, giving rise to sharp peaks and facilitates assignment of chemical shift values of different peaks to variation in local environments [186, 187]. Although, MAS is an efficient technique used for obtaining high resolution NMR patterns from solid samples, in many cases, due to spinning, side bands appear along with central isotropic peak for nuclei having wide range of chemical shift. These side-bands are mirror images of the isotropic peak and spread from the isotropic peak by integer multiples of spinning frequency. For nuclei with spin value ½, side-band pattern is a measure of chemical shift anisotropy and valuable information regarding symmetry of electronic environment around a probe nucleus can be obtained from intensity distribution of side-bands. However, in presence of large number of isotropic peaks, number of side-bands also increases, and there can be overlap between side-bands and isotropic peaks, which makes MAS NMR pattern complicated.

In the present study, ^{13}C CP MAS NMR (cross polarization magic angle spinning nuclear magnetic resonance) patterns were recorded using a Bruker Avance 400 machine having a standard bore MAS accessory at a basic frequency of 100.5 MHz for ^{13}C nuclei. A 90° pulse width of 5 μs, a contact time of 10 ms with a relaxation time of 15 s were employed for recording the NMR patterns. Samples were spun at a frequency of 10 kHz. All chemical shift values are expressed with respect to tetra-methyl silane as the reference material.

2.2.7.3 Mössbauer spectroscopy

Mössbauer spectroscopy is used to probe minute changes in energy levels of an atomic nucleus in response to its surrounding environment. It is based on recoilless emission and resonance absorption of gamma rays by identical nuclei bound in a solid matrix [188]. This phenomenon (Mössbauer effect) was first observed by Rudolph Mössbauer in 1957 in ^{191}Ir and due to this invention he won 1961 Nobel Prize in Physics. When the atoms are within a solid matrix, effective mass of nucleus is very much high. In this situation, the recoiling mass is effectively the mass of whole system, so if gamma-ray energy is small enough, recoil of nucleus is too low to be transmitted as a phonon giving rise to recoil-free event. The relative number of recoil-free events (and hence the strength of signal) strongly depend upon gamma-ray energy and hence the Mössbauer effect is detected only in those isotopes with very low lying excited states. The resolution of this technique is largely dependent upon lifetime of excited state. These two factors limit the number of isotopes that can be used successfully in Mössbauer spectroscopy. For Mössbauer spectroscopy ^{57}Fe isotope is most commonly used because it has a very low energy gamma-ray as well as long-lived excited state. A simple Mössbauer spectrum from identical source and absorber is shown in Fig. 2.11.

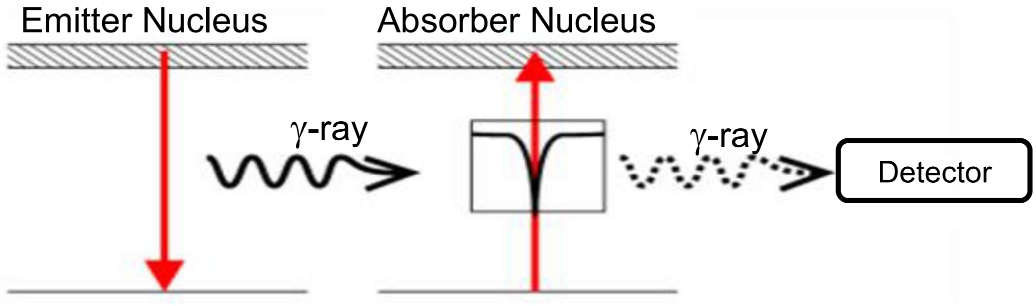

Fig. 2.11 *Schematic representation of Mössbauer effect.*

Isomer shift (Electrical monopole interaction).

Isomer shift is an important parameter in Mössbauer spectroscopy which arises due to the difference in chemical environments around emitting and absorbing nuclei. It describes the monopole interaction of the electronic charge density (especially s-electron density) over non-zero volume of the nucleus leading to alteration in nuclear energy level. Thus any difference in the s-electron environment between source and absorber results in a shift of the resonance energy of transition. Larger the isomer shift the more sensitive will be the Mössbauer nuclei to small differences in chemical environments. As the shift cannot be measured directly it is quoted relative to a known absorber. For example, ^{57}Fe Mössbauer spectra will often be quoted relative to α-iron at room temperature. The isomer shift value is defined by the following equation:

$$IS = \delta = CZe^2\left(R_{ex}^2 - R_g^2\right)[|\psi(0)|_{abs}^2 - |\psi(0)|_{sou}^2] \qquad (2.17)$$

Here Ze represents positive charge of the nucleus, R_g and R_{ex} are the effective radii of ground and excited nuclear states, respectively. The factor C in equation 2.17 depends on the shape of nuclear charge distribution.

The isomer shift is very sensitive to differences in valence states. Electron charge density at the nucleus is affected directly by change in number of bonding electrons in s orbitals, and indirectly by screening of s-electrons by p or d electrons. Hence, information regarding valence states, ligand bonding states, extents of electron shielding and electron drawing power of electronegative groups can be obatined from isomer shift value in Mossbauer spectrum. In the present study, ^{57}Fe Mössbauer spectroscopy has been used to see the effect of hydrogenation on the structural properties Fe containing alloys. Upon hydrogenation, these alloys show an increased isomer shift.

Quadrupole splitting (Electrical quadrupole interaction)

Quadrupole splitting arises due to electrical quadrupole interaction for all nuclei with $I>1/2$ (I is angular momentum quantum number). For these nuclei, nuclear charge distribution is not spherically symmetric producing nuclear quadrupole moment. This nuclear quadrupole moment interacts with asymmetrical electric field (EFG $\neq 0$, where EFG stands for Electric Field Gradient characteristic of electronic charge distribution) and splits the nuclear energy states.

For example, ^{57}Fe is having $I = 3/2$ for its first nuclear excited state and is split into two substates with $m_I = \pm 1/2$ and $m_I = \pm 3/2$ due to electrical quadrupole interaction. This is shown in Fig. 2.12 as a two lines spectrum or doublet.

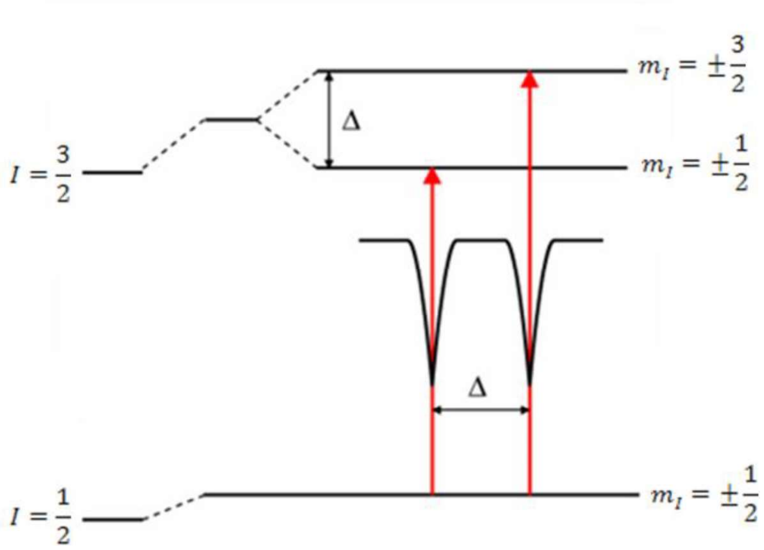

Fig. 2.12 *Quadrupole splitting in* ^{57}Fe.

The extent of the splitting depends on asymmetry in electronic charge distribution. For ^{57}Fe the magnitude of the quadrupole splitting is given by

$$QS = \frac{1}{2}(e^2 q_{ZZ} Q)(1+\eta^2/3)^{\frac{1}{2}} \qquad (2.18)$$

where q_{ZZ} is the principal component of EFG, η is asymmetry parameter and value of QS is highly sensitive to charge state (high spin and low spin) as well as the nearest neighbour environment of the probe atom.

Magnetic hyperfine interaction

Nuclear magnetic moment experiences dipolar interaction with the applied magnetic field leading to further splitting of nuclear levels (Zeeman splitting). The source of magnetic field experienced by the nucleus may be external or internal. The internal magnetic field is generated by local magnetic moments of atom's own unpaired electrons.

This magnetic field removes nuclear degeneracy and splits nuclear levels with a spin of I into (2I+1) substates, and can be expressed by the relation

$$E_{ml} = -g_n \beta_n m_I H_{eff} \qquad (2.19)$$

where g_n is gyromagnetic ratio, β_n is the nuclear Bohr magneton, m_I is the component of nuclear spin I, H_{eff} is the effective magnetic field at the nucleus. Transitions between the excited state and ground state can occur only when $\Delta I = 1$, $\Delta m_I = 0, \pm 1$. This selection rule leads to hyperfine splitting and appearance of sextet for ^{57}Fe as illustrated in Fig. 2.13, with line spacing being proportional to H_{eff}.

The positions of sextet lines are related to the splitting of the nuclear energy levels whereas their intensities are related to the angle between the Mössbauer γ-ray and the nuclear magnetic moment. Hence a pure polycrystalline iron metal gives a symmetric sextet with intensities in the ratio 3:2:1:1:2:3 and the line separation is a measure of hyperfine field strength at the nucleus. The interactions mentioned above i.e. isomer shift, quadrupole splitting and magnetic splitting alone or in combination are used to analyse Mossbauer spectra and correlate them to structural features.

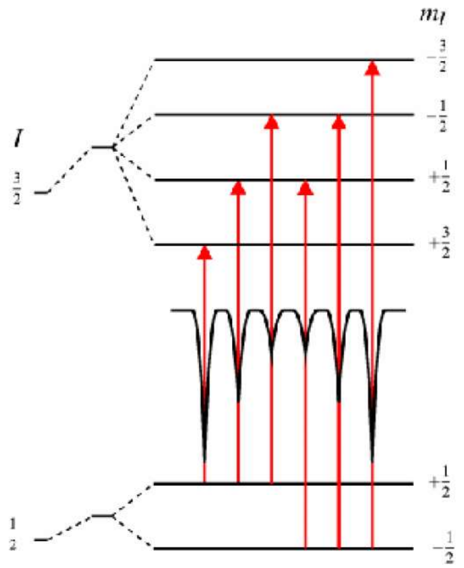

Fig. 2.13 *Magnetic splitting of the nuclear energy levels.*

In the present study, Room temperature ^{57}Fe Mössbauer spectra were recorded using a Mössbauer spectrometer (Nucleonix Systems Pvt. Ltd., Hyderabad, India) operated in constant acceleration mode (triangular wave) in transmission geometry. ^{57}Co embedded in Rh matrix was used as the monochromatic source of gamma ray. The spectrometer was calibrated with α-Fe and the isomer shift values given in this study are with respect to α-Fe.

2.3 Sievert's Type Setup

Initial hydrogen charging-discharging of metals/alloys/intermetallic compounds/carbon based materials have been carried out in an indigenously developed Sievert's type set up. In most of the studies the final hydrogen storage data has been verified and recorded in a fully automated Sievert's type of volumetric set up (IMI analyzer from Hiden Isochema, UK, model HTP1) and reported here. The hydrogen uptake by any sample is determined based on Sievert's principle [189]. In the home made set up all the necessary calculations are done manually whereas these tedious jobs are performed automatically in the IMI analyzer. The photographs of both the systems are given in Fig 2.14 ((a) and (b), respectively). The schematic diagram of indigenously developed Sievert's type set up is shown in Fig. 2.15.

Fig 2.14 *Sievert's type set up (a) indigenously developed, and (b) fully automated.*

The main components of indigenously developed Sievert's set up are:

i. *A high-pressure manifold connected to the pressure transducer*

ii. *Vacuum line*

iii. *Hydriding reactor*

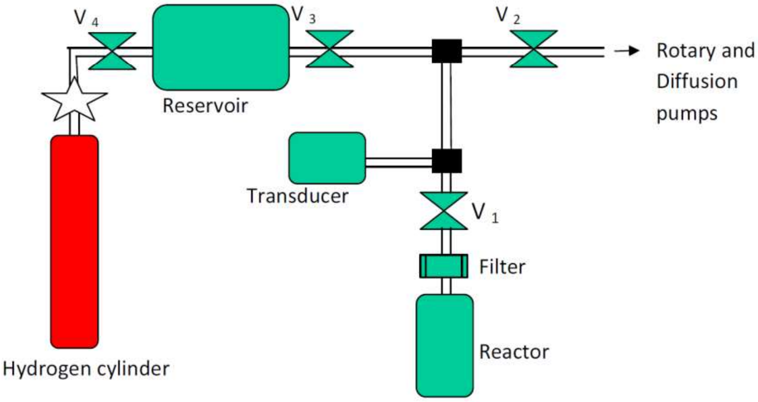

Fig. 2.15 *Schematic diagram of indigenously developed Sievert's type set up.*

The indigenously developed setup is made up of SS316 so that it can withstand high temperature and pressure. The reactor is of cylindrical shape with inner and outer diameters of ~24 mm and ~37 mm, respectively. The height of the reactor is ~210 mm. The sample holder is of 20 mm diameter and 39 mm height. It is placed inside the reactor and a spacer rod is placed above the sample holder to reduce the excess volume. The reactor is connected with the manifold through screw connection and Viton "O" ring. The "O" ring is cooled externally by passing water through the Cu coil to prevent damage at high temperature. A filter with 200 mesh size is put in the line which connects reactor and manifold, to avoid the contamination of the system with fine hydride particles. An on-off valve (V_1) is placed in between the reactor chamber and manifold and this is used to expose the sample to hydrogen atmosphere. In order to carry out initial activation of samples under high temperatures and hydrogen absorption-desorption studies at elevated temperatures, the reactor is inserted partially into a tubular furnace. A chromel-alumel thermocouple, attached with the reactor, is used for temperature measurement. The manifold is connected to the vacuum system (rotary and diffusion pump) through valve V_2. The set-up has been tested carefully in high vacuum (10^{-6} mbar) and high pressure (60 bar.). Volume calibration for different parts of the setup has been carried out using gas law.

Volume Calibration:

The volumes of importance during the experiment are mainly (a) the manifold volume and (b) the reactor volume. The manifold includes the space between valves V_1, V_2, V_3 and V_4. The volumes of manifold and reactor are denoted as V_M and V_R, respectively. The entire system is evacuated to 10^{-6} mbar. By operating appropriate valves, hydrogen from the cylinder is admitted into the manifold with volume V_M. By operating the valve V_1 the gas is expanded into the reactor with volume V_R. Thus the gas with volume V_M and pressure P_1 is expanded into a volume of ($V_M + V_R$) and pressure P_2. This can be expressed as:

$$V_M P_1 = (V_M + V_R) P_2$$

The above experiment of expanding the hydrogen gas is repeated after placing the spacer rod (of volume V_c) inside the reactor of volume V_R. Let the initial pressure of hydrogen gas in volume V_M be P_1' before expansion and the total volume after expansion be $(V_M + V_R - V_c)$. After expansion the final pressure is P_2'. Thus we get,

$$V_M P_1' = (V_M + V_R - V_c) P_2'$$

By solving the above two equations, in which P_1, P_1', P_2, P_2'and V_c are known quantities, the volume of the manifold (V_M) and the volume of the reactor (V_R) can be calculated. A series of calculations for evaluating the volumes V_M and V_R are carried out over a large range of hydrogen pressures and a calibration chart has been made which has been used during experimental work. In the automated Sieverts' type set up volume calibration is done automatically by a mass flow controller (MFC) using helium gas.

Prior to the experiment, the whole setup was evacuated under a diffusion vacuum of 10^{-6} mbar. For most of the alloy/intermetallic compounds, rigorous activation is required which involves heating the sample under diffusion vacuum for 2 hours at 673 K. After activation, the sample is allowed to come down to the working temperature under vacuum and hydrogen gas is introduced into the reaction chamber. Sufficient time is given to equilibrate hydrogen gas between reactor and manifold and the equilibrium pressure is considered as the final pressure. From the final pressure of the system, the amount of hydrogen uptake by the sample can be calculated using the known volume of reactor, manifold and total volume (obtained from prior calibration). During desorption study, the measurement steps that are followed are opposite to absorption steps. The amount of desorbed hydrogen is calculated from the increase in equilibrium pressure. To get the pressure composition isotherm, the equilibrium pressure is plotted against the amount of hydrogen absorbed/desorbed. For carrying out the hydrogenation kinetics at a particular experimental temperature, the alloy/intermetallic compound is kept at a certain initial pressure, and the amount of hydrogen absorbed with respect to time is recorded by monitoring the pressure drop. The hydride samples were surface poisoned by air exposure at liquid nitrogen temperature before taking it out from reactor.

The home-made Sievert's set up is having the following limitatioins:

i. The transducer used in this instrument can not measure pressure below 0.02 atm.

ii. The instrument has not been tested beyond 60 atm pressure.

iii. It does not take care of sample volume during calculation of absorbed hydrogen.

iv. The thermocouple is placed outside the instrument, thus it needs larger time for equilibration of temperature

Our home-made set up in its present form cannot be used for studying the hydrogen storage properties of carbon based materials with desired accuracy due to their large volume. As there are many erroneous reports of very high hydrogen uptake by CNTs, we were concerned about the accuracy of hydrogen adsorption data of carbon based physisorbed systems. The reactor of the automated set up was copper made, gold coated and having a volume of 10 cc. The IMI analyzer ruled out the methodological errors during measurement of hydrogen uptake and this was done by proper assessment of sample volume. The instrument used helium pycnometric method to determine the volume of sample and the hydrogen uptake data were automatically corrected for buoyancy using sample volume. Moreover, the instrument covers a wide range of temperature (-150 ºC to 500 ºC) and pressure (0.1 mbar to 100 bar). In addition, the instrument also provides facility for carrying out in situ desorption studies of hydride samples as already mentioned in Section 2.2.6.3. We also took care of equilibration time, another likely source of error, during the measurement of sorption data with both the instruments.

Chapter 3

Hydrogen Storage Properties of Carbon Based Materials

In the context of solid state hydrogen storage by physisorption route, carbon based structures have attracted significant interest due to their high surface area, wide variety of possible structural modifications, many inexpensive synthesis methods available from a broad range of low-cost precursors, light weight, chemical stability and biocompatibility [190-194]. Besides, technological importance of carbon based systems has been recognized by some of the premier scientific awards such as 1996 Nobel Prize in Chemistry (fullerenes), the 2008 Kavli Prize in Nanoscience (carbon nanotubes), and the 2010 Nobel Prize in Physics (graphene). Early experimental reports of hydrogen storage on carbon based nano-materials showed very promising results [44, 195] and evoked many researchers to carry out hydrogenation experiments on different types of carbon based materials such as carbon nanotubes, graphite, graphene, activated carbon etc. A brief description of various carbon based physisorbed systems has been given in Chapter 1. Adsorbed hydrogen does not form any chemical bond, rather they interact with the adsorbent surface through weak van der Waals forces. As a consequence, these carbonaceous adsorbents suffer from poor hydrogen uptake at ambient condition. Carbon nanotubes (CNT), discovered by Iijima in 1991, [38] are one of the best known allotrope of carbonaceous material for gas adsorption by virtue of its very high surface area. Though there were some initial overstated or overestimated claims [44, 195], later it was proved that significant amount of hydrogen may not be possible to store in bare CNTs (see Fig. 3.1). The variation of hydrogen storage capacities in different reports is mainly due to the presence of metallic impurities in CNTs, presence of amorphous carbon and also due to the difference in sensitivity of hydrogen storage apparatus [196, 197]. Recently Broom et al. [198] published an excellent review article regarding irreproducibilities encountered in hydrogen storage material research and shed light on controversial hydrogen storage results of nanostructured carbons.

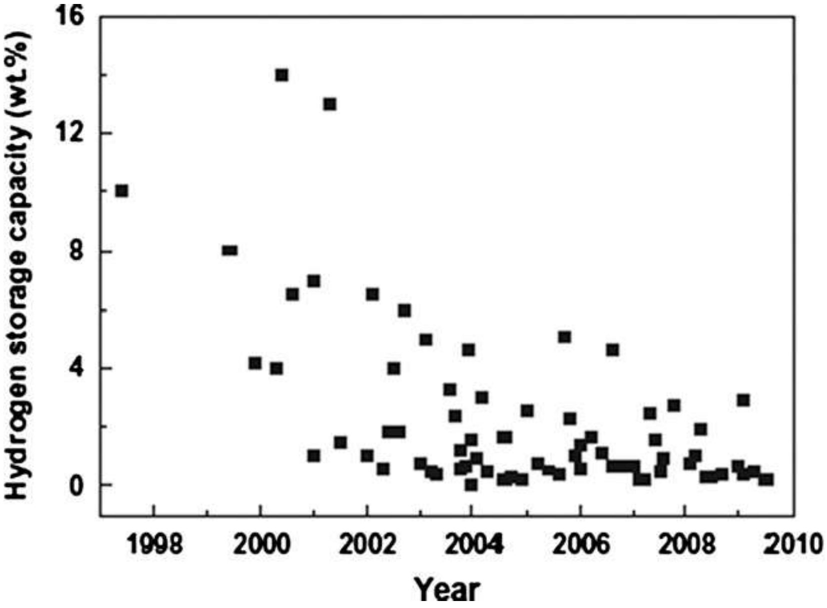

Fig. 3.1 *Publication year-wise hydrogen storage capacities of CNTs [199].*

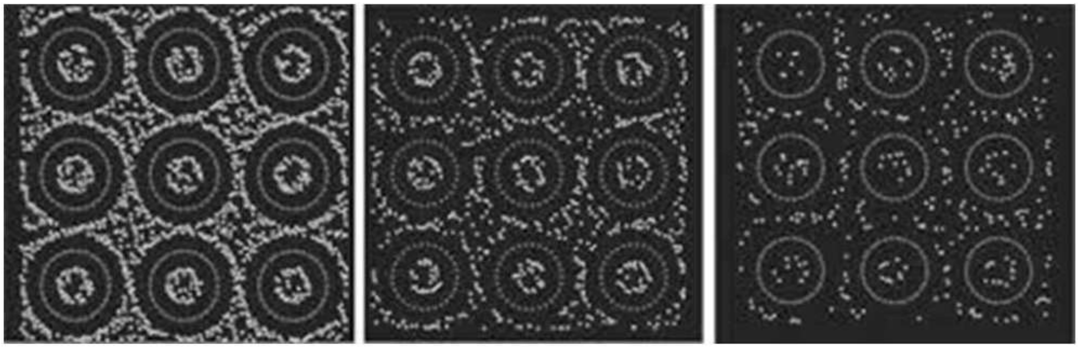

Fig. 3.2 *Hydrogen storage in CNTs as obtained from grand canonical Monte Carlo simulations under 100 bar pressure at 77 K (left), 175 K (middle), and 293 K (right) [197].*

Carbon nanotubes can store hydrogen only at very low temperatures as pictorially depicted in Fig. 3.2. This is due to low interaction energy between H_2 and the CNTs like all other physisorbed systems, which is approximately 5-10 kJ/mol. For hydrogen storage application, modification of bare CNTs is required to increase binding energy of hydrogen on CNT surface. It can be done by creating defects on CNT. Defects can be made in several ways: (i) creating a vacancy, (ii) adsorption of an adatom (impurity), and (iii) substitution of C by other metal or non-metal elements. In some of the recent reports metal doped CNTs have been studied extensively for their hydrogen storage properties and the results show that depending upon the experimental condition and preparation methods, hydrogen storage capacities vary. Suttisawat et al. has impregnated Pd on CNTs by refluxing method and achieved hydrogen storage capacity of 0.37 wt.% at 196 ºC and 68 bar. Under similar condition, V deposited CNTs exhibited hydrogen uptake of 0.4 wt.% [55]. The maximum reversible hydrogen storage capacity exhibited by Pt-Pd alloy decorated MWCNTs is 2 wt.% at 298 K and 20 atm. Hydrogen storage capacity was found to be 0.18 wt.% for ~ 14% Pd doped CNTs at 298 K and pressures over the range of 1.67-2.2 MPa. In another report, hydrogen storage capacity was evaluated for Ni-CNTs and for the sample containing optimum concentration of Ni, hydrogen storage capacity was found to be 1.02 wt.% (at 6.89 MPa and 25 °C). Until now various elements have been doped in CNTs and their hydrogen storage properties have been evaluated [200-202]. Among them, palladium is found to be quite promising mainly because of its high stability and good spillover efficiency.

The present chapter not only focuses on the study of hydrogen storage behavior of Pd doped carbon nanotubes, furthermore it explores the hydrogenation properties of comparatively less studied turbostratic carbon system. Turbostratic carbon is an unique class of carbon having structural ordering in between that of amorphous carbon phase and crystalline graphite phase. Amorphous carbon phase generally contains varying amounts of sp^3 hybridized carbon atoms whereas graphite phase contains sp^2 hybridized carbon atoms with highly delocalized π electron density. Turbostratic carbon also has graphite-like layered structure but in this case, there is no stacking between the layers and the layers are bent. Generally turbostratic carbon samples are prepared by mechanical milling of graphite for long durations [203, 204], which is a very energy intensive process. Annealing of turbostratic carbon products at very high temperature leads to formation of highly ordered graphitic carbon phase as it is thermodynamically more stable form of carbon. Previous studies by different groups [205-209] have shown that in spite of having an extended electron cloud around the carbon atoms, graphite show low hydrogen storage capacity. This is probably due to the strong interaction among the graphene layers that inhibits the hydrogen gas molecules to enter into these interlayer spaces. On the other hand, turbostratic carbon phase is expected to have interesting hydrogen storage properties due to their short range structural ordering. Here, short range order implies lack of extended ordered arrangement of carbon atoms in the sample. Such discontinuity in the carbon network is thought to facilitate hydrogen storage.

The present chapter of this thesis has been divided into three sections

3.1 Hydrogen adsorption on Pd doped carbon nanotubes
3.2 Hydrogen storage behavior of turbostratic carbon system
3.3 Conclusion

3.1 Hydrogen adsorption on Pd doped carbon nanotubes

This section deals with hydrogen storage studies on multiwalled carbon nanotubes (MW-CNTs) which were prepared using chemical vapor deposition method by our colleagues in Rare Earth Development Section (REDS), BARC. Pd doped CNTs have been prepared by two different routes, namely, wet impregnation and polyol methods. The samples were characterized by techniques like X-ray diffraction (XRD), Energy dispersive X-ray spectroscopy (EDS) and Infrared spectroscopy (IR). The Pd doped CNTs prepared by wet impregnation and polyol methods were subjected to detailed hydrogen adsorption studies at variable temperatures and pressures. Transmission Electron Microscopy (TEM) and Thermo

Gravimetric Analysis (TGA) were carried out to get further insight regarding Pd-CNT interaction existing in the samples.

3.1.1. Experimental

3.1.1.1 Sample preparation

Multiwalled carbon nanotubes (MW-CNTs) were synthesized by chemical vapour deposition of acetylene diluted with nitrogen in a fixed bed reactor at 700 ºC. The details regarding the experimental set up and procedure can be found elsewhere [172]. CNTs were purified by treating with hydrochloric acid for two hours. Finally they were rinsed with deionized water to remove traces of acid. The purified product was characterized by TEM (JEOL 2000FX).

Preparation of Pd doped CNTs was done in two steps which is shown pictorially in Fig. 3.3.

1. Functionalization of CNT support by acid treatment
2. Attachment of Pd nanoparticles

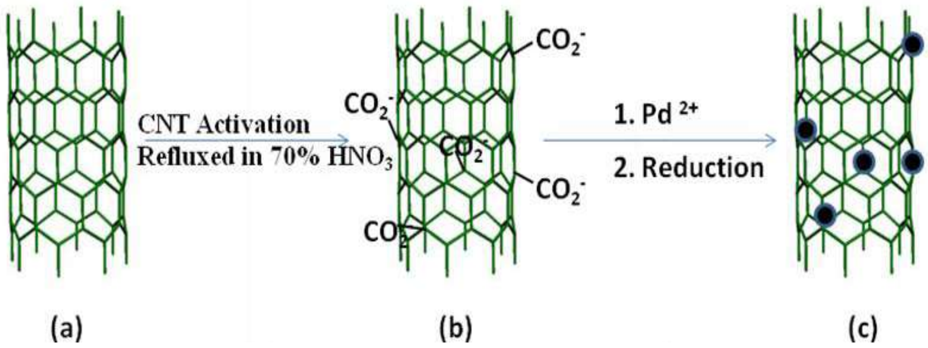

Fig. 3.3 *Dispersion of Pd nano particle on the activated carbon (a) Pristine CNT (b) Activated CNT (c) Pd dispersed CNT.*

Carbon nanotubes are hydrophobic in nature. For Pd^{2+} or Pd species to interact with CNT surface it needs to be made hydrophilic by appropriate functionalization of the surface. The functionalization (activation) of MW-CNT surface was done by refluxing the MW-CNT with 70% HNO_3 at 100ºC for 12 hrs. The product was washed repeatedly with deionized water, dried in an oven at 80ºC for 12 hrs. Pd was dispersed on activated MW-CNT by two different routes viz. wet impregnation and polyol method. In the wet impregnation route $PdCl_2$ solution was added to 2 gm of the activated CNT and the solution was stirred overnight followed by vacuum drying. The resulting product was heated in 8% hydrogen in Ar at 623 K (flow rate 60 ml/min) for 2 hrs to reduce the Pd precursor to Pd metal. Hence forth this sample will be referred as Pd-WI. The alternative way which has been adopted for Pd dispersion on the MW-CNT is the polyol method. Around 2 gm of activated CNT was dispersed in ethylene glycol by treating in an ultrasonic bath for 60 mins. $PdCl_2$ solution was added to this dispersed suspension and the pH was adjusted to 6 by adding few drops of 0.1 M NaOH solution and heated subsequently to reduce $PdCl_2$ to Pd. The resulting mixture was filtered and washed with distilled water and acetone. The solid was dried in a vacuum oven at 80-100°C to obtain the supported Pd catalyst powder. This sample will be referred as Pd-PM henceforth.

3.1.1.2 Characterization of the samples

The Pd doped CNTs were characterized by X-ray diffraction (XRD) (INEL France make, EQUINOX) using Cr K_α radiation (λ = 2.29 Å). The morphology and diameter of MW-CNTs and Pd nanoparticles were determined using a Transmission electron microscope (Jeol 2000 Fx). Elemental composition of the MW-CNTs was determined by EDS (Oxford instrument, Model: INCAE350) technique. The FT-IR spectra were recorded using Bomem MB 102 FTIR with a resolution of 2 cm^{-1}. The samples were mixed with dry KBr powder and made into a thin pellet and mounted inside the sample chamber of FTIR machine, prior to the recording of FTIR patterns.

Thermogravimetry (TG) was performed to investigate MW-CNT yield by heating the samples in a thermobalance (Setaram Setsys Evolution 1750-TG-DTA) in air up to 750°C at a heating rate of 5 K/min. The weight loss of the sample with time and temperature was recorded. Same experiment was repeated for the Pd doped samples also to see the interaction between CNT and Pd.

3.1.1.3 Hydrogen storage property measurements

Hydrogen adsorption isotherms were recorded at different temperatures using IMI analyzer (Hiden Isochema, UK). Known weight of the sample was loaded in the sample holder and sealed using a metallic gasket. Before hydrogen adsorption, helium pycnometric measurement was done to correct for the sample volume. Prior to recording adsorption isotherms, the sample was degassed under turbo vacuum at a temperature of 120°C with a heating rate of 5 K/min. The isothermal measurements were done at different temperatures up to a hydrogen pressure of 50 atm.

3.1.2. Results

3.1.2.1 Phase characterization by powder XRD

Fig. 3.4 shows the powder X-ray diffraction pattern of Pd doped CNT samples. Due to the intrinsic nature of multiwalled carbon nanotubes, X-ray diffraction pattern is similar to that of graphite. A graphite like peak (002) can be seen at an angle of 39.03°.

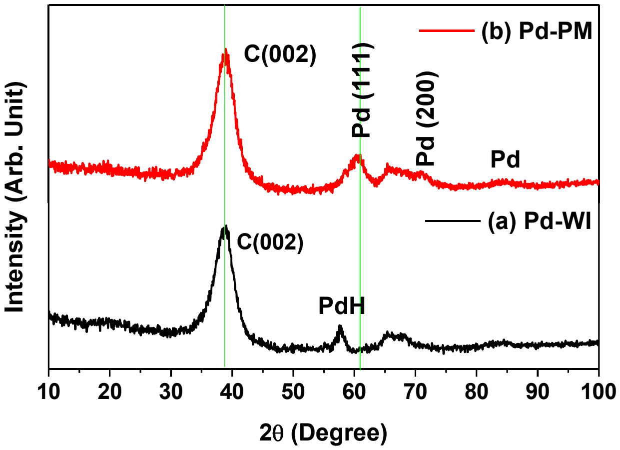

Fig. 3.4 *X-ray diffraction profiles of Pd doped CNTs prepared by different routes.*

In Pd-PM sample the main Pd peak is exactly matching with the reported value (JCPDS card no 7440-05-3). The most intense peak due to (111) plane appears at 61.05°. The less intense peak at 71.81° is due to (200) plane. For Pd-WI sample, there is a shift in the peak position towards the lower 2θ value indicating expansion of the lattice. In this sample, during the preparation, the $PdCl_2$ impregnated CNT was heated under hydrogen atmosphere and during this process Pd hydride was formed. Formation of palladium hydride and subsequent expansion of Pd lattices responsible for shift in the diffraction peaks to lower 2θ values.

EDS analysis was employed to determine elemental composition of Pd doped MW-CNTs and representative elemental composition curves are shown in Fig. 3.5(a) and 3.5(b). From the area under the peaks, Pd concentration is found to be ~ 5 wt. % in both the samples. The amount of Pd doping was also checked with ICP-AES technique and found to be in conformity with EDS results.

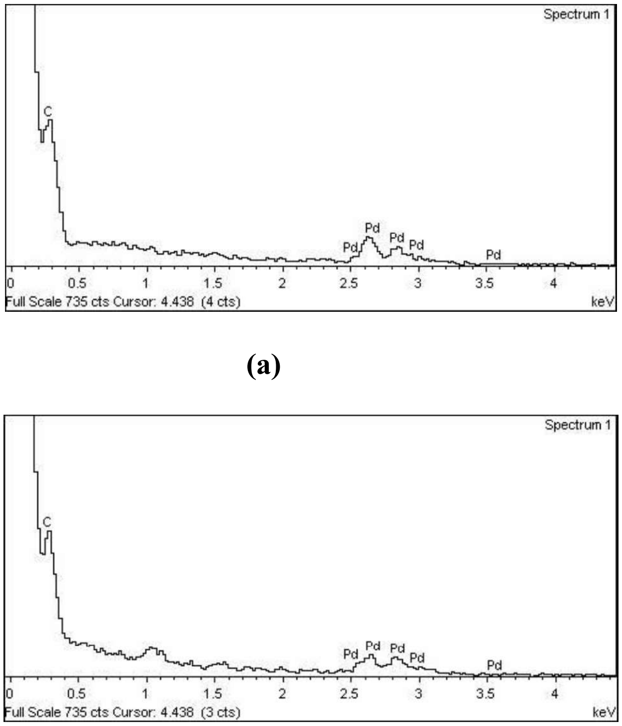

(a)

(b)

Fig 3.5 *EDS curves for (a) Pd-WI and (b) Pd-PM samples.*

3.1.2.2 FTIR results

FT-IR spectroscopy is extensively used for evaluation of functional groups of chemically modified carbon nanotubes. Fig. 3.6 shows FT-IR spectra of pristine and activated MW-CNT samples. Based on previous FTIR studies [210, 211], the peak observed ~ 1561 cm^{-1}, is attributed to the graphite like E_u mode of vibration, also known as the G band originating from sp^2 hybridized carbon. In the pristine MW-CNT spectrum absorptions at 2848 cm^{-1} and 2920 cm^{-1}, correspond to symmetrical stretching of C-H bonds in CH_3 and CH_2 groups, respectively. In both the spectra, the absorptions at 1638 cm^{-1} and 1022 cm^{-1} correspond to C=C stretching and C-C skeleton vibrations, respectively. The peak at 1384 cm^{-1} corresponds to C-C stretching of the nanotube. Also, in the pristine sample, the C–O asymmetric stretching bands at 1151 cm^{-1} and 1080 cm^{-1}, which are associated with ether type linkages, can be clearly seen. The broad adsorption band at 3439 cm^{-1} corresponds to OH stretching vibrations. However, the mechanisms behind the introduction of these oxygen containing functionalities in the prepared multiwalled carbon nanotubes are still unknown. The activated MW-CNT shows quite similar FT-IR spectra as the pristine CNT. In the activated multiwalled carbon nanotube sample, intensity of υ_{asCH3} and υ_{asCH2} bands has decreased slightly due to treatment in highly oxidizing environment. Fig. 3.7 shows the FTIR spectra of Pd-WI and Pd-PM samples. In the wet impregnation route $PdCl_2$ was reduced to Pd by heating the sample in hydrogen atmosphere. During this time some of the hydrogen goes into CNT network. As a result there is an increase in the intensity of bands at 2846 cm^{-1} and 2920 cm^{-1}, which corresponds to the symmetrical stretching of C-H linkage in CH_3 and CH_2 groups, respectively. For Pd doped CNTs synthesized by the polyol method these two bands are less intense. Further there is a decrease in the intensity of all the bands corresponding to the CNT skeleton (1642 cm^{-1} & 1030 cm^{-1}). This is because for Pd-PM sample the extent of dispersion of the Pd metals (and subsequent interaction with carbon network) is higher compared to the other sample and as a result the aromatic character of the CNT decreases.

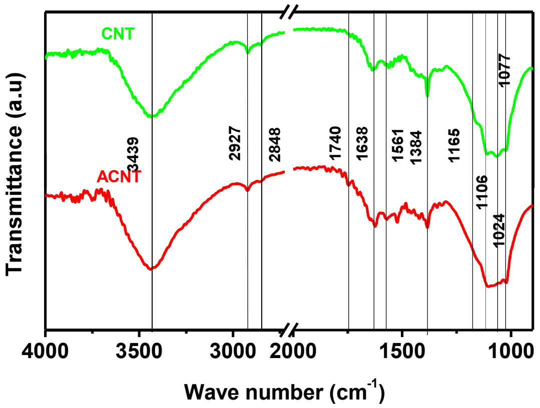

Fig 3.6 *FTIR spectra of pristine and activated carbon nanotube.*

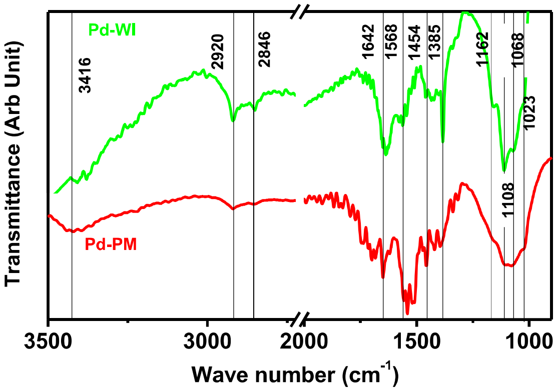

Fig 3.7 *FTIR spectra of Pd-WI and Pd-PM.*

3.1.2.3 Hydrogen storage properties

The hydrogen uptake of synthesized palladium nanoparticles was measured on Hiden HTP volumetric system upto 40 bar at 289 K. Pd shows a very fast hydrogen uptake under 1 bar of hydrogen pressure and after that the storage capacity remains almost constant upto 50 bar indicating the saturation of hydrogen uptake [212]. The total hydrogen storage capacity was found to be 0.68 wt.% which is close to the literature value. The result can be considered as the standard for further hydrogen storage experiments on Pd doped CNTs. Hydrogen storage properties of pristine MW-CNT were also investigated at different temperatures to serve as a base line for the doped samples [Fig. 3.8]. The hydrogen uptake at room temperature in MWCNTs is found to be very low and vary almost linearly with change in pressure. The uptake was 0.056 wt.% at 50 bar for MWCNT and this relatively low value is due to very low surface physisorption at room temperature which is also in conformity with the earlier studies [212]. The hydrogen storage properties of Pd doped CNT prepared by wet impregnation route and polyol method measured in the temperature range of 123-333 K and upto 50 bar hydrogen pressures are discussed in the following paragraph.

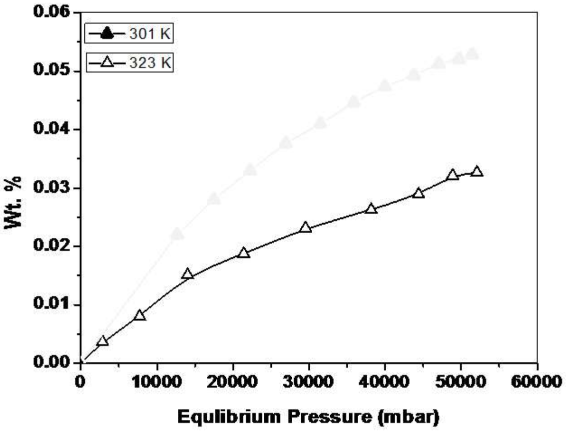

Fig. 3.8 *Hydrogen storage in MWCNT.*

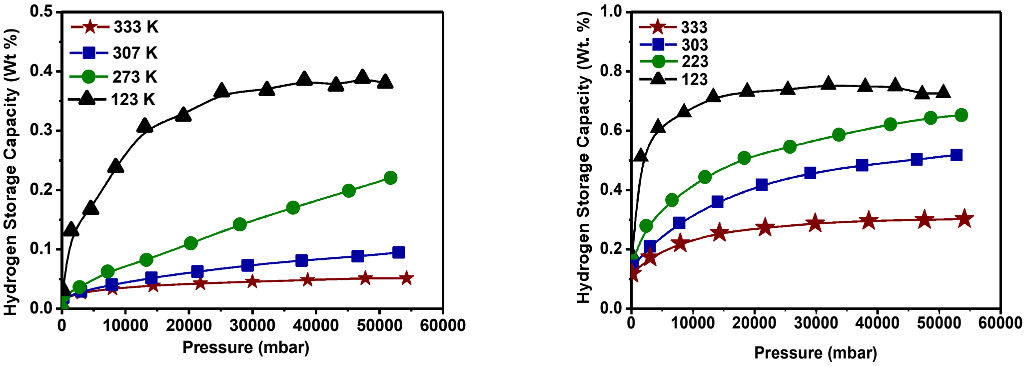

(a) **(b)**

Fig. 3.9 *Hydrogen storage in (a) Pd-WI and (b) Pd-PM.*

The hydrogen adsorption isotherms obtained by the volumetric method at 123, 273, 307 and 333 K upto a hydrogen pressure of 50 bar is shown in Fig. 3.9. For the Pd-WI sample the maximum hydrogen storage capacities are found to be 0.05, 0.09, 0.20 and 0.40 wt.% at 333, 307, 273, and 123 K, respectively. The decrease in storage capacity with increase in temperature is quite expected as the amount of adsorbed hydrogen depends profoundly on temperature due to increase of kinetic energy of hydrogen molecule with increase in temperature. From interpolation of obtained data, hydrogen storage capacities at higher pressure can also be found out. The hydrogen storage capacities of the Pd-PM sample was found to be 0.29, 0.45 0.6 and 0.7 wt. % at 333, 307, 273, and 123 K, respectively.

3.1.3. Discussions

Hydrogen adsorption study reveals that the Pd-PM sample shows better hydrogen storage capacities compared to the Pd-WI sample. To understand this, samples were further characterized by TEM and TGA (thermo-gravimetric analysis) techniques. Fig. 3.10 (a) shows TEM images of as prepared CNT after leaching the catalyst using HCl. The undoped CNTs have diameter of about 20-30 nm and a length of several micrometers as can be seen from the TEM image (Fig. 3.10 (a)).

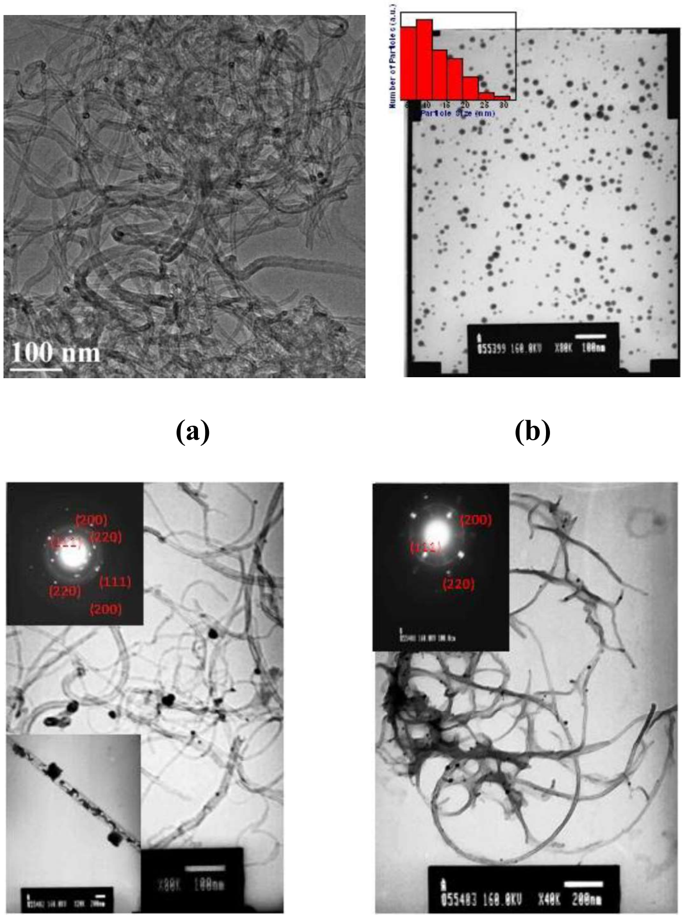

(a) (b)

(c) (d)

Fig. 3.10 *TEM images of (a) Pristine CNT (b) Pd nanoparticle (c) Pd-WI (d) Pd-PM.*

TEM images corresponding to Pd nanoparticles are shown in Fig. 3.10 (b). Pd particles are found to have size in the range of 5-20 nm with average size around 10 nm as can be seen from Fig. 3.10 (b). TEM images of Pd-CNT sample prepared through wet impregnation method are shown in Fig. 3.10 (c). From the image it is seen that along with smaller Pd nanoparticles there exists bigger size particles also, which may be generated due to the agglomeration of Pd nanoparticles on the outer side of the carbon nanotube wall. This is further confirmed by taking enlarged image of Pd doped CNT (lower inset of Fig 3.10 (c)). The Pd nanoparticles can get attached both on inner and outer walls of the nanotubes and the ones at the outer walls can grow further in size. In the selected area electron diffraction (SAED) pattern (upper inset of Fig. 3.10 (c)) sharp and clear diffraction rings are observed characteristic of single crystalline Pd nanoparticles. The rings correspond to (111), (200) and (220) lattice planes of single crystalline Pd with FCC structure. From the diffraction rings lattice parameter has been calculated and found to be 4.02 Å, which is higher than Pd metal (3.89 Å) as here the Pd metal remains in the hydrogenated form as discussed earlier. TEM image of the sample prepared by polyol method is shown in Fig 3.10 (d). From the image it is clear that Pd nanoparticles are much better dispersed in Pd-PM sample compared to the sample prepared by wet impregnation route. This is because in polyol method, reduction of Pd^{2+} is taking place at low temperature in the reaction medium.

Unlike Pd-WI sample, the agglomeration of Pd nanoparticles on the outer wall of CNT's is not observed in Pd-PM sample. Possible reason for this could be that ethylene glycol acts as capping agent in ployol method of sample preparation and thus preventing agglomeration of Pd nanoparticles on CNT surface. CNTs are hydrophobic in nature and hence the dispersion of Pd by wet impregnation route is less effective; even though reports show that activation of CNT improves metal dispersion [211]. In polyol method, ethylene glycol molecule can diffuse readily through the CNTs, and under such conditions effective atomic scale mixing of

Pd and CNT results, leading to a very fine dispersion Pd on CNTs. Liang and coworkers [213] reported similar observation for the Pt doped CNT, where they have shown that Pt dispersed on CNT prepared by polyol method shows more homogenous dispersion as well as lower particle size distributions.

Pd metal acts as a catalyst to dissociate H_2 molecule to hydrogen atoms. Due to the better dispersion of Pd metals on CNT surface in Pd-PM sample Pd nanoparticles can more effectively dissociate hydrogen molecule. The H atoms thus generated can migrate on the carbon nanotube support and can diffuse further into different surfaces of multiwalled carbon nanotube support and get adsorbed at CNT surfaces. The whole mechanism is called spillover mechanism which increases hydrogen storage capacities of the Pd dispersed CNT compared to the physical mixture of Pd nanoparticle and multiwalled CNT. The mechanism has been schematically shown in Fig. 3.11.

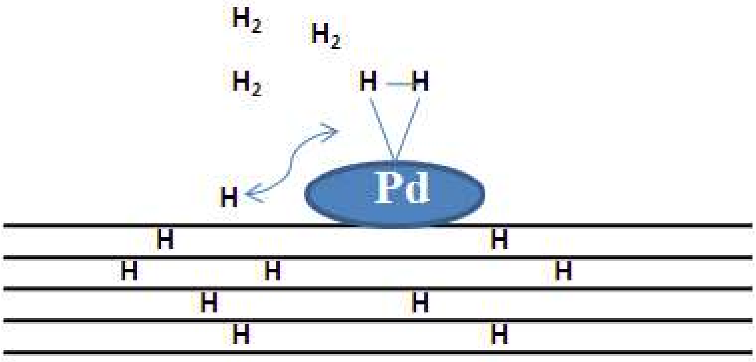

Fig. 3.11 *Hydrogen spillover mechanism of Pd doped CNT.*

The extent of spillover can be calculated approximately in a very simple way. If we consider only the physical mixture of 5% Pd nanoparticle and 95% MW-CNT, the total hydrogen storage capacity should be (0.95X0.056+0.05X0.68 =) 0.086 wt.% at room temperature. But due to interaction between Pd nanoparticle and CNTs, the spill-over mechanism comes into picture and the hydrogen storage capacity increases. The increase in the hydrogen storage capacity can be quantified by the spillover of hydrogen to carbon nanotube. In Pd-WI sample the extent of spill-over is almost zero, where as for Pd-PM it is 0.364 at room temperature. The main factors responsible for the efficient spillover mechanism in case of Pd-PM sample are the high dispersion of Pd nanoparticles on MW-CNT and also the strong binding between Pd nanoparticles and carbon nanotube. To get insight about the interaction of Pd on the CNT surface, thermogravimetric analysis was done on the pristine MW-CNT, activated MW-CNT, and Pd doped MW-CNT.

Fig. 3.12 presents thermogravimetric (TG) curves for MW-CNTs in presence of air. For the pristine MW-CNT sample, up to 475 °C, there is a weight loss of 4.51 wt. %, which is due to burning of disordered carbon. The total weight loss upto 475°C is very less which suggests that the amount of disordered carbon within the MW-CNT sample of present study is very low. A rapid and sharp weight loss between 475 to 625°C can be attributed to the oxidation of carbon nanotubes resulting into CO_2. The residue found after complete oxidation of carbon species is 0.8 wt. % of the original sample indicating that the sample is quite pure. The remaining 0.8 wt. % is due the presence of catalyst impurity used while preparing CNTs.

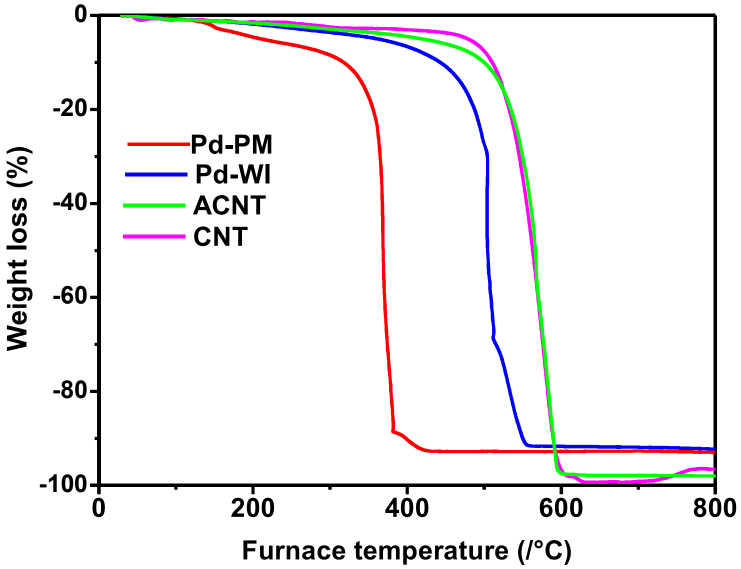

Fig. 3.12 *Thermogravimetric analysis of CNT, activated CNT, Pd-WI, Pd-PM.*

Activated CNT shows slightly lower desorption temperature as compared to the untreated CNT due to incorporation of the functional groups on the carbon nanotube surface and creation of defects. There is a significant decrease in the weight loss temperature in Pd doped CNT's indicating the direct interaction of Pd with CNT. In case of the first sample, i.e., the Pd doped activated CNT prepared by the wet impregnation route, the weight loss starts around 400°C and it continues till the value reaches 91% up to a temperature of 550°C. The residue is due to the presence of Pd and calculating the difference between the weight loss of the activated CNT and Pd doped activated CNT, it is found that there is 6.5 wt. % Pd present in the sample. The Pd doped CNT sample prepared by polyol method shows slightly different nature of thermo-gravimetric curve. There is an additional weight loss around 150°C which is due to the combustion of ethylene glycol moiety attached with the sample. The major weight loss peak due to the combustion of the carbon nanotube appears at 350°C which is lesser than the undoped activated CNT as well as Pd-WI. This is because the oxidation of MW-CNTs is catalyzed by metal doping [214]. In the Polyol method the dispersion of the Pd particles are much better compared to the wet impregnation route and the particle sizes are lower when compared with that of Pd-WI sample. This accounts for the fact that oxidation process starts at much lower temperature in Pd-PM sample compared to the Pd-WI sample. Interaction of Pd on CNT can lead to defects on the CNT and also can alter the electronic structure of CNT which in turn can modify the hydrogen storage capacity. The present research shows by modifying the synthesis procedure same doping element can behave differently on the carbon nanotube surface and thus can favourably alter the hydrogen storage capacities.

3.1.4. Summary

Pd doped multiwalled carbon nanotubes (MW-CNTs) has been prepared using chemical vapor deposition technique in presence of catalyst, and Pd nanoparticles were dispersed on it by wet impregnation and polyol methods. The hydrogen absorption study confirmed that Pd doped MW-CNT's store higher amount of hydrogen compared to the bare CNT's. More interestingly the Pd doped CNT prepared by polyol method shows higher hydrogen storage capacity than samples prepared by conventional wet impregnation method. The hydrogen adsorption results have been correlated with the extent of dispersion of the Pd nanoparticles on the CNT surfaces. TEM images shows that the polyol route gives much better dispersion of Pd nanoparticles on the MW-CNT with smaller Pd nanoparticles size distribution. The thermogravimetric studies have confirmed the improved interaction between the Pd nanoparticles and CNT's surface for Pd-PM sample compared to Pd-WI sample. The results prove that better dispersion of Pd nanoparticles improves the spillover of hydrogen thus increases the hydrogen storage capacity.

3.2 Hydrogen storage behavior of turbostratic carbon system

The present section of this chapter represents the synthesis method of turbostratic carbon sample from a commonly available material, sucrose, using zeolite-Y as template. As-prepared samples were annealed at different temperatures and the structural evolution occurring in both microscopic and macroscopic levels have been investigated in detail using small angle x-ray scattering, solid state NMR and Raman spectroscopic techniques. Hydrogen storage properties of these samples have also been investigated at various temperatures. This is the first time that structural evolution of such samples and its implications in hydrogen storage properties are being investigated as a function of annealing temperatures.

3.2.1. Experimental

3.2.1.1 Sample preparation

The carbon samples were synthesized by using zeolite-Y (SiO_2:Al_2O_3 = 5:1) as template and sucrose as carbon precursor. The chemicals, sucrose (Thomas Baker Pvt. Ltd.) and HF (Merck) were used as received without any further treatment and zeolite-Y (Aldrich) was dried completely by heating at 150°C in an oven. The sucrose solution was soaked in zeolite-Y and then reacted with con. H_2SO_4. The sucrose–zeolite composite was then placed in a drying oven and the temperature was slowly increased up to 100°C over a period of 2 hrs and maintained at this temperature for 5 hrs. The sample turned dark brown during the heat treatment in the oven. The composite was then annealed by slowly increasing the temperature up to 700°C with a heating rate of 5 K/min in Ar flow for 5 hrs to obtain carbon–zeolite composite. The carbon-zeolite composite was treated in excess amount of 40% aqueous HF solution at room temperature for 24 hrs to remove the template. The obtained carbon was filtered and washed with deionized water for several times to ensure complete removal of HF from the sample. It was dried at 150ºC for 6 hrs. Two more sets of templated carbon were prepared following the same procedure, but annealing temperature was increased to 800°C and 900°C. The samples were named as TC-700, TC-800 and TC-900 respectively. Fig. 3.13 shows the schematic of turbostratic carbon preparation.

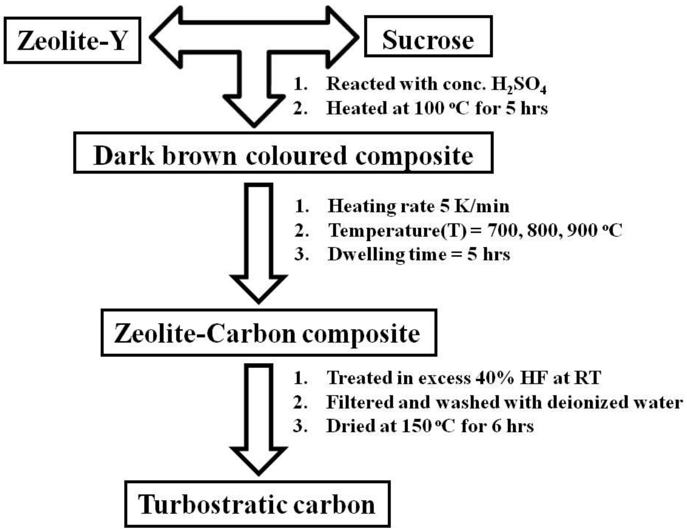

Fig. 3.13 *Schematic of turbostratic carbon preparation.*

3.2.1.2 Characterization of the samples

X-Ray Diffraction (XRD) studies on the samples were performed using a Philips powder X-ray diffractometer (model PW 1071) with monochromatic CuK_α radiation in the 2θ

range of 20° to 70°. Thermogravimetric study was performed on a thermal analyzer (Setaram Setsys Evolution 1750-TG-DTA) under oxygen flow with a heating rate of 10 °C /min. SAXS measurements were carried out using a Rigaku small angle goniometer mounted on rotating anode x-ray generator. Scattered x-ray intensity I (q) was recorded using a scintillation counter with pulse height analyzer by varying the scattering angle 2θ, where q is the scattering vector given by 4π.sin (θ) / λ and λ is the wavelength of incident (Cu-K_α) X-rays. The intensities were corrected for sample absorption and smearing effects of collimating slits [215]. Raman spectra were recorded using 532 nm laser on a home-made spectrometer equipped with N_2 cooled CCD. ^{13}C CP MAS NMR (cross polarization magic angle spinning nuclear magnetic resonance) experiments were recorded using a Bruker Avance 400 machine having a standard bore MAS accessory at a basic frequency of 100.5 MHz for ^{13}C nuclei. A 90° pulse width of 5 μs, a contact time of 10 ms with a relaxation time of 15 s were employed for recording the NMR patterns. Samples were spun at a frequency of 10 kHz. All chemical shift values are expressed with respect to tetra-methyl silane as the reference material.

3.2.1.3 Hydrogen storage property measurements

The hydrogen storage properties of turbostratic carbon samples were evaluated based on the same procedure and instrument described earlier in section 3.1.1.3.

3.2.2. Results and discussions

XRD patterns of carbon samples TC-700, TC-800 and TC-900 are shown in Fig. 3.14. TC-700 shows two broad peaks of relatively low intensities at 2θ values around 20° and 44°, indicating poorly crystalline nature of the sample. These broad peaks at 20° and 44° correspond to (002) and (101) planes of turbostratic form of carbon. The shift of peak corresponding to (002) reflection towards lower diffraction angle (as compared to that of graphite at 2θ = 26.3°) indicates increased interlayer spacing (between adjacent graphene layers) in turbostratic carbon [216]. On increasing the annealing temperature from 700°C to

800°C and then to 900°C, the peaks become more prominent and (002) peak shifts towards higher diffraction angle. The shift in the peak position suggests decreased inter layer distance [217] and enhanced intensity corresponds to increased translational ordering in the carbon sample annealed at relatively higher temperatures. These results were further substantiated by derivative thermogravimetric (DTG) studies, which showed a combustion temperature of 485°C, 515°C and 520°C for TC-700, TC-800 and TC-900 (Fig. 3.15) respectively. It may be noted that the combustion temperatures are in between that of amorphous and graphitic carbon [218]. Observation of DTG peaks at relatively higher temperatures also supports the enhanced ordering and associated increase in the extent of inter layer interactions as well as bond strengthening with increase in annealing temperature.

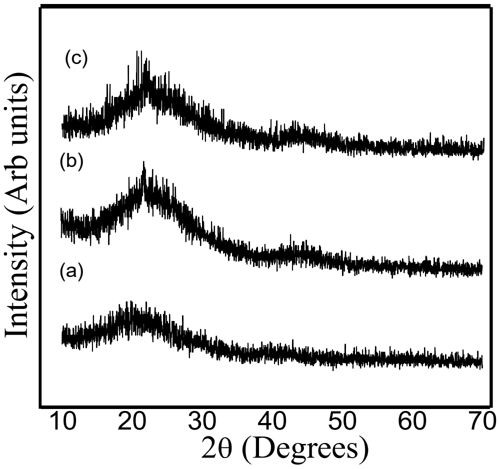

Fig. 3.14 *XRD patterns for (a) TC-700, (b) TC-800 and (c) TC-900.*

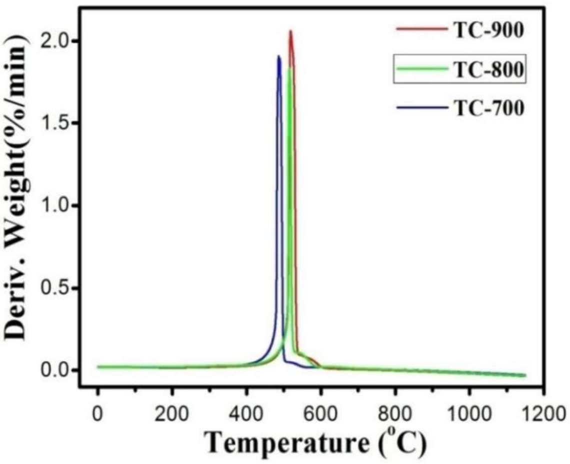

Fig. 3.15 *Derivative thermogravimetric patterns for TC-700, TC-800 and TC-900.*

Fig. 3.16 shows the SAXS data for TC-700, TC-800 and TC-900 plotted on log-log scale. The SAXS profiles were analyzed based on the structural model of pores in solid carbon matrix. It may be noticed that the scattering profiles of TC-700 and TC-800 vary linearly over wider q-range, indicating a power-law behavior, $I(q) \sim q^{-\alpha}$, for the intensity. In such a case, the value of 4 for α indicates smooth surface of scattering objects, whereas a non-integer value for α indicates a fractal nature of the structural morphology. For mass fractals with dimension D_m, $\alpha = D_m \leq 3$, whereas for surface fractals with dimension D_s, $\alpha = (6\text{-}D_s) > 3$ and $2 \leq D_s \leq 3$. Thus, the slope of the scattering curve on log-log scale indicates the type of the fractal. Usually, the power-law scattering is observed in a limited q-range determined by upper and lower cutoff of length scales between which the structure is fractal type. A detailed discussion on the functionality of I (q) for fractal systems is discussed in literature [219].

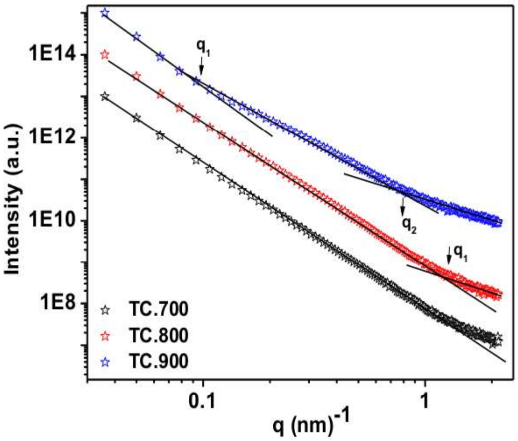

Fig. 3.16 *Small angle x-ray scattering profiles. Lines are guide to the eye.*

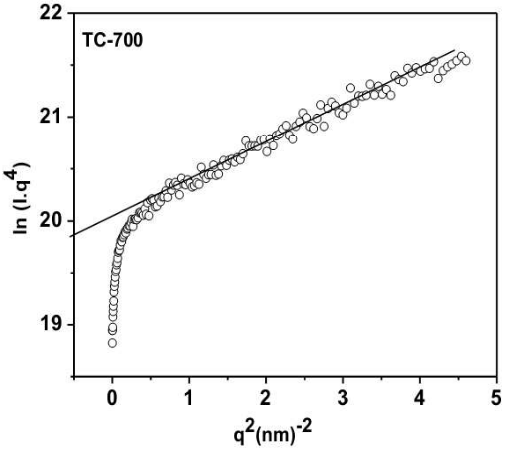

Fig. 3.17 *Plot of ln ($I.q^4$) vs q^2 used to evaluate specific surface area and interface thickness. Line is guide to the eye.*

In this study, for TC-700 and TC-800 samples α is 3.45, indicating the surface fractal nature of particles with rough particle-pore interfaces. The fractal dimension Ds is 2.55 which is in good agreement with that for coal samples [220-223]. The radius of basic particles is of the order $r_1 \sim \pi/q_1$ where q_1 is the lower cut-off of the fractal regime. The parameters obtained from the SXAS data are given in Table 3.1. For TC-900 sample, the SAXS curve shows change of slope of the linearity at two regions indicating the presence of two different structures. For $q < q_1$, α is 3.95 indicating large size carbon clusters of radius r_2 with nearly smooth surfaces. For $q > q_1$, α is 2.84 suggesting mass fractal aggregates of smaller carbon particles with fractal dimension (Dm), an indicator of compactness of 2.84. Such coexistence of two different structural morphologies on different length scales in carbon materials has been observed in earlier studies also [221]. Thus, the temperature 900°C seems to be the threshold temperature at which the structural morphology of the carbon sample undergoes significant changesFor a two-phase material with an interfacial thickness (σ), the scattering intensity can be expressed as $I(q) \sim I_o\ e^{-(\sigma^2 q^2)}$ (3.1)

Using the Porod's law in the high q-region

$$\lim_{q\to\infty} (q)^4\, I(q) = k\ e^{-(\sigma^2 q^2)} \qquad (3.2)$$

where k is the Porod constant. Hence from the plot of *q^2 vs ln(q^4.I(q))* the values of σ and k can be obtained [221, 223-226]. Fig. 3.17 shows typical plot for TC-700 sample. From these parameters, the specific surface area (S/V) can be estimated using the formula $\frac{S}{V} = \pi\left({}^{k}/_{Q}\right)$ where Q is the Porod invariant which is given by

$$Q = \int_0^\infty I(q).q^2 dq \qquad (3.3)$$

The average micro-pore radius can be calculated using the relation,

$$r_p = \frac{4Q}{\pi k} \qquad (3.4)$$

The parameters obtained using the above formalisms are included in Table 3.1.

Table 3.1 *Structural parameters obtained from SAXS data. Symbols are as described in text.*

Sample	Ds	Dm	σ (nm)	S.S.A (m^2/gm)	r_1 (nm)	r_2 (nm)	Average Pore radius (nm)
TC-700	2.52		0.36	111	2.4		17.3
TC-800	2.56		0.39	121	2.6		16.5
TC-900	2.06	2.84	0.36	413	2.8	31.4	4.8

It may be noted that the thickness of the pore-particle interface remains unchanged with heating temperature. The specific surface area of the particles in the samples TC-700 and TC-800 are nearly same. However, a steep rise in the value is noticed upon increase in the temperature to 900°C. Similarly, the effective pore radius is nearly same for TC-700 and TC-800 but it decreases significantly for TC-900. Such changes in morphology, surface area and pore size can have significant affect on the hydrogen adsorption characteristics of the samples. To investigate these aspects, ^{13}C MAS NMR, Raman spectroscopic and hydrogen adsorption studies were carried out on the samples and the results are described below.

Fig. 3.18 shows the ^{13}C CP MAS NMR patterns of turbostratic carbon samples. For the purpose of comparison, ^{13}C CP MAS NMR pattern of standard graphite powder is also shown in the same figure. The TC-700 sample is characterized by a sharp peak around 110 ppm superimposed over a broad peak around 123 ppm. Based on previous ^{13}C NMR studies [218, 227], it is inferred that the sharp peak around 110 ppm is due to the residual hydroxy species on the surface whereas the broad peak at 123 ppm (with an FWHM of 25 ppm) originates from sp^2 hybridized carbon [228]. With increase in annealing temperature to 800°C, the sharp peak disappears and line width of the broad peak increases to 29 ppm. However, the chemical shift value is found to remain same as that for TC-700. The disappearance of 110 ppm peak indicates removal of hydroxy species from the surface with heat treatment, whereas increase in line width indicates an increase in chemical shift anisotropy around carbon atoms. Such an increase in chemical shift anisotropy is possible only when discrete sp^2 carbon atoms (structural units) undergo clustering, leading to increased inter-electronic interactions. On further increasing the annealing temperature to 900°C (for TC-900 sample), line width increases to a value of 42 ppm while the chemical shift value remains nearly unchanged. Thus, NMR results confirm that for TC-900, there is an increase in the extent of clustering and associated increase in the interaction of 2p$_z$ orbital of sp^2 carbon atoms constituting the cluster.

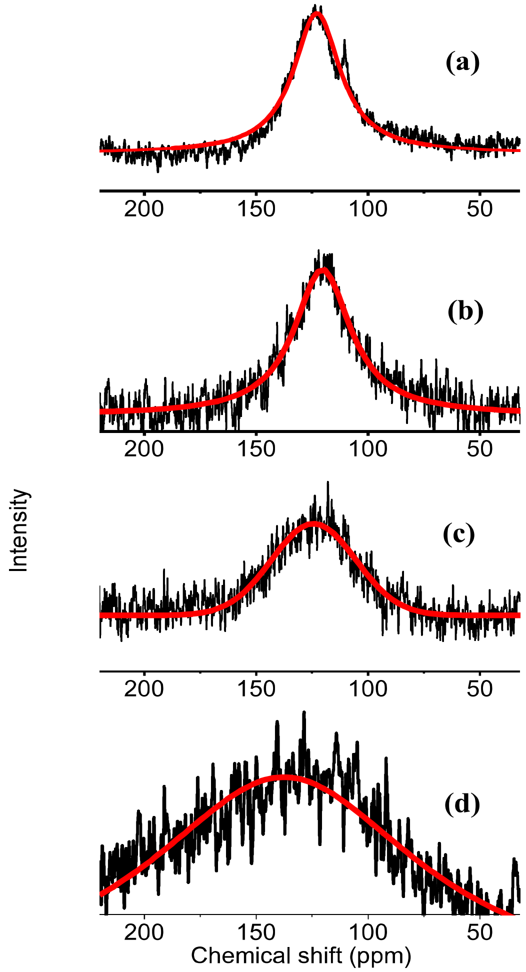

Fig. 3.18 *^{13}C CP MAS NMR patterns of (a) TC-700, (b) TC-800, (c) TC-900 and (d) graphite.*

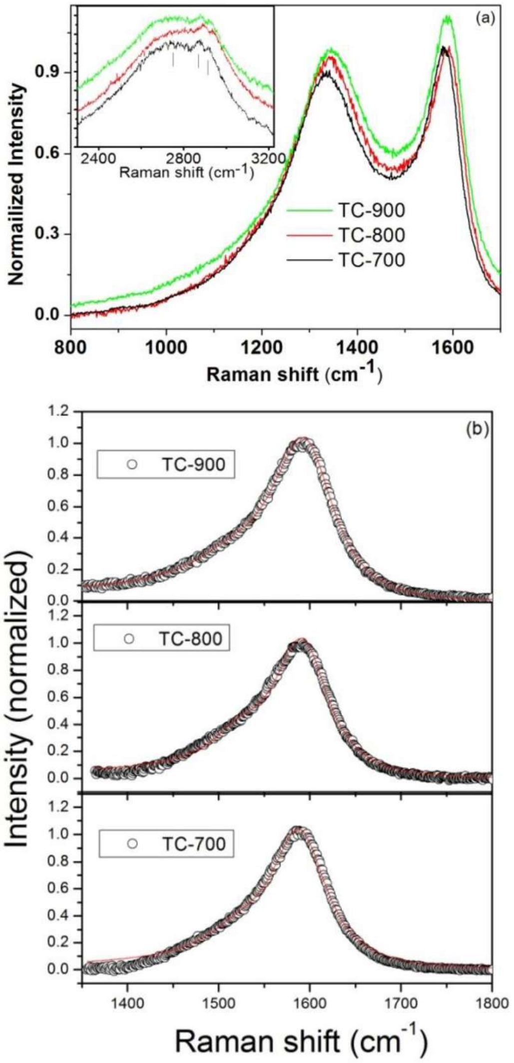

Fig. 3.19 *(a) Raman spectrum of TC-700, TC-800 and TC-900 showing D and G-bands (top). Inset shows higher order Raman spectra (2D, 2LO and D+G).* ***Fig 3.19*** *(b) Shows G-band fitted with BWF and Lorentzian line shape profiles.*

The graphite sample has higher extent of lateral overlapping of $2p_z$ orbital compared to the samples of present study. This should give rise to a much broader NMR spectrum for the graphite sample. It is indeed seen that the NMR spectrum for graphite is quite broad with a line width of around 141 ppm as (Fig. 3.18(d)). As the graphite sample is highly conducting, the extent of penetration of radio frequency waves in the sample is very less. This accounts for the poor signal to noise ratio in the corresponding NMR pattern. Thus from SAXS and NMR studies it is confirmed that, upon increasing the annealing temperature from 700°C to 900°C, small clusters of sp^2 carbon become larger in size with smoother surface.

Fig. 3.19 (a) shows Raman spectrum from samples TC-700, TC-800 and TC-900. These spectra show well defined *G*-peak and *D*-peak, typical of aromatic sp^2 bonded carbon. The position of *G*-band and D-band, do not change appreciably with heat treatment temperature and appears around 1588 and 1344 cm^{-1} respectively. The D band can be fitted by a Lorentzian line shape, and is known to be arising due to the disorder in graphene layers. The turbostratic carbon has various kinds of surface imperfections e.g. edge terminations and defects, due to which these samples have intense D-band. The G band on the other hand is due to in plane symmetric vibrations of carbon atoms in aromatic graphene ring brought about by the lateral overlapping of $2p_z$ orbital of C atoms. Perfect crystalline graphite without any defect should contain only this band. From the above composite spectrum, G-band is de-convoluted by first fitting D-band with a Lorentzian line shape and then subtracting the intensity of D band from the overall spectrum. The intensity, I, of G- band thus obtained is finally fitted to the sum of a Lorentz and a Breit Wigner Fano (BWF) line shape (see Fig. 3.19 (b)), represented in the following form:

$I = \frac{[1+({\omega_R}/{Q})]^2}{1+{\omega_R}^2}$, $\omega_R = \frac{\omega-\omega_{BWF}}{\Gamma}$, where ω_{BWF} represents the central frequency, Γ represents the broadening parameter, ω_R represents the reduced Raman frequency and $1/Q$ represents the asymmetry of the peak and is a representative of the interaction between discrete vibrational levels and electronic continuum arising due to metallic nature of the sample [229]. The fitted parameters for different samples are listed in Table 3.2. Position of the Lorentzian is found to be in the range of 1509 to 1520 cm^{-1}, and is attributed to residual intensity due to D band affecting the line shape profile of G-band. Although contribution due to this Lorentzian is very low compared to the contribution due to BWF line, its presence is required to have proper BWF profile line parameters. Depending on strength of interaction ($1/Q$ value) the position of G-peak and its width is affected. Breit-Wigner line shape arises only when electronic density of states at Fermi level has a finite value i.e. when the sample is having metallic nature. It is observed that G peak of TC-900 sample is more asymmetric with higher value of $1/Q$ compared to that of TC-700 and TC-800 ($1/Q$ for TC-700, TC-800 and TC-900 are -0.07, -0.093 and -0.128 respectively). Also, the broadening parameter and central peak position (i.e. ω_{BWF}) increases consistently with increase in temperature, as depicted clearly in Table 3.2. The increased extent of overlapping of the $2p_z$ orbitals of C atoms as well as the removal of hydroxy groups in TC-900 sample (as mentioned above), lead to increased electronic density of states and associated increase in the electron-phonon interaction. It is worthwhile to mention here that electric field dependent Raman Spectroscopic studies [230] have revealed that injection of charge carriers in graphene sheets results in increased ω_{BWF} position. Further, increase in the value of $1/Q$ indicates increased electron density of states at Fermi level [230] and hence also increased metallic behaviour. In the present study, increase in electron density occurs as a result of improved extent of lateral overlapping of $2p_z$ orbital as well as removal of hydroxy groups as confirmed from NMR studies.

The band appearing in the range of 2300 to 3200 cm^{-1} has a large width (~ 480 cm^{-1}), and is characteristic of turbostratic carbon (inset of Fig. 3.19 (a)). It is composed of three peaks, with peak maxima around 2730 cm^{-1}, 2875 cm^{-1}, 2915 cm^{-1} (indicated in the spectrum). These peaks are attributed to the overtone of D mode (G'), overtone of LO (2LO) and D+G mode, respectively. The peak at 2730 cm^{-1} is the most dominant peak and is very broad in nature. The other peaks are sharp, but not so dominant. The observed band is different from other carbonaceous materials e.g. graphene, graphite, carbon nano-tubes etc., which have sharp bands. In case of amorphous carbon these peaks are merged into each other, while in perfect graphene sheet one observes sharp peaks at these positions. Splitting of this band (inset of Fig. 3.19 (a)) is a clear indication of onset of c axis ordering.

Table 3.2 *G-band fitting parameters obtained by a sum of Lorentzian and a Breit Wigner Fano line shape analysis.*

Sample	TC-700	TC-800	TC-900
	Lorentzian	Lorentzian	Lorentzian
Position	1518	1520	1509
Width	84	64	95
Weight	18	16	13
	BWF	BWF	BWF
ω_{BWF}	1590.6	1594	1598
$1/Q$	-0.07	-0.093	-0.128
Γ	38	37	42

Raman results clearly demonstrate that the central peak position of G band (ω_{BWF}) and the *1/Q* parameter systematically increases with increase in annealing temperature. This can be explained based on the clustering effect of C atoms and associated increase in the extent of overlapping of $2p_z$ orbital of carbon atoms. This also increases the extent of long range ordering with increase in annealing temperature. Such effects increase the bond strength and favours improved electron phonon interaction. The results are in concurrence with the inferences derived from SAXS studies.

It will be interesting to know the hydrogen adsorption properties of these samples and their variation with annealing temperature. Fig. 3.20 (a, b and c) represents the hydrogen adsorption isotherms of TC-700, TC-800 and TC-900 samples measured over the temperature range 123 K to 303 K and hydrogen pressures up to 45 bar. Hydrogen uptake decreases with increase in temperature for all the samples as evident from the figure. The decreasing trend of hydrogen adsorption capacity with temperature is in agreement with other studies [231]. It is noticed that the experimental isotherms at lower temperature (123 K) show two distinct sections. At very low pressures (up to 3 bar), the isotherms are too steep, beyond which nearly flat region, characteristic of saturated hydrogen adsorption is observed.

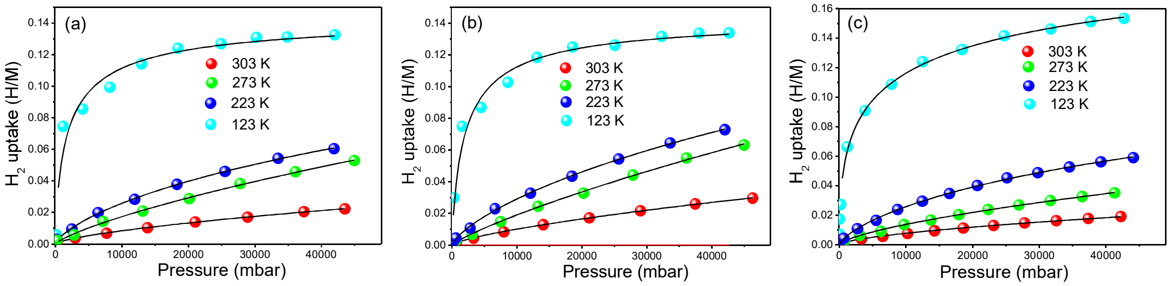

Fig. 3.20 *Volumetric hydrogen adsorption isotherms of (a) TC-700, (b) TC-800 and (c) TC-900.*

The isotherms for all the samples can be fitted well with Freundlich model. From the fitted isotherms, maximum hydrogen uptakes are found to be 0.131 H/M, 0.133 H/M and 0.152 H/M (where H/M represents number of hydrogen atoms per atomic weight of carbon) for TC-700, TC-800, TC-900, respectively at 123 K and 45 bar. This results in hydrogen storage capacities of 1.08, 1.1 and 1.25 wt.% for TC-700, TC-800, TC-900, respectively. These results are in line with the findings of Wu et al. who obtained hydrogen storage capacity of 1.5 wt.% under a pressure of 10 bar at 77 K for as-produced turbostratic carbon nanofiber [232]. Rashidi et al. investigated hydrogen storage capacities of single walled carbon nanotubes (SWNT) with different purity and found a maximum adsorption capacity of 0.8 wt.% for SWNTs with 95% purity [233]. Kajiura et al. [50] reported maximum hydrogen uptake of 0.43 wt.% by SWNT at 298 K and 80 bar pressure. Gravimetric hydrogen storage capacity of 0.075 wt.% was reported by Rather et al. [234] for pristine CNT whereas that of TiO_2 functionalized CNT was found to be 0.4 wt.% at 298 K and 18 atm pressure. Further, the hydrogen storage ability of unmodified MWNTs was claimed to be 0.71 wt.% by Huang et al. [235] under ambient pressure and moderate temperature. Thus, the turbostratic carbon samples in the present study show better hydrogen storage behavior compared to that of MWCNTs. Wang et al. [236] studied the hydrogen storage properties of chemically activated fungi-based porous carbons and found maximum hydrogen uptake ~4.5 wt.% at 77 K and 35 bar pressure. Chen et al. reported quite high hydrogen storage ability of porous carbon material fabricated from rice hull as 7.7 wt.% at 77 K and 12 bar pressure [237]. From the comparative evaluation it is clear that hydrogen storage capacity of turbostratic carbon samples are better than that of CNTs and functionalized CNTs. However it is found to be lower than that of activated carbon and porous carbon materials. It is known that the increase in surface area and an optimum pore size in carbon based materials facilitate higher hydrogen adsorption [73, 238]. Hence, the higher hydrogen storage capacity of TC-

900 sample compared to other turbostratic carbons can be explained based on higher specific surface area and reduced pore size, as determined from SAXS study.

To further understand the observed variation in hydrogen adsorption capacity of the samples, the isosteric heat of adsorption, Q_{st} values, (heat of adsorption at constant hydrogen uptake) has been calculated from hydrogen sorption isotherms at different temperatures using the Clausius-Clapeyron equation (Equation 3.5),

$$Q_{st=} - R\left[\frac{dlnP}{d\left({}^{1}/{}_{T}\right)}\right]_{H/M} \tag{3.5}$$

where “P” is the saturation pressure of adsorption and T is absolute temperature of adsorption.

The variation of the isosteric heat of adsorption Q_{st} as a function of hydrogen uptake (H/M) is shown in Fig. 3.21 for all the samples. For TC-700 and TC-800 samples, Q_{st} decreases exponentially with increase in hydrogen uptake, whereas for TC-900 sample, the value remains almost constant. Multi-exponential behavior observed for TC-700 and TC-800 samples, indicate the heterogeneity present on their surfaces. This agrees well with the existence of rough surfaces present in these samples as confirmed by SAXS results. Constant Q_{st} values observed for TC-900 suggests that the sample is having energetically homogenous adsorption sites, characteristic of smooth surface for the particles.

The Q_{st} values are nearly same (~ 10 kJ/mol) at lower hydrogen uptake (0.005 H/M; i.e. in Henry’s law region) for all the samples. At lower hydrogen uptake, H_2 - H_2 interaction is negligible making each hydrogen molecule accessible to the whole carbon surface. Moreover, at this low coverage region, hydrogen will preferably interact with carbon surface through the strong binding sites which are thermodynamically favorable. Hence, the interaction energy of hydrogen gas molecules with the carbon samples is maximum in

Henry's law region. With increase in hydrogen uptake, the less favourable sites on the carbon surface also take part in carbon-H_2 interaction, particularly for TC-700 and TC-800 samples, as the sample surface is more heterogeneous. The surface being more homogeneous in TC-900 sample, the Q_{st} values remain almost same with hydrogen uptake.

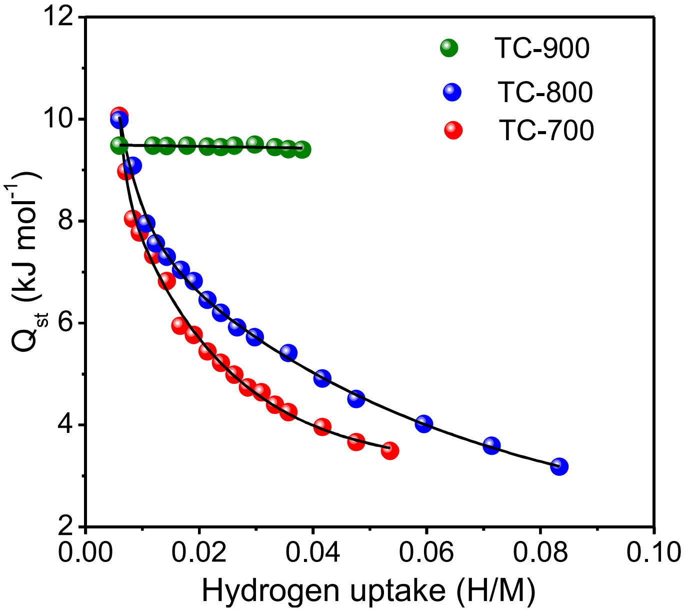

Fig. 3.21 *Q_{st} as a function of hydrogen uptake for TC-700, TC-800 and TC-900.*

3.2.3. Summary

Turbostratic carbon samples have been prepared from sucrose using zeolite as hard template. Upon increasing the annealing temperature from 700°C to 900°C, carbon clusters which are surface fractal in nature with rough surfaces become larger in size with smooth surfaces. Simultaneously, much smaller particles agglomerate to mass fractal aggregates. Based on structural analysis, it is confirmed that with increase in annealing temperatures, the extent of sp^2 carbon network formation increases. This is followed by a decrease in the extent of discontinuous regions, as revealed by increase in chemical shift anisotropy (indicated from

NMR) and improved electron phonon interaction (indicated from Raman scattering). Isosteric heat of adsorption involved in hydrogen adsorption further confirmed the smooth and homogenous surface existing for the sample annealed at 900°C as compared to those annealed at 700°C and 800°C. Increased surface area and reduced pore size observed for the 900°C heated sample is responsible for its better hydrogen adsorption properties.

3.3. Conclusion

The hydrogen storage behavior of pristine and Pd doped carbon nanotubes is reported in this chapter. CNTs were doped with Pd nanoparticles by wet impregnation method as well as by polyol route. The room temperature hydrogen uptake of bare CNT is only 0.056 wt.% at 50 bar of hydrogen pressure and this hydrogen storage capacity is remarkably improved for Pd doped CNT by polyol route. However Pd doped CNT prepared by wet impregnation route shows poor hydrogen uptake like bare CNT. In this chapter, the role of spill over mechanism has been nicely depicted to explain the observed increase in storage capacity of Pd-PM sample. The dispersion of Pd nanoparticle on the CNT is much better for the sample prepared by polyol route and this leads to enhanced interaction between Pd nanoparticles and CNT. The metal-support interaction is good enough to account for the superior hydrogen storage behavior of Pd-PM sample. Even after doping with Pd nanoparticles, the storage capacity of CNT does not exceed 1 wt.%. On the other hand, turbostratic carbons prepared from easily available sucrose can store 1.25 wt.% of hydrogen at 123 K and 45 bar of hydrogen pressure. The isosteric heat of hydrogen adsorption is ~10 kJ/mol for such type of turbostratic carbon without any metal doping or functionalization.

Chapter 4

Hydrogen Storage Properties of Ti-Nb Based Alloys

Over the last few decades, metals and alloys have been extensively investigated as hydrogen storage materials because of their chemical reactivity towards hydrogen gas at moderate temperature and pressure leading to metal hydride formation (chemisorption of hydrogen). The pioneering work of Libowitz et al. [239-242], revealed that β-titanium alloys have better prospects for higher hydrogen storage density than other metal based alloys (conventional AB_2 and AB_5 types, where A is good hydride forming metals such as Ce, Zr, La, and B forms unstable hydride like Fe, Co, Ni, Cr). Titanium (Ti) has two allotropes (shown in Fig. 4.1) and its low temperature allotrope (α-Ti) has hexagonal closed packed (HCP) crystal structure.

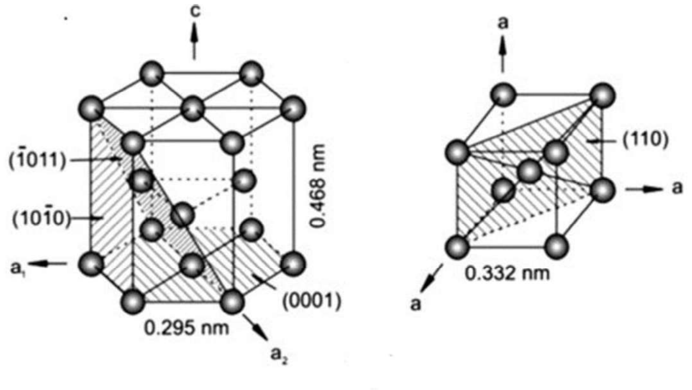

Fig. 4.1 *Structures of α-phase (HCP) and β-phase (BCC) titanium (Ti) [251].*

The difference in the atomic volume between Ti and Nb is only about 2%, which results in a β-isomorphous system with a body-centered cubic structure [252]. The results of the work by

Lee et al. [253] indicate that in Ti-Nb binary system, microstructure is greatly affected by relative amount of Ti and Nb. For Ti-Nb alloys, the relative stability of BCC-based structure (β phase) increases as relative concentration of Nb increases. It has been found from their study that only with Nb contents higher than 30 wt.%, β phase is almost entirely preserved. The binary Ti-Nb phase diagram predicted by Lee et al. does not differ much from the equilibrium phase diagram proposed by Murray [254] as shown in Fig. 4.2.

In the present study hydrogen absorption properties have been evaluated for $Ti_{0.67}Nb_{0.33}$ (Ti-49 wt.% Nb) alloy, which exists in BCC structure. From the Ellingham diagram, it is confirmed that oxygen partial pressure needed to form Ti and Nb oxides are very low, as a result they have high affinity towards oxygen. Due to the formation of oxide layer on the alloy surface, hydrogen absorption rate is slow [255, 256]. Nedyakha et al. [257] have shown that, when Fe is added as an additional element to Ti-Nb alloy, its oxidation resistance is greatly improved. Studies by Maeland et al. [241] have shown that addition of Ge, Ni, Fe and Si lead to an enhancement in hydrogen absorption kinetics of Ti-Nb based BCC alloys. Based on these inferences, it is thought that an effective way to improve hydrogenation behavior of $Ti_{0.67}Nb_{0.33}$ alloy can be incorporation of Fe as third element.

Keeping this in mind, Ti-Nb alloys containing different amounts of Fe have been prepared and their crystal structure, hydrogen absorption behavior and hydriding kinetics have been investigated. Detailed kinetic study has been carried out only on $Ti_{0.67}Nb_{0.13}Fe_{0.20}$ alloy as it showed optimum hydrogen absorption capacity and kinetics among the alloys studied. The role of Fe in improving hydrogen absorption properties of Ti-Nb alloy, although Fe is a non-hydride forming element (enthalpy of hydride formation for Fe is +14 kJ/mol of H_2), is discussed in this chapter. In addition to hydrogen absorption studies, ^{57}Fe Mössbauer spectroscopic study of Fe containing alloys and their corresponding hydrides have been carried out to know the effect of Fe substitution as well as hydrogenation on the electronic structure of the alloys.

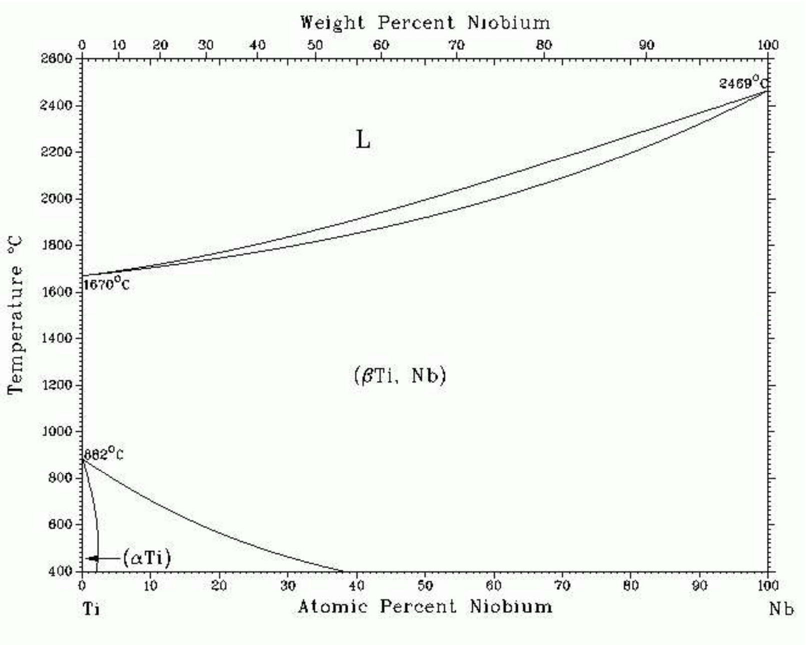

Fig. 4.2 *Phase diagram of Ti-Nb system according to Murray [254].*

4.1 Experimental

The alloys $Ti_{0.67}Nb_{0.33-x}Fe_x$ (x = 0.00, 0.13, 0.20) were prepared by arc melting suitable proportions of high purity (>99.99%) Ti, Nb, and Fe in a water cooled copper hearth under argon atmosphere. The sample buttons were turned over and re-melted several times to ensure homogeneity. Phase characterization of as cast alloys and their hydrides was carried out by X-ray diffraction (XRD) using monochromatic CuK_α radiation. Compositional analysis of the alloys was done using Energy dispersive X-ray spectrometer (Oxford instrument Inc, UK made (Model INCA E350)). EDS data represent the bulk elemental composition which arises from electron beam interaction volume formed within the sample.

Electron energy used for measurements was maintained at 20 keV. As prepared alloy buttons were cut and polished prior to loading in SEM chamber for EDS analysis.

The alloys were charged with hydrogen gas to form corresponding hydrides using a home-made Sievert's type of set up already described in Chapter 2. Prior to hydrogen charging, the alloys needed activation which involved heating the sample under diffusion vacuum (10^{-6} mbar) for 2 h at 673 K. After activation, the sample was cooled to working temperature under vacuum, followed by introduction of hydrogen gas into the reaction chamber. Hydriding of the samples were carried out over a pressure range of 0.02-25 atm. at 298 K. Hydrogen absorption kinetics data of the samples were recorded after one absorption-desorption cycle, by following the change in pressure at constant temperature as a function of time. The hydride samples were surface poisoned at liquid nitrogen temperature using air before being taken out. Hydrogen storage capacities of $Ti_{0.67}Nb_{0.33-x}Fe_x$ (x = 0.00, 0.13, 0.20) alloys were determined using a hydrogen estimation set up as shown in Fig. 4.3.

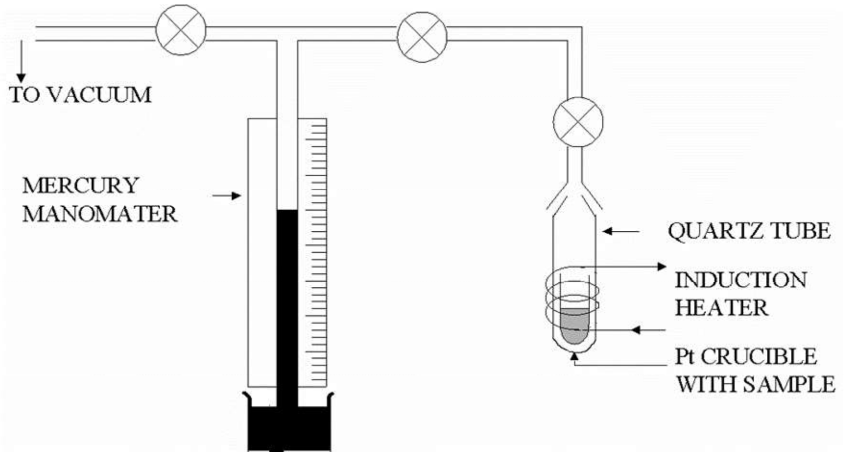

Fig. 4.3 *Schematic diagram of hydrogen estimation set up used in this study.*

Around 25 mg of hydride sample was introduced into the sample holder of the calibrated estimation set up and heated to 1473 K using an induction heater. From fall in mercury level the volume of H_2 released was calculated and subsequently the H/M value.

The apparatus mainly consists of glass manifold with a mercury manometer for pressure measurement. One end of manifold is connected to a vacuum system and the other end to a quartz chamber. The apparatus was calibrated by decomposition of calcium carbonate ($CaCO_3$) inside it. Known amount of $CaCO_3$ was heated at high temperature leading to evolution of known amount of CO_2 gas. Now by observing the pressure change in the mercury level, volume of the cell and manifold can be calibrated.

Morphological characterization of the alloy hydrides was carried out with SEM, Model ATS2100, SERON INC, South Korea.

Mössbauer spectra were recorded at room temperature using a Mössbauer spectrometer (Nucleonix Systems Pvt. Ltd., Hyderabad, India) operated in constant acceleration mode (transmission geometry). Mössbauer spectra were recorded at three different velocities, at a maximum velocity of ±10.5 mm/s, ±6.5 mm/s and ±2.5 mm/s. The wide scale of velocity was applied to check for additional lines, apart from the contribution of narrow central lines. Mössbauer spectra were fitted using the WinNormos fit programme.

4.2 Results and Discussions

4.2.1 Composition analysis by EDS

To verify the elemental composition of the alloys, energy dispersive spectroscopic (EDS) analysis was carried out at different positions on the alloys. Fig. 4.4 shows EDS mapping of the alloys. Average composition of the alloys, both in terms of weight% and atom%, are given in Table 4.1 and the theoretical values are mentioned in parenthesis. EDS analysis confirmed the compositions of constituent elements in all the three alloys (match well with the amounts initially taken for the preparation of the alloys).

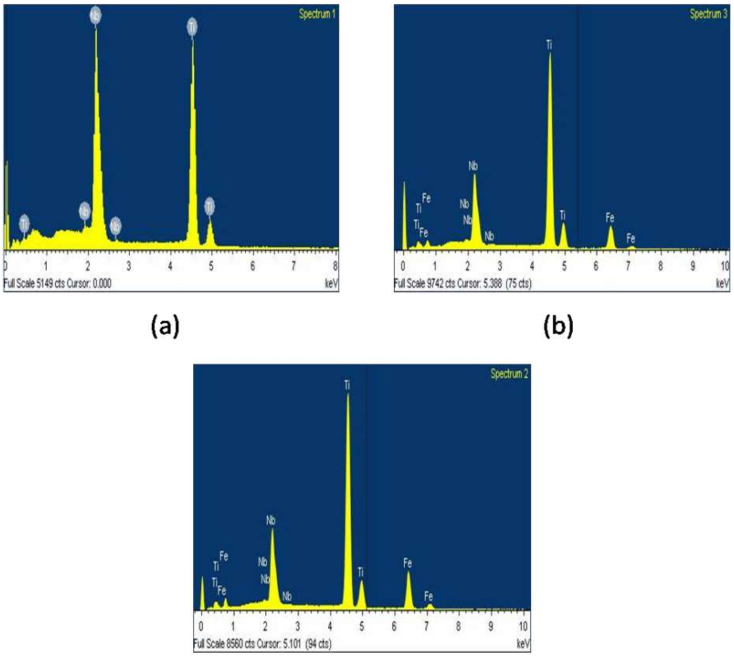

(a) (b)

(c)

Fig. 4.4 *EDS mappings of (a) $Ti_{0.67}Nb_{0.33}$, (b) $Ti_{0.67}Nb_{0.20}Fe_{0.13}$ and (c) $Ti_{0.67}Nb_{0.13}Fe_{0.20}$ alloys.*

Table 4.1 *Relative concentrations of different elements present in the alloys obtained from EDS analysis. The theoretical weight% and atom% are given in parenthesis.*

Alloys	Elements					
	Ti		Nb		Fe	
	Weight%	Atom%	Weight%	Atom%	Weight%	Atom%
$Ti_{0.67}Nb_{0.33}$	48.95	65.86	51.05	34.15	-	
	(50.75)	(66.67)	(49.25)	(33.33)	-	
$Ti_{0.67}Nb_{0.20}Fe_{0.13}$	57.26	67.14	29.16	19.45	13.58	13.42
	(55.08)	(66.67)	(32.07)	(20.00)	(12.85)	(13.33)
$Ti_{0.67}Nb_{0.13}Fe_{0.20}$	56.45	66.09	24.53	14.81	19.02	19.10
	(57.53)	(66.67)	(22.33)	(13.33)	(20.14)	(20.00)

4.2.2 Crystal structure

XRD patterns of $Ti_{0.67}Nb_{0.33}$, $Ti_{0.67}Nb_{0.20}Fe_{0.13}$ and $Ti_{0.67}Nb_{0.13}Fe_{0.20}$ alloys are shown in Fig. 4.5. $Ti_{0.67}Nb_{0.33}$ is found to exist in BCC structure, with a lattice parameter of 3.283 Å, which is in good agreement with the earlier reported values [258].

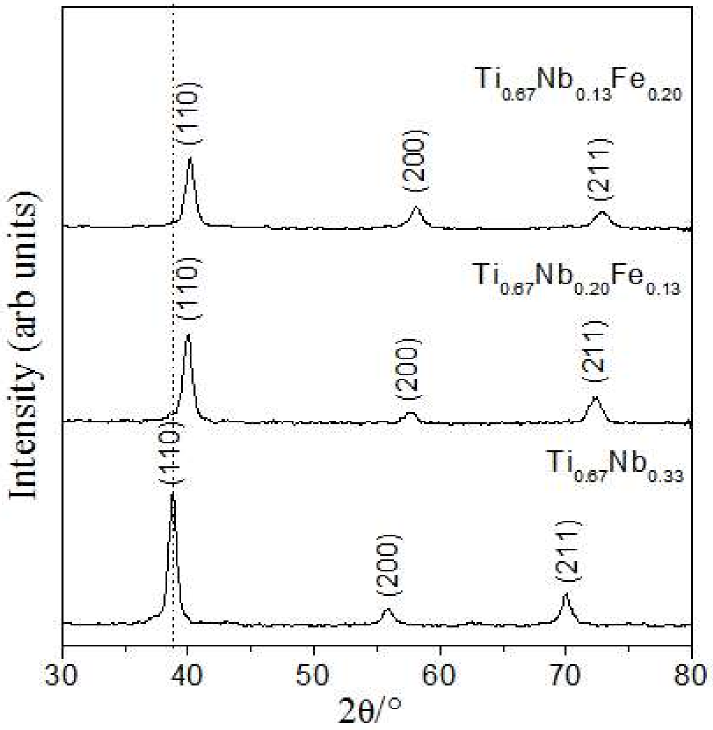

Fig. 4.5 *XRD patterns of* $Ti_{0.67}Nb_{0.33}$, $Ti_{0.67}Nb_{0.20}Fe_{0.13}$ *and* $Ti_{0.67}Nb_{0.13}Fe_{0.20}$ *alloys.*

For $Ti_{0.67}Nb_{0.33}$ alloy, the peak corresponding to atomic plane (110) occurs at 2θ = 38.78°. The vertical line drawn near 38.78° clearly indicates shift in the peak position with increase in iron content. When niobium is substituted by 40 and 60 at.% iron, this peak shifts to 39.99° and 40.17°, respectively, indicating that the lattice parameter decreases with increase in Fe substitution. The lattice parameters of these two alloys $Ti_{0.67}Nb_{0.20}Fe_{0.13}$ and $Ti_{0.67}Nb_{0.13}Fe_{0.20}$ are found to be 3.189 and 3.174 Å, respectively (Table 4.2). The reduction of lattice parameter with increasing Fe content is due to smaller atomic radius (r) of Fe as compared to that of Ti and Nb [r(Ti) ~ r(Nb) > r(Fe)]. The results imply that iron gets dissolved in the $Ti_{0.67}Nb_{0.33}$ matrix, without changing the crystal structure, and hence the lattice parameter decreases.

4.2.3 Hydrogen absorption studies

Absorbed hydrogen concentrations and maximum hydrogen absorption capacities of the alloys after one activation cycle are listed in Table 4.2. The table shows that $Ti_{0.67}Nb_{0.33}$ can absorb a maximum of 1.12 H atoms/formula unit (H/M) forming a hydride with a composition of $Ti_{0.67}Nb_{0.33}H_{1.12}$ at room temperature and 21 atm. of hydrogen pressure. The H/M value obtained was less than the theoretical value [259, 260], though further studies showed that with increase in activation cycles the hydrogen storage capacity increases. Fe substituted alloy $Ti_{0.67}Nb_{0.20}Fe_{0.13}$ is found to absorb a maximum of 1.21 H/M to form hydride with formula $Ti_{0.67}Nb_{0.20}Fe_{0.13}H_{1.21}$ at room temperature. This implies that maximum hydrogen absorption capacity of $Ti_{0.67}Nb_{0.33}$ alloy does not increase appreciably by 40 atom% Fe substitution. The higher Fe substituted alloy $Ti_{0.67}Nb_{0.13}Fe_{0.20}$ absorbed a maximum of 1.49 H/M leading to formation of $Ti_{0.67}Nb_{0.13}Fe_{0.20}H_{1.49}$. In case of Fe substituted alloys, hydrogen storage capacity increases due to better activation of the sample on heating at 673 K under diffusion vacuum. In ideal experimental case (sufficient activation, temperature), the capacity of the compound $Ti_{0.67}Nb_{0.33}$ should be higher than that of Fe substituted samples. From H/M value, the maximum hydrogen absorption capacity of $Ti_{0.67}Nb_{0.33}$ alloy was calculated to be 1.76 wt.%. Due to lower molecular weight of Fe and enhanced H/M value with increase in Fe content, the gravimetric hydrogen storage densities of the alloys are expected to follow the same trend as H/M values. The maximum hydrogen absorption capacities of iron substituted alloys are found to be 2.06 and 2.62 wt.%, respectively at room temperature.

Table 4.2 *Values of lattice parameters, unit cell volumes, absorbed hydrogen concentrations and maximum hydrogen storage capacities of alloys along with their crystal structures. The theoretical values of hydrogen storage capacities (H/M and wt.%) are given in parenthesis.*

Alloy composition	Phases	Lattice parameter (Å)	Unit cell volume (Å^3)	Hydrogen concentration (H atoms/ formula unit)	Maximum hydrogen storage capacity (wt. %)
Ti [Ref. 259]	BCC	3.306	36.133	2.00	4.01
$Ti_{0.67}Nb_{0.33}$	BCC	3.283	35.385	1.12 (2)	1.76 (3.08)
$Ti_{0.67}Nb_{0.20}Fe_{0.13}$	BCC	3.189	32.431	1.21 (1.74)	2.06 (2.91)
$Ti_{0.67}Nb_{0.13}Fe_{0.20}$	BCC	3.174	31.976	1.49 (1.6)	2.62 (2.80)
Nb [Ref. 259]	BCC	3.299	35.904	2.00	2.07

Fig. 4.6 shows SEM images of $Ti_{0.67}Nb_{0.33-x}Fe_x$ alloys after hydrogenation. The average particle size of the hydride of $Ti_{0.67}Nb_{0.33}$ alloy is about 100-450 µm. The decrease in the particle size is due to pulverization induced by hydrogenation. The fractures observed in Fig. 4.6 at 5000x magnification are caused by enormous internal strain developed by volume expansion during hydrogenation process. The large difference in cell volume between α and

β hydride phases generates dislocations at interface of the two phases resulting in enormous strain. The alloys become brittle and get pulverized into small particles. Due to decrease in particle size the surface area increases, which is beneficial for hydrogen absorption [261]. Based on the SEM images, average particle size of hydrides of other two alloys, $Ti_{0.67}Nb_{0.20}Fe_{0.13}$ and $Ti_{0.67}Nb_{0.13}Fe_{0.20}$ after one complete cycle of hydrogen absorption-desorption are 50-250 µm and 25-100 µm, respectively. The SEM images confirms that hydrogen induced pulverization is more prominent in alloys with increasing concentration of Fe.

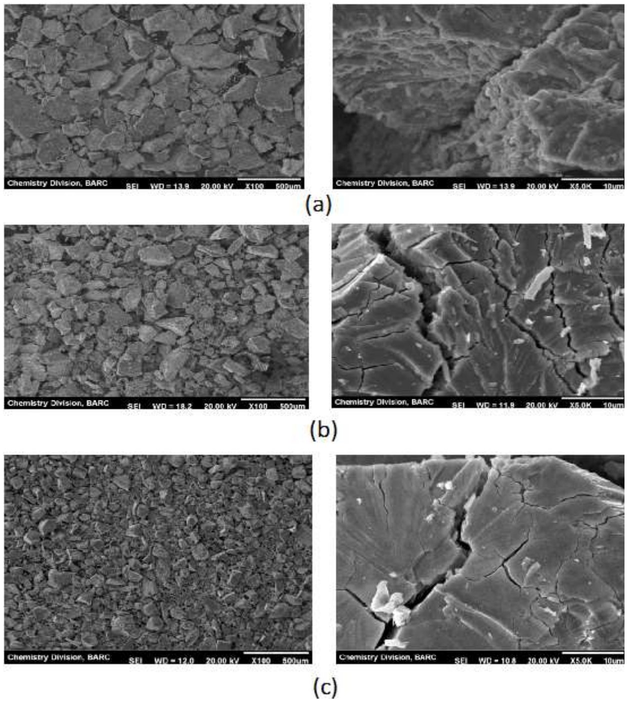

Fig. 4.6 *SEM images of hydrides of (a)* $Ti_{0.67}Nb_{0.33}$*, (b)* $Ti_{0.67}Nb_{0.20}Fe_{0.13}$ *and (c)* $Ti_{0.67}Nb_{0.13}Fe_{0.20}$ *recorded at 100x and 5000x magnifications.*

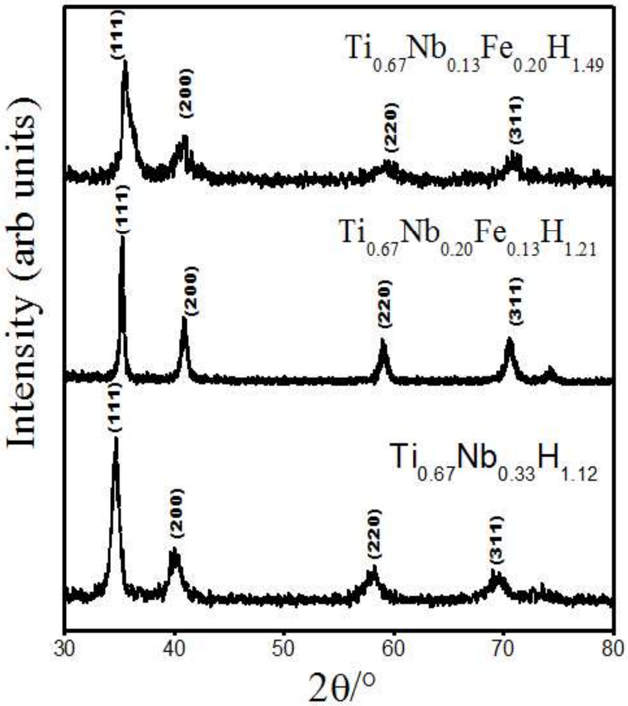

Fig. 4.7 *XRD patterns for saturated hydrides of (a)* $Ti_{0.67}Nb_{0.33}$*, (b)* $Ti_{0.67}Nb_{0.20}Fe_{0.13}$ *and (c)* $Ti_{0.67}Nb_{0.13}Fe_{0.20}$*.*

To know the effect of hydrogen absorption on the structural properties of the hydrogenated alloys their XRD patterns were recorded and shown in Fig. 4.7. Upon hydrogenation, each of the three alloys undergoes structural change from BCC to FCC. The lattice parameters and unit cell volumes of the hydrides have been calculated and given in Table 4.3.

Table 4.3 *Values of lattice parameters and unit cell volumes of the hydrides.*

Hydride composition	Phases	Lattice parameter(Å)	Unit cell volume(Å^3)
TiH_2 [Ref. 259]	FCC	4.44	87.528
$Ti_{0.67}Nb_{0.33}H_{1.12}$	FCC	4.497	90.941
$Ti_{0.67}Nb_{0.20}Fe_{0.13}H_{1.21}$	FCC	4.421	86.425
$Ti_{0.67}Nb_{0.13}Fe_{0.20}H_{1.49}$	FCC	4.408	85.659
NbH_2 [Ref. 259]	FCC	4.562	94.943

4.2.4 Hydrogen absorption kinetics of $Ti_{0.67}Nb_{0.33-x}Fe_x$ alloys

Kinetics of hydrogen absorption for $Ti_{0.67}Nb_{0.33-x}Fe_x$ (x = 0.00, 0.13, 0.20) alloys has been studied using a Sieverts' type setup at room temperature and 25 atm. pressure after one absorption-desorption cycle. The rate of hydrogen absorption is shown as change of reacted fraction (ζ) with time in Fig. 4.8.

It is clear from qualitative behavior of the kinetic plots that the reaction starts immediately without any incubation period for all the three alloys in $Ti_{0.67}Nb_{0.33-x}Fe_x$ series and the hydrogen absorption kinetics are found to be quite fast. $Ti_{0.67}Nb_{0.33}$ alloy reaches 76.8% of saturation value [ζ = 0.768] within 2 minutes. Whereas, for iron containing alloys, $Ti_{0.67}Nb_{0.20}Fe_{0.13}$ and $Ti_{0.67}Nb_{0.13}Fe_{0.20}$, ζ values at 2 minutes extend up to 0.839 and 0.892, respectively. The results indicate that iron substitution for niobium facilitates kinetics of hydrogen absorption. This is also clear from the extent of pulverization seen from SEM images in Section 4.2.3. Incorporation of Fe in the alloy induces more pulverization upon hydrogenation, which favors faster hydrogen absorption kinetics.

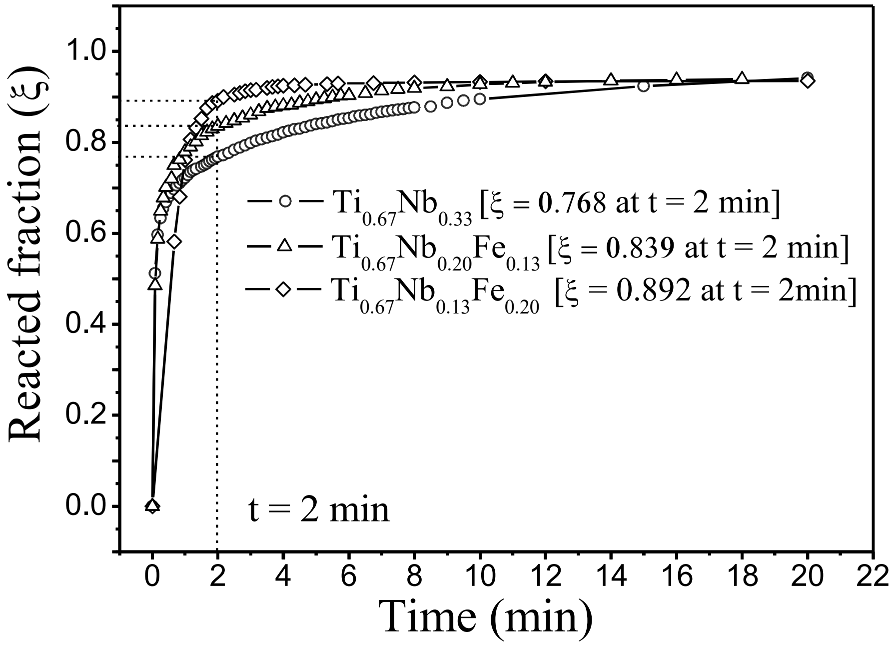

Fig. 4.8 *Kinetics of hydrogen absorption for* $Ti_{0.67}Nb_{0.33-x}Fe_x$ *(x = 0.00, 0.13, 0.20) alloys at room temperature.*

Maeland et al. [241] have noted that substitution by smaller atoms in group 5 metals (V, Nb, Ta) or group 5 metal stabilized BCC titanium alloys promote kinetics of hydrogen absorption. They have explained this in terms of trapping energy at subsurface sites. Bonding of trapped hydrogen at subsurface sites of some group 5 metals (Nb, Ta) is known to be stronger than chemisorption, and hydrogen becomes tightly bound below the first few layers leading to slow diffusion of hydrogen into bulk. This is reflected as poor hydrogen absorption kinetics. Subsurface acts as a "valve" and regulates passage of hydrogen from surface to bulk. It has been found that with increasing concentration of Fe in ternary $Ti_{0.67}Nb_{0.33-x}Fe_x$ alloys, kinetics of hydrogenation reaction becomes faster. This accelerated reaction kinetics can be attributed to substitution of Nb by smaller size Fe atom in Ti-Nb BCC alloy. The associated strain in the ternary alloy helps to open the “valve” by reducing the subsurface trapping energy.

4.2.5 Detailed hydrogen absorption kinetics study of $Ti_{0.67}Nb_{0.13}Fe_{0.20}$ alloy

In $Ti_{0.67}Nb_{0.33-x}Fe_x$ series, $Ti_{0.67}Nb_{0.13}Fe_{0.20}$ shows maximum hydrogen absorption capacity and fastest absorption kinetics. In this section hydrogenation kinetics of this alloy is discussed in detail. From earlier studies [262-264], it is known that hydriding reaction of metal or metallic alloy proceeds via different mechanisms. The processes (mainly surface processes) corresponding to the α-phase solid solution take place within a very short time, hence should not be considered as rate limiting step. In the next stage of hydrogenation, the hydride phase starts growing by chemical reaction. When the β-phase hydride is formed completely, hydrogen atoms are redistributed in hydride phase and diffusion of hydrogen in β-phase seems to be the rate-determining step [265, 266]. Therefore the entire hydrogenation rate can be envisaged as combination of a chemical reaction rate and a diffusion rate. Typically, in (α + β) mixed phase region, the process is chemical reaction rate limited; but at the later stage, the hydrogenation rate goes through a transition where it is increasingly dominated by diffusion of hydrogen in β-phase hydride.

In Fig. 4.9 the reacted fraction of $Ti_{0.67}Nb_{0.13}Fe_{0.20}$ alloy has been plotted as a function of time. It has been found that the alloy requires 1 minute for the reacted fraction to reach 0.75, 0.90, 0.91 and 0.93 of hydrogen absorption at 298, 373, 423 and 473 K, respectively. This also confirms the fact, that with increase in temperature, the hydrogen absorption rate increases. To analyze the hydrogen-alloy reaction mechanism, the kinetic data has been fitted with models which give mathematical description of what is occurring experimentally.

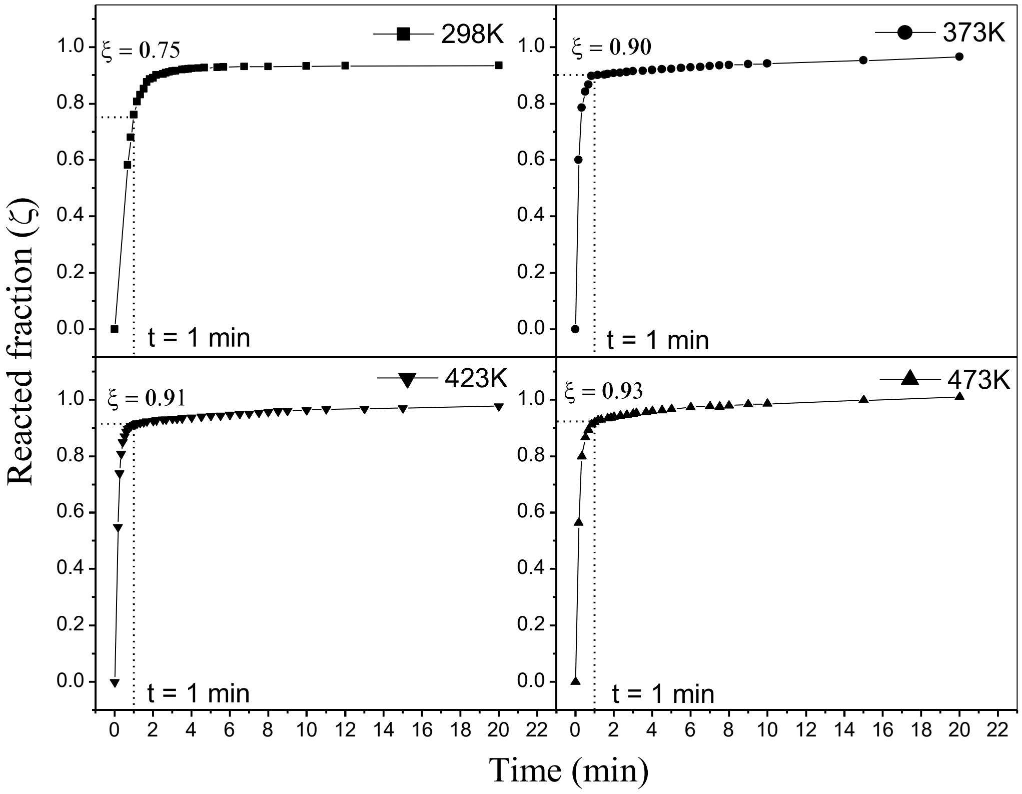

Fig. 4.9 *Kinetics of hydrogen absorption for* $Ti_{0.67}Nb_{0.13}Fe_{0.20}$ *alloy over the temperature range of 298-473 K. The ζ values at time (t) = 1 min for different temperatures are mentioned in the figure.*

It has been found that, the experimental data can be fitted reasonably well using two models. In other words, hydrogen absorption kinetics involves two different rate controlling mechanisms. Hydrogen absorption curves for reacted fraction $\zeta < 0.90$, at four different temperatures from 298 to 473 K can be fitted with good accuracy (Fig. 4.10) by chemical reaction rate expression $[(1 - \zeta)^{-1} - 1] = kt$ [93], where k is the rate constant. From the above result it is inferred that second order chemical reaction progresses homogeneously throughout the

(α + β) phase region and is the rate controlling step in the short time range during hydriding of the alloy.

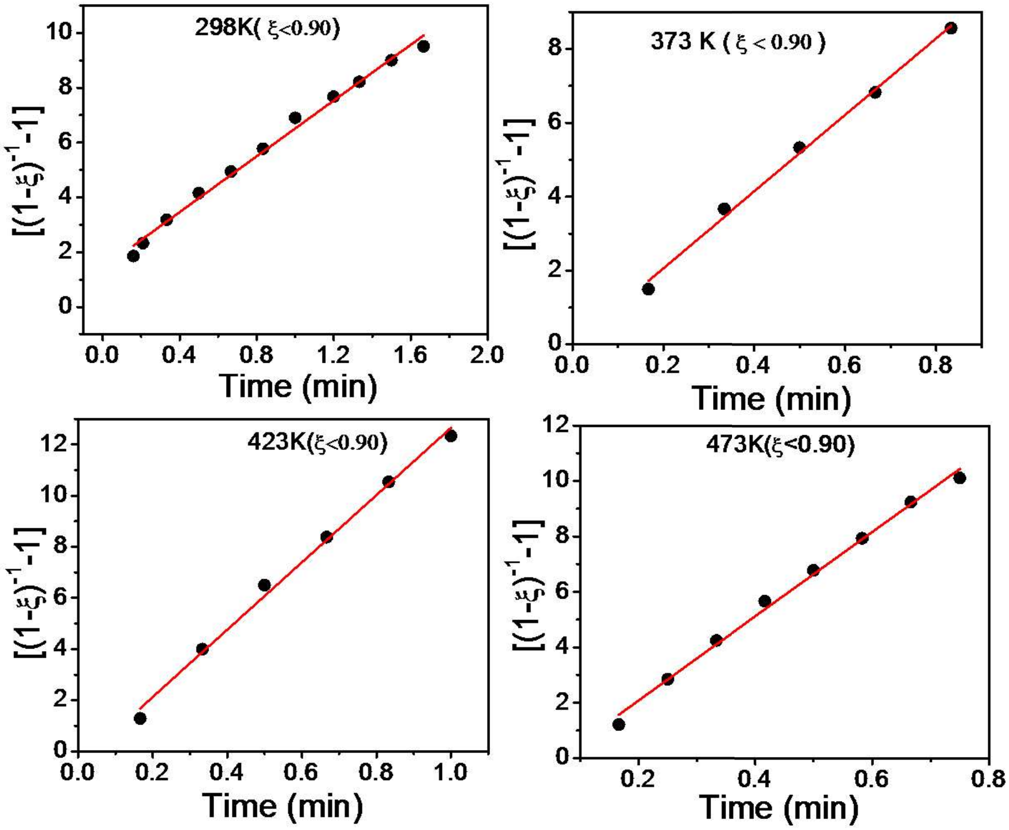

Fig. 4.10 *Plot of* $[(1-\zeta)^{-1}-1]$ *versus time for hydrogenation of* $Ti_{0.67}Nb_{0.13}Fe_{0.20}$ *alloy in (α+β) phase region at different temperatures (298 K-423 K).*

The experimental data for $Ti_{0.67}Nb_{0.13}Fe_{0.20}$ alloy at $\zeta > 0.90$ fits well with Jander diffusion model which is based on the assumption of spherical solid particles. Here the hydrogenation kinetics can be expressed by the parabolic type of rate equation, $[1-(1-\zeta)^{1/3}]^2 = kt$ [93, 267, 268]. This indicates that the rate-limiting step of hydrogen absorption process is three-dimensional diffusion of hydrogen in the β-phase (Fig. 4.11).

The rate constants (k) of two different processes at different temperatures can be found out from slope of the curves and are summarized in Table 4.4. The other parameters like correlation-coefficient (ϕ) along with corresponding kinetic equations and rate determining steps (rds) are also given in Table 4.4. It can be clearly seen from the tabulated values of correlation-coefficients, that all are very close to 1, indicating that the fitting is good with corresponding rate equations and the calculated activation energies of the two processes based on the k values are reliable. Activation energy E_a, for both the regions is obtained from slope of the Arrhenius plot (ln(k) vs. 1/T) as shown in Fig. 4.12.

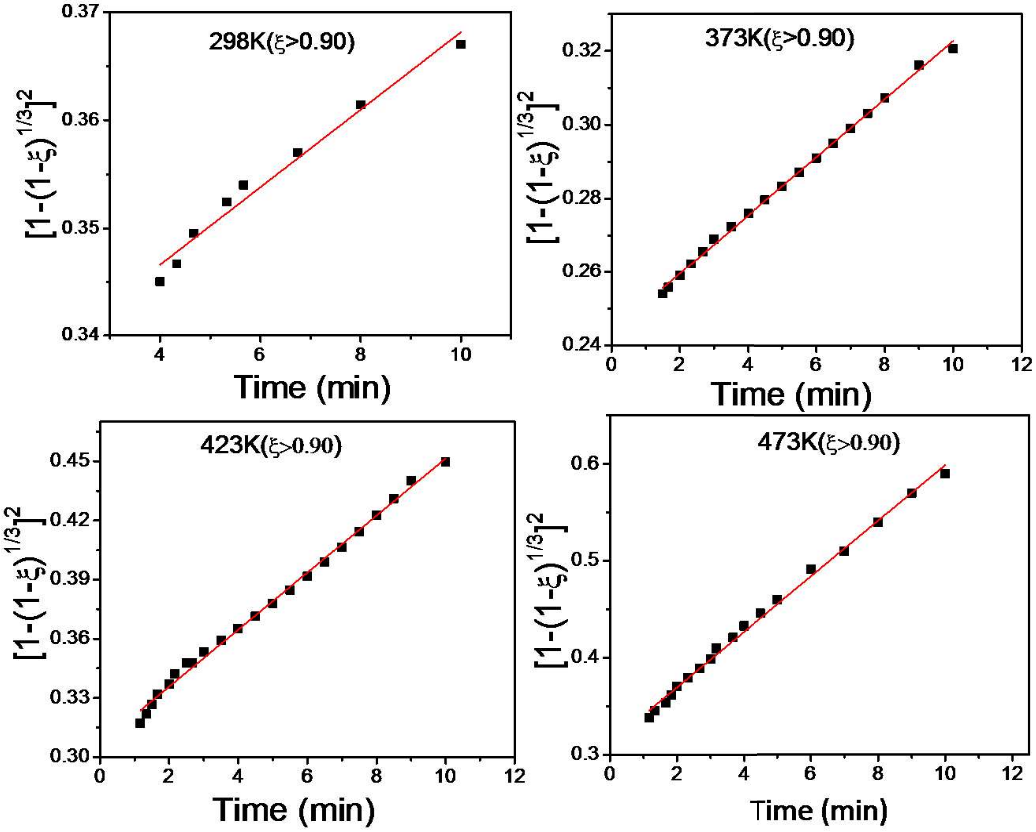

Fig. 4.11 *Plot of* $[1-(1-\zeta)^{1/3}]^2$ *versus time for hydrogenation of* $Ti_{0.67}Nb_{0.13}Fe_{0.20}$ *alloy in β-phase region at different temperatures (298 K-423 K).*

The calculated activation energies are found to be 7.34 kJ/mol for (α + β)-phase region and 15.1 kJ/mol for β-phase region. The activation energy in (α + β)-phase region is smaller than that in β-phase region. It is obvious that smaller the activation energy faster the reaction rate is.

Hence it can be concluded that the rate of f hydrogen absorption is faster in (α + β)-phase region compared to that in β-phase region over the temperature range 298 K to 473 K.

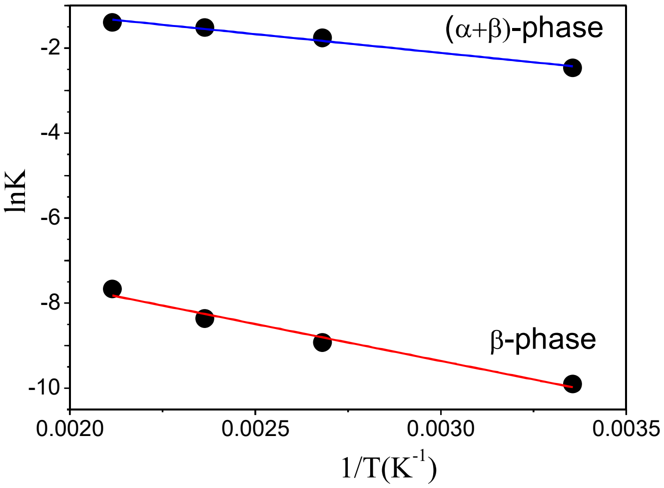

Fig.4.12 *Arrhenius plots for the hydrogenation of* $Ti_{0.67}Nb_{0.13}Fe_{0.20}$ *alloy in the (α+β) phase region and β-phase region.*

Table 4.4 *Kinetic parameters, best fitting equations and activation energies* (E_a) *for hydrogen absorption of* $Ti_{0.67}Nb_{0.13}Fe_{0.20}$ *alloy.*

Stages	(α +β) phase region (ζ<0.90)				β phase region (ζ>0.90)			
Temp.	298K	373K	423K	473K	298K	373K	423K	473K
Equation	$[(1-\zeta)^{-1}-1] = kt$				$[1-(1-\zeta)^{1/3}]^2 = kt$			
k (sec^{-1})	0.085	0.172	0.219	0.248	0.00005	.000133	.000233	.000467
ϕ	0.9913	0.9968	0.9930	0.9937	0.9731	0.9978	0.9952	0.9958
rds	Chemical Reaction				Three dimensional diffusion			
E_a (kJ/mol)	7.34				15.1			

4.2.6 Mössbauer Study

The influence of Fe substitution and hydrogenation on electronic and structural properties of $Ti_{0.67}Nb_{0.33-x}Fe_x$ alloys has been probed with ^{57}Fe Mössbauer spectroscopy. The results obtained from the analysis of Mössbauer spectra are given in Table 4.5. Mössbauer spectra for $Ti_{0.67}Nb_{0.33-x}Fe_x$ alloys (x = 0.13, 0.20) are fitted with one singlet and one symmetric doublet respectively (Fig. 4.13 (a, b)).

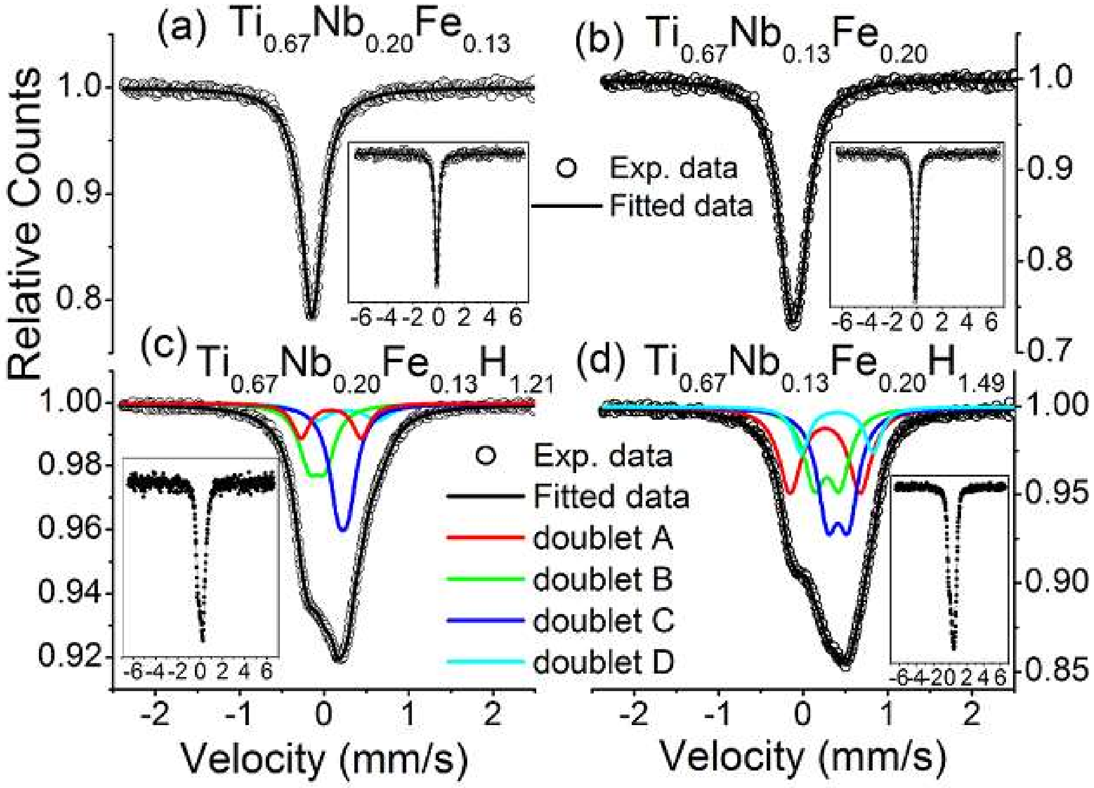

Fig. 4.13 *Room temperature* ^{57}*Fe Mössbauer spectra of* $Ti_{0.67}Nb_{0.33-x}Fe_x$ *alloys with (a) x = 0.13 and (b) x = 0.20. Corresponding spectrum from* $Ti_{0.67}Nb_{0.33-x}Fe_xH_y$ *sample with x =0.13, y = 1.21 and x = 0.20, y = 1.49 are shown in Fig. 4.13(c) and (d) respectively.*

The values of quadrupole moment (eQ = 0) and electric field gradient (EFG ~ 0) are zero for singlet, it means that the nucleus is fully spherical ($I \leq ½$, I is the nuclear spin quantum number) and sample possesses fully cubic symmetry. Doublet arises due to electric quadrupole interaction between nuclear quadrupole moment (eQ ≠ 0, $I > ½$) and inhomogeneous electric field (EFG ≠ 0) as already discussed in Chapter 2. For the doublet, the electric quadrupole interaction splits the first nuclear excited state ($I = 3/2$) of ^{57}Fe into two sub levels. In Mössbauer spectrum, quadrupole splitting (ΔE_Q) for doublet is equal to the difference between two lines

(ΔE_Q = line 2 – line 1) in mm/s. There is no quadrupole splitting ($\Delta E_Q = 0$) for $Ti_{0.67}Nb_{0.20}Fe_{0.13}$ alloy whereas $\Delta E_Q = 0.122$ mm/s for the alloy $Ti_{0.67}Nb_{0.13}Fe_{0.20}$, indicating absence of electric field gradient (EFG) in the former sample (x = 0.13). This is understandable as EFG increases with increase in Fe content in the sample. This, in turn, reveals that the nuclei of Fe atoms remain spherical in $Ti_{0.67}Nb_{0.20}Fe_{0.13}$ alloy and it losses the symmetry in $Ti_{0.67}Nb_{0.13}Fe_{0.20}$ alloy [269]. The value of isomer shift (measured relative to α-Fe metal foil) is found to be $\delta = -0.1502(5)$ mm/s for $Ti_{0.67}Nb_{0.20}Fe_{0.13}$ alloy whereas, for $Ti_{0.67}Nb_{0.13}Fe_{0.20}$ alloy, $\delta = -0.1388(6)$ mm/s. It indicates that the electron charge density around Fe nucleus changes with change in the extent of Fe substitution. Further both the alloys (x = 0.13, 0.20) show negative δ values indicating higher charge density at the Fe nucleus [270] in these alloys compared to α-Fe ($\delta = 0.0$ mm/s). Increase in isomer shift ($\delta = -0.1502(5)$ mm/s to $\delta = -0.1388(6)$ mm/s) is due to decrease in electronic charge density at the Fe nucleus for higher Fe containing alloy $Ti_{0.67}Nb_{0.13}Fe_{0.20}$. This is in accordance with the explanation of ^{57}Fe isomer shift values given by Walker et al [270]. In Fe substituted $Ti_{0.67}Nb_{0.33}$ alloys, as Fe ($3d^6 4s^2$) concentration increases at the expense of Nb ($3d^{10} 4s^2 4d^4 5s^1$), the overall number of d electrons decreases causing an expansion of s electron wave function. This reduces the s-electron charge density around Fe nucleus and hence δ is expected to increase upon Fe substitution for Nb [269, 271, 272]. Similar type of paramagnetic Mössbauer spectra were observed by Singh et al. for FeTi and $Fe_{46}Ti_{50}Mn_4$ alloys [272]. Here also the isomer shift was found to be negative (-0.228 and -0.57 mm/s, respectively) at room temperature compared to α-Fe. Mössbauer spectra of hydrides also show similar trend; larger isomer shifts for the hydride of higher Fe containing alloy, $Ti_{0.67}Nb_{0.13}Fe_{0.20}H_{1.49}$ compared to $Ti_{0.67}Nb_{0.20}Fe_{0.13}H_{1.21}$. Mössbauer spectra of the hydrides $Ti_{0.67}Nb_{0.33-x}Fe_x$ (x = 0.13, 0.20; y = 1.21, 1.49) are shown in Fig. 4.13 (c and d, respectively). To ensure the paramagnetic nature of the alloys with x = 0.13, 0.20, their Mössbauer spectra were recorded at higher velocity (±6.5 mm/s). The higher velocity Mössbauer spectra of $Ti_{0.67}Nb_{0.33-x}Fe_x$ (x = 0.13, 0.20) alloys are shown in inset of Fig. 4.13 (a and b, respectively). The spectra do not show magnetic hyperfine splitting (Zeeman splitting/sextet) assuring both samples are paramagnetic at room temperature and there is no unalloyed Fe left. This is also evident from XRD patterns that show only BCC phase and no peak due to iron.

Table 4.5 *Mössbauer parameters extracted from room temperature Mössbauer spectra for* $Ti_{0.67}Nb_{0.33-x}Fe_x$ *(x = 0.13, 0.20) alloys and* $Ti_{0.67}Nb_{0.33-x}Fe_xH_y$ *(x = 0.13, 0.20; y = 1.21, 1.49, respectively) hydrides. Isomer shift values are relative to α-Fe metal foil.*

Fe substitution (x)	Iron Sites	Isomer shift (δ) mm/s	Quadrupole splitting (ΔE_Q) mm/s	Line width (Γ) mm/s	Relative Area, R_A (%)	Fitting quality χ^2
$Ti_{0.67}Nb_{0.20}Fe_{0.13}$	Singlet	-0.1502(5)	0.0	0.305(2)	100	0.875444
$Ti_{0.67}Nb_{0.13}Fe_{0.20}$	Doublet	-0.1388(6)	0.122(3)	0.324(4)	100	0.9960
$Ti_{0.67}Nb_{0.20}Fe_{0.13}H_{1.21}$	Doublet A (red)	0.082(4)	0.71(2)	0.24(2)	14.2	1.01396
	Doublet B (green)	-0.086(7)	0.191(6)	0.29(1)	30.7	
	Doublet C (blue)	0.222(4)	0.122(4)	0.26(2)	36.7	
	Doublet D (cyan)	0.27(2)	0.73(4)	0.40(2)	18.4	
$Ti_{0.67}Nb_{0.13}Fe_{0.20}H_{1.49}$	Doublet A (red)	0.261(5)	0.83(1)	0.32(1)	33.8	1.08036
	Doublet B (green)	0.281(7)	0.30(1)	0.26(3)	24.1	
	Doublet C (blue)	0.412(5)	0.245(5)	0.29(1)	32.6	
	Doublet D (cyan)	0.402(8)	0.85(2)	0.23(2)	9.5	

It is interesting to note (Fig. 4.13 (c and d)) that Mössbauer spectra of hydrides fitted with four doublets (A, B, C and D) show different δ values. This indicates four different types of local environments around Fe nuclei in both the hydrides. The values of δ are higher for hydrides compared to the parent alloys and all of them show nonzero values of ΔE_Q. From δ values of four doublets, it is seen that, on hydrogen absorption, the isomer shift increases remarkably. The increase in isomer shift can be correlated with two factors: (i) an increase in volume with hydrogenation and (ii) reduction of the s-electron charge density at the Fe nuclei with hydrogen absorption because of 4s charge transfer from Fe to H resulting in metal hydrogen bond [271, 272]. Singh et al [272] also observed gradual increase in isomer shift for FeTi alloy under hydriding process. The δ values of $Ti_{0.67}Nb_{0.13}Fe_{0.20}H_{1.49}$ hydride are higher than those of $Ti_{0.67}Nb_{0.20}Fe_{0.13}H_{1.21}$ hydride which can be explained in terms of greater Fe substitution and higher hydrogen content in the former sample. The ΔE_Q values associated with four doublets of $Ti_{0.67}Nb_{0.13}Fe_{0.20}H_{1.49}$ hydride are larger than those of $Ti_{0.67}Nb_{0.20}Fe_{0.13}H_{1.21}$ hydride. The higher ΔE_Q value for $Ti_{0.67}Nb_{0.13}Fe_{0.20}H_{1.49}$ hydride is due to higher EFG around Fe nuclei which reflects more reduction of local symmetry around iron nuclei by more number of interstitial hydrogen in this hydride.

4.3 Conclusions

In this chapter, hydrogen absorption properties of $Ti_{0.67}Nb_{0.33-x}Fe_x$ (x = 0.00, 0.13, 0.20) alloys have been investigated. All the three alloys exist as single phase BCC solid solution and the lattice parameter decreases with increase in Fe content. The maximum storage capacities of $Ti_{0.67}Nb_{0.33}$, $Ti_{0.67}Nb_{0.20}Fe_{0.13}$ and $Ti_{0.67}Nb_{0.13}Fe_{0.20}$ alloys are 1.76, 2.06 and 2.62 wt.%, respectively at room temperature. It has been found that Fe improves hydriding kinetics and therefore on Fe substitution a higher hydrogen storage capacity is reached under the experimental conditions used here. The detailed hydrogen absorption kinetics study of $Ti_{0.67}Nb_{0.13}Fe_{0.20}$ alloy at different temperatures reveals that chemical reaction in the (α + β) mixed phase region and three dimensional diffusion of hydrogen in the β-phase region are the two rate determining steps, and E_a values for these two processes are 7.34 and 15.1 kJ/mol, respectively. Mössbauer investigations of Fe substituted alloys $Ti_{0.67}Nb_{0.33-x}Fe_x$ ($x = 0.13, 0.20$) and their related hydrides revealed that both Fe substitution and hydrogen absorption lead to remarkable increase in isomer shift. The quadrupole splitting also increases on hydrogenation indicating more asymmetry around iron nuclei after hydrogenation.

Chapter 5

Hydrogen Storage Properties of Ti-V Based Alloys

Vanadium is a well-known beta isomorphous element and recently, most of the research on metal hydrides is focused on Ti-V based solid solution alloys with body centered cubic (BCC) phase structure. Hydrogen diffusion rate in V metal is very high and alloying it with Ti reduces the rate of diffusion. Interestingly, Ti-V alloy shows higher hydrogen content compared to single V or single Ti metal. In particular, Ti-V-Cr alloys have shown promising hydrogen storage properties [246, 273-275]. Earlier studies by our group have confirmed that the alloy with composition Ti_2CrV can absorb ~ 4 wt.% hydrogen at room temperature [129]. To the best of our knowledge Ti_2CrV alloy possesses highest hydrogen storage capacity among all Ti-V based alloys investigated. However, the alloy suffers from difficult activation and comparatively higher desorption temperature hindering its practical application as hydrogen storage material [276, 277].

Present chapter presents two different approaches to solve the above mentioned problems of Ti-Cr-V based alloys namely by Zr substitution and by composite formation. From literature survey, it was found that Zr is often selected to substitute Ti in Ti-V based BCC solid solutions to generate a secondary phase. The secondary phase is mainly AB_2 type Laves phase which shows excellent catalytic effect during hydrogen absorption-desorption process [278, 279]. These alloys are usually known as “Laves phase related BCC solid solution” as introduced by Iba and Akiba [246, 280]. In these alloys BCC phase forms a 3D framework with Laves phase at the grain boundaries [281, 282]. Homma et al. [283] have mentioned that in such alloys, BCC solid solution is the main hydrogen absorbing phase whereas the Laves phase acts as penetration path for hydrogen in the initial stage of hydrogen absorption. Hence, it is expected that the Laves phase will make activation process easy. Hang et al. [284] have reported that with increase in Zr content in $Ti_{10}V_{84-x}Fe_6Zr_x$ (x = 1-8) alloys, activation behavior is drastically improved due to increased abundance of Zr rich Laves phase. It is also evident from the work of Shashikala et al. [285] that comparatively lower temperature desorption sites arise in Zr containing Laves phase related BCC solid solutions. However, the effect of Zr substitution on the overall hydrogen absorption desorption characteristics of Ti-V-Cr alloy needs further investigation to optimize storage properties and this is the subject matter of present chapter.

In the second approach, instead of promoting Laves phase formation by Zr incorporation, composite materials containing both BCC Ti_2CrV alloy and Zr based Laves Phase compounds have been prepared and evaluated for hydrogen absorption properties. Such composite materials may lead to improved hydrogen storage property due to interface effects arising from significant density of interface boundaries. Yu et al. [286] has reported that Ti-30V-15Mn-15Cr containing 10 wt. % AB_5 composite showed higher discharge capacity due to enhanced electrochemical-catalytic activity from the alloy surface covered with AB_5 phase. Similar results have been reported in other papers also [287-289], where composite formation greatly affects hydrogen storage properties. Detailed investigation has been done on the effects of alloying $LaNi_5$ with $Ti_{0.32}Cr_{0.43}V_{0.25}$ on its structure and hydrogen storage properties and the results suggest that there is decrease in plateau pressure as well as hydrogen storage capacities [289]. Hydrogen storage properties of $Ti_{0.32}Cr_{0.43}V_{0.25}$ alloy and its composite with $TiMn_2$ shows that the composite formation decreases the maximum hydrogen storage capacity, though there is decrease in hydrogen desorption temperature and increase in hydrogen absorption kinetics [290]. It is already mentioned that Laves phase related BCC solid solution is a very interesting class of alloy where the Laves phase acts as catalyst for absorption and desorption of hydrogen. Hence it would be meaningful to evaluate hydrogen storage properties of Ti_2CrV hydrogen storage alloys by preparing composite with $ZrFe_2$ based Laves phase. $ZrFe_2$ itself shows very little hydrogen absorption, but certain amount of V incorporation in $ZrFe_2$ phase forms $ZrFe_{2-x}V_x$ (x = 0.0-0.2) solid solution and improves hydrogen storage properties [291, 292]. Keeping this in mind, influence of $ZrFe_{1.8}V_{0.2}$ Laves phase on hydrogen storage properties of Ti_2CrV alloy has been investigated by systematically increasing the amount of secondary Laves phase.

The present chapter has been divided into three different sections. First section of this chapter deals with synthesis of alloys and composite materials, their hydrides and characterization techniques. The details of experimental results obtained from this study is being presented in the next section and this will be followed by conclusions of the study

5.1 Experimental details

Alloy samples were prepared by arc-melting the constituent elements in a Zr-gettered argon atmosphere using a non-consumable tungsten electrode. All the raw materials are having purity > 99.99%. The alloy ingots were remelted several times in an attempt to homogenize alloy compositions. Composite materials are prepared by two step arc melting procedure. Particular alloys were taken in desired ratio and arc melted together. The composites thus prepared, were wrapped in Ta foil and heated in a quartz tube under vacuum at 400 ºC. The quartz tubes were sealed under vacuum and annealed at 900 ºC for 2 days to ensure proper phase formation. Crystal structures of the alloys, composites and their corresponding hydrides were examined by XRD (Philips PW1710). Detailed micro-structural characterization and X-ray microanalysis were carried out using a CAMECA SX 100 electron probe micro-analyzer (EPMA) employing a focused electron beam accelerated to voltage of 20 kV. The stabilized beam current was kept at 4 nA and 20 nA for imaging and X-ray analysis, respectively. Prior to structural analysis, small coupons of alloy/composite samples were mounted in resin and made scratch free by grinding with various grades of emery paper (coarser to finer ones) and subsequently polished upto mirror finish using 1 micron sized diamond paste. The polished samples were then cleaned with acetone in an ultrasonic bath and coated with thin Au film to prevent charge build up. Beam size was kept at <1 μm to decrease the convolution effect so that good compositional estimates can be obtained. Raw intensity data were rectified for atomic number, absorption and fluorescence using the PAP method [293].

Hydrogen charging was carried out using an automated Sievert's type set up (IMI analyzer, Hiden Isochema, HTP1, UK) already discussed in Chapter 2. During hydrogenation, respective sample was loaded into a gold coated copper reactor and measuring system was evacuated through a turbo molecular vacuum pump. During activation process, the sample was heated under diffusion vacuum (10^{-6} mbar) for 2 h at 673 K. After activation, the sample was allowed to cool down at working temperature under vacuum. Pressure-composition isotherms were studied over the temperature range 298-393 K and upto a hydrogen pressure of 20 bar. Kinetics of hydrogenation was investigated at different temperatures under 5 bar of hydrogen pressure after one hydrogen absorption-desorption cycle in a home-made Sieverts's type set up as mentioned in previous chapter. In the same volumetric set up hydriding- dehydriding cycling tests were also performed for selected samples. High purity hydrogen (99.999% purity) was used for PCI measurements, kinetic study as well as for cycling study without any further purification.

Temperature programmed desorption (TPD) study of the hydride samples was carried out *in-situ* in the automated hydriding set up using He as the carrier gas with a constant heating rate of 5 K/min. Differential Scanning Calorimetric (DSC) study of the hydride samples was performed using DSC823^e Mettler-Toledo instrument under argon flow with a temperature ramping rate of 10 K/min.

The particle size distribution of the hydrides was determined by laser scattering technique (CILAS 1064L, France). Morphology of the hydrides was investigated by Scanning Electron Microscopy (SERON INC South Korea, Model ATS 2100).

5.2 Results and discussions

5.2.1 Effect of Zr substitution on hydrogen storage properties of Ti_2CrV alloy

In this study, the crystal structure, microstructure and hydrogen absorption/desorption properties of $Ti_{0.43}Zr_{0.07}Cr_{0.25}V_{0.25}$ alloy have been reported. Thermodynamic as well as kinetic aspects of hydrogen absorption process have also been studied in detail.

5.2.1.1 X-ray diffraction study

Fig. 5.1 shows the XRD pattern of as prepared $Ti_{0.43}Zr_{0.07}Cr_{0.25}V_{0.25}$ alloy. From the pattern, it is clear that two distinct crystallographic phases, namely C14 Laves phase with $MgZn_2$ type hexagonal structure and Ti-based solid solution phase with BCC structure, coexist in the alloy. The lattice parameter of the main BCC phase was determined to be a = 3.106 Å which is larger than that of the unsubstituited alloy as found by Kumar et al. (a = 3.10Å) [129]. This is due to partial substitution of Ti by larger size Zr ($r_{Zr} > r_{Ti}$) in BCC lattice. Lattice parameters of secondary C14 Laves phase are listed in Table 5.1. In order to further clarify the composition of the alloy, elemental mapping has been carried out along with back scattered electron (BSE) imaging. BSE also confirms the existence of two phases in the sample.

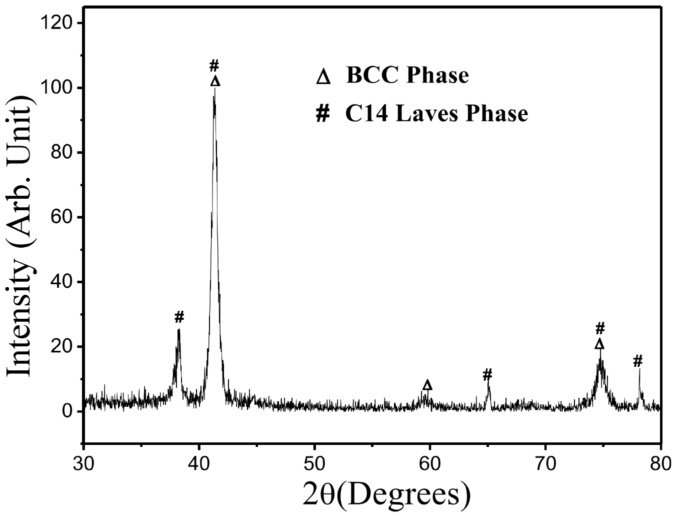

Fig. 5.1 *XRD pattern of* $Ti_{0.43}Zr_{0.07}Cr_{0.25}V_{0.25}$ *alloy.*

Table 5.1 *Unit cell parameters of* $Ti_{0.43}Zr_{0.07}Cr_{0.25}V_{0.25}$ *alloy before and after hydrogenation.*

Composition	Phases	Lattice parameter (Å)	Unit cell volume (Å^3)
$Ti_{0.43}Zr_{0.07}Cr_{0.25}V_{0.25}$	BCC	a = 3.106	29.96
	C14 Laves phase	a = 5.1, c = 8.353	188.16
$Ti_{0.43}Zr_{0.07}Cr_{0.25}V_{0.25}H_{6.98}$	FCC	a = 4.359	82.82
(1st cycle)	C15 Laves phase	a = 7.712	428.67
$Ti_{0.43}Zr_{0.07}Cr_{0.25}V_{0.25}H_{5.46}$	FCC	a = 4.357	82.71
(15th cycle)	C15 Laves phase	a = 7.519	425.09

5.2.1.2 Microstructure

Representative BSE image with atomic number contrast (Fig. 5.2 (a)) reveals that the alloy microstructure is comprised of two phases designated as grey matrix and white precipitates. A small fraction of pits introduced during metallographic polishing appears as black dots in the image. Micron sized white regions (precipitates) are distributed randomly throughout the matrix.

Upon inspection at higher magnification it is revealed that the white precipitates are actually clusters of fine dendrites having rod shape morphology (Fig. 5.2 (b)). Such dendrites are commonly observed in as cast structure of alloys and are formed during solidification. Furthermore, the white precipitates have a sharp interface with the grey matrix (regions). Similar two phase microstructures have been reported earlier in $Ti_{10}V_{84-x}Fe_6Zr_x$ (x = 1-8) alloys by Hang et al. [284]. In order to observe the overall distribution of elements over a wider area (100 µm x 100 µm), detailed X-ray mapping for Ti, V, Cr and Zr was carried out using wavelength dispersive spectroscopy (WDS) and is represented in Fig. 5.3.

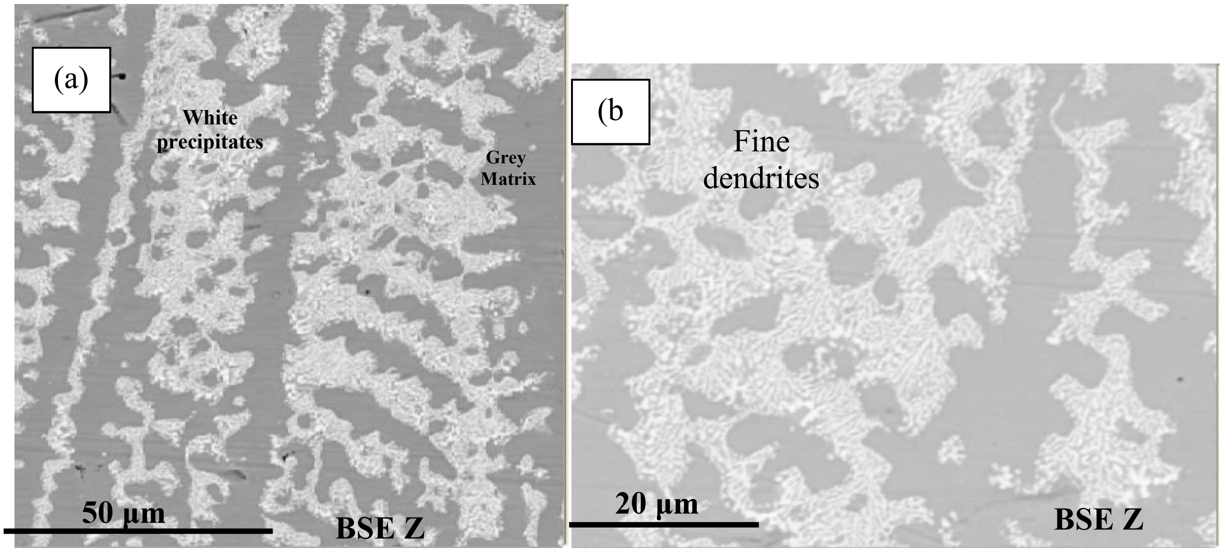

Fig. 5.2 *Backscatter electron (BSE) image of* $Ti_{0.43}Zr_{0.07}Cr_{0.25}V_{0.25}$ *alloy at (a) lower magnification, (b) higher magnification.*

It is evident from X-ray maps that the grey matrix is rich in Ti, V and Cr but depleted in Zr while the white precipitate mainly contains Zr and Cr. Enrichment of Zr in white precipitates is thus responsible for giving bright phase contrast in BSE images. These white precipitates are mainly Zr-Cr based compound containing minor amounts of Ti and V. The grey matrix, on the other hand is a Ti-V-Cr based solid solution with minor amounts of Zr. Thus the micrstructtural results are in line with the findings from X-ray diffraction pattern.

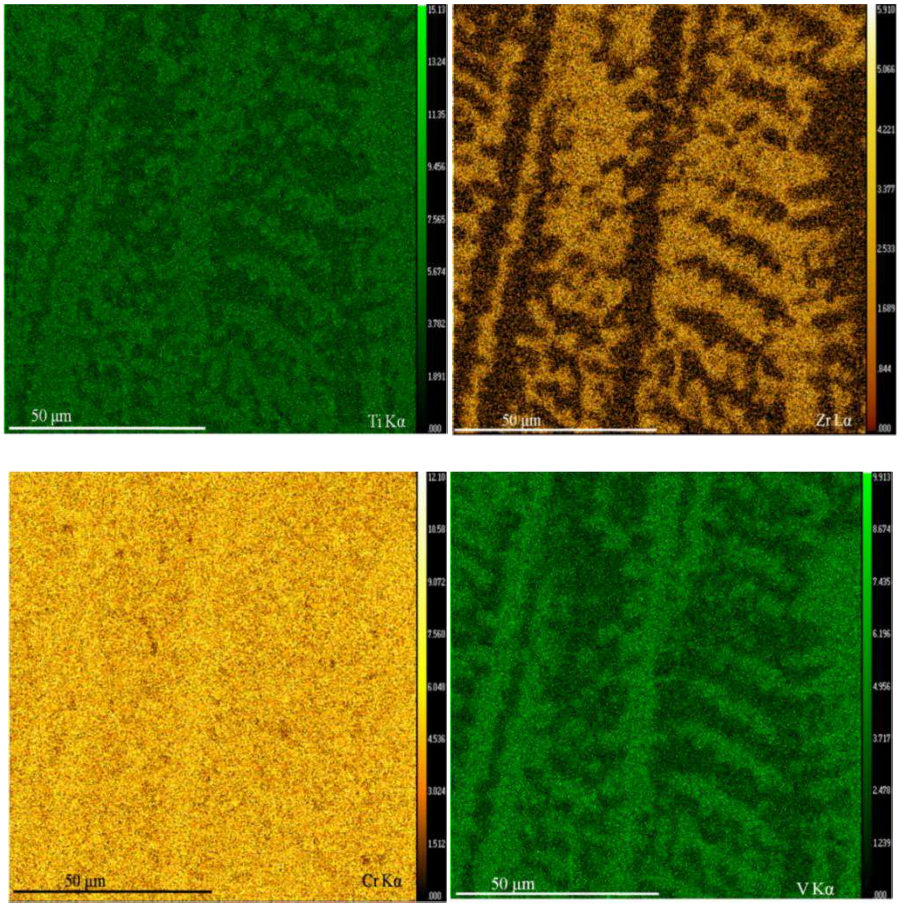

Fig. 5.3 *Elemental mapping of* $Ti_{0.43}Zr_{0.07}Cr_{0.25}V_{0.25}$ *alloy.*

5.2.1.3 Hydrogen storage properties

5.2.1.3.1 Thermodynamics

Fig. 5.4 (a) shows characteristic pressure composition absorption isotherms of the alloy measured at 298 K, 313 K, and 343 K, respectively. Three regions namely α, α+β, β are clearly visible in the absorption isotherms at 298 K. α phase corresponds to hydrogen atoms entering into the solid solution phase. As hydrogen concentration goes on increasing, hydride phase (β) formation takes place and remains in equilibrium with α phase. At the completion of β phase formation, hydrogen atoms redistribute into another solid solution phase and the hydrogen storage capacity get saturated. The equilibrium plateau pressure (P_{eq}) at each temperature is obtained from the midpoint of absorption isotherm plateau. It is difficult to determine P_{eq} from the absorption isotherms specially at elevated temperatures due to their sloping nature. The isotherm at 298 K shows an equilibrium hydrogen pressure of 0.12 bar. The absorption isotherms corresponding to higher temperatures show a remarkable decrease in plateau width and increase in steepness of the plateau. The plateau region in the characteristic PCI diagram corresponds to miscibility gap where partially immiscible α and β phases coexist. With increase in temperature mutual solubility of these two phases increases and the miscibility gap decreases. Hence, the absorption and desorption plateau become narrow and reversible hydrogen storage capacity decreases with increase in temperature. Apart from plateau width, another important parameter to elucidate the plateau performance of hydrogen absorption is sloping factor (S_f) which is commonly expressed as,

$$S_f = \frac{d(\ln P)}{d(H/M)} \tag{5.1}$$

S_f reflects the steepness of the plateau. The calculated S_f values along with P_{eq} and maximum storage capacities (C_{max}) at different temperatures are listed in Table 5.2. Gradually increasing S_f values at elevated temperatures indicate that hydrogen absorption performance deteriorates with temperature.

The heat of hydride formation (△H) and entropy change (△S) of the alloy can be measured using absorption isotherms at different temperatures according to Van't Hoff equation at thermodynamic equilibrium.

$$\ln P_{eq} = -{}^{\Delta H}/_{RT} + {}^{\Delta S}/_{R} \tag{5.2}$$

where, T is the absolute temperature, R is the gas constant, P_{eq} is the equilibrium pressure. Van't Hoff plot of $\ln P_{eq}$ vs. $1000/T$ for hydrogen absorption are displayed in Fig. 5.4 (b).

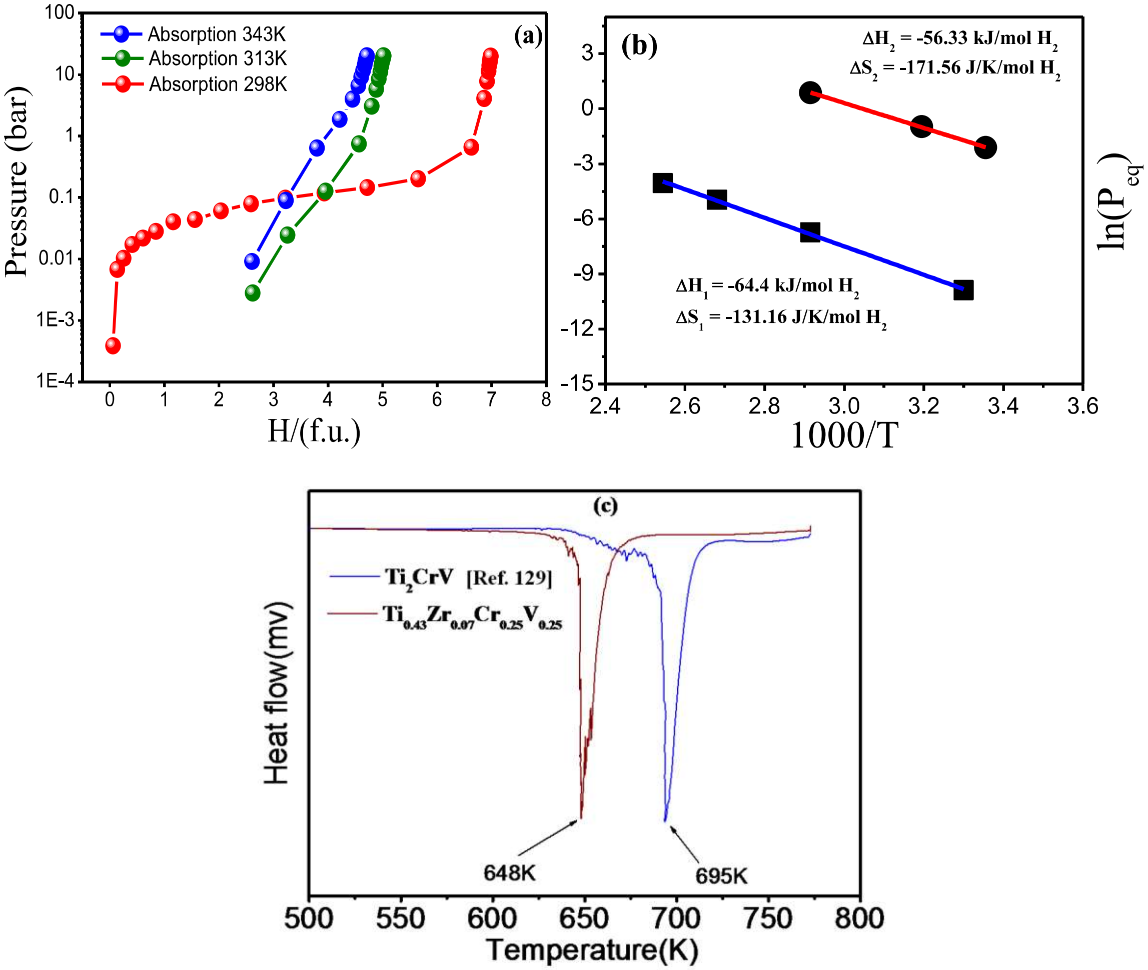

Fig. 5.4 *Hydrogen absorption isotherms (a), Van't Hoff plot (b) and DSC profile (c) of* $Ti_{0.43}Zr_{0.07}Cr_{0.25}V_{0.25}$ *alloy. The DSC profile of* Ti_2CrV *hydride is also given as reference in Fig. 5.4(c).*

ΔH and ΔS values derived from slope and intercept of Van't Hoff plot are listed in Table 5.2. These values are in good agreement with ΔH and ΔS values obtained by Bibienne et al. [294]. Value of ΔH for hydrogenation for unsubstituted Ti_2CrV alloy is found to be -64.4 kJ/mol H_2 whereas that of $Ti_{0.43}Zr_{0.07}Cr_{0.25}V_{0.25}$ is -56.33 kJ/mol H_2. This indicates that Zr substitution makes the hydride unstable which is also reflected as remarkably lower value of desorption temperature for $Ti_{0.43}Zr_{0.07}Cr_{0.25}V_{0.25}$ alloy compared to the parent one. Desorption peaks for hydrides of $Ti_{0.43}Zr_{0.07}Cr_{0.25}V_{0.25}$ and Ti_2CrV are found to be 648 K and 695 K, respectively as can be seen from Fig. 5.4 (c). Kumar et al. [129] have found an equilibrium plateau pressure less than 0.02 atm for hydride of Ti_2CrV alloy at room temperature. Comparatively higher plateau pressure was found for $Ti_{0.43}Zr_{0.07}Cr_{0.25}V_{0.25}$ alloy (see Fig. 5.4 (a)). Thus Zr incorporation makes hydride decomposition easier and increases the plateau pressure about 5 times.

Table 5.2 *The hydrogen storage characteristics of* $Ti_{0.43}Zr_{0.07}Cr_{0.25}V_{0.25}$ *alloy.*

Temperature (K)	P_{eq}(bar)	C_{max} (H/f.u.)	C_{max} (wt%)	S_f	ΔH (kJ/mol H_2)	ΔS (J/K/mol H_2)
298	0.12	6.98	3.19	0.39	-56.33	-171.56
313	0.376	5.01	2.31	0.52		
343	2.39	4.71	2.18	0.66		

5.2.1.3.2 Cycling Test

Hydrogen storage materials generally tend to degrade when subjected to repeated hydrogen absorption desorption cycles [295-297]. The measurement of absorption-desorption cycles for the alloy shows that hydrogen storage capacity of the alloy decreases by ~ 20% from its initially activated level upon 15 cycling as can be seen from Fig. 5.5.

Edalati et al. [298] have mentioned formation of lattice defects such as dislocations in the hydride of Ti-V based systems after 1st hydrogenation cycle. Nakamura et al. [299] suggested that these defective sites can't absorb hydrogen reversibly. Zhou et al. [300] have also considered that irreversible hydride phase is mainly responsible for hydrogen storage capacity loss in successive cycles. The hydrogen storage capacity after nth cycle [301] is defined as:

$$C(n) = \mathrm{C}(0)\exp(-\mathrm{k_d}n) \tag{5.3}$$

where, $\mathrm{C}(0)$ is the hydrogen storage capacity after one absorption-desorption cycle and $\mathrm{k_d}$ represents degradation rate of the hydride during cycling. Value of $\mathrm{k_d}$ depends on nature of the alloy as well as on hydriding-dehydriding conditions.

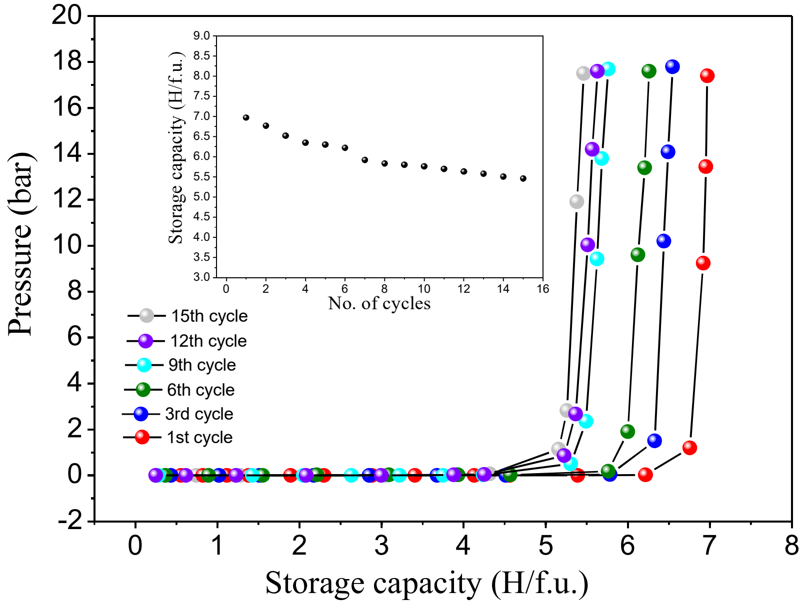

Fig. 5.5 *H_2 absorption isotherms (at 298 K) of $Ti_{0.43}Zr_{0.07}Cr_{0.25}V_{0.25}$ alloy at different cycles. The inset shows variation of storage capacity as a function of cycling number at 298 K.*

The degradation rate of alloy is calculated as 0.019 from equation (5.3) whereas that of the parent alloy [129] is 0.0296 indicating better cyclic stability of Zr substituted alloy [only 10 cycles were considered for calculation of degradation rate] compared to the parent one. All hydride-forming metals in Ti-Cr-V based alloys are susceptible to oxide formation even in presence of low level of oxygen and this is one of the main reasons for deterioration of hydrogen absorbing capacity [302, 303]. Upon hydrogen absorption-desorption cycles, the alloy is pulverized into small particles as discussed in the next paragraph and hence probability of oxide formation enhances. Zr is a better oxygen getter compared to Ti. Hence, Zr preferably reacts with oxygen and hydrogen absorption by Ti rich BCC phase (main hydrogen absorbing phase in $Ti_{0.43}Zr_{0.07}Cr_{0.25}V_{0.25}$ alloy) remains almost unaffected from oxygen poisoning. Thus, Zr substitution improves the cycle life of Ti_2CrV alloy. XRD patterns of the alloy hydrides after 1st and 15th cycle are displayed in Fig. 5.6.

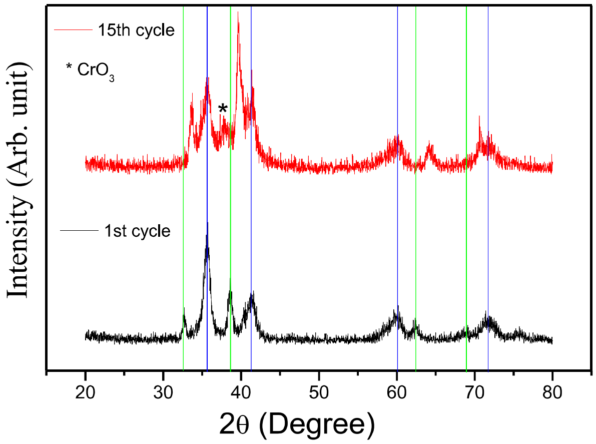

Fig. 5.6 *XRD patterns for the hydrides of $Ti_{0.43}Zr_{0.07}Cr_{0.25}V_{0.25}$ alloy after 1st and 15th cycles (vertical blue and green lines correspond to FCC and C15 Laves phase, respectively).*

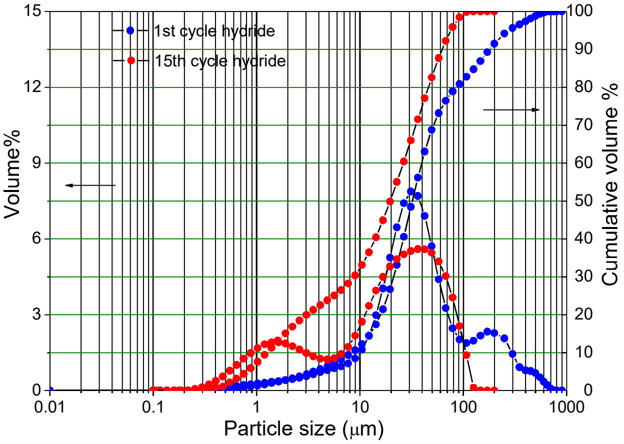

Fig. 5.7 *Particle size distribution for hydrides of $Ti_{0.43}Zr_{0.07}Cr_{0.25}V_{0.25}$ alloy after 1st and 15th cycles.*

The lattice parameters and cell volumes of the hydrides determined from XRD patterns are listed in Table 5.1. Upon hydrogenation the BCC phase has been converted into FCC phase whereas the secondary Laves phase has undergone both phase change and volume expansion. After 15th cycle, cell volume of matrix remains almost same as that of 1st cycled hydride whereas the hydrogen content of secondary phase is relatively less. This is clearly visible from the corresponding peak shift towards higher 2θ angle. Loss of attached hydrogen from secondary phase in consecutive hydrogen absorption-desorption cycles is also responsible for decrease in storage capacity after 15cycles. Fig. 5.6 shows generation of extra phase for 15th cycled hydride. The extra phase can be assigned as TiH_x ($TiH_{0.71}$, PCPDF 40-0980; β-Ti, PCPDF 44-1288) where $0<x<0.71$. Bulyk et al. [304] have reported hydrogen induced Cr phase separation in Ti containing $ZrCr_2$ intermetallic compound. There is also possibility of oxide phase (CrO_3) [PCPDF 77-0125] formation from the segregated Cr in the 15th cycled hydride.

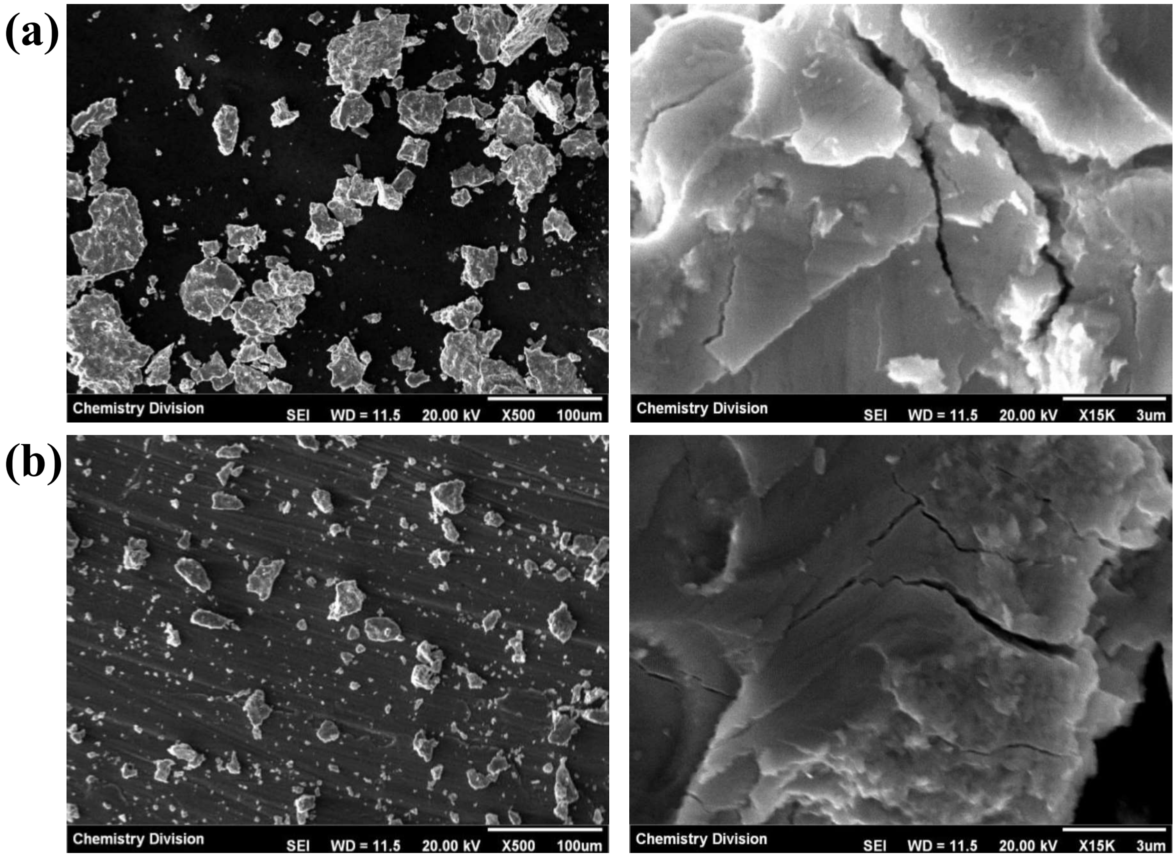

Fig. 5.8 *SEM images of $Ti_{0.43}Zr_{0.07}Cr_{0.25}V_{0.25}$ alloy hydride after (a) 1st cycle and (b) 15th cycle recorded at 500x and 15000x magnifications.*

Particle size distribution of $Ti_{0.43}Zr_{0.07}Cr_{0.25}V_{0.25}$ alloy hydride after 1st and 15th cycles are depicted in Fig. 5.7. After 1st hydriding dehydriding cycle most of the hydride particles are in the size range of 15-65 μm with less fraction of particles having mean size around 170 μm. After 15th cycle the particle sizes are distributed over two ranges with mean peaks around 1.5 μm and 34 μm. SEM micrographs of 1st cycled and 15th cycled hydrides as shown in Fig. 5.8 further confirm the decrease in particle sizes on successive hydriding dehydriding cycles. Fig. 5.8 clearly shows some visible cracks on the surface of both the hydrides. These cracks are generated due to volume expansion of alloy lattice on hydrogenation and consecutive lattice shrinkage during hydrogen desorption. The pulverization process breaks the alloy into small particles and continues over repeated cycles [305].

5.2.1.3.3 Kinetics

Fig. 5.9 shows hydrogenation curves (i.e., the reacted fraction as a function of time) of $Ti_{0.43}Zr_{0.07}Cr_{0.25}V_{0.25}$ alloy measured at 298 K, 373 K, and 473 K under isothermal conditions.

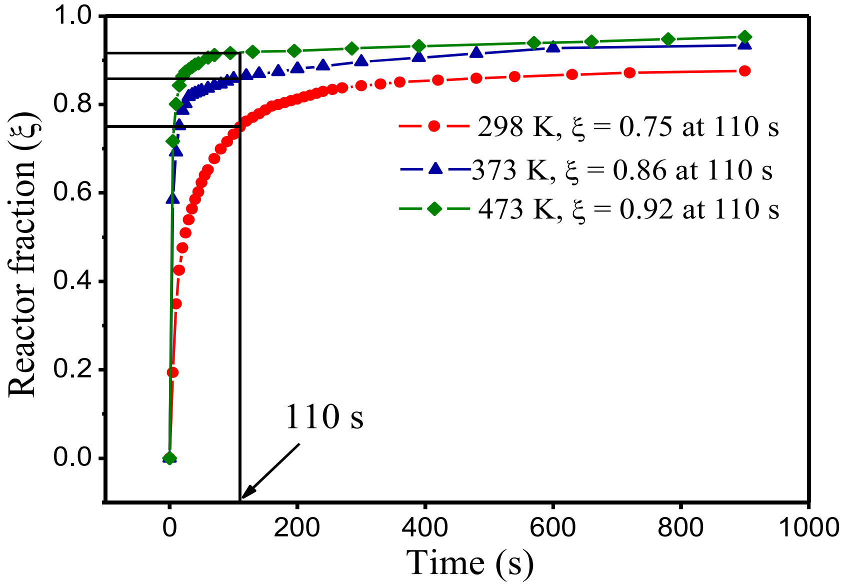

Fig. 5.9 *Hydrogen absorption kinetics of* $Ti_{0.43}Zr_{0.07}Cr_{0.25}V_{0.25}$ *alloy at different temperatures.*

The higher hydrogenation rate in the initial stage can be attributed to the higher driving force due to large difference between the initial pressure and the equilibrium pressure in the beginning. After the initial stage, the reaction becomes relatively slower. Absorption kinetics behavior observed at higher temperatures (373 K and 473 K) is essentially similar to that observed at 298 K, but the initial reaction rate was faster and the time period until saturation was reduced at higher temperatures. As shown in Fig. 5.9, the reacted fraction ζ reached 0.75 within 110 s at 298K while during the same time it reached 0.86 and 0.92 at 373 K and 473 K, respectively. With increase in temperature, the movement of hydrogen atoms will be accelerated, hydrogen absorption will be faster; as a result the time required for the saturation of reaction will be reduced remarkably.

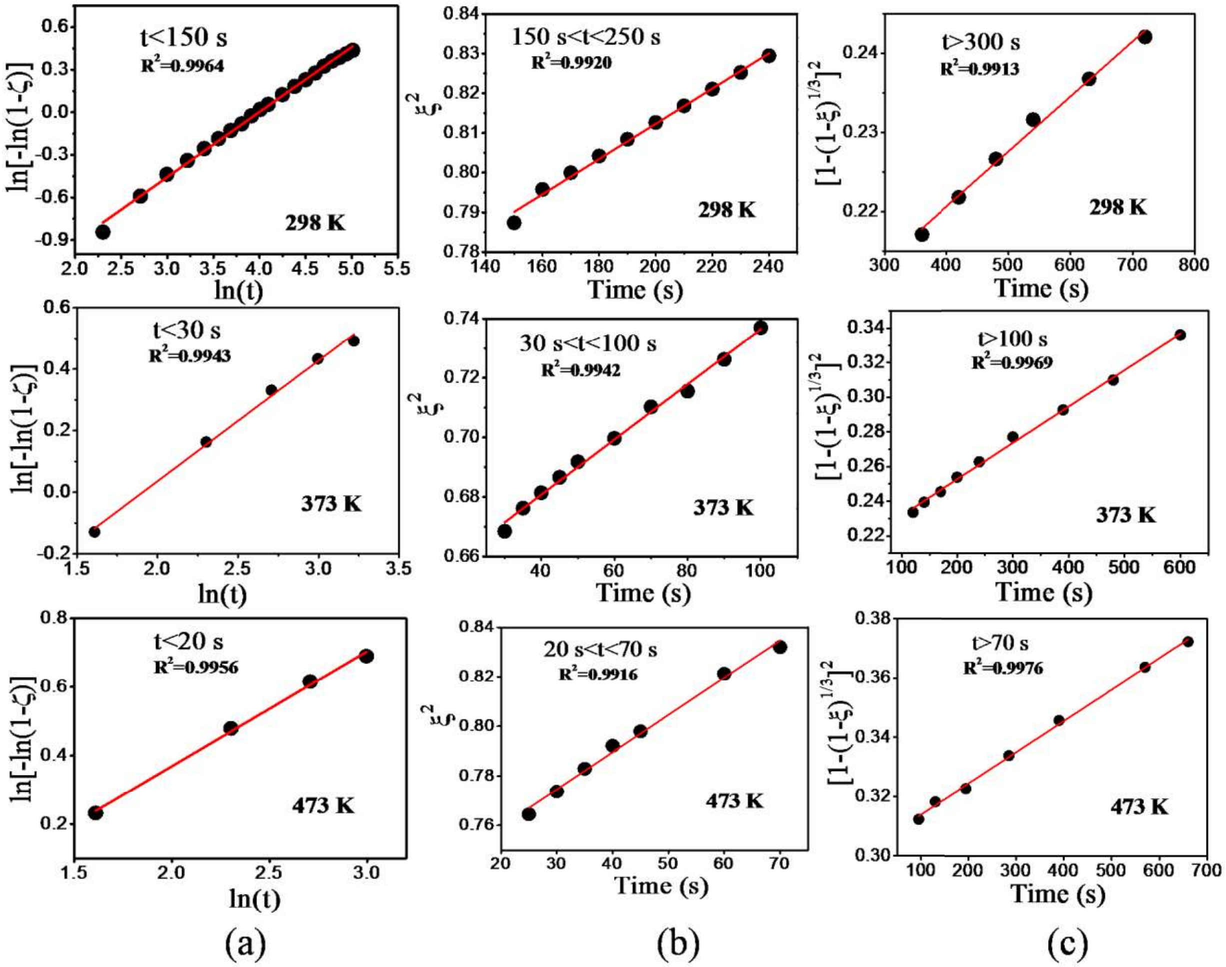

Fig. 5.10 *Fitting of hydrogen absorption kinetics of* $Ti_{0.43}Zr_{0.07}Cr_{0.25}V_{0.25}$ *alloy at three stages (a) nucleation and growth (b) 1D diffusion and (c) 3D diffusion.*

Further, it is interesting to know the underlying mechanism of hydrogen absorption reaction of $Ti_{0.43}Zr_{0.07}Cr_{0.25}V_{0.25}$ alloy. In the subsequent text, relationship between ζ and t for $Ti_{0.45}Zr_{0.05}Cr_{0.25}V_{0.25}$ alloy is modeled by fitting the kinetics data with different rate equations. The kinetics data for the initial stage at all three experimental temperatures (298 K, 373 K and 473 K) is found to fit extremely well with KJMA model (see Fig. 5.10). The corresponding R^2 values of the linear regression equations are found to be close to 1.The results, thus, indicate that alloy-hydrogen reaction predominantly proceeds through nucleation and growth mechanism for the initial absorption period. However, the kinetics data after initial stage cannot be fitted by this model, rather they can be fitted satisfactorily using 1D diffusion and 3D Jander diffusion models. The rate constants along with the best fitting kinetic models have been represented in Table 5.3.

Table 5.3 *Rate constants at different temperatures for* $Ti_{0.43}Zr_{0.07}Cr_{0.25}V_{0.25}$ *alloy.*

Stages	Best fitting kinetic model	Temperature (K)	Rate constant (k)
1	$\ln(-\ln(1-\xi)) = n\ln k + n\ln t$	298	0.0184
		373	0.1485
		473	0.4081
2	$\xi^2 = kt$	298	4.44×10^{-4}
		373	9.22×10^{-4}
		473	1.5×10^{-3}
3	$[1-(1-\xi)^{1/3}]^2 = kt$	298	6.94×10^{-5}
		373	1.05×10^{-4}
		473	2.14×10^{-4}

From the model fitting it is very clear that the rate-controlling step shifts from nucleation and growth towards diffusion with progress of reaction. The variation from 1D to 3D diffusion mechanism is due to continuous change in geometry resulting from the progress of reaction. Using the best fitting models, the rate constants k have been determined at three different temperatures for three different hydriding stages. Associated activation energies have been calculated using Arrhenius equation. Activation energies of hydrogen absorption for

$Ti_{0.43}Zr_{0.07}Cr_{0.25}V_{0.25}$ alloy are found to be 20.91 kJ/mol, 8.18 kJ/mol and 7.46 kJ/mol for nucleation and growth, 1D diffusion and 3D diffusion controlled stages, respectively.

5.2.1.4 Summary

From the pressure composition absorption isotherms, the fundamental thermodynamic parameters for hydride formation have been evaluated. Stability of the hydride is remarkably less compared to the hydride of unsubstituted alloy Ti_2CrV. The nature of pressure composition absorption isotherms does not change even after 15 hydriding-dehydriding cycles. Zr substituted alloy shows better cyclic performance compared to its parent alloy. $Ti_{0.43}Zr_{0.07}Cr_{0.25}V_{0.25}$ alloy in the present study shows a maximum hydrogen storage capacity of 3.19 wt.% at 20 bar and 298K. The alloy reaches 3/4th of the reacted fraction within less than 2 minutes at 298K. Thus, this alloy seems to be a promising hydrogen storage material with improved desorption behavior, better cyclic performance and fast enough sorption kinetics.

5.2.2 Effect of composite formation on hydrogen storage properties of Ti_2CrV alloy

A series of composites of Ti_2CrV alloy with $ZrFe_{1.8}V_{0.2}$ Laves phase were prepared and subjected to XRD, EPMA and hydrogen absorption-desorption studies to address the following issues:

(1) effect of $ZrFe_{1.8}V_{0.2}$ Laves phase on crystal and microstructure of Ti_2CrV alloy

(2) effect of composite formation on hydrogen storage capacity of Ti_2CrV alloy

(3) effect of $ZrFe_{1.8}V_{0.2}$ Laves phase on characteristic plateau pressure of Ti_2CrV alloy

(4) detailed kinetic analysis of most suitable materials and determination of the effect of secondary phase on rate constants of different stages, and most importantly

(5) effect of Laves phase on *in-situ* hydrogen desorption temperature of Ti_2CrV alloy.

The systems studied are:Ti_2CrV alloy, Ti_2CrV + 5% $ZrFe_{1.8}V_{0.2}$(composite-1), Ti_2CrV + 10% $ZrFe_{1.8}V_{0.2}$ (composite-2) and Ti_2CrV + 20% $ZrFe_{1.8}V_{0.2}$ (composite-3).

5.2.2.1 X-ray diffraction study

XRD patterns of annealed Ti_2CrV alloy, composite-1, composite-2 and composite-3 are illustrated in Fig. 5.11.

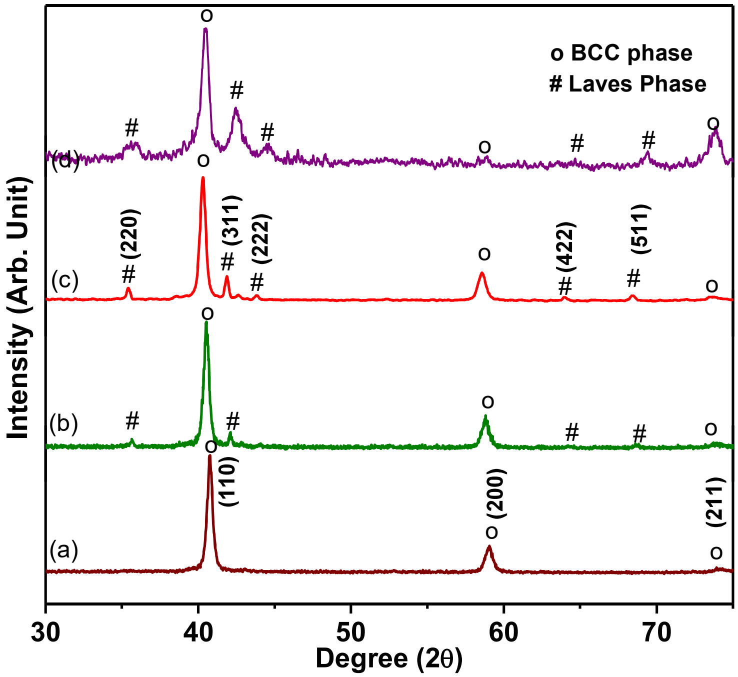

Fig. 5.11 *X-ray diffraction profiles of Ti_2CrV (a), $Ti_2CrV+5\%ZrFe_{1.8}V_{0.2}$ (b), $Ti_2CrV+10\%ZrFe_{1.8}V_{0.2}$ (c), and $Ti_2CrV+20\%ZrFe_{1.8}V_{0.2}$ (d).*

Annealed Ti_2CrV forms pure body centered cubic (BCC) solid solution with a lattice parameter of 3.127 Å, which is in line with our earlier study [306]. Small change in lattice parameter may be due to annealing treatment of the sample. For composite-1 XRD pattern clearly indicates the existence of two phases. Along with main BCC phase (marked by ‘o’), peaks due to C15 Laves phase (space group Fd3m) can be easily resolved, which indicates that both BCC phase as well as the C15 phase retain their identity after composite formation. The peaks corresponding to the secondary phase has been identified and marked by ‘#’ in Fig. 5.11.

Lattice parameter of the main BCC phase of composite-1 is found be 3.129 Å. It can be noted that the lattice parameter changes only slightly after addition of secondary phase in composite-1. The lattice parameter of the BCC phase of composite-2 and composite-3 is found to be 3.140 and 3.156 Å, respectively. Increase in peak intensity corresponding to $ZrFe_2$ Laves phase in composite-3 compared to composite-1 and composite-2 is as expected. In composite-2 and composite-3 the secondary phase shows lattice parameter of 7.04 and 7.08 Å, respectively. It can be noted that along with increase in concentration of the secondary phase, there is small but systematic increase in the cell parameter of the BCC phase. Concentration of the secondary phase and changes in cell parameters is expected to affect hydrogen storage performances.

5.2.2.2 Microstructure

Representative back scattered electron (BSE) images of annealed Ti_2CrV alloy and its composite with $ZrFe_{1.8}V_{0.2}$ are presented in Fig. 5.12.

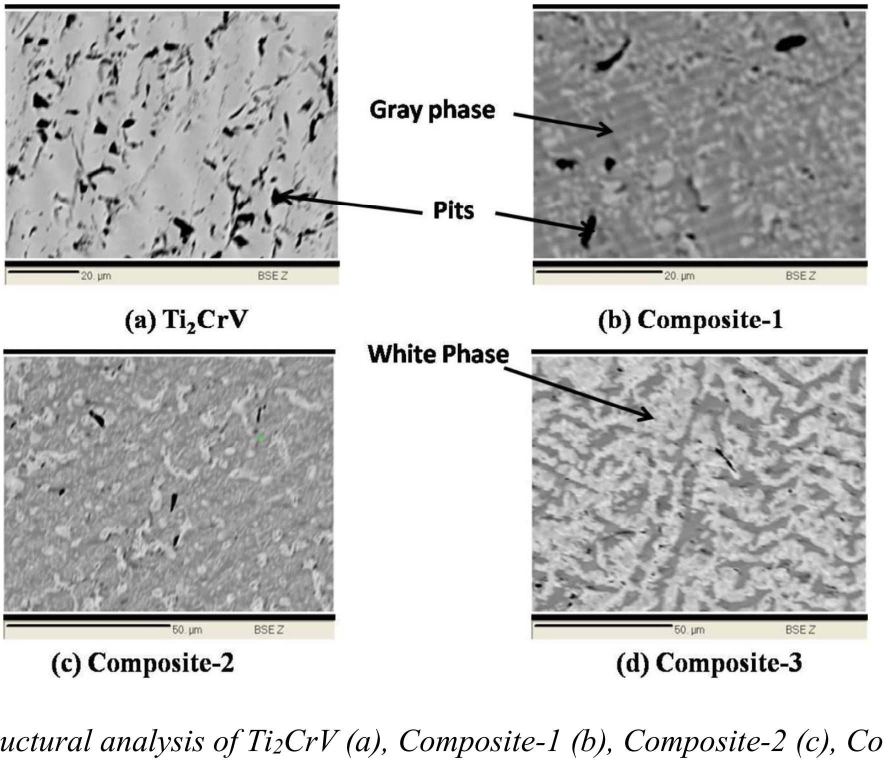

Fig. 5.12 *Microstructural analysis of Ti_2CrV (a), Composite-1 (b), Composite-2 (c), Composite-3 (d)*

Ti_2CrV shows single phase structure [Fig. 5.12 (a)] with no definite phase separation. Black colored phases are nothing but polishing pits present on the surface. Average chemical compositions of the matrix determined by Wave length Dispersed Spectrometer (WDS) are shown in Table 5.4. For all samples, the data were taken at four/five different locations. For Ti_2CrV alloy it can be seen that the elements are almost homogeneously distributed in the alloy. Average elemental abundance matches well with the expected ones.

Table 5.4 *Chemical compositions of* Ti_2CrV *and the composites (mass %).*

Alloy	Ti_2CrV	Composite-1		Composite-2		Composite-3	
Precipitate colour	Gray	Gray	White	Gray	White	Gray	White
Ti	52.08	53.90	33.82	55.34	39.26	57.61	36.02
Cr	24.28	19.44	40.71	16.19	28.29	13.52	19.08
V	23.64	24.29	16.71	25.00	16.12	22.27	23.15
Fe	-	1.93	4.50	2.94	8.22	5.46	12.37
Zr	-	0.49	4.35	0.52	8.11	1.14	9.38

BSE image of composite-1 shows presence of small isolated white phases distributed within gray matrix. In BSE image intensity of back-scattering electron is proportional to atomic number of individual elements in the illuminated area. So it is quite obvious that the darker area (gray) indicates Zr depleted phase, whereas the white portion indicates Zr rich phase. For the composites, elemental composition has been studied repeatedly both in white and gray phases and average values are presented in Table 5.4.

The data indicates that gray phase is mostly consisting of Ti, whereas the white phase largely consists of Zr. Other elements, such as Fe, Cr and V are more or less homogeneously distributed within the two phases in the composite. With increase in concentration of $ZrFe_{1.8}V_{0.2}$

phase microstructure of white phase changes. In composite-2, due to larger area white-colored region (increased extent of Zr-rich phase), there can be segregation of phase giving rise to laminar structure. In the BSE profile, one can see that the white phases are distributed in gray matrix both in rod-like laminar shape with length in the range of 5-30 mm, and in smaller domains. In composite-3, with further increase in concentration of Zr-rich phase, its morphology changes to dendrite structure. So a comparison of white phases in composite-1, -2 and -3 clearly indicates that there is an increase in volume of the white phase as well as degree of networking, which is consistent with the results from XRD studies.

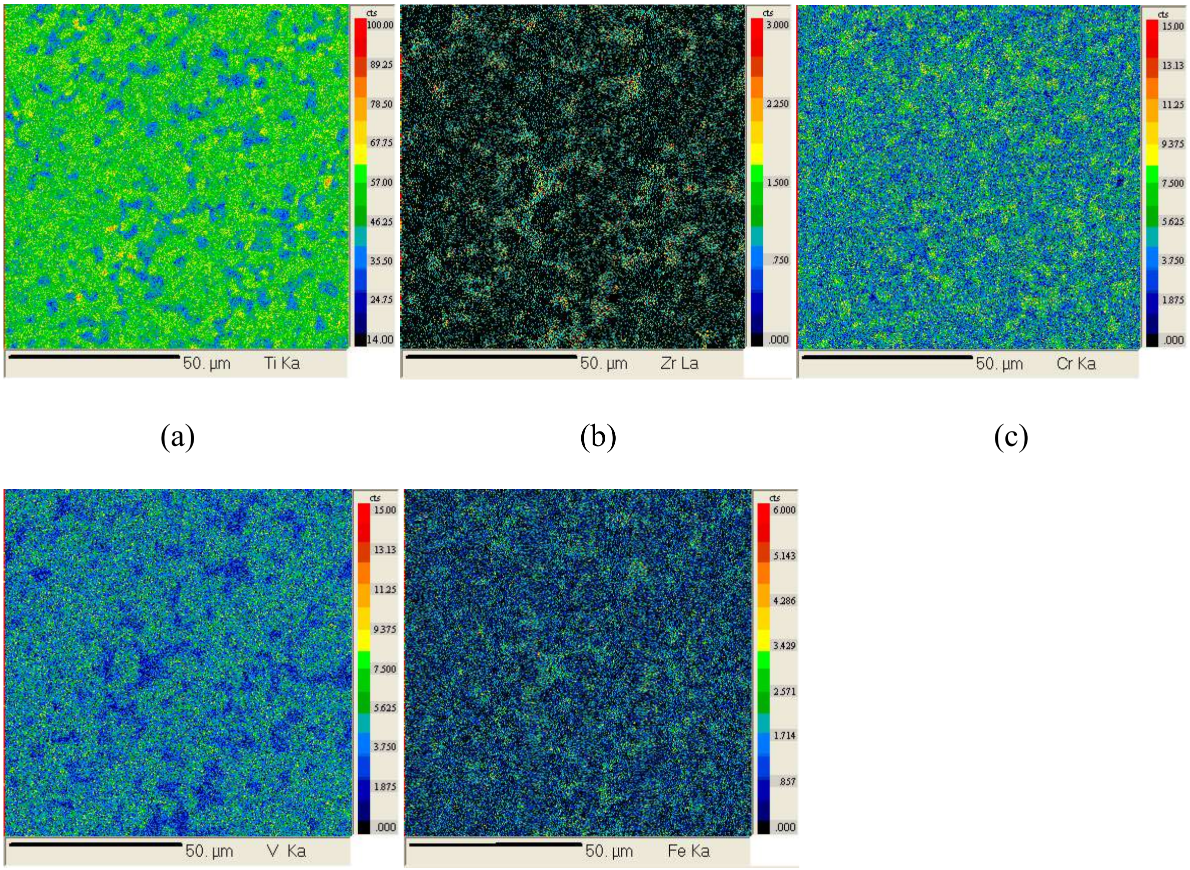

(a) (b) (c)

(d) (e)

Fig. 5.13 *Elemental mapping of Composite-2.*

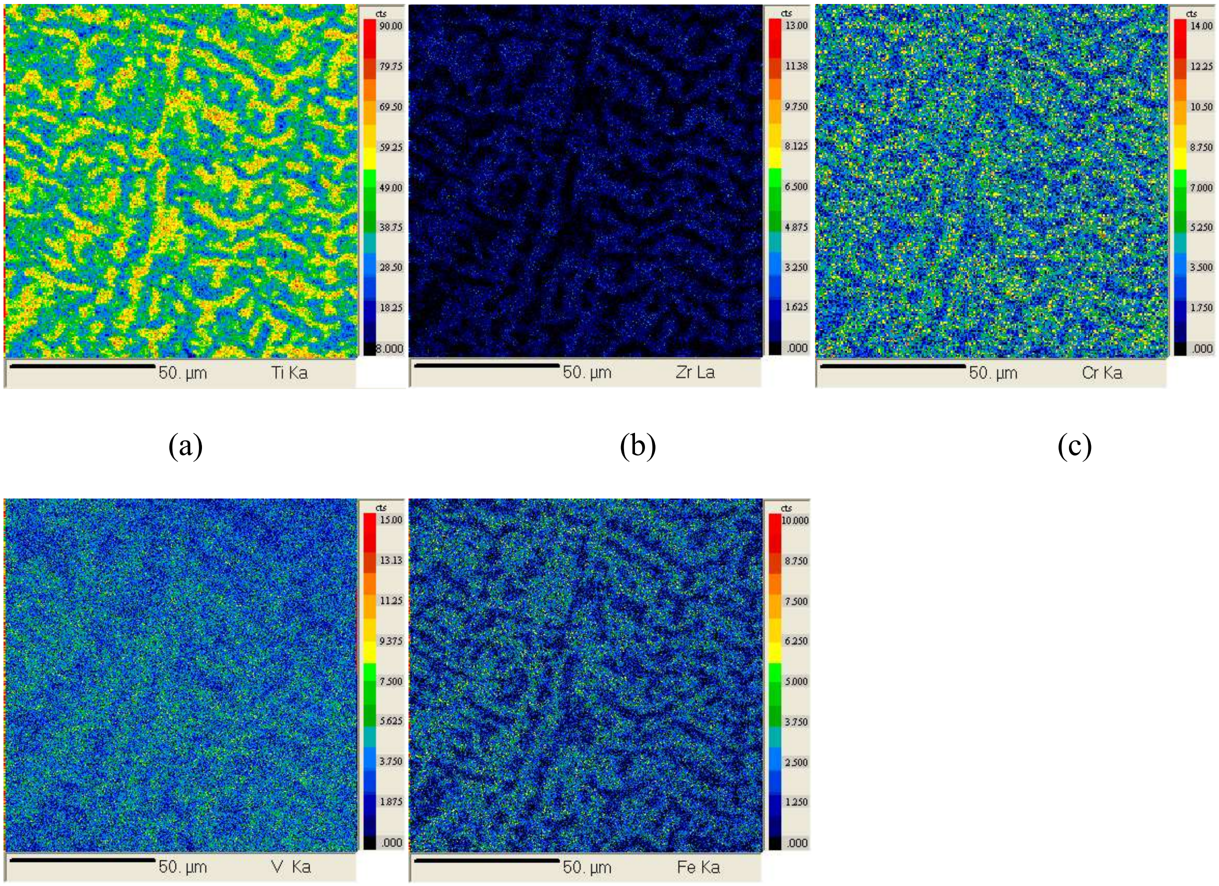

(a) (b) (c)

(d) (e)

Fig. 5.14 *Elemental mapping of Composite-3.*

The output from the proportional counter of a wavelength dispersive (WD) spectrometer can be used to construct an X-ray image of the sample showing spatial distribution of different elements in composite structures. Fig. 5.13 & 5.14 show representative spatial distribution of Ti, Zr, Cr, V and Fe atoms in the two phases of composite-2 and composite-3, respectively. The images clearly show that concentration of Ti atom is more in gray phase compared to white phase, though there is certain amount of Ti impurities in white phase also. On the other hand, the concentration of Zr is more in white phase, which is in line with the elemental analysis. There is almost homogeneous distribution of Cr and V metal in both the phases; whereas the white phase is rich in Fe. The results of the microstructural analysis indicate that, the gray phase is mainly Ti-

Cr-V based solid solution. On the other hand, white phase is Zr, Fe and V rich phase with Ti and Cr impurities. It is quite obvious that during arc melting and annealing treatment, there is diffusion of certain amount of metal atoms though thee grain boundaries, which gives rise to these types of impurities. It is also evident from CrK_{α} (Fig. 5.14(c)) image that the white phase contains higher Cr than the gray matrix. This indicates substantial amount of Cr and Ti have migrated from gray phase to the white phase. However, Zr remains within the white phase only. This may be due to higher atomic radius of Zr compared to Ti and Cr.

5.2.2.3 Hydrogen storage properties

5.2.2.3.1 Pressure composition isotherm

Pressure composition isotherms of annealed samples of Ti_2CrV alloy, composite-1, composite-2 and composite-3 are obtained to examine the effect of additional phase on plateau pressure and total hydrogen absorption capacity. In Fig. 5.15 the equilibrium pressures are plotted with respect to H/formula unit (H/M). Maximum hydrogen storage capacity of Ti_2CrV alloy is found to be 3.9 wt.% (H/M = 8.0), which is in line with our previous study [306]. In earlier report, we have got slightly higher hydrogen storage capacity (4.0 wt.%) at room temperature and 20 bar hydrogen pressure. The slight difference in hydrogen storage capacity may be due to lower pressure range studied here and the annealing treatment of the sample. As expected with increase in temperature the total hydrogen storage capacity decreases and the plateau pressure increases. Hydrogen absorption plateau at 303 K is found to be around 0.01 bar and it increases to 0.2, 0.8 and 2.1 bar at 343, 373 and 393 K, respectively. It can be seen from the pressure composition isotherms that the extent of hysteresis increases with increase in temperature. Hydrogen storage capacities are found to be 3.1 wt.% (H/M = 6.3), 2.8 wt.% (H/M = 5.7), 2.5 wt.% (H/M = 5.0) at 343, 373, and 393 K, respectively for Ti_2CrV.

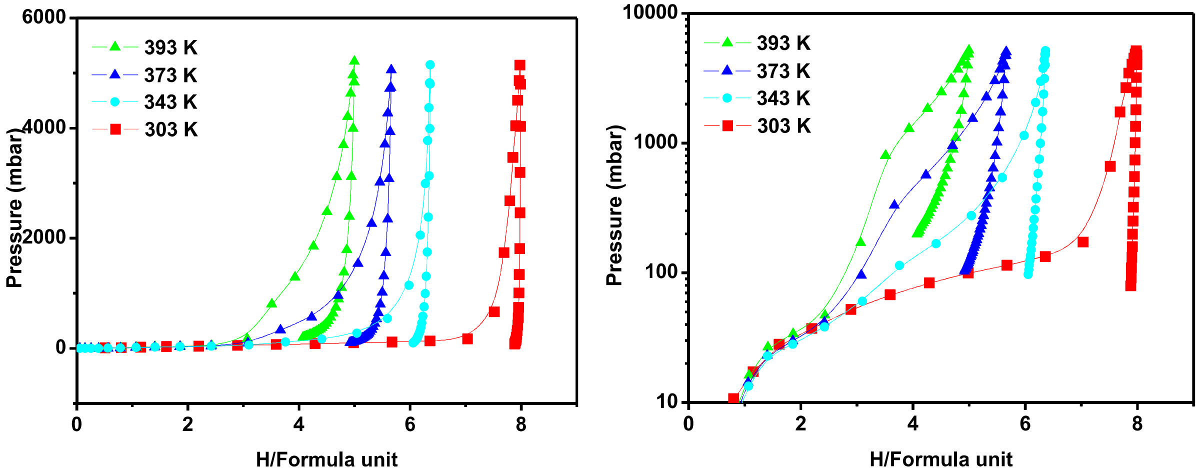
6000
4000
2000
0
Pressure (mbar)
0
2
4
6
8
H/Formula unit
393 K
373 K
343 K
303 K
10000
1000
100
10
Pressure (mbar)
H/Formula unit

(a)

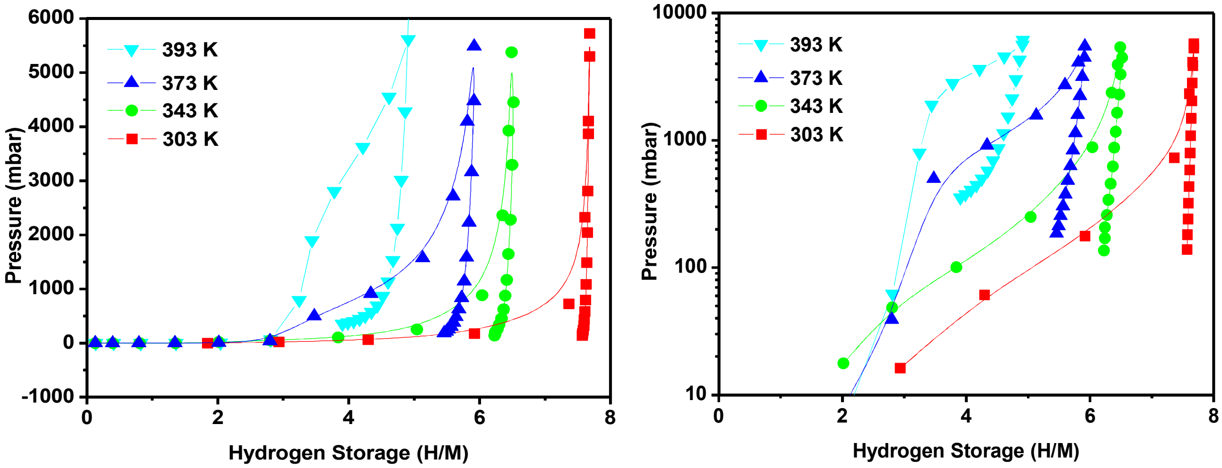
6000
5000
4000
3000
2000
1000
0
-1000
Pressure (mbar)
0
2
4
6
8
Hydrogen Storage (H/M)
393 K
373 K
343 K
303 K
10000
1000
100
10
Pressure (mbar)
Hydrogen Storage (H/M)

(b)

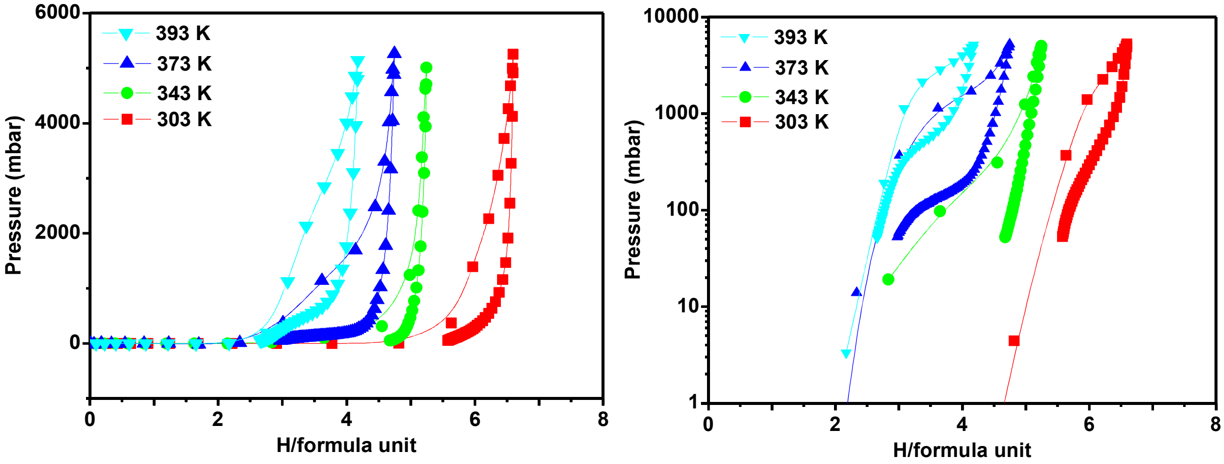
6000
4000
2000
0
Pressure (mbar)
0
2
4
6
8
H/formula unit
393 K
373 K
343 K
303 K
10000
1000
100
10
1
Pressure (mbar)
H/formula unit

(c)

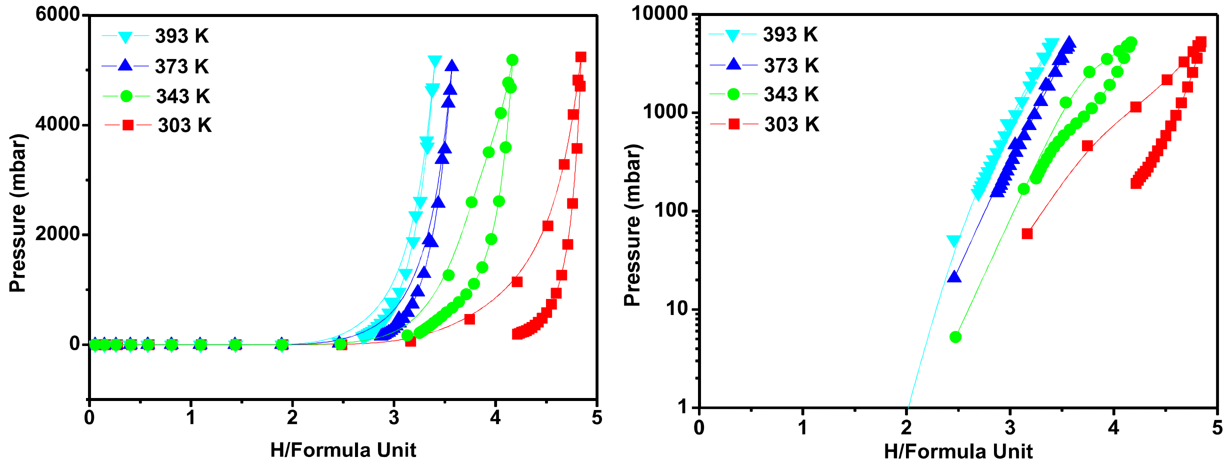

(d)

Fig. 5.15 *Pressure composition isotherm (PCI) of* Ti_2CrV *(a), Composite-1 (b), Composite-2 (c), and Composite-3 (d). Each PCI has been given both in linear scale and in log scale (y-axis) for better understanding of variation of hydrogen storage capacity and plateau pressure.*

Composite-1, composite-2 and composite-3 show hydrogen storage capacity of 3.7 wt.% (H/M = 7.7), 3.3 wt.% (H/M = 6.6), and 2.4 wt.% (H/M = 4.9), respectively, at room temperature and 5 bar hydrogen pressure (Table 5.5). This implies that total hydrogen storage capacity of Ti_2CrV alloy decreases after composite formation with $ZrFe_{1.8}V_{0.2}$ alloy. This is explained based on the fact that during composite formation individual atoms diffuse through phase boundary, as revealed by the EPMA study, leading to small changes in Ti and Cr concentrations in the BCC phase. This can affect both hydrogen storage capacity and thermodynamics significantly [275]. Again, due to addition of secondary phase the plateau pressure increases, so the amount of absorbed hydrogen decreases for a nominal pressure of 5 bar. It can be noted that composite-3 shows no plateau and hysteresis at 373 K and 393 K indicating that the plateau pressure is higher than 5 bar at these temperatures. From hydrogen storage data, it is apparent that due to vast decrease in the hydrogen storage capacity at room temperature, composite-3 is not suitable for hydrogen storage application. Further analyses on hydrogen absorption kinetics were done on composite-1 and composite-2.

Table 5.5 *Hydrogen storage capacities of Ti_2CrV alloy and the composites.*

Alloy	Temp(K)	Ti_2CrV	Composite-1	Composite-2	Composite-3
H/M	303	8.3	7.7	6.6	4.8
	343	6.4	6.5	5.2	4.2
	373	5.7	5.9	4.7	3.6
	393	5.0	4.8	4.1	3.4
Wt%	303	3.9	3.7	3.2	2.4
	343	3.1	3.2	2.6	2.0
	373	2.8	2.9	2.3	1.8
	393	2.5	2.4	2.0	1.7

5.2.2.3.2 Kinetic analysis

For composite-1 hydrogen absorption kinetics has been measured at 303, 373 and 423 K and the corresponding reacted fractions (α) are found to be 0.76, 0.90 and 0.97, within two minutes (Fig. 5.16). Generally during hydriding process, an induction period is encountered before hydrogen absorption due to the presence of surface oxides layers or adsorbed gas with alloys. Surface layers inhibit hydrogen absorption until there is a crack formation. For samples of present study, there is very less or no incubation period as the kinetics data has been taken after one hydriding-dehydriding cycle. In the process, the alloys get activated and oxide layers get dissolved into the alloy and this helps to obtain correct kinetics data. It can also be noted that hydrogen absorption rate of composite-2 is much faster than composite-1 and its corresponding α values are 0.97, 0.94, 0.92 and 0.89 at 303, 353, 373 and 423 K, respectively in 1 min [Fig. 5.17].

In the following section, the hydrogen absorption kinetics has been analyzed to get further details about hydrogen absorption mechanism of composite-1 and composite-2.

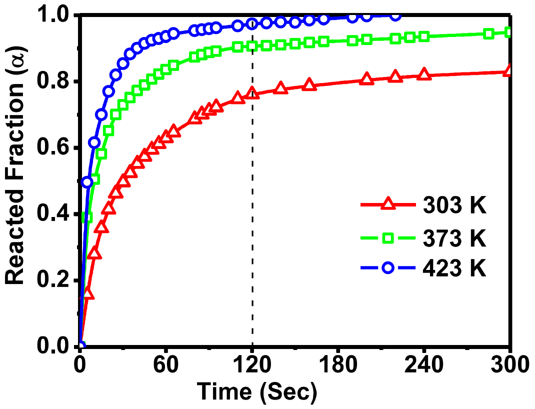

Fig. 5.16 *Hydrogen absorption kinetics of composite-1 at different temperatures.*

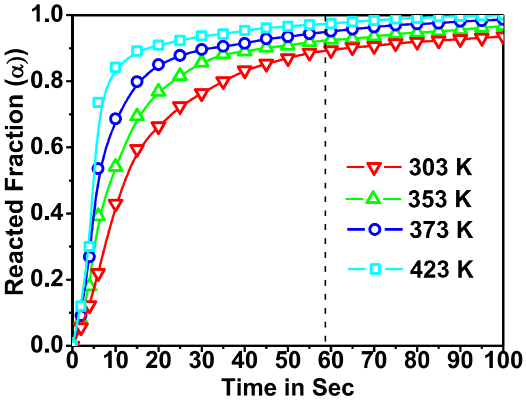

Fig. 5.17 *Hydrogen absorption kinetics of composite-2 at different temperatures.*

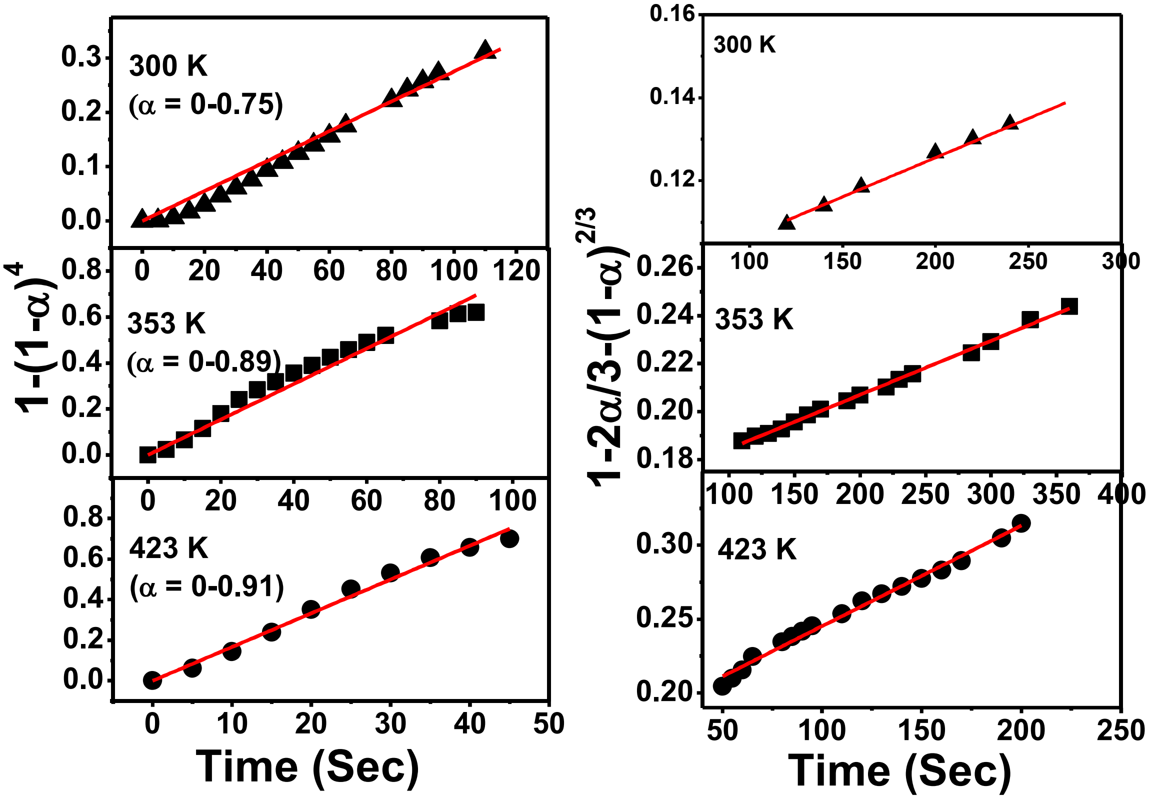

Fig. 5.18 *Hydrogen absorption kinetics of composite-1, Chemical reaction (a) & 3-D diffusion.*

For composite-1, total hydrogen absorption kinetics can be fitted with two different equations for two stages; the first is the hydrogen absorption stage, where chemical reaction occurs between hydrogen and composite-1, and second step is the hydrogen diffusion stage through the composite matrix. Mathematical expressions involved in these two steps are ($k_1t = 1-(1-\alpha)^4$) and ($k_2t = 1-2\alpha/3-(1-\alpha)^{2/3}$), respectively [Fig. 5.18]. Table 5.6 shows the mathematical expressions and rate constants of hydrogen absorption reaction at different stages and at different temperatures for composite-1. With increasing temperature, the rate constants increase for a single stage. At the same temperature, the rate constants follow the relation $k_1 > k_2$ at different stages. It indicates that the chemical reaction occurs in faster rate compared to 3D-diffusion.

Table 5.6 *Hydrogen absorption kinetic fitting parameters of composite-1.*

Fitting equation $kt = 1-(1-\alpha)^4$		
Temperature (°C)	Rate constant (k_1)	R^2
RT (α = 0-0.75)	0.0027	0.9937
60 (α = 0-0.89)	0.0077	0.9918
150 (α = 0-0.91)	0.0167	0.9962
Fitting equation ($kt=1-2\alpha/3-(1-\alpha)^{2/3}$)		
Temperature	Rate constant (k_2)	R^2
RT (α = 0.75-1.0)	1.89×10^{-4}	0.9898
60 (α = 0.89-1.0)	2.25×10^{-4}	0.9969
150 (α = 0.91-1.0)	6.81×10^{-4}	0.9893

For composite-2 also hydrogen absorption kinetics has been fitted [Fig. 5.19]. Here the initial hydrogen absorption is chemical reaction stage, but in this case hydrogen diffusion occurs in two different rates. Initially when the alloy concentration is higher, diffusion occurs at a faster rate compared to diffusion through hydride rich phase. So in this case, total hydrogen absorption mechanism has been alienated in three different stages. In initial chemical reaction stage, the reaction has been fitted with the equation (k_1t=1-(1-α)^4). The rate of chemical reaction stage found to be faster than composite-1 and as expected, the reaction rate increases with temperature. Two segments of hydrogen diffusion can be fitted with same rate expression [(k_2t=1-2α/3-(1-α)$^{2/3}$)] and the diffusion rate gets slower when the matrix becomes hydride rich as can be seen in Table 5.7. From the apparent rate constants of the reactions, it has been found that both chemical reaction and diffusion rate are faster for composite-2. The faster hydrogen absorption rate in composite-2 can be attributed to larger concentration of secondary phase, which introduces more grain boundaries. Despite the fact that there are differences in hydrogen absorption kinetics of composite-1 and composite-2, in both the cases the hydrogen absorption rate is quite satisfactory for practical application.

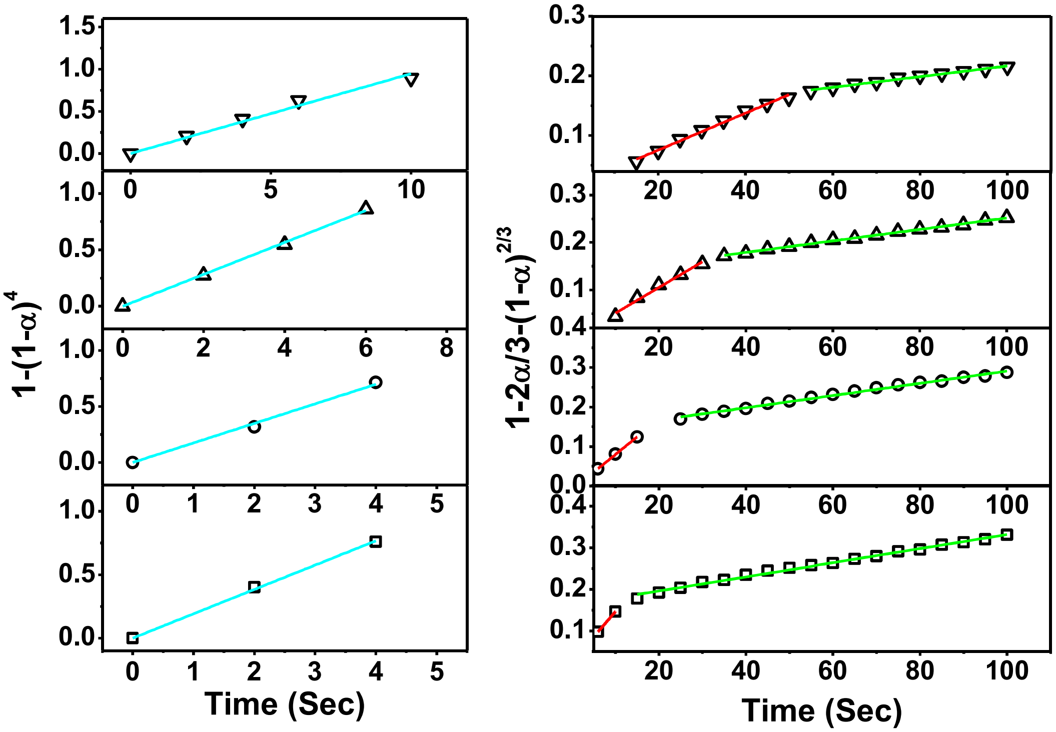

Fig. 5.19 *Hydrogen adsorption kinetics of composite-2, Chemical reaction (a) & 3-D diffusion.*

Table 5.7 *Hydrogen absorption kinetic fitting parameters of composite-2.*

Fitting equation $\mathbf{Kt = 1-(1-\alpha)^4}$

Temperature (ºC)	Rate constant (k_1)	R^2
RT (α = 0-0.4)	0.0946	0.993
80 (α = 0-0.4)	0.1415	0.999
100 (α = 0-0.4)	0.1747	0.996
150 (α = 0-0.4)	0.1920	0.999

Fitting equation $\mathbf{(kt=1-2\alpha/3-(1-\alpha)^{2/3})}$

Temperature (ºC)	Rate constant (k_2)	R^2
RT (α = 0.4-0.88)	0.0031	0.991
80 (α = 0.4-0.88)	0.0054	0.979
100 (α = 0.4-0.88)	0.0089	0.999
150 (α = 0.4-0.88)	0.0122	0.992

Fitting equation $\mathbf{(kt=1-2\alpha/3-(1-\alpha)^{2/3})}$

Temperature (ºC)	Rate constant (k_3)	R^2
RT (α = 0.88-1.0)	$8.9X10^{-4}$	0.989
80 (α = 0.88-1.0)	0.00121	0.995
100 (α = 0.88-1.0)	0.00155	0.992
150 (α = 0.88-1.0)	0.01218	0.996

5.2.2.3.3 Temperature programmed desorption

Temperature programmed desorption has been studied *in-situ* without exposing samples in air atmosphere to compare desorption behavior of different hydrides. In-situ desorption can give a better understanding about stability of hydride. The experiment was carried out at a positive pressure (1.2 bar) of carrier gas (helium) up to 500 K at a heating rate of 5 K/min. Gas outflow rate was measured with respect to temperature with a mass flow controller and the results have been presented in Fig. 5.20.

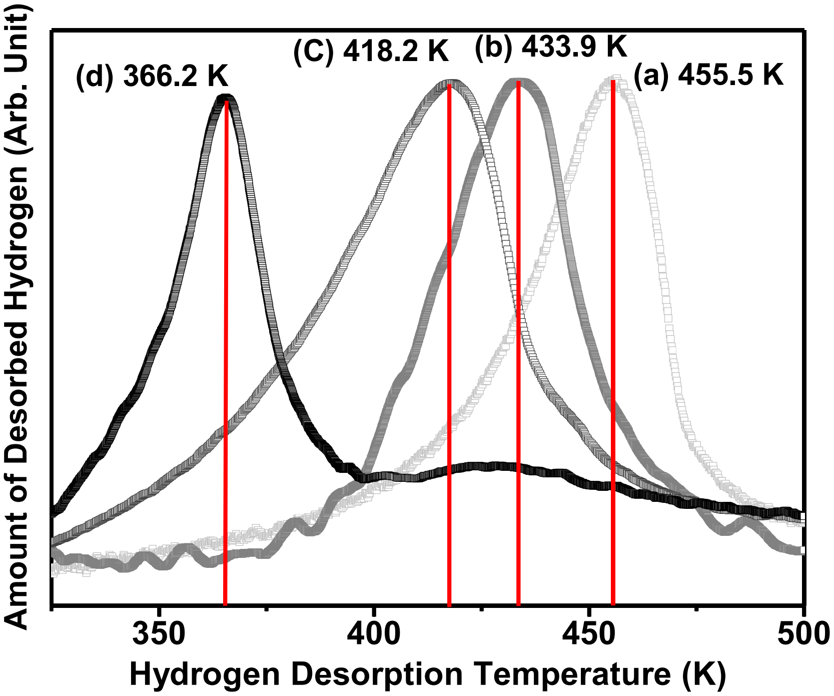

Fig. 5.20 *In-situ temperature programmed desorption profile of* Ti_2CrV *(a), Composite-1 (b), Composite-2 (c), Composite-3 (d).*

For Ti_2CrV alloy, hydrogen desorption starts around 300 K and found to have desorption peak at 455.5 K. By fitting the peak using Gaussian distribution function, the FWHM is found to be 39.3 K. In composite-1, as expected, desorption peak temperature comes down at 433.9 K though the peak becomes broader than Ti_2CrV sample with a FWHM of 42.10 K. Due to presence of higher concentration of additional phase, desorption profile of composite-2 is very broad. Hydrogen desorption starts from 313 K and the peak temperature is found to be at 418.2 K with FWHM = 54.86 K for composite -2. It is obvious that in presence of additional phase, inhomogeneous desorption sites are created in the sample leading to broadening of desorption peak. With further increase in Zr-rich phase concentration in composite -3, due to phase segregation (as already seen in EPMA), nature of desorption profile is found to be different. Here in fact two desorption peaks can be identified. Major low temperature desorption peak is found to be at 366.2 K with FWHM = 35.53 K, whereas another broad high temperature desorption peak can be found around 425 K. So from the above study it is apparent that composite-1 is the most suitable material for hydrogen storage application due to its good hydrogen storage properties and better hydrogen desorption behavior.

5.2.2.4 Summary

In this study, Ti_2CrV alloy and its composite with different concentrations of $ZrFe_{1.8}V_{0.2}$ alloy were prepared by two stage arc melting route. Microstructure analysis shows coexistence of two phases in all the composites. With increase in concentration of $ZrFe_{1.8}V_{0.2}$ alloy, morphology of Zr rich phase changes from dots to laminar to dendrites. Hydrogen storage capacity and the plateau pressure are found to be largely dependent on concentration of Zr rich phase. As the secondary phase concentration increases, hydrogen storage capacity decreases and the plateau pressure increases. With increase in concentration of Zr-rich phase, corresponding hydrides become more destabilized. Among the studied composites, Ti_2CrV + 5% $ZrFe_{1.8}V_{0.2}$ has best hydrogen storage properties with hydrogen storage capacity of 3.7 wt.% at room temperature and hydrogen desorption peak at 434 K.

5.3 Conclusion

From the above studies, it is concluded that presence of Zr based Laves phase in BCC matrix of Ti-Cr-V based alloy (no matter how the Laves phase has been incorporated) improves its hydrogen storage property drastically. The maximum hydrogen storage capacities of Zr substituted Ti_2CrV alloy ($Ti_{0.43}Zr_{0.07}Cr_{0.25}V_{0.25}$ composition) and composite of Ti_2CrV alloy (Ti_2CrV + 5% $ZrFe_{1.8}V_{0.2}$) are found to be 3.19 wt.% and 3.7 wt.% respectively at room temperature. Presence of Zr rich Laves phase reduces hydrogen uptake of parent Ti_2CrV alloy slightly, however it improves the desorption temperature remarkably. $Ti_{0.43}Zr_{0.07}Cr_{0.25}V_{0.25}$ alloy shows better cyclic stability compared to Ti_2CrV alloy.

Chapter 6

Hydrogen Storage Properties of Zr-Ti-Ni Based Compounds

Previous studies (described in Chapter 5) have confirmed that presence of Zr based Laves phase is effective in improving the hydrogen storage behavior of Ti_2CrV alloy. To have a better understanding of the role of such Laves phases on hydrogen storage properties, detailed studies were carried out on the hydriding performance of representative Zr based Laves phase compounds. Since Zr and Ti are good hydride forming elements, they are commonly used as major components of Laves phase compounds for hydrogen storage applications [292, 307]. It is necessary, at this stage, to know what are Laves phase compounds and their different structural features. Laves phase compounds are compact ordered materials and are represented by the general formula AB_2 where the ideal radii ratio, $(^{r_A}/_{r_B})$ should be ~ 1.225. There are mainly three types of Laves phase structures: C14 (hexagonal, $MgZn_2$ type), C15 (cubic, $MgCu_2$ type) and C36 (hexagonal, $MgNi_2$ type). Among them C14 and C15 Laves phase compounds have been widely studied for hydrogen storage because of easy activation and excellent diffusivity of absorbed hydrogen [308-310]. The structure is very interesting from the perspective of hydrogen absorption due to its ability to accommodate hydrogen atoms in its tetrahedrally coordinated interstices. For both C14 and C15 structures, there are 17 such interstices per AB_2 formula unit namely A2B2 (12 numbers), AB3 (4 numbers), and B4 (1 number) type. The interstices are only partially populated due to the spatial and electronic limitations during hydrogen filling in these sites. As a result, a maximum of 6 hydrogen atoms can be absorbed per AB_2 formula unit. In most of the cases, H atom preferably goes into larger A2B2 interstitial sites followed by AB3 site, whereas the smallest B4 site remains unoccupied [311]. There are several reports on Zr based binary Laves phase compounds (C14/C15 structure) such as ZrV_2, $ZrMn_2$, $ZrCr_2$ which show quite good hydrogen storage capacities. For example, theoretical hydrogen storage capacity of binary compound ZrV_2 is reported to be ~ 3 wt.% [2, 312]. However, the stability of their hydrides is too high for practical application. Extensive efforts have been made to improve hydrogen storage performance of Zr based binary Laves phase compounds mainly by partial elemental substitution in either A or B site or both the sites. Previous studies [310, 313-315] reveal that Ti substitution is effective in reducing the hydride stability and improving hysteresis behavior of Zr based Laves phase compounds. However, hydrogen storage capacity decreases on Ti substitution. This can be attributed to decrease of unit cell volume and change in hydrogen affinity upon Ti substitution [316]. It is important to optimize the Zr/Ti ratio in order to achieve suitable hydrogen storage properties in C14/C15 Laves phase compounds.

In this chapter, the effect of changing Zr/Ti ratio on the hydrogen storage properties of ZrTiNi, a Zr based ternary Laves phase compound, has been discussed in detail. The equiatomic ZrTiNi compound is reported to crystallize in C14 Laves phase structure [317]. Bououdina et al. [318] inferred from their investigations on ZrMM′(M = Ti/V; M′ = Ni/Co) alloy systems, that hydrogen absorption properties of Zr based ternary Laves phase compounds can be tuned by changing proportion of M and M′. In the present chapter, efforts have been devoted to the study of hydriding performance of Zr-Ti-Ni based ternary systems for different proportion of Zr and Ti.

The main focus of this chapter is to give a clear picture of the hydrogen absorption behavior of representative Zr-Ti-Ni system with respect to phase (microstructural) evolution.

Four compounds with compositions ZrTiNi, $Zr_{1.3}Ti_{0.7}Ni$, $Zr_{1.7}Ti_{0.3}Ni$ and Zr_2Ni were investigated. Hydriding kinetics has been thoroughly investigated at different temperatures. In general, hydrogen absorption reaction consists of several steps [319-321] which include (1) physisorption of hydrogen molecules, (2) dissociation of hydrogen molecules to hydrogen atoms, (3) surface penetration of hydrogen atoms, (4) diffusion of hydrogen atoms through the hydride layer, and (5) hydride formation at the metal hydride interface. The slowest step among the above, known as rate-determining step (rds), decides the overall kinetics of hydrogen absorption. In the present study, the rds has been identified through analysis of the experimental kinetics data and activation energy associated with the hydriding reaction has been determined. This chapter also gives insight into the mechanism governing hydriding reaction of the Zr-Ti-Ni intermetallic compounds.

6.1 Experimental

The compounds $Zr_{2-x}Ti_xNi$ ($x = 0, 0.3, 0.7, 1.0$) were prepared by arc melting the constituent elements of high purity (>99.99%) in a water cooled copper hearth under argon atmosphere. The sample buttons were turned over and re-melted 4-5 times to ensure homogeneity. Both as cast compounds and their hydrides were characterized by X-ray diffraction (XRD) technique using monochromatic CuK_α radiation with Si as a standard reference. The as cast samples were brittle and each sample was ground to fine powder before recording the powder XRD pattern.

Hydrogen absorption studies were carried out in a fully automated hydrogen storage setup (IMI analyzer, HIDEN ISOCHEMA, UK, Model HTP1) as already discussed in Chapter 2. The activation procedure involved heating the sample under diffusion vacuum (10^{-6} mbar) for 2 hr at 673 K. After activation, the sample was cooled to working temperature under vacuum, followed by introduction of hydrogen into reaction chamber. The pressure-composition isotherms (PCI) were measured in the pressure range of 0.002-5 atm. Experiments on the hydrogen absorption kinetics of activated samples were carried out in a home-made Sievert's type of set up. The kinetics data were recorded after one absorption-desorption cycle, by following the pressure drop with time at a constant temperature. The hydride samples were surface passivated at liquid nitrogen temperature using air before being taken out.

6.2 Kinetics measurements (theoretical background)

The classic KJMA model assumes random nucleation and non-directional growth of nuclei (transformed region) where the sample volume is assumed to be infinite. The impingement of growing nuclei is also considered in this kinetic model. Under the basic assumptions of KJMA model, the reacted fraction ξ evolves exponentially with time and is given by

$$\xi = 1 - exp(-kt^n) \qquad (6.1)$$

where, k is the rate constant and n is the so-called Avrami exponent. In order to extract the kinetic parameters, k and n, Eq. 6.1 can be represented in a much simpler way as follows,

$$ln[-ln(1-\xi)] = nlnt + lnk \qquad (6.2)$$

k and n can be easily calculated from the intercept and slope of the typical "double-logarithmic plot" of $ln[-ln(1-\xi)]$vs lnt. The Avrami exponent is an important kinetic parameter in tracing the reaction mechanism. The parameter "n" contains two terms and is given by,

$$n = n_n + n_{gd} \qquad (6.3)$$

where, $n_n$is related to nucleation and n_{gd} corresponds to growth mechanism.

$$n_n = \begin{array}{l} 0, \text{instant nucleation (site saturation)} \\ 1, \text{constant nucleation rate} \end{array}$$

$$> 1, increasing\ nucleation\ rate$$

$$< 1\ but > 0, decreasing\ nucleation\ rate$$

n_{gd} comprises of two terms and expressed as $n_{gd} = d/m$ where d, the dimensionality of the growth, ranges from 1 to 3 for one dimensional to three dimensional growth. The value of "m" indicates whether the growth is interface limited (m = 1) or diffusion controlled (m = 2).

Temperature variation (thermal activation) affects the growth rate significantly and the nucleation density is also strongly dependent on temperature. Usually the Avrami exponent is not temperature sensitive but the rate constant k is highly temperature dependent. Using the derived rate constants "k" at different temperatures, the apparent activation energy (E_a) for hydriding reaction is evaluated from the Arrhenius equation (Eq. 6.4)

$$k = Aexp(E_a/RT) \qquad (6.4)$$

where, A is the temperature independent pre-exponential factor, $R$is the universal gas constant (8.314 J mol^{-1} K^{-1}), and T is the absolute temperature.

6.3 Results and discussions

6.3.1 XRD study of the compounds

Fig. 6.1 shows XRD patterns of as cast ZrTiNi, $Zr_{1.3}Ti_{0.7}Ni$, $Zr_{1.7}Ti_{0.3}Ni$ and Zr_2Ni samples. Nature of phases present in different samples and corresponding unit cell parameters are summarized in Table 6.1. It has been found that the ZrTiNi compound (Zr/Ti ratio = 1) consists of hexagonal C14 Laves phase (space group $P6_3/mmc$) with $MgZn_2$ type structure. With increase in Zr/Ti ratio new diffraction peaks appear. These new peaks correspond to C16 phase characteristic of Zr_2Ni compound. It is worth noting that the peak intensity of C14 Laves phase decreases and that of C16 phase increases with gradual increase in Zr concentration. When all Ti is replaced by Zr, the C14 Laves phase totally disappears and mainly C16 phase (space group

I4/mcm) with $CuAl_2$ type structure prevails. For $Zr_{1.3}Ti_{0.7}Ni$, $Zr_{1.7}Ti_{0.3}Ni$ and Zr_2Ni samples, in addition to main reflection peaks a few weak peaks are also observed which correspond to NiZr and $Ni_{10}Zr_7$ secondary phases. The c/a ratio for C14 Laves phase remains constant (c/a = 1.63) on varying Zr/Ti ratio but the value changes significantly for C16 phase (c/a = 0.808 to 0.819). Existence of minor phases can be ascribed to the non-equilibrium solidification process of the arc-melted samples and due to their small amounts they can be ignored.

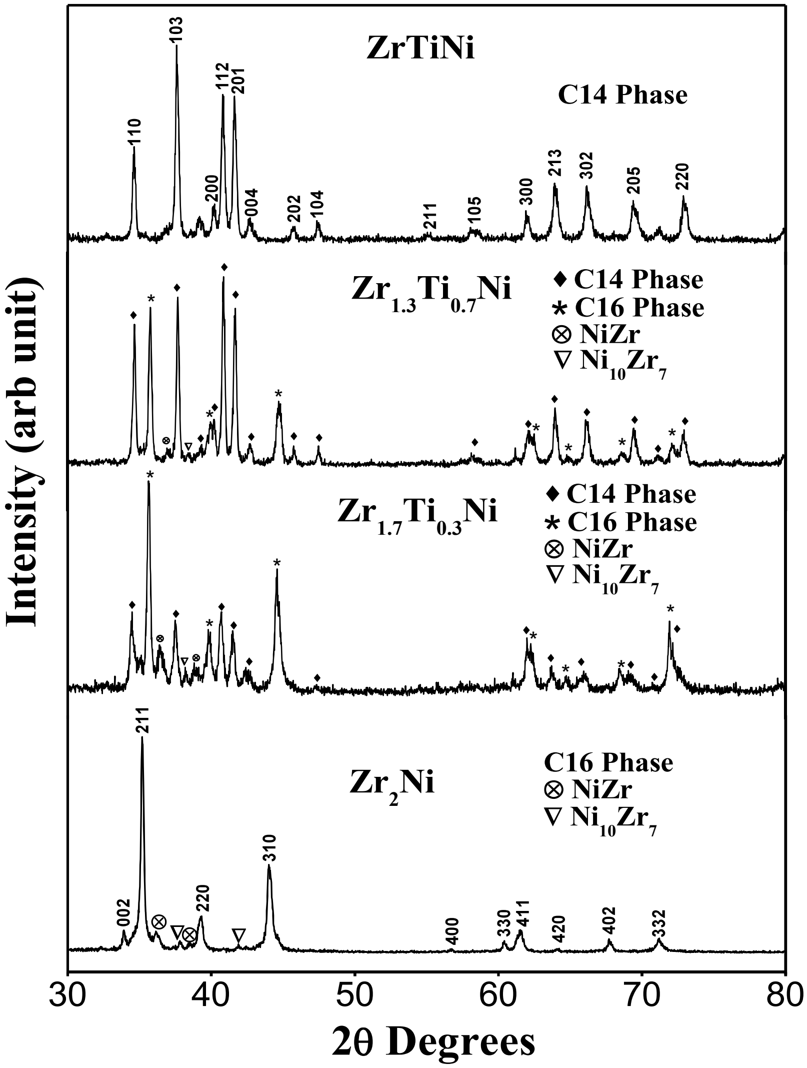

Fig. 6.1 *XRD pattern for ZrTiNi, $Zr_{1.3}Ti_{0.7}Ni$, $Zr_{1.7}Ti_{0.3}Ni$ and Zr_2Ni compounds.*

Table 6.1 *Lattice parameters, c/a ratios and unit cell parameters of ZrTiNi,* $Zr_{1.3}Ti_{0.7}Ni$, $Zr_{1.7}Ti_{0.3}Ni$ *and* Zr_2Ni *compounds.*

Samples	Phases	a (Å)	c (Å)	c/a	V (Å^3)
ZrTiNi	C14 Phase	5.2050	8.4857	1.63	199.093
$Zr_{1.3}Ti_{0.7}Ni$	C14 Phase	5.2050	8.4846	1.63	199.070
	C16 Phase	6.4830	5.2409	0.808	220.27
$Zr_{1.7}Ti_{0.3}Ni$	C14 Phase	5.2050	8.4824	01.63	199.016
	C16 Phase	6.4830	5.2658	0.812	221.32
Zr_2Ni	C16 Phase	6.4830	5.3082	0.819	223.09

6.3.2 Hydrogen absorption properties

Fig. 6.2 presents the pressure composition absorption isotherms for ZrTiNi, $Zr_{1.3}Ti_{0.7}Ni$, $Zr_{1.7}Ti_{0.3}Ni$ and Zr_2Ni samples. It is found from the isotherms that number of H atoms absorbed per one molecule of ZrTiNi is 3.10 under 5 bar pressure which results in a gravimetric hydrogen storage capacity of 1.54 wt.%. With increase in Zr/Ti ratio the plateau pressure was remarkably decreased. The result is as per the expectation because the atomic size of Zr is larger with respect to Ti leading to increase in unit cell volume. In addition to the size effect, Zr is having higher hydrogen affinity compared to Ti as already mentioned at the beginning of this chapter. According to Pauling scale, electronegativity (χ) of hydrogen is 2.2, therefore Zr with $\chi = 1.33$ will have more affinity towards hydrogen compared to Ti which has higher electronegativity ($\chi = 1.54$). The greater affinity of Zr towards hydrogen results in higher hydride stability which is also responsible for the observed decrease in plateau pressure. With the consequent change in plateau pressure, the absorption capacity is also affected. The hydrogen concentration in $Zr_{1.3}Ti_{0.7}Ni$ compound is enhanced from 3.10 to 3.25 H/M under 5 bar pressure. However, the increase in storage capacity is remarkable for higher Zr containing compound. For example the compound $Zr_{1.7}Ti_{0.3}Ni$ is found to absorb 4.5 hydrogen atoms per formula unit. This can be attributed to the increase in unit cell volume as well as to the dominance of C16 phase at higher concentration of Zr as evidenced from XRD pattern. Zr_2Ni with $CuAl_2$ type structure is reported [283] to absorb higher amount of hydrogen compared to ZrTiNi with $MgZn_2$ type structure and in our present study we have also found that it can absorb 4.77 H/M. The gravimetric hydrogen storage capacities of the ZrTiNi, $Zr_{1.3}Ti_{0.7}Ni$, $Zr_{1.7}Ti_{0.3}Ni$ and Zr_2Ni samples at 298 K and 5 bar pressure are found to be 1.54, 1.52, 1.93 and 1.94 wt.%, respectively at room temperature.

6.3.3 XRD study of the hydrides

XRD patterns of ZrTiNi, $Zr_{1.3}Ti_{0.7}Ni$, $Zr_{1.7}Ti_{0.3}Ni$ and Zr_2Ni samples after hydrogenation are shown in Fig. 6.3. It is inferred that hydride phase $ZrTiNiH_{3.10}$ possesses the same symmetry as the parent compound ZrTiNi but the unit cell volume is enhanced as it is clear from shift in the diffraction peak maxima towards lower angles. The other hydrides $Zr_{1.3}Ti_{0.7}NiH_{3.25}$, $Zr_{1.7}Ti_{0.3}NiH_{4.50}$ and $Zr_2NiH_{4.77}$ also retain the structure of their parent compounds. The first two hydrides show mixed phase structures containing both C14 and C16 phases whereas the hydride $Zr_2NiH_{4.77}$ is found to have a single-phase structure (C16 phase) with increased unit cell volume. It is worth mentioning here that Hara et al. [323] reported hydrogen induced disproportionation in Zr_2Ni alloy. In our present study, to avoid disproportionation of Zr_2Ni phase, hydrogen was introduced into the reaction chamber in small steps upto a pressure of 5 bar. XRD pattern shows that Zr_2Ni retains its structural identity upon hydrogenation which agrees well with the observation made earlier by Chikdene et al. [324] and Aubertin et al. [325]. Also, the absence of peaks corresponding to ZrNi and ZrH_2 phases [$Zr_2Ni + H_2 = ZrNi + ZrH_2$] in the XRD pattern, further ascertains that there is no hydrogen induced disproportionation of Zr_2Ni sample under the present experimental conditions.

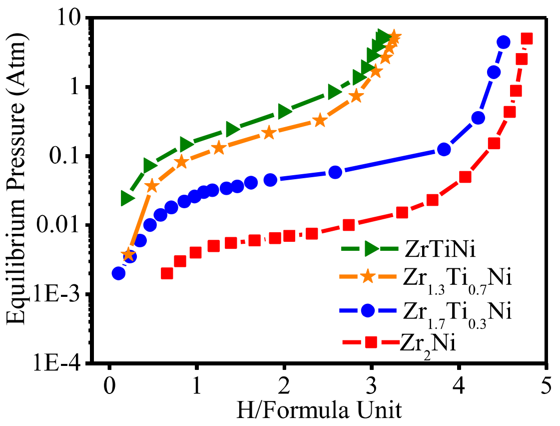

Fig. 6.2 *P-C absorption isotherms of ZrTiNi, $Zr_{1.3}Ti_{0.7}Ni$, $Zr_{1.7}Ti_{0.3}Ni$ and Zr_2Ni samples at 298 K.*

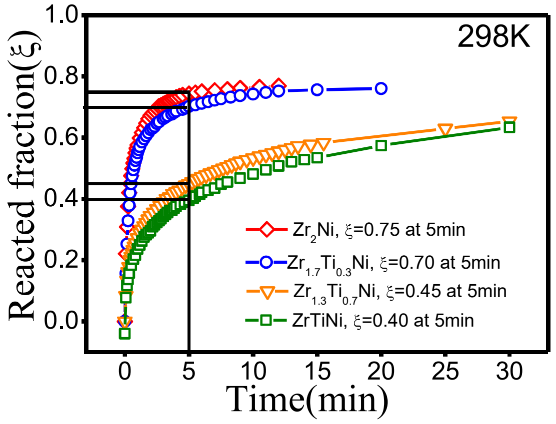

Fig. 6.4 *Kinetics of hydriding reaction for ZrTiNi, $Zr_{1.3}Ti_{0.7}Ni$, $Zr_{1.7}Ti_{0.3}Ni$ and Zr_2Ni samples at 298 K.*

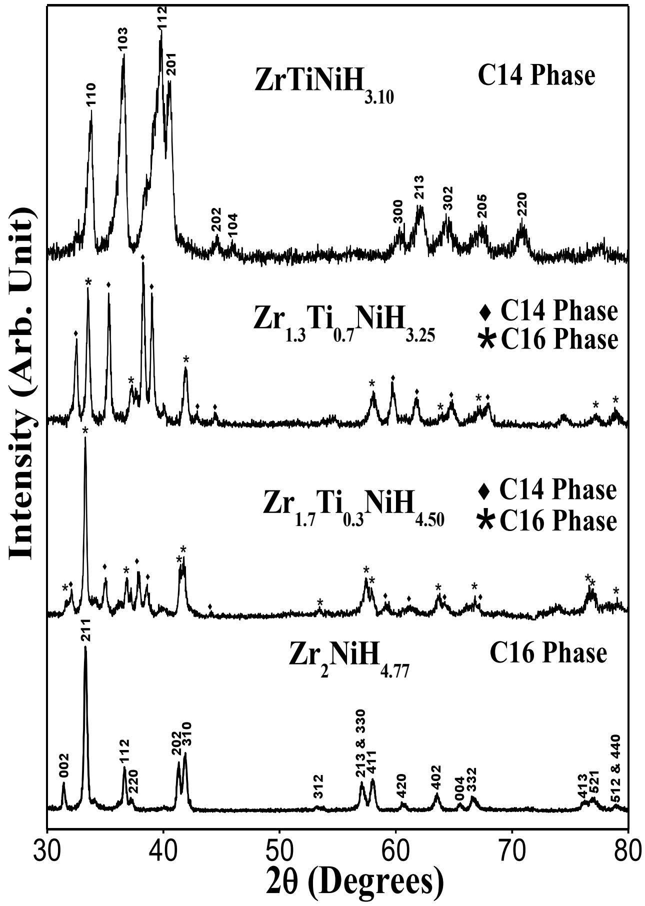

Fig. 6.3 *XRD pattern for the hydrides of ZrTiNi, $Zr_{1.3}Ti_{0.7}Ni$, $Zr_{1.7}Ti_{0.3}Ni$ and Zr_2Ni samples.*

6.3.4 Kinetics study of the compounds

In the present study, the kinetics of hydrogen absorption for ZrTiNi, $Zr_{1.3}Ti_{0.7}Ni$, $Zr_{1.7}Ti_{0.3}Ni$ and Zr_2Ni samples have been studied using a Sieverts' type of setup over the temperature range from 298 K to 473 K under an initial hydrogen pressure of 5 bar. The initial pressure was kept same for all the cases because kinetics is affected on changing the applied pressure. The rate of hydrogen absorption is shown as change of reacted fraction (ζ) with time in Fig. 6.4. It is clear from the kinetics plot shown in Fig. 6.4, that ζ increases with time and will reach a saturation value after certain time duration depending on the rate of hydriding reaction. ZrTiNi reaches around 40% of the saturation value [$\zeta = 0.40$] within 5 minutes. The kinetics does not change appreciably for $Zr_{1.3}Ti_{0.7}Ni$ compound. The ζ value after 5 minutes increases to 0.45 in case of $Zr_{1.3}Ti_{0.7}Ni$. The kinetics of hydrogen absorption at room temperature is found to accelerate remarkably for higher Zr containing compounds. The figure shows, for $Zr_{1.7}Ti_{0.3}Ni$, the reacted fraction ζ reaches 70% of the saturation value within 5 minutes. Significant increase in absorption kinetics can be attributed to the larger radius of Zr as compared to that of Ti. With increase in Zr concentration the lattice expands and the size of the interstitial sites also increases. In addition to the size effect, Zr has higher hydrogen affinity compared to Ti. As a result, the energy required in accommodating the hydrogen atoms in the interstitial sites decreases and this facilitates hydrogen absorption process. This is reflected in the corresponding activation energies for hydriding reaction in sec. 6.3.6.

6.3.5 Analysis of hydrogen absorption kinetics

Fig. 6.5(a-d) shows the variation of hydriding kinetics with temperature for all the four samples. A quick look at the plots confirms that there is no incubation period during hydrogenation of these samples. Although the nature of kinetic plots at higher temperatures

(373 K and 473 K) is similar to that at 298 K, the reaction rate is faster at elevated temperatures as expected.

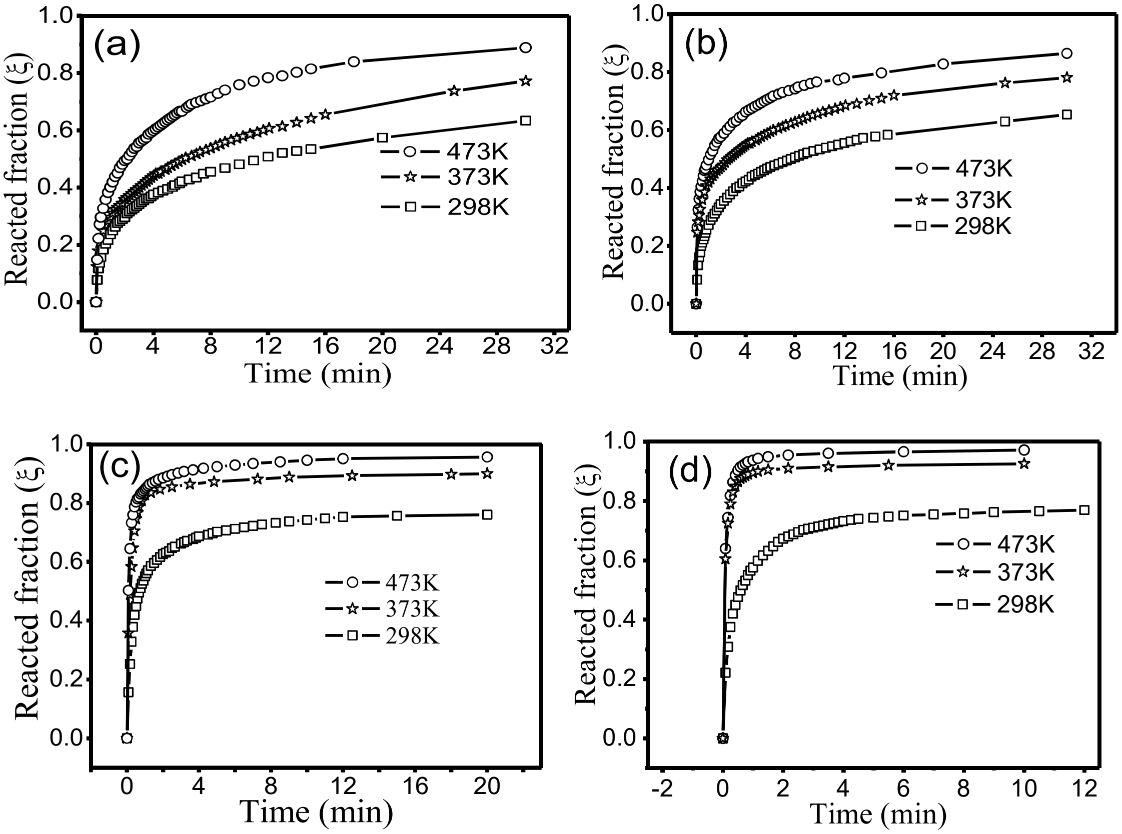

Fig. 6.5 *Kinetics of hydriding reaction for (a) ZrTiNi (b) $Zr_{1.3}Ti_{0.7}Ni$, (b) $Zr_{1.7}Ti_{0.3}Ni$, and (d) Zr_2Ni samples over the temperature range of 298-473 K.*

Fig. 6.6-6.9 presents the KJMA plots of $ln[-ln(1-\xi)]$ vs ln(t) for ZrTiNi, $Zr_{1.3}Ti_{0.7}Ni$, $Zr_{1.7}Ti_{0.3}Ni$ and Zr_2Ni samples respectively at three different temperatures. The plots show good linearity with R^2 (linearity constant) > 0.99, in the temperature range from 298 K to 473 K, which indicates that KJMA model can satisfactorily describe hydriding process for the studied samples.

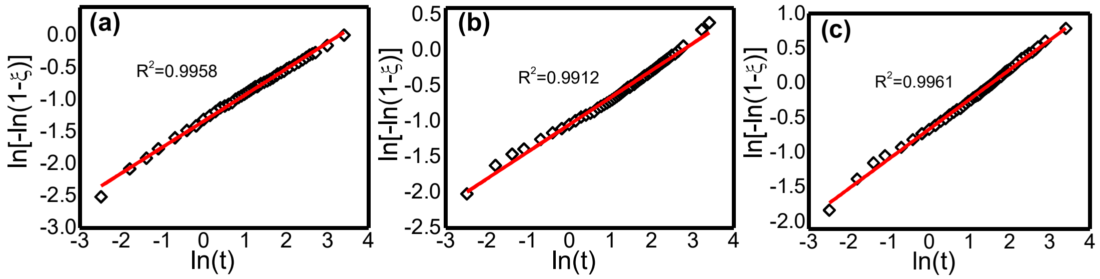

Fig. 6.6 *Plot of* $ln[-ln(1-\xi)]$ *versus ln(t) for the hydriding reaction of ZrTiNi sample at (a) 298 K, (b) 373 K and (c) 473 K.*

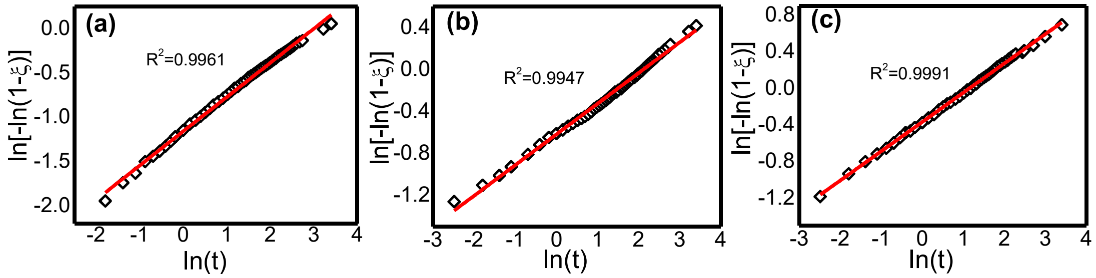

Fig. 6.7 *Plot of* $ln[-ln(1-\xi)]$ *versus ln(t) for the hydriding reaction of* $Zr_{1.3}Ti_{0.7}Ni$ *sample at (a) 298 K, (b) 373 K and (c) 473 K.*

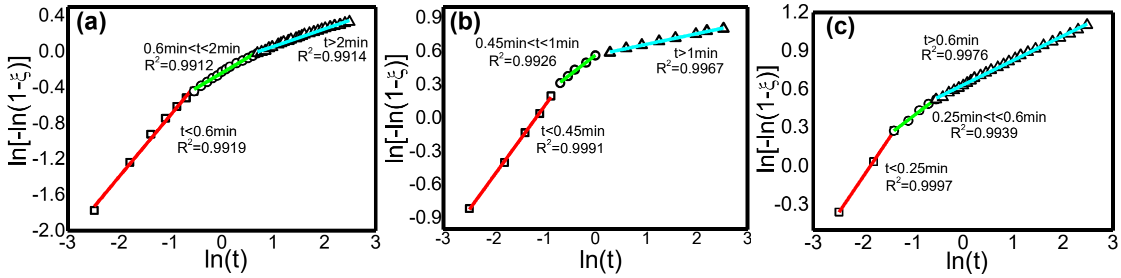

Fig. 6.8 *Plot of* $ln[-ln(1-\xi)]$ *versus ln(t) for the hydriding reaction of* $Zr_{1.7}Ti_{0.3}Ni$ *sample at (a) 298 K, (b) 373 K and (c) 473 K.*

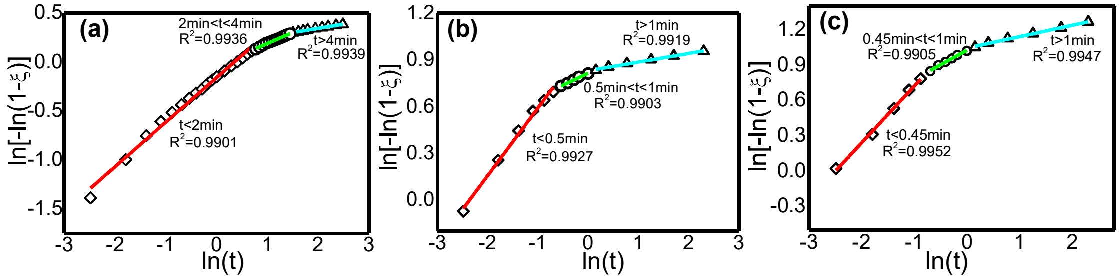

Fig. 6.9 *Plot of* $ln[-ln(1-\xi)]$ *versus ln(t) for the hydriding reaction of* Zr_2Ni *sample at (a) 298 K, (b) 373 K and (c) 473 K.*

In case of ZrTiNi, the whole range of kinetics data is fitted with one linear segment. Kinetic analysis of $Zr_{1.3}Ti_{0.7}Ni$ compound apparently shows similar type of fitting as that of ZrTiNi, whereas for higher Zr containing compounds the nature of fitting totally changes. Most surprisingly, the kinetic data of $Zr_{1.7}Ti_{0.3}Ni$ and Zr_2Ni samples were also fitted with KJMA model ($R^2 > 0.99$) but three linear segments of different slopes were required for data fitting. Each of the linear segments represents a different zone of reaction, viz. α, $(\alpha+\beta)$ and β phases. The slope change is related to different phase transformations, viz. from α to $(\alpha+\beta)$ and from $(\alpha+\beta)$ to β. For a given initial pressure, the reaction kinetics of $Zr_{1.7}Ti_{0.3}Ni$ and Zr_2Ni samples are faster compared to the higher Ti containing compounds. Hence, for these two samples the hydrogen absorption process in all the three phases namely α, $(\alpha+\beta)$ and β can be clearly envisaged in the limited time frame of kinetic analysis. For both $Zr_{1.7}Ti_{0.3}Ni$ and Zr_2Ni samples the time span of α phase decreases with increasing temperature indicating faster nucleation rate at higher temperature.

The Avrami exponents and rate constants derived from the double-logarithmic plot have been listed in Table 6.2 and Table 6.3, respectively.

Table 6.2 *Avrami exponents (n) for ZrTiNi, $Zr_{1.3}Ti_{0.7}Ni$, $Zr_{1.7}Ti_{0.3}Ni$ and Zr_2Ni samples.*

Composition	Avrami Exponent								
	298K			373K			473K		
	1st stage	2nd stage	3rd stage	1st stage	2nd stage	3rd stage	1st stage	2nd stage	3rd stage
ZrTiNi	0.35			0.37			0.42		
$Zr_{1.3}Ti_{0.7}Ni$	0.38			0.29			0.32		
$Zr_{1.7}Ti_{0.3}Ni$	0.72	0.34	0.19	0.68	0.35	0.12	0.66	0.30	0.17
Zr_2Ni	0.60	0.30	0.13	0.57	0.29	0.18	0.56	0.32	0.16

Table 6.3 *Rate constants (k) for ZrTiNi, $Zr_{1.3}Ti_{0.7}Ni$, $Zr_{1.7}Ti_{0.3}Ni$ and Zr_2Ni samples. Rate constants derived by using modified KJMA model is mentioned in parenthesis.*

		Composition			
Temperature	k	ZrTiNi	$Zr_{1.3}Ti_{0.7}Ni$	$Zr_{1.7}Ti_{0.5}Ni$	Zr_2Ni
298K	1st stage	0.2594	0.3147	0.8530	0.9999
		(0.0287)	(0.0301)	(0.7942)	(0.9997)
	2nd stage			0.9656	0.7890
				(0.8993)	(0.454)
	3rd stage			1.1841	0.8714
				(2.875)	(0.423)
373K	1st stage	0.5146	0.5390	2.7927	2.0915
		(0.1741)	(0.1537)	(4.4300)	(3.569)
	2nd stage			2.2956	1.7623
				(11.8189)	(6.610)
	3rd stage			2.2956	1.7683
				(180.14)	(35.251)
473K	1st stage	0.6646	0.6921	3.3398	2.9212
		(0.3413)	(0.3279)	(5.7413)	(6.349)
	2nd stage			2.7957	1.9883
				(22.544)	(9.885)
	3rd stage			2.8462	1.8853
				(690.56)	(52.621)

For all the samples, Avrami exponents derived in the temperature range from 298 K to 473 K are less than 1 and this can be justified if:

(a) the growth contribution is negligible (n_{gd}= 0) and this is possible only when growth rate is significantly faster than the nucleation rate such that the hydriding kinetics is entirely dominated by nucleation process [326]. Vigeholm et al. also found faster growth rate compared to nucleation in Mg based systems [327]

(b) both nucleation and growth rates are decreasing with time [328]

(c) an instantaneous nucleation followed by diffusion of hydrogen atom through the growing nuclei.

Lower value of Avrami exponent was also found by Tien et al during the formation of magnesium hydride [329]. Value of "*n*" is apparently independent of the hydrogenation temperature only when there is no change in the nucleation mechanism. For $Zr_{1.7}Ti_{0.3}Ni$ and Zr_2Ni compounds, Avrami exponents corresponding to the first stage of hydrogenation at three different temperatures remain almost constant indicating similar type of nucleation and growth mechanism during the initial stage. This is also valid for second and third stages of hydrogenation. However, for these samples "*n*" values associated with different stages of hydrogenation vary significantly, indicating a change in nucleation and growth mechanism. For the other two compounds with lower Zr content "*n*" values does not vary remarkably with temperature again confirming that Avrami exponents are less sensitive to reaction temperature.

6.3.6 Activation energies

The values of apparent activation energies for the hydriding reaction, obtained through the Arrhenius plot are presented in Fig. 6.10. A large number of kinetic studies [97, 330, 331] utilized KJMA model to determine activation energies. However, it is impossible to separate the effect of reaction order with this approach. The present study shows that with change in Zr/Ti ratio, reaction order changes as reflected in the corresponding Avrami exponent values of ZrTiNi, $Zr_{1.3}Ti_{0.7}Ni$, $Zr_{1.7}Ti_{0.3}Ni$ and Zr_2Ni samples. Hence the calculation of activation energy using standard KJMA model is questionable while comparing the hydriding kinetics of compounds with different Zr/Ti ratios [332]. The modified KJMA model is expressed as:

$$\xi = 1 - exp(-kt)^n \qquad (6.5)$$

The equation can be rearranged to a linear form as follows:

$$ln[-ln(1-\xi)] = nlnt + nlnk \qquad (6.6)$$

The intercept would now be *nlnk* rather than *lnk*. In order to calculate rate constant "*k*" using modified KJMA model, the average of "*n*" values at three different hydrogenation temperatures was considered. The Arrhenius plots obtained by using modified "*k*" values are shown in Fig. 6.11. The modified rate constants and activation energies are listed in parenthesis in Table 6.3 and 6.4, respectively.

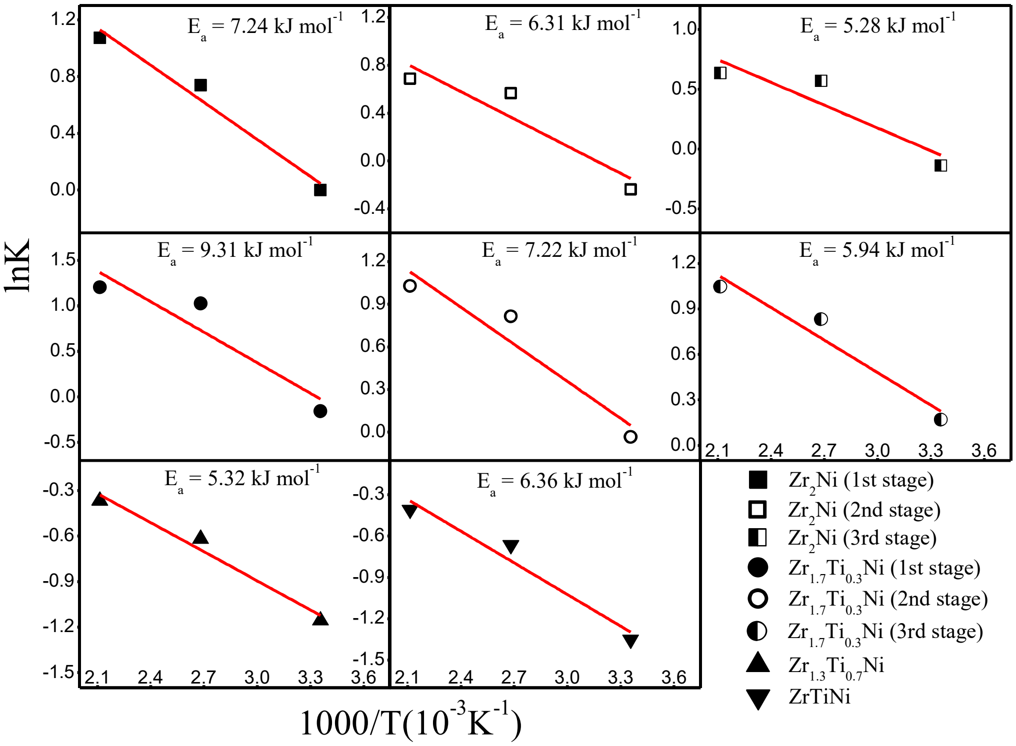

Fig. 6.10 *Arrhenius plots for the hydriding reaction of ZrTiNi, $Zr_{1.3}Ti_{0.7}Ni$, $Zr_{1.7}Ti_{0.3}Ni$ and Zr_2Ni sampleswhen normal KJMA model is used.*

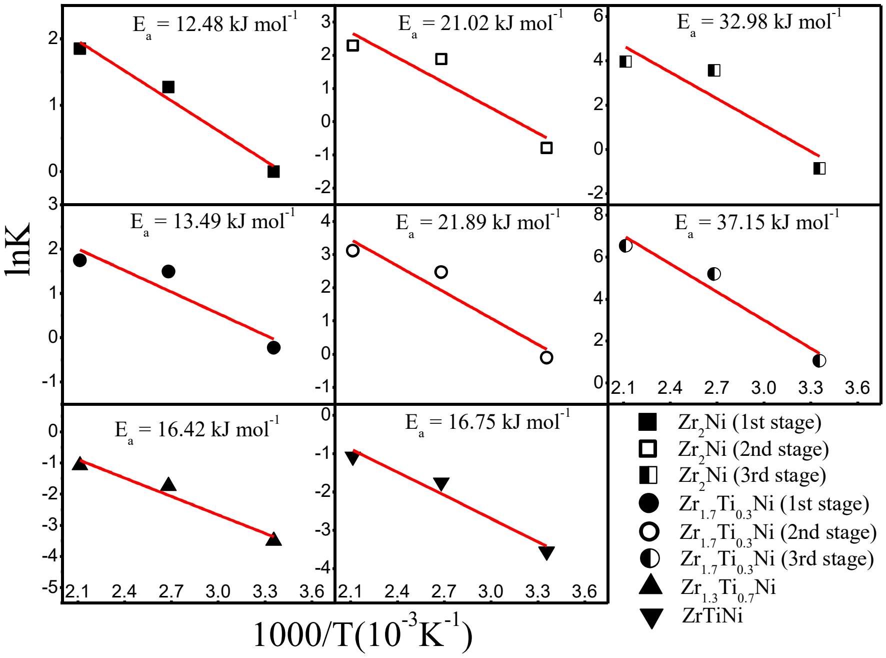

Fig. 6.11 *Arrhenius plots for the hydriding reaction of ZrTiNi, $Zr_{1.3}Ti_{0.7}Ni$, $Zr_{1.7}Ti_{0.3}Ni$ and Zr_2Ni sampleswhen modified KJMA model is used.*

Table 6.4 *Activation energies (E_a) for ZrTiNi, $Zr_{1.3}Ti_{0.7}Ni$, $Zr_{1.7}Ti_{0.3}Ni$ and Zr_2Ni samples. Activation energies derived by using modified KJMA model is mentioned in parenthesis.*

	E_a (kJ/mol)		
Cmposition	1st JMA	2nd JMA	3rd JMA
ZrTiNi	6.36 (16.75)		
$Zr_{1.3}Ti_{0.7}Ni$	5.32 (16.42)		
$Zr_{1.7}Ti_{0.3}Ni$	9.31 (13.49)	7.22 (21.89)	5.94(37.15)
Zr_2Ni	7.24 (12.48)	6.31 (21.02)	5.28(32.98)

As evident from Table 6.4, there is no correlation between the activation energies of the samples (determined using classical KJMA model) and relative concentration of Zr and Ti. However, the activation energies derived by using modified KJMA model show a decreasing trend with increase in Zr/Ti ratio. For higher Zr containing compounds, the rate of reaction increases remarkably and the activation energy (E_a) decreases as already predicted in sec. 6.3.4.

6.4 Conclusions

Increase in Zr/Ti ratio decreases the plateau pressure of equiatomic ZrTiNi compound remarkably with a substantial increase in hydrogen uptake (H/M). Crystal structures of the hydrides with different Zr/Ti ratio imitate those of their parent alloys with a change in lattice parameters. Upon increasing Zr concentration, the rate of hydrogen absorption increases considerably. From the kinetic analysis of experimental data it is inferred that variation in Zr/Ti ratio changes the reaction order (Avrami exponents are different for different compounds) i.e. the mechanism of hydriding reaction. Among the studied compounds $Zr_{1.7}Ti_{0.3}Ni$ shows best hydriding performance with room temperature hydrogen uptake of 1.93 wt.%, improved plateau pressure and fast enough kinetics. The modified KJMA model was successfully employed to explain the observed trend in the activation energies associated with hydrogenation of the studied compounds. The value of E_a decreases with increase in Zr concentration and this has been explained in terms of structural modification brought about by changing Zr/Ti ratio.

Chapter 7

Conclusion and Future Scope

The motivation of this dissertation is to develop basic understanding on hydrogen storage properties of systems which absorb hydrogen either by physisorption or chemisorption. Hydrogen storage characteristics of carbon based materials as well as Ti based BCC alloys and Zr based intermetallic compounds have been studied in detail. Major conclusions from the hydrogen storage investigations of the studied materials are summarized below.

Pristine CNT samples used in the present study (**Chapter 3**), is found to store only 0.056 wt.% hydrogen at room temperature and under 50 bar pressure. However, Pd incorporated CNTs prepared by polyol method show hydrogen uptake of 0.29 wt.% at 333K. There is no remarkable improvement of the hydrogen storage capacity when doping is done by wet impregnation route. This has been explained based on the atomic scale mixing of Pd nanoparticles and CNTs.

Advanced techniques like ^{13}C CP MAS NMR and SAXS were employed for the characterization of turbostratic carbon samples annealed at three different temperatures (700°C, 800°C and 900°C). It is inferred from these studies that with increase in annealing temperature, carbon clusters having surface fractal nature with rough surfaces become smoother with increase in size. Due to smooth and homogeneous surface, the isosteric enthalpy of hydrogen adsorption remains constant with hydrogen uptake for 900°C annealed sample. Besides, this sample (among the studied turbostratic carbons) shows highest hydrogen uptake of 1.25 wt.% at 123 K which is much better compared to Pd doped CNTs prepared by polyol route. This is due to relatively higher surface area and smaller pore size present in the former sample.

Apart from carbon based materials, present study also contributes towards the improvement of hydrogen storage performance of Ti-Nb and Ti-V based BCC alloy systems (**Chapter 4** and **Chapter 5,** respectively). Ti-Nb alloy suffers from poor activation due to oxide layer formation over the alloy surface. Fe substitution improves the activation of Ti-Nb alloy and enhances the rate of hydrogen absorption. Among the studied alloys in $Ti_{0.67}Nb_{0.33-x}Fe_x$ series, $Ti_{0.67}Nb_{0.13}Fe_{0.20}$ shows highest hydrogen uptake with fastest hydriding kinetics.

Ti-V based alloy with Ti_2CrV composition is reported to show hydrogen storage capacity ~ 4 wt.% at room temperature. The main disadvantage of this alloy is that it desorbs at relatively higher temperature. Keeping this in mind, two different approaches have been tried to reduce the desorption temperature: (i) partial substitution of Ti by Zr and (ii) composite formation with $ZrFe_2$ based Laves phase. The enthalpies of hydride formation for Zr substituted and unsubstituted Ti_2CrV alloy are found to be -56.33 and -64.4 kJ/mol of H_2 which indicates that Zr substitution significantly destabilize the hydride. In case of Ti_2CrV + x (= 5%, 10%, 20%) $ZrFe_{1.8}V_{0.2}$ composite materials, with increase in Zr rich secondary Laves phase concentration plateau pressure increases indicating decrease in hydride stability. Thus, both the approaches are effective in reducing the stability of the hydride which leads to significant decrease in hydrogen desorption temperature. However, the storage capacity of Ti_2CrV alloy decreases in both the approaches. All the composite materials as well as the Zr substituted alloy show satisfactory hydriding kinetics.

The detailed kinetic analysis of Ti-Nb-Fe based alloys, Zr substituted Ti_2CrV alloy and Ti_2CrV + $ZrFe_{1.8}V_{0.2}$ composite (through model fitting) reveals that hydrogenation of these systems involves more than one rate limiting steps. The rate limiting steps during the hydrogenation are:

(i) random nucleation and growth followed by one dimensional and three dimensional diffusion of H atoms, for Zr substituted Ti_2CrV alloy.

(ii) chemical reaction of H atoms with solid (either alloy or composite) followed by three dimensional diffusion of H atoms, for Ti-Nb-Fe alloy and Ti_2CrV + $ZrFe_{1.8}V_{0.2}$ composite system.

Studies on Zr-Ti-Ni based intermetallic compound (**Chapter 6**) have revealed that with increase in Zr/Ti ratio the room temperature hydrogen uptake increases and kinetics of hydrogen absorption also becomes fast. Experimental kinetics data of hydrogenation have been analyzed employing both classical and modified Kolmogorov-Johnson-Mehl-Avrami (KJMA) models. Dissimilar values of Avrami exponents for different compounds indicate that change in Zr/Ti ratio changes reaction order i.e. the mechanism of hydrogen absorption reaction. The present chapter has shown the importance of introducing modified KJMA model over the classical one in explaining the activation energies of hydrogenation for Zr-Ti-Ni system.

Future Scope: As an extension of this thesis work it is proposed that further work needs to be carried out for improving the gravimetric storage capacity of Ti-Cr-V based alloy system. The presence of Zr based Laves phase improves its desorption behavior but at the cost of its storage capacity. To increase hydrogen storage capacity they can be alloyed with light metal hydride such as magnesium hydride (MgH_2) which is known to have theoretical hydrogen storage capacity of 7.6 wt.%. However, MgH_2 has some disadvantages such as sluggish kinetics and very high thermodynamic stability. Doping MgH_2 powder with nanocatalysts is one of the options for accelerating slow kinetics and this will be investigated in future. There are studies on the hydrogen storage properties of Mg based alloys demonstrating their abilities to absorb hydrogen at comparatively lower temperatures. Unfortunately, alloying causes dramatic degradation of the hydrogen storage capacity of Mg. Thus, only alloying of Mg and Ti-Cr-V system will not be effective to overcome the obstacles associated with single Mg or single Ti-Cr-V system. However, a combination of processes like alloying, nanostructuring and grain refinement on Mg-Ti-Cr-V based systems can lead to improved hydrogen absorption/desorption properties. Hence, it is proposed to prepare Mg-Ti-Cr-V based nanocomposites modified with large amount of surface imperfections and nanostructured grains by different techniques and study their hydrogen absorption desorption performances in future.

As a future work, it is also proposed to study hydrogenation and dehydrogenation behavior of magnesium carbon composite system to see the synergistic effect of physisorption and chemisorption on the overall hydrogen storage performance of the composite. The beneficial effect of carbon additive to the hydrogen storage properties of magnesium has already been mentioned in Chapter 1. It is also demonstrated that ball milling leads to destruction of carbon species into stacked graphene layers and the thin layers of graphene over the growing MgH_2 nuclei act as hydrogen transferring interface. As a result the hydrogen storage performance of Mg-C composite material can be improved. In this thesis, it has been shown that Pd doped CNTs prepared by polyol route effectively dissociates hydrogen molecules into hydrogen atoms by spillover mechanism. Hence, it is proposed that, if a composite of Mg and Pd doped CNT is formed, the active hydrogen atoms generated by spillover mechanism can be easily transferred to the surface of Mg through the graphene layers as schematically depicted in Fig. 7.1. Subsequently magnesium hydride will be formed and the graphene layer will reduce the probability of oxidation and agglomeration of Mg particles in successive hydrogenation dehydrogenation cycles.

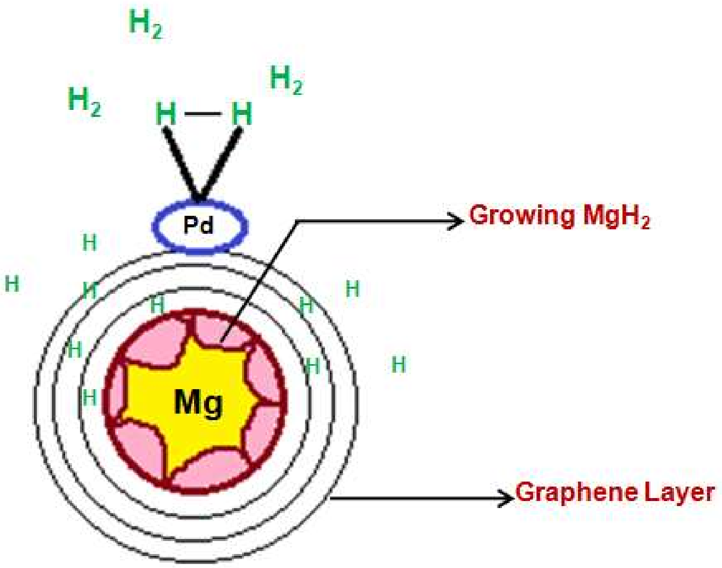

Fig. 7.1 *Schematic of hydrogen absorption by composite of Mg and Pd doped C.*

Again, all the interstitial hydrides suffer from poor thermal conductivities. This aspect has not been addressed in the present thesis. The heat associated with hydrogenation dehydrogenation of the alloys need to be removed efficiently for employing them as practical hydrogen storage materials in storage tanks. Composite of Mg-based hydrogen storage materials with graphite has shown significant improvement of thermal conductivity along with fast dynamics of hydrogen uptake and release [333]. Like graphite, CNTs are also reported to have high thermal conductivities. Moreover, CNTs being lightweight are not supposed to deteriorate the storage capacity of Mg-CNT composites.

References

1. Yang J, Sudik A, Wolverton C, Siegel DJ. High capacity hydrogen storage materials: attributes for automotive applications and techniques for materials discovery. Chem Soc Rev 2010;39:656-75.
2. Schlapbach L, Zuttel A. Hydrogen-storage materials for mobile applications. Nature 2001;414:353-8.
3. Mpourmpakis G, Tylianakis E, Froudakis GE. Carbon nanoscrolls: a promising material for hydrogen storage. Nano Lett 2007;7:1893-7.
4. Chen P, Zhu M. Recent progress in hydrogen storage. Mater Today 2008;11:36-43.
5. Eberle U, Felderhoff M, Schüth F. Chemical and physical solutions for hydrogen storage. Angew Chem Int Ed 2009;48:6608-30.
6. Turner JA. Sustainable hydrogen production. Science 2004;305:972-4.
7. Bockris JO. The origin of ideas on a hydrogen economy and its solution to the decay of the environment. Int J Hydrogen Energy 2002;27:731-40.
8. Zuttel A, Borgschulte A, Schlapbach L. Hydrogen as a future energy carrier. Weinheim: Wiley-VCH Verlag GmbH & Co. KGaA (2008).
9. Hydrogen, fuel cells and infrastructure technologies program. U.S. Department of Energy (2007).
10. Targets for onboard hydrogen storage systems for light-duty vehicles. Freedom Car and Fuel Partnership, U.S. Department of Energy. http://energy.gov/eere/fuelcells/doe-technical-targets-onboard-hydrogen-storage-light-duty-vehicles.
11. Møller KT, Jensen TR, Akiba E, Li HW. Hydrogen-a sustainable energy carrier. Prog Nat Sci: Mater Int 2017;27:34-40
12. Das LM. On-board hydrogen storage systems for automotive application. Int J Hydrogen Energy 1996;21:789-800.

13. Trudeau ML. Advanced materials for energy storage. MRS Bull 1999;24:23-6.

14. Blomqvist A, Araújo CM, Srepusharawoot P, Ahuja R. Li-decorate metal-organic framework 5: a route to achieving a suitable hydrogen storage medium. Proc Nat Acad Sci USA 2007;104:20173-6.

15. Hoang TKA, Antonelli DM. Exploiting the Kubas interaction in the design of hydrogen storage materials. Adv Mater 2009;21:1787-1800.

16. Alam N, Mokaya R. Characterisation and hydrogen storage of Pt-doped carbons template by Pt-exchanged zeolite Y. Micropor Mesopor Mat 2011;142:716-24.

17. Rowsell JLC, Yaghi OM. Strategies for hydrogen storage in metal-organic frameworks. Angew Chem Int Ed 2005;44:4670-9.

18. Dong J, Wang X, Xu H, Zhao Q, Li J. Hydrogen storage in several microporous zeolites. Int J Hydrogen Energy 2007;32:4998-5004.

19. Han SS, Furukawa H, Yaghi OM, Goddard WA 3rd. Covalent organic frameworks as exceptional hydrogen storage materials. J Am Chem Soc 2008;130:11580-1.

20. Germain J, Fréchet JM, Svec F. Nanoporous polymers for hydrogen storage. Small 2009;5:1098-111.

21. Sakintuna B, Lamari-Darkrim F, Hirscher M. Metal hydride materials for solid hydrogen storage: a review. Int J Hydrogen Energy 2007;32:1121-40.

22. Orimo SI, Nakamori Y, Eliseo JR, Zuttel A, Jensen CM. Complex hydrides for hydrogen storage. Chem Rev 2007;107:4111-32.

23. Peng B, Chen J. Ammonia borane as an efficient and lightweight hydrogen storage medium. Energy Environ Sci 2008;1:479-83.

24. Kunowsky M, Marco-Lózar JP, Linares-Solano A. Material demands for storage technologies in a hydrogen economy. J Renew Energy 2013;2013:Article ID 878329.

25. Rouquerol F, Rouquerol J, Sing KSW. Adsorption by powders and porous solids: principles, methodology and applications. Academic Press, London (1999).
26. Do DD. Adsorption analysis: equilibria and kinetics. Imperial College Press, London (1998).
27. Potgieter JH. Adsorption of methylene blue on activated carbon: an experiment illustrating both the Langmuir and Freundlich isotherms. J Chem Educ 1991;68(4):349-350.
28. Khan AR, Riazi MR, Al-Roomi YA. A thermodynamic model for liquid adsorption isotherms. Sep Purif Technol 2000;18:237-50.
29. Murai S, Imajo S, Takasu Y, Takahashi K, Hattori K. Removal of phthalic acid esters from aqueous solution by inclusion and adsorption on β-cyclodextrin. Environ Sci Technol 1998;32:782-7.
30. Fabrizius-Homan DJ, Cooper SL. A comparison of the adsorption of three adhesive proteins to biomaterial surfaces. J Biomater Sci Polym Ed 1991;3(1):27-47.
31. Burris DR, Antworth, CP, Stauffer TB, Macintyre WG. Humic acid-modified silica as a model aquifer material. Environ Toxicol Chem 1991;10:433-40.
32. Pan HH, Ritter JA, Balbuena PB. Examination of the approximations used in determining the isosteric heat of adsorption from the Clausius-Clapeyron equation. Langmuir 1998;14:6323-7.
33. Sircar S, Mohr R, Ristic C, Rao MB. Isosteric heat of adsorption: theory and experiment. J Phys Chem B 1999;103:6539-46.
34. Bhatia SK, Myers AL. Optimum conditions for adsorptive storage. Langmuir 2006;22:1688-1700.
35. Thomas KM. Hydrogen adsorption and storage on porous materials. Catal Today 2007;120:389-98.

36. Murray LJ, Dinca M, Long, JR. Hydrogen storage in metal-organic frameworks. Chem Soc Rev 2009;38:1294-1314.
37. Chahine R, Bose TK. Characterization and optimization of adsorbents for hydrogen storage. Hydrogen Energy Prog XI, Proc of the 11th World Hydrogen Energy Conf 1996;2:1259-63.
38. Iijima S. Helical microtubules of graphitic carbon. Nature 1991;354:56-8.
39. Popov VN. Carbon nanotubes: properties and application. Mater Sci Eng R 2004;43:61-102.
40. Venkateswaran UD, Masica DL, Sumanasekera GU, Furtado CA, Kim UJ, Eklund PC. Diameter dependent wall deformations during the compression of a carbon nanotube bundle. Phys Rev B 2003;68:241406(1-4).
41. Fan WJ, Zhang RQ, Teo BK, Aradi B, Frauenheim T. Prediction of energetically optimal single-walled carbon nanotubes for hydrogen physisorption. Appl Phys Lett 2009;95:013116(1-3).
42. Maddox MW, Gubbins KE. Molecular simulation of fluid adsorption in buckytubes. Langmuir 1995;11:3988-96.
43. Thess A, Lee R, Nikolaev P, Dai HJ, Petit P, Robert J, Xu CH, Lee YH, Kim SG, Rinzler AG, Colbert DT, Scuseria GE, Tomanek D, Fischer JE, Smalley RE. Crystalline ropes of metallic carbon nanotubes. Science 1996;273:483-7.
44. Dillon AC, Jones KM, Bekkedahi TA, Kiang CH, Bethune DS, Heben MJ. Storage of hydrogen in single-walled carbon nanotubes. Nature 1997;386:377-9.
45. Chen P, Wu X, Lin J, Tan KL. High H_2 uptake by alkali-doped carbon nanotubes under ambient pressure and moderate temperatures. Science 1999;285:91-3.
46. Liu C, Fan YY, Liu M, Cong HT, Cheng HM, Dresselhaus MS. Hydrogen storage in single walled carbon nanotubes at room temperature. Science 1999;286:1127-9.

47. Chen Y, Shaw DT, Bai XD, Wang EG, Lund C, Lu WM, Chung DDL. Hydrogen storage in aligned carbon nanotubes. Appl Phys Lett 2001;78:2128-30.
48. Tibbetts GG, Meisner GP, Olk CH. Hydrogen storage capacity of carbon nanotubes, filaments, and vapor-grown fiber. Carbon 2001;39:2291-301.
49. Ritschel M, Uhlemann M, Gutfleisch O, Leonhardt A, Graff A, Taschner C, et al. Hydrogen storage in different carbon nanostructures. Appl Phys Lett 2002;80:2985-7.
50. Kajiura H, Tsutsui S, Kadono K, Kakuta M, Ata M. Hydrogen storage capacity of commercially available carbon materials at room temperature. Appl Phys Lett 2003;82:1105-7.
51. Baughman RH, Zakhidov AA, Heer WA. Carbon nanotubes-the route toward applications. Science 2002;297:787-92.
52. Leonard AD, Hudson JL, Fan H, Booker R, Simpson LJ, O'Neill KJ, et al. Nanoengineered carbon scaffolds for hydrogen storage. J Am Chem Soc 2009;131:723-8.
53. Mishra A, Banerjee S, Mohapatra SK, Graeve OA, Misra M. Synthesis of carbon nanotube-TiO_2 nanotubular material for reversible hydrogen storage. Nanotechnology 2008;19:445607(1-7).
54. Züttel A, Sudan P, Mauron P, Kiyobayashi T, Emmenegger C, Schlapbach L. Hydrogen storage in carbon nanostructures. Int J Hydrogen Energy 2002;27:203-12.
55. Suttisawat Y, Rangsunvigi P, Kitiyanan B, Williams M, Ndungu P, Lototskyy MV, Nechaev A, Linkov V, Kulprathipanja S. Investigation of hydrogen storage capacity of multi-walled carbon nanotubes deposited with Pd or V. Int J Hydrogen Energy 2009;34:6669-75.
56. Rather S. Hydrogen uptake of cobalt and copper oxide-multiwalled carbon nanotube composites. Int J Hydrogen Energy 2017;42:11553-9.

57. Ioannidou O, Zabaniotou A. Agricultural residues as precursors for activated carbon production-a review. Renew Sustainable Energy Rev 2007;11:1966-2005.
58. Mohamed AR, Mohammadi M, Darzi GN. Preparation of carbon molecular sieve from lignocellulosic biomass: a review. Renew Sustainable Energy Rev 2010;14:1591-9.
59. Oh GH, Park CR. Preparation and characteristics of rice-straw based porous carbons with high adsorption capacity. Fuel 2002;81:327-36.
60. Dickinson AD. Great leaders of the world, stories of achievement. Garden City Publishing Co, Inc Garden city, New York (1937).
61. Rodríguez-Reinoso F, Molina-Sabio M, González MT. The use of steam and CO_2 as activating agents in the preparation of activated carbons. Carbon 1995;33:15-23.
62. Sevilla M, Mokaya R. Energy storage applications of activated carbons: supercapacitors and hydrogen storage. Energy Environ Sci 2014;7:1250-80.
63. Zhang F, Ma H, Chen J, Li GD, Zhang Y, Chen JS. Preparation and gas storage of high surface area microporous carbon derived from biomass source cornstalks. Bioresour Technol 2008;99:4803-8.
64. Zhang F, Li GD, Chen JS. Effects of raw material texture and activation manner on surface area of porous carbons derived from biomass resources. J Colloid Interface Sci 2008;327:108-14.
65. Hsu LY, Teng H. Influence of different chemical reagents on the preparation of activated carbons from bituminous coal. Fuel Process Technol 2000;64:155-66.
66. Sevilla M, Valle-Viǵon P, Fuertes AB. N-doped polypyrrole-based porous carbons for CO_2 capture. Adv Funct Mater 2011;21:2781-7.
67. Eletskii PM, Yakovlev VA, Fenelonov VB, Parmon VN. Texture and adsorptive properties of microporous amorphous carbon materials prepared by the chemical activation of carbonized high-ash biomass. Kinet Catal 2008;49:708-19.

68. Xiao Y, Dong H, Long C, Zheng M, Lei B, Zhang H, Liu Y. Melaleuca bark based porous carbons for hydrogen storage. Int J Hydrogen Energy 2014;39:11661-7.
69. Nijkamp MG, Raaymakers J, van Dillen AJ, de Jong KP. Hydrogen storage using physisorption-materials demands. Appl Phys A Mater Sci Process 2001;72:619-23.
70. Wang J, Senkovska I, Kaskel S, Liu Q. Chemically activated fungi-based porous carbons for hydrogen storage. Carbon 2014;75:372-80.
71. Wang H, Gao Q, Hu J. High hydrogen storage capacity of porous carbons prepared by using activated carbon. J Am Chem Soc 2009;131:7016-22.
72. Budd PM, Ghanem B, Msayib K, McKeown NB, Tattershall C. A nanoporous network polymer derived from hexaazatrinaphthylene with potential as an adsorbent and catalyst support. J Mater Chem 2003;13:2721-6.
73. Yang ZX, Xia YD, Mokaya R. Enhanced hydrogen storage capacity of high surface area zeolite-like carbon materials. J Am Chem Soc 2007;129:1673-9.
74. Ma Z, Kyotani T, Liu Z, Terasaki O, Tomita A. Very high surface area microporous carbon with a three-dimensional nano-array structure: synthesis and its molecular structure. Chem Mater 2001;13:4413-5.
75. Han S, Kim M, Hyeon T. Direct fabrication of meso-porous carbons using in-situ polymerized silica gel networks as a template. Carbon 2003;41:1525-32.
76. Stadie NP, Vajo JJ, Cumberland RW, Wilson AA, Ahn CC, Fultz B. Zeolite-templated carbon materials for high-pressure hydrogen storage. Langmuir 2012;28:10057-63.
77. Sevilla M, Alam N, Mokaya R. Enhancement of hydrogen storage capacity of zeolite-templated carbons by chemical activation. J Phys Chem C 2010;114:11314-9.
78. Nakano T, Nozue Y. Orbital degeneracy and magnetic properties of potassium clusters incorporated into nanoporous crystals of zeolite A. J Comput Methods Sci Eng 2007;7:443-62.

79. Langmi HW, Book D, Walton A, Johnson SR, Al-Mamouri MM, Speight JD, Edwards PP, Harris IR, Anderson PA. Hydrogen storage in ion-exchanged zeolites. J Alloys Compd 2005;404:637-42.
80. Vitillo JG, Ricchiardi G, Spoto G, Zecchina A. Theoretical maximal storage of hydrogen in zeolitic frameworks. Phys Chem Chem Phys 2005;7:3948-54.
81. Kaye SS, Dailly A, Yaghi OM, Long JR. Impact of preparation and handling on the hydrogen storage properties of Zn_4O(1,4-benzenedicarboxylate)$_3$ (MOF-5). J Am Chem Soc 2007;129:14176-7.
82. Yaghi OM, O'Keeffe M, Ockwig NW, Chae HK, Eddaoudi M, Kim J. Reticular synthesis and the design of new materials. Nature 2003;423:705-14.
83. Li M, Li D, O'Keeffe M, Yaghi OM. Topological analysis of metal-organic frameworks with polytopic linkers and/or multiple building units and the minimal transitivity principle. Chem Rev 2014;114:1343-70.
84. Rosi NL, Eckert J, Eddaoudi M, Vodak DT, Kim J, O'Keeffe M, Yaghi OM. Hydrogen storage in microporous metal-organic frameworks. Science 2003;300:1127-9.
85. Hafizovic J, Bjørgen M, Olsbye U, Dietzel PDC, Bordiga S, Prestipino C, Lamberti C, Lillerud KP. The inconsistency in adsorption properties and powder XRD data of MOF-5 is rationalized by framework interpenetration and the presence of organic and inorganic species in the nanocavities. J Am Chem Soc 2007;129:3612-20.
86. Suh MP, Park HJ, Prasad TK, Lim DW. Hydrogen Storage in Metal-Organic Frameworks. Chem Rev 2012;112:782-835.
87. Phan A, Doonan C, Uribe-Romo FJ, Knobler CB, O'keeffe M, Yaghi OM. Synthesis, structure, and carbon dioxide capture properties of zeolitic imidazolate frameworks. Acc Chem Res 2009;43:58-67.

88. McKeown NB, Budd PM, Book D. Microporous polymers as potential hydrogen storage materials. Macromol Rapid Commun 2007;28:995-1002.
89. Budd PM, Butler A, Selbie J, Mahmood K, McKeown NB, Ghanem B, Msayib K, Book D, Walton A. The potential of organic polymer-based hydrogen storage materials. Phys Chem Chem Phys 2007;9:1802-8.
90. Ghanem BS, Msayib KJ, McKeown NB, Harris KDM, Pan Z, Budd PM, Butler A, Selbie J, Book D, Walton A. A triptycene-based polymer of intrinsic microposity that displays enhanced surface area and hydrogen adsorption. Chem Commun 2007:67-9.
91. Makhseed S, Samuel J. Hydrogen adsorption in microporous organic framework polymer. Chem Commun 2008:4342-4.
92. McKeown NB, Budd PM. Polymers of intrinsic microporosity (PIMs): organic materials for membrane separations, heterogeneous catalysis and hydrogen storage. Chem Soc Rev 2006;35:675-83.
93. Khawam A, Flanagan DR. Solid-state kinetic models: basics and mathematical fundamental. J Phys Chem B 2006;110:17315-28.
94. Hancock JD, Sharp JH. Method of comparing solid-state kinetic data and its application to the decomposition of kaolinite, brucite, and $BaCO_3$. J Am Ceram Soc 1972;55:74-7.
95. Sharp JH, Brindley GW, Achar BNN. Numerical data for some commonly used solid state reaction equations. J Am Ceram Soc 1966;49:379-82.
96. Ginstling AM, Brounshtein BI. Concerning the diffusion kinetics of reaction in spherical particle. J Appl Chem USSR 1950;23:1327-38.
97. Muthukumar P, Satheesh A, Linder M, Mertz R, Groll M. Studies on hydriding kinetics of some La-based metal hydride alloys. Int J Hydrogen Energy 2009;34:7253-62.
98. Avrami M, Kinetics of phase change. I General theory. J Chem Phys 1939;7:1103-12.

99. Ivey DG, Northwood DO. Storing energy in metal hydrides: a review of the physical metallurgy. J Mater Sci 1983;18:321-47.

100. Nørskov JK, Houmøller A, Johansson PK, Lundqvist BI. Adsorption and dissociation of H_2 on Mg surfaces. Phys Rev Lett 1981;46:257-60.

101. Spatz P, Aebischer HA, Krozer A, Schlapbach L. The diffusion of H in Mg and the nucleation and growth of MgH_2 in thin films. Z Phys Chem 1993;181:393-7.

102. Jain IP, Lal C, Jain A. Hydrogen storage in Mg: a most promising material. Int J Hydrogen Energy 2010;35:5133-44.

103. Polanski M, Nielsen TK, Cerenius Y, Bystrzycki J, Jensen TR. Synthesis and decomposition mechanisms of Mg_2FeH_6 studied by in-situ synchrotron X-ray diffraction and high-pressure DSC. Int J Hydrogen Energy 2010;35:3578-82.

104. Yamada T, Yin J, Tanaka K. Hydrogen storage properties and phase structures of Mg-rich Mg-Pd, Mg-Nd and Mg-Pd-Nd alloys. Mater Trans 2001;42:2415-21.

105. Cao Z, Ouyang L, Wu Y, Wang H, Liu J, Fang F, Sun D, Zhang Q, Zhu M. Dual-tuning effects of In, Al, and Ti on the thermodynamics and kinetics of $Mg_{85}In_5A_{15}Ti_5$ alloy synthesized by plasma milling. J Alloys Compd 2015;623:354-8.

106. Norek M, Nielsen TK, Polanski M, Kunce I, Płociński T, Jaroszewicz LR, Cerenius Y, Jensen TR, Bystrzycki J. Synthesis and decomposition mechanisms of ternary Mg_2CoH_5 studied using in situ synchrotron X-ray diffraction. Int J Hydrogen Energy 2011;36:10760-70.

107. Liang G, Schulz R. The reaction of hydrogen with Mg-Cd alloys prepared by mechanical alloying. J Mater Sci 2004;39:1557-62.

108. Higuchi K, Kajioka H, Toiyama K, Fujii H, Orimo S, Kikuchi Y. In situ study of hydriding dehydriding properties in some Pd/Mg thin films with different degree of Mg crystallization. J Alloys Compd 1999;295:484-9.

109. Chen J, Yang HB, Xia YY, Kuriyama N, Xu Q, Sakai T. Hydriding and dehydriding properties of amorphous magnesium-nickel films prepared by a sputtering method. Chem Mater 2002;14:2834-6.

110. Orimo S, Fujii H. Materials science of Mg-Ni based new hydrides. Appl Phys A Mater Sci Process 2001;72:167-86.

111. Webb CJ. A review of catalyst enhanced magnesium hydride as a hydrogen storage material. J Phys Chem Solids 2015;84:96-106.

112. Zaluska A, Zaluski L, Ström-Olsen JO. Synergy of hydrogen sorption in ball-milled hydrides of Mg and Mg_2Ni. J Alloys Compd 1999;289:197-206.

113. Suryanarayana C. Mechanical alloying and milling. Prog Mater Sci 2001;46:1-184.

114. Huot J, Ravnsbæk DB, Zhang J, Cuevas F, Latroche M, Jensen TR. Mechanochemical synthesis of hydrogen storage materials. Prog Mater Sci 2013;58:30-75.

115. Varin RA, Czujko T, Wronski Z. Particle size, grain size and γ-MgH_2 effects on the desorption properties of nanocrystalline commercial magnesium hydride processed by controlled mechanical milling. Nanotechnology 2006;17:3856-65.

116. Nielsen TK, Besenbacher F, Jensen TR. Nanoconfined hydrides for energy storage. Nanoscale 2011;3:2086-98.

117. Fuster V, Castro FJ, Troiani H, Urretavizcaya G. Characterization of graphite catalytic effect in reactively ball-milled MgH_2-C and Mg-C composites. Int J Hydrogen Energy 2011;36:9051-61.

118. Rud AD, Lakhnik AM. Effect of carbon allotropes on the structure and hydrogen sorption during reactive ball-milling of Mg-C powder mixtures. Int J Hydrogen Energy 2012;37:4179-87.

119. Aminorroaya S, Liu HK, Cho Y, Dahle A. Microstructure and activation characteristics of Mg-Ni alloy modified by multi-walled carbon nanotubes. Int J Hydrogen Energy 2010;35:4144-53.

120. Jia Y, Guo Y, Zou J, Yao X. Hydrogenation/dehydrogenation in MgH_2-activated carbon composites prepared by ball milling. Int J Hydrogen Energy 2012;37:7579-85.

121. Lototskyy MV, Sibanyoni JM, Denys RV, Williams M, Pollet BG, Yartys VA. Magnesium-carbon hydrogen storage hybrid materials produced by reactive ball milling in hydrogen. Carbon 2013;57:146-60.

122. Lototskyy MV, Yartys VA, Pollet BG, Bowman RC. Metal hydride hydrogen compressors: a review. Int J Hydrogen Energy 2014;39:5818-51.

123. Corré S, Bououdina M, Fruchart D, Adachi G. Stabilisation of high dissociation pressure hydrides of formula $La_{1-x}Ce_xNi_5$ ($x = 0\text{-}0.3$) with carbon monoxide. J Alloys Compd 1998;275:99-104.

124. Zaluska A, Zaluski L, Ström-Olson JO. Structure, catalysis and atomic reactions on the nano-scale: a systematic approach to metal hydrides for hydrogen storage. Appl Phys A 2001;72:157-65.

125. Davids MW, Lototskyy MV, Nechaev A, Naidoo Q, Williams M, Klochko Y. Surface modification of TiFe hydrogen storage alloy by metal-organic chemical vapour deposition of palladium. Int J Hydrogen Energy 2011;36:9743-50.

126. Bououdina M, Soubeyroux JL, Fruchart D, Rango PD. Study of the hydrogenation/dehydrogenation processes of $ZrCr_{0.7}Ni_{1.3}$, a Laves phase-rich multi-component system, by in-situ neutron diffraction under hydrogen gas pressure. J Alloys Compd 2001;327:185-94.

127. Bououdina M, Grant D, Walker G. Review on hydrogen absorbing materials-structure, mirostructure, and thermodynamic properties. Int J Hydrogen Energy 2006;31:177-82.

128. Yu XB, Wu Z, Xia BJ, Xu NX. Enhancement of hydrogen storage capacity of Ti-V-Cr-Mn BCC phase alloys. J Alloys Compd 2004;372:272-7.

129. Kumar A, Shashikala K, Banerjee S, Nuwad J, Das P, Pillai CGS. Effect of cycling on hydrogen storage properties of Ti_2CrV alloy. Int J Hydrogen Energy 2012;37:3677-82.

130. Yu XB, Yang ZX, Feng SL, Wu Z, Xu NX. Influence of Fe addition on hydrogen storage characteristics of Ti-V-based alloy. Int J Hydrogen Energy 2006;31:1176-81.

131. Pan H, Li R, Liu Y, Gao M, Miao H, Lei Y, Wang Q. Structure and electrochemical properties of the Fe substituted Ti-V-based hydrogen storage alloys. J Alloys Compd 2008;463:189-95.

132. Rusman NAA, Dahari M. A review on the current progress of metal hydrides material for solid-state hydrogen storage applications. Int J Hydrogen Energy 2013;41:12108-26.

133. Bogdanovic B, Scwickardi M. Ti-doped alkali metal aluminium hydrides as potential novel reversible hydrogen storage materials. J Alloys Compds 1997;253-254:1-9.

134. Genma R, Okada N, Sobue T, Uchida H-H. Mechanically milled alanates as hydrogen storage materials. Int J Hydrogen Energy 2006;31(2):309-11.

135. Christian M, Aguey-Zinsou KF. Destabilisation of complex hydrides through size effects. Nanoscale 2010;2:2587-90.

136. Stavila V, Bhakta RK, Alam TM, Majzoub EH, Allendorf MD. Reversible Hydrogen Storage by $NaAlH_4$ Confined within a Titanium-Functionalized MOF-74(Mg) Nanoreactor. ACS Nano 2012;6 (11):9807-17.

137. Zheng SY, Fang F, Zhou GY, Chen GR, Ouyang LZ, Zhu M, Sun DL. Hydrogen Storage Properties of Space-Confined $NaAlH_4$ Nanoparticles in Ordered Mesoporous Silica. Chem Mater 2008;20:3954-8.

138. Cai W, Wang H, Sun D, Zhang Q, Yao X, Zhu M. Destabilization of $LiBH_4$ dehydrogenation through H^+-H^- interactions by cooperating with alkali metal hydroxides. RSC Adv 2014;4:3082-9.

139. Zhong Y, Kang X, Wang K, Wang P. Improved reversible dehydrogenation of $LiBH_4$-MgH_2 composite by the synergistic effects of Al and MgO. Int J Hydrogen Energy 2014;39:2187-93.

140. Wellons MS, Berseth PA, Zidan R. Novel catalytic effects of fullerene for $LiBH_4$ hydrogen uptake and release. Nanotechnology 2009;20:204022(1)-204022(4).

141. Huang J, Yan Y, Ouyang L, Wang H, Liu J, Zhu M. Increased air stability and decreased dehydrogenation temperature of $LiBH_4$ via modification within poly(methylmethacrylate). Dalton Trans 2014;43:410-3.

142. Tu G, Xiao X, Jiang Y, Qin T, Li S, Ge H, et al. Composite cooperative enhancement on the hydrogen desorption kinetics of $LiBH_4$ by co-doping with $NbCl_5$ and hexagonal BN. Int J Hydrogen Energy 2015;40:10527-35.

143. Ward PA, Teprovich JA Jr, Peters B, Wheeler J, Compton RN, Zidan R. Reversible hydrogen storage in a $LiBH_4$-C60 nanocomposite. J Phys Chem C 2013;117:22569-75.

144. Chen P, Xiong Z, Luo J, Lin J, Tan KL. Interaction of hydrogen with metal nitrides and imides. Nature 2002;420:302-4.

145. Ichikawa T, Hanada N, Isobe S, Leng HY, Fujii H. Hydrogen storage properties in Ti catalyzed Li-N-H system. J Alloys Compds 2005;404-406:435-8.

146. Aguey-Zinsou KF, Yao J, Guo ZX. Reaction paths between $LiNH_2$ and LiH with effects of nitrides. J Phys Chem B 2007;111:12531-6.

147. Luo W, Sickafoose S. Thermodynamic and structural characterization of the Mg-Li-N-H hydrogen storage system. J Alloys Compds 2006;407:274-81.

148. Goodell PD, Rudman PS. Hydriding and dehydriding rates of the $LaNi_5$-H system. J Less-Comm Met 1983;89:117-25.

149. Briki C, Belkhiria S, Dhaou MH, Askri F, Jemni A. Dynamic study of a new design of a tanks based on metallic hydrides. Int J Hydrogen Energy 2018;43:1566-76.

150. Nahm KS, Kim WY, Hong SP, Lee WY. The reaction kinetics of hydrogen storage in $LaNi_5$. Int J Hydrogen Energy 1992;17:333-8.

151. Jia Y, Han S, Zhang W, et al. Hydrogen absorption and desorption kinetics of MgH_2 catalyzed by MoS_2 and MoO_2. Int J Hydrogen Energy 2013;38(5):2352-6.

152. Zou J, Zeng X, Ying Y, Chen X, Guo H, Zhou S, Ding W. Study on the hydrogen storage properties of core-shell structured Mg-RE (RE = Nd, Gd, Er) nano-composites synthesized through arc plasma method. Int J Hydrogen Energy 2013;38:2337-46.

153. Gross AF, Vajo JJ, Van Atta SL, Olson GL. Enhanced hydrogen storage kinetics of $LiBH_4$ in nanoporous carbon scaffolds. J Phys Chem C 2008;112:5651-7.

154. Itoh H, Arashima H, Kubo K, Kabutomori T, Ohnishi K. Improvement of Cyclic Durability of BCC Structured Ti-Cr-V Alloys. J Alloys Compd 2005;404:417-20.

155. Aoki M, Noritake T, Ito A, Ishikiriyama M, Towata S. Improvement of Cyclic Durability of Ti-Cr-V Alloy by Fe Substitution. Int. J. Hydrogen Energy 2011;36:12329-32.

156. Selvaraj S, Jain A, Kumar S, Zhang T, Isobe S, Miyaoka H, Kojima Y, Ichikawa T. Study of cyclic performance of V-Ti-Cr alloys employed for hydrogen compressor. Int J Hydrogen Energy 2018;43:2881-9.

157. Kim H, Sakaki K, Ogawa H, Nakamura Y, Nakamura J, Akiba E, Machida A, Watanuki T, Proffen T. Origin of degradation in the reversible hydrogen storage capacity of $V_{1-x}Ti_x$ alloys from the atomic pair distribution function analysis, J Phys Chem C 2013;117:26543-50.

158. Ming Y, Purewal J, Yang J, Xu C, Veenstra M, Gaab M, Muller U, Siegel DJ. Stability of MOF-5 in a hydrogen gas environment containing fueling station impurities. Int J Hydrogen Energy 2016;41:9374-82.

159. Pedersen AS, Vigeholm B, Kjøller J, Larsen B. The effect of cycling in impure hydrogen on the hydrogen capacity of magnesium powder. Int J Hydrogen Energy 1987;12:765-71.

160. Lim KL, Liu Y, Zhang QA, Lin KS, Chan SLI. Cycle stability improvement of La-Mg-Ni based alloys via composite method J Alloys Compd 2016;661:274-81.

161. Nagel M, Komazaki Y, Suda S. Effective thermal conductivity of a metal hydride bed augmented with a copper wire matrix. J Less-Common Met 1986;120:35-43.

162. Laurencelle F, Goyette J. Simulation of heat transfer in a metal hydride reactor with aluminium foam. Int. J. Hydrogen Energy 2007;32:2957-64.

163. Fleming WH, Khan JA, Rhodes CA. Effective heat transfer in a metal-hydride based hydrogen separation process. Int J Hydrogen Energy 2001;26:711-24.

164. Suda S, Komazaki Y, Kobayashi N. Effective thermal conductivity of metal hydride beds. J Less-Common Met 1983;89:317-24.

165. Bonnetot B, Chahine G, Claudy P, Diot M, Letoffe JM. Sodium tetrahydridoaluminate $NaAIH_4$ and hexahydridoaluminate Na_3AIH_6 molar heat capacity and thermodynamic properties from 10 to 300 K. J Chem Thermodyn 1980;12(3):249-54.

166. Mayer U, Groll M, Supper W. Heat and mass transfer in metal hydride reaction beds: Experimental and theoretical results. J Less-Common Met 1987;131:235-44.

167. Muthukumar P, Singhal A, Bansal GK. Thermal modeling and performance analysis of industrial-scale metal hydride based hydrogen storage container. Int J Hydrogen Energy 2012;37:14351-64.

168. Mellouli S, Askri F, Dhaou H, Jemni A, Nasrallah SB. Numerical simulation of heat and mass transfer in metal hydride hydrogen storage tanks for fuel cell vehicles. Int J Hydrogen Energy 2010;35:1693-1705.

169. Bellosta von Colbe JM, Metz O, Lozano GA, Pranzas PK, Schmitz HW, Beckmann F, Schreyer A, Klassen T, Dornheim M. Behavior of scaled-up sodium alanate hydrogen storage tanks during sorption. Int. J. Hydrogen Energy 2012;37:2807-11.

170. Johnson TA, Jorgensen SW, Dedrick DE. Performance of a full-scale hydrogen-storage tank based on complex hydrides. Faraday Discuss 2011;151:327-52.

171. Johnson TA, Kanouff MP, Dedrick DE, Evans GH, Jorgensen SW. Model-based design of an automotive-scale, metal hydride hydrogen storage system. Int J Hydrogen Energy 2012;37:2835-49.

172. Dasgupta K, Sen D, Mazumder S, Basak CB, Joshi JB, Banerjee S. Optimization of parameters by Taguchi method for controlling purity of carbon nanotubes in chemical vapour deposition technique. J Nanosci Nanotechnol 2010;10:4030-7.

173. Klug HP, Alexander LE. X-ray diffraction procedures. Wiley-Interscience Publication, New York (1974).

174. Cullity BD. Elements of X-ray diffraction. Addison-Wilson Publishing Comp Inc, USA (1959).

175. Jakkal VS, Powderx: a Fortran software for refining the unit cell parameters from the powder diffraction pattern. Private communication.

176. Cahn RW, Haasen P, Kramer EJ. Material Science and Engineering: Characterisation of Materials. VCH Publisher Inc, New York (1991).

177. Reed SJB. Electron Microprobe Analysis (2nd Ed.). Cambridge University Press (1993).

178. Glatter O, Kratky O. Small-angle X-ray Scattering. Academic Press, London (1982).

179. Guinier A, Fournet G. Small Angle Scattering of X-rays. John Wiley (1955).

180. Atkins PW. Physical Chemistry (5th Ed). Freeman WH, New York (1994).

181. Haines PJ, Wilburn FW. Differential thermal analysis and differential scanning calorimetry, Thermal Methods of Analysis. (P. J. Haines, Ed.). pp. 63-122. Blackie Academic and Professional, London. (1995).

182. Redhead PA. Thermal desorption of gases. Vacuum 1962;12:203-11.

183. Long DA. The Raman effect: a unified treatment of the theory of Raman scattering by molecules. John Willey & Sons Ltd (2002).

184. Herzberg G. Molecular spectra and molecular structure-II infrared and Raman spectra of polyatomic molecules. D. Van Nostrand Company: USA (1945).

185. Banwell BN, McCash EM. Fundamentals of molecular spectroscopy. Tata McGraw-Hill publishers Ltd (4th Ed), New Delhi (2000).

186. Andrew ER, Bradbury A, Eades RG. Removal of dipolar broadening of nuclear magnetic resonance spectra of solids by specimen rotation. Nature 1959;183:1802-3.

187. Lowe IJ. Free induction decays of rotating solids. Phys Rev Lett 1959;2:285-7.

188. Mössbauer Spectroscopy Group, Introduction to Mössbauer Spectroscopy, Royal Society of Chemistry (RSC) website.

189. Checchetto R, Trettel G, Miotello A. Sievert-type apparatus for the study of hydrogen storage in solids. Meas Sci Technol 2004;15:127-30.

190. Lee J, Kim J, Hyeon T. Recent progress in the synthesis of porous carbon materials. Adv Mater 2006;18:2073-94.

191. Xu WC, Takahashi K, Matsuo Y, Hattori Y, Kumagai M, Ishiyama S, et al. Investigation of hydrogen storage capacity of various carbon materials. Int J Hydrogen Energy 2007;32:2504-12.

192. Nishihara H, Kyotani T. Templated nanocarbons for energy storage. Adv Mater 2012;24:4473-98.

193. Masika E, Mokaya R. Hydrogen storage in high surface area carbons with identical surface areas but different pore sizes: direct demonstration of the effects of pore size. J Phys Chem C 2012;116:25734-40.

194. Yang SJ, Kim T, Im JH, Kim YS, Lee K, Jung H, Park CR. MOF-derived hierarchically porous carbon with exceptional porosity and hydrogen storage capacity. Chem Mater 2012;24:464-70.

195. Chambers A, Park C, Baker RTK, Rodriguez NM. Hydrogen storage in graphite nanofiber. J Phys Chem B 1998;102:4253-6.

196. Hirscher M, Becher M. Hydrogen storage in carbon nanotubes. J Nanosci Nanotechnol 2006;3:3-17.

197. Froudakis GE. Hydrogen storage in nanotubes & nanostructures. Mater Today 2011;14:324-8.

198. Broom DP, Hirscher M. Irreproducibility in hydrogen storage material research. Energy Environ Sci 2016;9:3368-80.

199. Liu C, Chen Y, Wu CZ, Xu ST, Cheng HM. Hydrogen storage in carbon nanotubes revisited. Carbon 2010;48:452-5.

200. Rather S, Zacharia R, Hwang SW, Naik M, Nahm KS. Hydrogen uptake of palladium-embedded MWCNTs produced by impregnation and condensed phase reduction method. Chem Phys Lett 2007;441:261-7.

201. Lin KY, Tsai WT, Chang JK. Decorating carbon nanotubes with Ni particles using an electroless deposition technique for hydrogen storage applications. Int J Hydrogen Energy 2010;35:7555-62.

202. Campesi R, Cuevas F, Gadiou R, Leroy E, Hirscher M, Vix-Guterl C, Latroche M. Hydrogen storage properties of Pd nanoparticle/carbon template composites. Carbon 2008;46:206-4.

203. Huang JY, Yasuda H, Mori H. Highly curved carbon nanostructures produced by ball-milling. Chem Phys Lett 1999;303:130-4.

204. Chen Y, Gerald JF, Chadderton LT, Chaffron L. Nanoporous carbon produced by ball milling. Appl Phys Lett 1999;74:2782-4.

205. Darkrim F, Vermesse J, Malbrunot P, Levesque D. Monte Carlo simulations of nitrogen and hydrogen physisorption at high pressures and room temperature. Comparison with experiments. J Chem Phys 1999;110:4020-7.

206. Patchkovsky S, Tse JS, Yurchenko SN, Zhechov L, Heine T, Seifert G. Graphene nanostructures as tunable storage media for molecular hydrogen. Proc Natl Acad Sci 2005;102:10439-44.

207. Lueking D, Pan L, Narayanan DL, Clifford CEB. Effect of expanded graphite lattice in exfoliated graphite nanofibers on hydrogen storage. J Phys Chem B 2005;109:12710-7.

208. Cabria I, López MJ, Alonso JA. Simulation of the hydrogen storage in nanoporous carbons with different pore shapes. Int J Hydrogen Energy 2011;36:10748-59.

209. Alonso JA, Cabria I, López MJ. Simulation of hydrogen storage in porous carbons. J Mater Res 2013;28:589-604.

210. Variava M, Church TL, Harris AT, Minett AI. Polyol-assisted functionalization of carbon nanotubes-a perspective. J Mater Chem A 2013;1:8509-20.

211. Georgakilas V, Gournis D, Tzitzios V, Pasquato L, Guldi DM, Prato M. Decorating carbon nanotubes with metal or semiconductor nanoparticles. J Mater Chem 2007;17:2679-94.

212. Ströbel R, Garche J, Moseley P, Jörissen L, Wolf G. Hydrogen storage by carbon materials. J Power Sources 2006;159(2):781-801.

213. Li W, Liang C, Zhou W, Qiu J, Zhou Z, Sun G, Xin Q. Preparation and characterization of multiwalled carbon nanotube-supported platinum for cathode catalysts of direct methanol fuel cells. J Phys Chem B 2003;107:6292-9.

214. Reyhani A, Mortazavi SZ, Moshfegh AZ, Nozad Golikand A, Amiri M. Enhanced electrochemical hydrogen storage by catalytic Fe-doped multi-walled carbon nanotubes synthesized by thermal chemical vapor deposition. J Power Sources 2009;188:404-10.

215. Schmidt PW, R. Hight R Jr. Slit height corrections in small angle X-ray scattering. Acta Cryst 1960;13:480-3.

216. Li ZQ, Lu CJ, Xia ZP, Zhou Y, Luo Z. X-ray diffraction patterns of graphite and turbostratic carbon. Carbon 2007;45:1686-95.

217. Kim C, Park SH, Cho JI, Lee DY, Park TJ, Lee WJ, Yang KS. Raman spectroscopic evaluation of polyacrylonitrile-based carbon nanofibers prepared by electrospinning. J Raman Spectrosc 2004;35:928-33.

218. W.E. Alvarez, B. Kitiyanan, A. Borgna, D.E. Resasco. Synergism of Co and Mo in the catalytic production of single-wall carbon nanotubes by decomposition of CO. Carbon 2001;39:547-58.

219. Schmidt PW. Small angle scattering studies of disordered, porous and fractal systems. J Appl Cryst 1991;24:414-35.

220. Bale HD, Schmidt PW. Small-angle X-Ray-scattering investigation of submicroscopic porosity with fractal properties. Phys Rev Lett 1984;53:596-9.

221. Ostafiychuk BK, Mandzyuk VI, Kulyk YO, Nagirna NI. SAXS investigation of nanoporous structure of thermal-modified carbon materials. Nanoscale Res Lett 2014;9:160(1-6).

222. Yoon S, Oh SM, Lee C. Direct template synthesis of mesoporous carbon and its application to supercapacitor electrodes. Mater Res Bull 2009;44:1663-9.

223. Boldon L, Laliberte F, Liu L. Review of the fundamental theories behind small angle X-ray scattering, molecular dynamics simulations, and relevant integrated application. Nano Rev 2015;6:25661(1)-25661(21).

224. Koberstein JT, Morra B, Stein RS. The Determination of diffuse-boundary thicknesses of polymers by small-angle X-ray scattering. J Appl Cryst 1980;13:34-5.

225. Ruland W. Small-angle scattering of two-phase systems: determination and significance of systematic deviations from Porod's law. J Appl Cryst 1971;4:70-3.

226. Kim JE, Jin WC, Ahn JH. Interfacial change on morphological transitions in styrene-isoprene diblock copolymer. Eur Polym J 2009;45:2450-4.

227. Kono H, Yunoki S, Shikano T, Fujiwara M, Erata T, Takai M. CP/MAS ^{13}C NMR study of cellulose and cellulose derivatives. 1. Complete assignment of the CP/MAS ^{13}C NMR spectrum of the native cellulose. J Am Chem Soc 2002;124:7506-11.

228. Pfeffe PE, Odier L, Dudley RL. Assignment of ^{13}C Cpmas Nmr spectra of crystalline methyl β-D-glucopyranoside and sucrose using deuterium labelling and interrupted proton decoupling. J Carbohydr Chem 1990;9:619-29.

229. Dresselhaus MS, Dresselhaus G, Saito R, Jorio A. Raman spectroscopy of carbon nanotubes. Phys Rep 2005;409:47-99.

230. Yan J, Zhang Y, Kim P, Pinczuk A. Electric field effect tuning of electron-phonon coupling in graphene. Phys Rev Lett 2007;98:166802(1)-166802(4).

231. Zhang H, Bhata VV, Feng PX, Contescu CI, Gallego NC. Effect of potassium-doping on the microstructure development in polyfurfuryl alcohol-derived activated carbon. Carbon 2012;50:5278-85.

232. Wu HC, Li YY, Sakoda A. Synthesis and hydrogen storage capacity of exfoliated turbostratic carbon nanofibers. Int J Hydrogen Energy 2010;35:4123-30.

233. Rashidi AM, Nouralishahi A, Khodadadi AA, Mortazavi Y, Karimi A, Kashefi K. Modification of single wall carbon nanotubes (SWNT) for hydrogen storage. 2010;35:9489-95.

234. Rather S, Mehraj-ud-din N, Zacharia R, Hwang SW, Kim AR, Nahm KS. Hydrogen storage of nanostructured TiO_2-impregnated carbon nanotubes. Int J Hydrogen Energy 2009;34:961-96.

235. Chen CH, Huang CC. Hydrogen storage by KOH-modified multi-walled carbon nanotubes. Int J Hydrogen Energy 2007;32:237-46.

236. Wang J, Senkovska I, Kaskel S, Liu Q. Chemically activated fungi-based porous carbons for hydrogen storage. Carbon 2014;75:372-80.

237. Chen H, Wang H, Xue Z, Yang L, Xiao Y, Zheng M, Lei B, Liu Y, Sun L. High hydrogen storage capacity of rice hull based porous carbon. Int J Hydrogen Energy 2012;37:18888-94.

238. Im SJ, Park SJ, Kim TJ, Kim YH, Lee YS. The study of controlling pore size on electrospun carbon nanofibers for hydrogen adsorption. J Colloid Interface Sci 2008;318:42-9.

239. Libowitz GG, Maeland AJ. Hydride formation by b.c.c. solid solution alloys. Mater Sci Forum 1988;31:177-96.

240. Libowitz GG, Maeland AJ. Lynch JF. Brookhaven National Laboratory Rep, BNL-37866, 1985.

241. Maeland AJ, Libowitz GG, Lynch JF. Hydride formation rates of titanium-based b.c.c. solid solution alloys. J Less Common Met 1984;104:361-4.

242. Maeland AJ, Libowitz GG, Lynch JF. Hydride formation rates of b.c.c. group V metals. J. Less Common Met 1984;104:133-9.

243. Tominaga Y, Nishimura S, Amemiya T, Fuda T, Tamura T, Kuriiwa T, Kamegawa A, Okada M. Protium absorption-desorption properties of Ti-V-Cr alloys with a BCC structure. Mater Trans JIM 1999;40:871-4.

244. Fuda T, Matsumoto K, Tominaga Y, Tamura T, Kuriiwa T, Kamegawa A, Okada M. Effect of additions of bcc former elements on protium absorbing properties of Cr-Ti-V alloys. Mater Trans JIM 2000;41:577-80.

245. Kubo K, Itoh H, Takahashi T, Ebisawa T, Kabutomori T, Nakamura Y, Akiba E. Hydrogen absorbing properties and structures of Ti-Cr-Mo alloys. J Alloys Compd 2003;356-357:452-5.

246. Cho SW, Han CS, Park CN, Akiba E. The hydrogen storage characteristics of Ti-Cr-V alloys. J Alloys Compd 1999;288:294-8.

247. Yoo JH, Shim G, Cho SW, Park CN. Effects of desorption temperature and substitution of Fe for Cr on the hydrogen storage properties of $Ti_{0.32}Cr_{0.43}V_{0.25}$ alloy. Int J Hydrogen Energy 2007;329:2977-81.

248. Yu XB, Wu Z, Xia BJ, Huang TZ, Chen JZ, Wang ZS, Xu NX. Hydrogen storage in Ti-V based body-centered-cubic phase alloys. J Mater Res 2003;18:2533-6.

249. Gao SJ, Huang LJ. Hydrogen absorption and desorption by Ti, Ti-5Cr and Ti-5Ni alloys. J Alloys Compd 1999;412:293-5.

250. Sibum H. Titanium and titanium alloys-from raw material to semi-finished products. Adv Eng Mater 2003;5:393-8.

251. Banerjee D, Williams JC. Perspectives on titanium science and technology. Acta Mater 2013;61:844-79.

252. Lee PJ. Abridged metallurgy of ductile alloy superconductors. Wiley Encyclopedia of Electrical and Electronics Engineering 1999;24:1-14.

253. Lee CM, Ju CP, Lin JHC. Structure-property relationship of cast Ti-Nb alloy. J Oral Rehabil 2002;29:314-22.

254. Murray JL. Phase diagrams of binary titanium alloys. ASM International, Materials Park, Ohio (1987).

255. Yu XB, Zu W, Huang TZ, Chen JZ, Xia BJ, Xu NX. Effect of surface oxide layer on activation performance of hydrogen storage alloy $TiMn_{1.25}Cr_{0.25}$. Int J Hydrogen Energy 2004;29: 81-6.

256. Wuhui L, Erdong W. Structure and hydrogen absorbing properties of ScCrMn alloy. J Alloys Compd 2012;511:169-75.

257. Nedyakha IM, Chernyi VG. Increasing the oxidation resistance of niobium at elevated temperatures. Sov Mater Sci 1968;2:457-8.

258. Fallah V, Stephen FC, Khajep A. Solidification behaviour and phase formation during pre-placed laser cladding of Ti-45Nb on mild steel. Surf Coat Tech 2010;204:2400-9.

259. Aleksanyan AG, Dolukhanyan SK, Shekhtman VS, Khasanov SS, Ter-Galstyan OP, Martirosyan MV. Formation of alloys in the Ti-Nb system by hydride cycle method and synthesis of their hydrides in self-propagating high-temperature synthesis. Int J Hydrogen Energy 2012;37:14234-9.

260. Dutta B, Keller T, Rettenmayr M, Jantsch U, Lupton DF. Effect of ternary Al, Ni additions on hydrogen absorption behaviour of Ti-45Nb alloys. Mater Sci Eng A 2004;382:57-63.

261. Hsu YS, Perng TP. Hydrogenation of multi-component Zr-base C15 type alloys. J Alloys Compd 1995;227:180-5.

262. Krishna MK, Ramaprabhu S. Hydrogen absorption characteristics in $Mm_xTb_{1-x}Co_2$ (x

= 0, 0.05, 0.1, 0.15, 0.2). Int J Hydrogen Energy 2007;32:1890-7.

263. Reddy ALM, Ramaprabhu S. Structural and hydrogen absorption kinetics studies of polymer dispersed and boron added Zr-based AB_2 alloy. Int J Hydrogen Energy 2006;31:867-76.

264. Li Q, Chou KC, Lin Q, Jiang LJ, Zhan F. Influence of the initial hydrogen pressure on the hydriding kinetics of the $Mg_{2-x}Al_xNi$ ($x = 0, 0.1$) alloys. Int J Hydrogen Energy 2004;29:1383-8.

265. Ramesh R, Rao KVSR. Hydrogen absorption characteristics of the $Zr_{1-x}Ho_xCo_2$ system in the pressure range 0-40 bar. J. Alloys Compd 1993;191:101-5.

266. Koh JT, Goudy AJ, Huang P, Zhou GA. Comparison of the hydriding and dehydriding kinetics of $LaNi_5$ hydride. J Less Common Met 1989;153:89-100.

267. Wang X, Zhao Y, Wang Y, Hou H, Zeng W. Kinetics of hydrogen absorption/desorption in TC21 alloy. J Alloys Compd 2010;490:562-7.

268. Liu B, Li J, Han S, Hu L, Pei L, Wang M. Microstructures and hydrogen storage properties of $LaMg_{8.40}Ni_{2.34-x}Al_x$ alloys. J Alloys Compd 2012;526:6-10.

269. Greenwood NN, Gibb NN. Mössouber Spectroscopy. Chapman and Hall Ltd, London (1971).

270. Walker LR, Wertheim GK, Jaccarino V. Interpretation of the Fe^{57} Isomer Shift. Phys Rev Lett 1961;6:98-101.

271. Jain A, Jain RK, Agarwal S, Sharma RK, Kulshrestha SK, Jain IP. Structural and Mössbauer spectroscopic study of cubic phase $ZrFe_{2-x}Mn_x$ hydrogen storage alloy. J Alloys Compd 2008;454:31-7.

272. Singh M, Jain IP. Mossbauer and positron life-time studies of FeTi and $Fe_{46}Ti_{50}Mn_4$. Int J Hydrogen Energy 1996;21:367-72.

273. Okada M, Kuriiwa T, Tamura T, Takamura H, Kamegawa A. Ti-V-Cr b.c.c. alloys with high protium content. J Alloys Compd 2002;330-332:511-6.

274. Towata S, Noritake T, Itoh A, Aoki M, Miwa K. Effect of partial niobium and iron substitution on short-term cycle durability of hydrogen storage Ti-Cr-V alloys. Int J Hydrogen Energy 2013;38:3024-9.

275. Kuriiwa T, Maruyama T, Kamegawa A, Okada M. Effects of V content on hydrogen storage properties of V-Ti-Cr alloys with high desorption pressure. Int J Hydrogen Energy 2010;35:9082-7.

276. Yu XB, Chen JZ, Wu Z, Xia BJ, Xu NX. Effect of Cr content on hydrogen storage properties for Ti-V based BCC-phase alloys. Int J Hydrogen Energy 2004;29:1377-81.

277. Yoo JH, Shim G, Park CN, Kim WB, Cho SW. Influence of Mn or Mn plus Fe on the hydrogen storage properties of the Ti-Cr-V alloy. Int J Hydrogen Energy 2009;34:9116-21.

278. Guéguen A, Joubert JM, Latroche M. Influence of the C14 $Ti_{35.4}V_{32.3}Fe_{32.3}$ Laves phase on the hydrogenation properties of the body-centered cubic compound $Ti_{24.5}V_{59.3}Fe_{16.2}$. J Alloys Compd 2011;509:3013-8.

279. Young K, Ouchi T, Nei J, Meng T. Effects of Cr, Zr, V, Mn, Fe, and Co to the hydride properties of Laves phase-related body-centered-cubic solid solution alloys. J Power Sources 2015;281:164-72.

280. Akiba E, Iba H. Hydrogen absorption by Laves phase related BCC solid solution. Intermetallics 1998;16:461-70.

281. Chai YJ, Zhao MS. Structure and electrochemical properties of $Ti_{0.25}V_{0.35}Cr_{0.40-x}Ni_x$ (x = 0.05-0.40) solid solution alloys. Int J Hydrogen Energy 2005;30:279-83.

282. Miao H, Gao MX, Liu YF, Lin Y, Wang JH, Pan HG. Microstructure and electrochemical properties of Ti-V-based multiphase hydrogen storage electrode alloys $Ti_{0.8}Zr_{0.2}V_{2.7}Mn_{0.5}Cr_{0.8-x}Ni_{1.25}Fe_x$ (x = 0.0-0.8). Int J Hydrogen Energy 2007;32:3947-53.

283. Homma H, Saitoh H, Misawa T, Ohnishi T. Effect of Laves phase on hydrogen behavior in V-Zr-Ti-Ni hydrogen absorption alloys. Mater Trans 2002;43:1110-5.

284. Hang Z, Xiao X, Tan D, He Z, Li W, Li S, Chen C, Chen L. Microstructure and hydrogen storage properties of $Ti_{10}V_{84-x}Fe_6Zr_x$ (x = 1-8) alloys. Int J Hydrogen Energy 2010;35:3080-6.

285. Shashikala K, Banerjee S, Kumar A, Pai MR, Pillai CGS. Improvement of hydrogen storage properties of TiCrV alloy by Zr substitution for Ti. Int J Hydrogen Energy 2009;34:6684-9.

286. Yu XB, Walker GS, Grant DM, Wu Z, Xia BJ, Shen J. Electrochemical hydrogen storage of Ti-V-based body-centered-cubic phase alloy surface-modified with AB_5 nanoparticles. Appl Phys Lett 2005;87:133121.

287. Park HS, Chourashiya M, Yang DC, Park CN, Park CJ. Hydrogen storage and electrochemical characteristics of $Ti_{0.32}Cr_{0.43-x}V_{0.25}Fe_x$ (x = 0 - 0.08) alloys and its composites with $LmNi_{4.1}Al_{0.25}Mn_{0.3}Co_{0.65}$ alloy. J Alloys Compd 2012;513:566-72.

288. Huanga T, Wu Z, Sun G, Xu N. Hydrogen storage characteristics of composite $TiCr_{1.8}$ + X wt.% $LaNi_5$ alloys. J Alloys Compd 2008;450:505-7.

289. Singh BK, Cho SW, Bartwal KS. Effect on structure and hydrogen storage characteristics of composite alloys $Ti_{0.32}Cr_{0.43}V_{0.25}$ with $LaNi_5$ and rare-earth elements La, Ce, Y. J Alloys Compd 2009;478:785-8.

290. Kumar A, Banerjee S, Bharadwaj SR. Hydrogen storage properties of $Ti_{0.32}Cr_{0.43}V_{0.25}$ alloy and its composite with $TiMn_2$. J Alloys Compd 2015;649:801-8.

291. Koultoukis ED, Makridis SS, Pavlidou E, Rango P, Stubos AK. Investigation of $ZrFe_2$-type materials for metal hydride hydrogen compressor systems by substituting Fe with Cr or V. Int J Hydrogen Energy 2014;39:21380-5.

292. Banerjee S, Kumar A, Pillai CGS. Improvement on the hydrogen storage properties of $ZrFe_2$ Laves phase alloy by vanadium substitution. Intermetallics 2014;51:30-6.

293. Pouchou JL, Pichoir F. Basic expressions of PAP computation for quantitative EPMA. In Proceedings of ICXOM 11, Ontario; August 1987:249-53.

294. Bibienne T, Razafindramanana V, Bobet JL, Huot J. Crystal structure and hydrogen storage properties of body centered cubic 52Ti-12V-36Cr alloy doped with Zr_7Ni_{10}. J Alloys Compd 2015;620:101-8.

295. Lin HC, Lin KM, Wu KC, Hsiung HH, Tsai HK. Cyclic hydrogen absorption-desorption characteristics of TiCrV and $Ti_{0.8}Cr_{1.2}V$ alloys. Int J Hydrogen Energy 2007;32:4966-72.

296. Chen ZL, Si TZ, Zhang QA. Hydrogen absorption-desorption cycle durability of $SmMgNi_4$. J Alloys Compd 2015;621:42-6.

297. Xie SC, Chen ZL, Li YT, Si TZ, Liu DM, Zhang QA. Hydrogen absorption-desorption features and degradation mechanism of $ErNi_3$ compound. J Alloys Compd 2014;585:650-5.

298. Edalati K, Shao H, Emami H, Iwaoka H, Akiba E, Horita Z. Activation of titanium-vanadium alloy for hydrogen storage by introduction of nanograins and edge dislocations using high-pressure torsion. Int J Hydrogen Energy 2016;41:8917-24.

299. Nakamura H, Nakamura Y, Fujitani S, Yonezu I. Cycle performance of a hydrogen-absorbing $La_{0.8}\ Y_{0.2}\ Ni_{4.8}\ Mn_{0.2}$ alloy. Int J Hydrogen Energy 1996;21:457-60.

300. Zhou C, Fang ZZ, Bowman RC. Stability of catalyzed magnesium hydride nanocrystalline during hydrogen cycling. Part I: kinetic analysis. J Phys Chem C 2015;119:22261-71.

301. Mordkovich VZ, Korostyshevsky NN, Baychtok YK, Mazus EI, Dudakova NV, Mordovin VP. Degradation of $LaNi_5$ by thermobaric cycling in hydrogen and hydrogen-nitrogen mixture. Int J Hydrogen Energy 1990;15:723-6.

302. Fromm E, Uchida H. Surface phenomena in hydrogen absorption kinetics of metals and intermetallic compounds. J Less Common Met 1987;131:1-12.

303. Fromm E, Wulz HG. Effect of oxygen surface contamination on the hydrogen absorption kinetics of metal films studied by a modified volumetric Wagener method. J Less Common Met 1984;101:469-79.

304. Bulyk II, Basaraba YB, Dovhyj YO. Influence of Ti on the hydrogen-induced phase-structure transformations in the $ZrCr_2$ intermetallic compound. Intermetallics 2006;14:735-41.

305. Ruz P, Kumar A, Banerjee S, Meena SS, Pillai CGS. Hydrogen absorption-characteristics and Mössbauer spectroscopic study of $Ti_{0.67}Nb_{0.33-x}Fe_x$ (x = 0.00, 0.13, 0.20) alloys. J Alloys Compd 2014;585:120-8.

306. Kumar A, Banerjee S, Pillai CGS, Bharadwaj SR. Hydrogen storage properties of $Ti_{2-x}CrVM_x$ (M = Fe, Co, Ni) alloys. Int J Hydrogen Energy 2013;38:13335-42.

307. Gesari SB, Pronsato ME, Visintin A, Juan A. Hydrogen storage in AB_2 Laves phase (A = Zr, Ti; B = Ni, Mn, Cr, V): binding energy and electronic structure. J Phys Chem C 2010;114:16832-6.

308. Jain A, Jain RK, Agarwal S, Ganesan V, Lalla NP, Phase DM, et al. Synthesis, characterization and hydrogenation of $ZrFe_{2-x}Ni_x$ (x = 0. 2, 0.4, 0.6, 0.8) alloys. Int J Hydrogen Energy 2007;32:3965-71.

309. Hong S, Fu CL. Hydrogen in Laves phase ZrX_2 (X = V, Cr, Mn, Fe, Co, Ni) compounds: binding energies and electronic and magnetic structure. Phys Rev B 2002;66:094109(1)-094109(6).

310. Zhang YL, Li JS, Zhang TB, Hu R, Xue XY. Microstructure and hydrogen storage properties of non-stoichiometric Zr-Ti-V Laves phase alloys. Int J Hydrogen Energy 2013;38:14675-84.

311. Yvon K, Fischer P. Hydrogen in intermetallic compounds I. Schlapbach L (Ed), Topics in applied physics, vol. 63, Springer, Berlin (1988).

312. Shaltiel D, Jacob I, Davidov D. Hydrogen absorption and desorption properties of AB_2 Laves-phase pseudobinary compounds. J Less-Common Met 1977;53:117-31.

313. Yang XW, Zhang TB, Hu R, Li JS, Xue XY, Fu HZ. Microstructure and hydrogenation thermokinetics of $ZrTi_{0.2}V_{1.8}$ alloy. Int J Hydrogen Energy 2010;35:11981-5.

314. Yang XW, Li JS, Zhang TB, Hu R, Xue XY, Fu HZ. Role of defect structure on hydrogenation properties of $Zr_{0.9}Ti_{0.1}V_2$ alloy. Int J Hydrogen Energy 2011;36:9318-23.

315. Yu JS, Lee SM, Cho K, Lee JY. The cycle life of $Ti_{0.8}Zr_{0.2}V_{0.5}Mn_{0.5-x}Cr_xNi_{0.8}$ (x = 0 to 0.5) alloys for metal hydride electrodes of Ni-Metal hydride rechargeable battery. J Electrochem Soc 2000;147:2013-7.

316. Iwakura C, Kasuga H, Kim I, Inoue H, Matsuoka M. Effect of alloy composition on electrochemical properties of the Zr-based Laves-phase hydrogen storage alloys. Electrochim Acta 1996;41:2691-4.

317. Levin I, Krayzman V, Chiu C, Moon KW, Bendersky LA. Local metal and deuterium ordering in the deuterated ZrTiNi C14 Laves phase. Acta Mater 2012;60:645-56.

318. Bououdina M, Lambert-Andron B, Ouladdiaf B, Pairis S, Fruchart D. Structural investigations by neutron diffraction of equi-atomic Zr-Ti(V)-Ni(Co) compounds and their related hydrides, J Alloys Compd 2003;356:54-8.

319. Bloch J, Mintz M. Kinetics and mechanisms of metal hydrides formation-a review. J Alloys Compd 1997;253-254:529-41.

320. Liang G, Hout J, Boily S, Schulz R. Hydrogen desorption kinetics of a mechanically milled MgH_2+ 5 at% V nanocomposite. J Alloys Compd 2000;305:239-45.

321. Martin M, Gommel C, Borkhart C, Fromm E. Absorption and desorption kinetics of hydrogen storage alloys. J Alloys Compd 2000;238:193-201.

322. Aubertin F, Campbell SJ. Phase separation in hydrides of Zr_2Ni. Hyperfine interactions 1990;54:767-74.

323. Hara M, Hayakawa R, Kaneko Y, Watanabe K. Hydrogen-induced disproportionation of Zr_2M (M = Fe, Co, Ni) and reproportionation. J Alloys Compd 2003;352:218-25.

324. Chikdene A, Baudry A, Boyer P, Miraglia S, Fruchart D, Soubeyroux JE. Neutron diffraction studies of $Zr_2NiH(D)_x$ hydrides. Z Phys Chem N F 1989;163:219-24.

325. Aubertin F, Campbell SJ, Gonser U. Hydrogenation of Zr_2Ni. Hyperfine Interact 1986;28:997-1000.

326. Porter MM, Yu J. Crystallization kinetics of poly(3-hydroxybutyrate) granules in different environmental conditions. J Biomater Nanobiotechno 2011;12:301-10.

327. Vigeholm B, Jensen K, Larsen B, Schroder-Pedersen A. Elements of hydride formation mechanisms in nearly spherical magnesium powder particles. J Less Common Met 1987;131:133-41.

328. Pradell T, Crespo D, Clavaguera N, Clavaguera-Mora MT. Diffusion controlled grain growth in primary crystallization: Avrami exponents revisited. J Phys: Condens Matter 1998;10:3833-44.

329. Tien HY, Tannir M, Wu CY, Ebrahimi F. Effect of hydride nucleation rate on the hydrogen capacity of Mg. Int J Hydrogen Energy 2009;34:6343-9.

330. Matsumoto I, Asano K, Sakaki K, Nakamura Y. Hydrogen absorption kinetics of magnesium fiber prepared by vapor deposition. Int J Hydrogen Energy 2011;36:14488-95.

331. Blanco MV, Borzone EM, Baruj A, Meyer GO. Hydrogen sorption kinetics of La-Ni-Sn storage alloys. Int J Hydrogen Energy 2014;39:5858-67.

332. Khanna Y, Taylor T. Comments and recommendations on the use of the Avrami equation for physico-chemical kinetics. Polym Eng Sci 1988;28:1042-5.

333. Pohlmann C, Röntzsch L, Kalinichenka S, Hutsch T, Kieback B. Magnesium alloy-graphite composites with tailored heat conduction properties for hydrogen storage applications. Int J Hydrogen Energy 2010;35:12829-36.